

Systems Design Study of the
Pioneer Venus Spacecraft
Final Study Report

Appendices to
Volume I
Section 7

Systems Design Study of the Pioneer Venus Spacecraft

Final Study Report

Appendices to Volume I Section 7 (Part 2 of 3)

(NASA-CR-137509) SYSTEMS DESIGN STUDY OF
THE PIONEER VENUS SPACECRAFT. APPENDICES
TO VOLUME 1, SECTION 7 (PART 2 OF 3)
Final Study Report (TRW Systems Group)
372 p HC \$21.75

N74-32309
Unclassified
CSCL 22B G3/31 47086

29 July 1973

Contract No. NAS2-7249

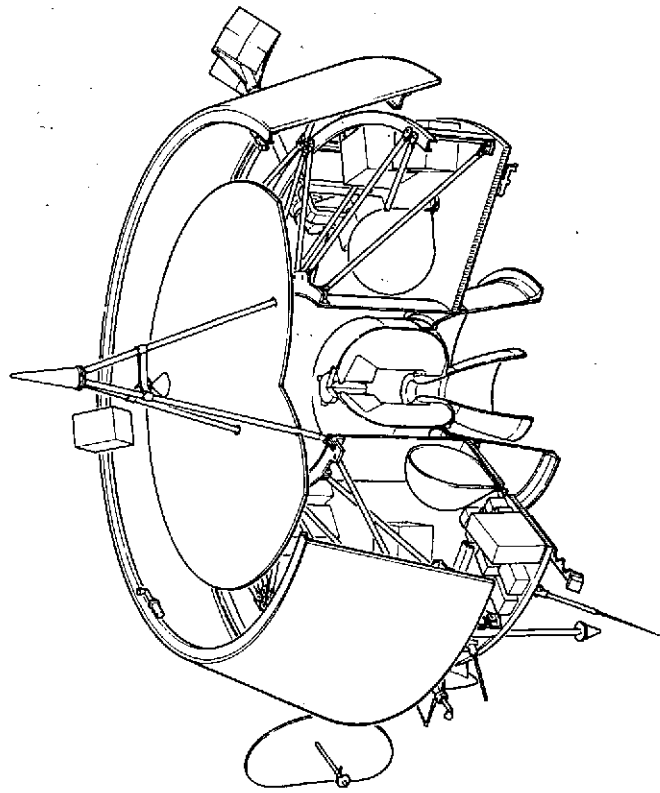
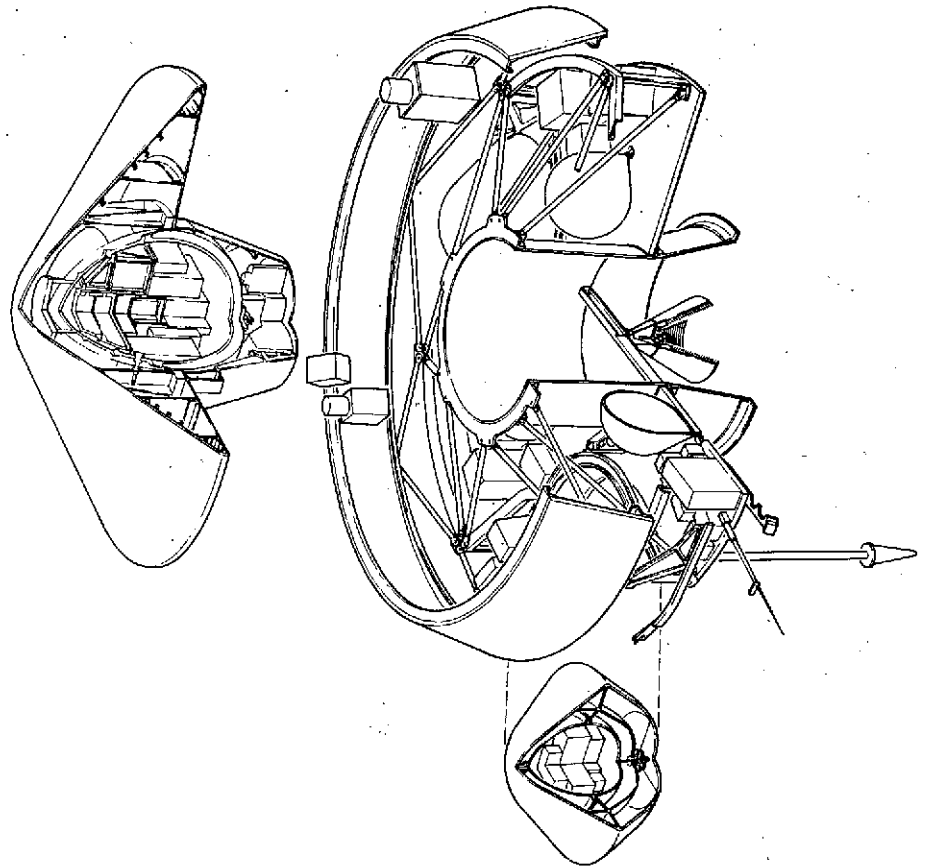
Prepared for

AMES RESEARCH CENTER
NATIONAL AERONAUTICS AND SPACE ADMINISTRATION

TRW
SYSTEMS GROUP

DATA FOR DRAFTING AND PRINTING

TRW
SYSTEMS GROUP



LIST OF VOLUMES

VOLUME I. TECHNICAL ANALYSES AND TRADEOFFS

SECTIONS 1-4 (PART 1 OF 4)

1. Introduction
2. Summary
3. Science Analysis and Evaluation
4. Mission Analysis and Design

VOLUME I. TECHNICAL ANALYSES AND TRADEOFFS

SECTIONS 5-6 (PART 2 OF 4)

5. System Configuration Concepts and Tradeoffs
6. Spacecraft System Definition

VOLUME I. TECHNICAL ANALYSES AND TRADEOFFS

SECTION 7 (PART 3 OF 4)

7. Probe Subsystem Definition

VOLUME I. TECHNICAL ANALYSES AND TRADEOFFS

SECTIONS 8-12 (PART 4 OF 4)

8. Probe Bus and Orbiter Subsystem Definition and Tradeoffs
9. NASA/ESRO Orbiter Interface
10. Mission Operations and Flight Support
11. Launch Vehicle-Related Cost Reductions
12. Long Lead Items and Critical Areas

VOLUME I APPENDICES

SECTIONS 3-6 (PART 1 OF 3)

VOLUME I APPENDICES

SECTION 7 (PART 2 OF 3)

VOLUME I APPENDICES

SECTIONS 8-11 (PART 3 OF 3)

VOLUME II. PRELIMINARY PROGRAM DEVELOPMENT PLAN

VOLUME III. SPECIFICATIONS

CR 137509

NASA [REDACTED]
TRW Document No. 2291-6010-RU-00

Systems Design Study of the Pioneer Venus Spacecraft

Final Study Report

Appendices to Volume I Section 7 (Part 2 of 3)

29 July 1973

Contract No. NAS2-7249

Prepared for

AMES RESEARCH CENTER
NATIONAL AERONAUTICS AND SPACE ADMINISTRATION



MARTIN MARIETTA

CONTENTS

SECTION 7 APPENDICES

- Appendix 7. 1A. Aeroheating of Sphere Cones and Spherical Segment Probes During Venus Entry
- Appendix 7. 1B. Effect of Aerodynamic Coefficients, Inertial Properties, and Roll Rate on the Dynamic Stability of Conical Probes
- Appendix 7. 1C. Wind Tunnel Test Results
- Appendix 7. 2A. Preliminary Evaluation of Teflon as a Reflecting Heat Shield for Venus Entry
- Appendix 7. 4A. Pressure Shell Temperature Gradients with Concentrated Insulation Penetrations
- Appendix 7. 5A. Parachute Sizing Analysis Summaries
- Appendix 7. 6A. Communications and Tracking Using Lognormal Carriers
- Appendix 7. 6B. Discussion on Communications Channel Models
- Appendix 7. 6C. Uncoded Error Probability Performance Comparisons for Lognormal and Rician Channel Models
- Appendix 7. 6D. Performance and Selection of a Coding Method for Pioneer Venus Entry Probes Using PSK/PM Modulation
- Appendix 7. 6E. Multiple Frequency Shift Keying (MFSK) with Convolutional Error Correcting Coding
- Appendix 7. 6F. Radio Absorption and Defocusing Losses in the Venus Atmosphere
- Appendix 7. 6G. Planet Backscatter Multipath Analysis
- Appendix 7. 6H. Telecommunications Design Control Tables for a Thor/Delta Mission
- Appendix 7. 6I. (This Appendix was Deleted)
- Appendix 7. 6J. Antennas Performance Tests with Antenna Mounted on Large Probe Mockup

CONTENTS (CONTINUED)

- Appendix 7. 6K. (This Appendix was Deleted)
- Appendix 7. 6L. Tradeoff Analysis of One-Way Versus Two-Way Doppler Tracing Hardware Implementation
- Appendix 7. 6M. Probe Telecommunications Design Control Tables, Atlas/Centaur Mission 1978 Arrival
- Appendix 7. 8A. Probe Battery Analysis and Selection
- Appendix 7. 8B. Regulated Versus Unregulated Power Bus

ACRONYMS AND ABBREVIATIONS

A	ampere
	analog
abA	abampere
AC	alternating current
A/C	Atlas/Centaur
ADA	avalanche diode amplifier
ADCS	attitude determination and control subsystem
ADPE	automatic data processing equipment
AEHS	advanced entry heating simulator
AEO	aureole/extinction detector
AEDC	Arnold Engineering Development Corporation
AF	audio frequency
AGC	automatic gain control
AgCd	silver-cadmium
AgO	silver oxide
AgZn	silver zinc
ALU	authorized limited usage
AM	amplitude modulation
a. m.	ante meridian
AMP	amplifier
APM	assistant project manager
ARC	Ames Research Center
ARO	after receipt of order
ASK	amplitude shift key
at. wt	atomic weight
ATM	atmosphere
ATRS	attenuated total reflectance spectrometer
AU	astronomical unit
AWG	American wire gauge
AWGN	additive white gaussian noise
B	bilevel
B	bus (probe bus)
BED	bus entry degradation

ACRONYMS AND ABBREVIATIONS (CONTINUED)

BER	bit error rate
BLIMP	boundary layer integral matrix procedure
BPIS	bus-probe interface simulator
BPL	bandpass limiter
BPN	boron potassium nitrate
bps	bits per second
BTU	British thermal unit
C	Canberra tracking station - NASA DSN
CADM	configuration administration and data management
C&CO	calibration and checkout
CCU	central control unit
CDU	command distribution unit
CEA	control electronics assembly
CFA	crossed field amplifier
cg	centigram
c.g.	center of gravity
CIA	counting/integration assembly
CKAFS	Cape Kennedy Air Force Station
cm	centimeter
c.m.	center of mass
C/M	current monitor
CMD	command
CMO	configuration management office
C-MOS	complementary metal oxide silicon
CMS	configuration management system
const	constant construction
COSMOS	complementary metal oxide silicon
c.p.	center of pressure
CPSA	cloud particle size analyzer
CPSS	cloud particle size spectrometer

ACRONYMS AND ABBREVIATIONS (CONTINUED)

CPU	central processing unit
CRT	cathode ray tube
CSU	Colorado State University
CTRF	central transformer rectifier filter
D	digital
DACS	data and command subsystem
DCE	despin control electronics
DDA	despin drive assembly
DDE	despin drive electronics
DDU	digital decoder unit
DDULEI	doubly differenced very long baseline interferometry
DEA	despin electronics assembly
DEHP	di-2-ethylhexyl phthalate
DFG	data format generator
DGB	disk gap band
DHC	data handling and command
DIO	direct input/output
DIOC	direct input/output channel
DIP	dual in-line package
DISS REG	dissipative regulator
DLA	declination of the launch azimuth
DLBI	doubly differenced very long baseline interferometry
DMA	despin mechanical assembly
DOF	degree of freedom
DR	design review
DSCS II	Defense System Communications Satellite II
DSIF	Deep Space Instrumentation Facility
DSL	duration and steering logic
DSN	NASA Deep Space Network
DSP	Defense Support Program
DSU	digital storage unit
DTC	design to cost
DTM	decelerator test model

ACRONYMS AND ABBREVIATIONS (CONTINUED)

DTP	descent timer/programmer
DTU	digital telemetry unit
DVU	design verification unit
E	encounter entry
EDA	electronically despun antenna
EGSE	electrical ground support equipment
EIRP	effective isotropic radiated power
EMC	electromagnetic compatibility
EMI	electromagnetic interference
EO	engineering order
EOF	end of frame
EOM	end of mission
EP	earth pointer
ESA	elastomeric silicone ablator
ESLE	equivalent station error level
ESRO	European Space Research Organization
ETM	electrical test model
ETR	Eastern Test Range
EXP	experiment
FFT	fast Fourier transform
FIPP	fabrication/inspection process procedure
FMEA	failure mode and effects analysis
FOV	field of view
FP	fixed price frame pulse (telemetry)
FS	federal stock
FSK	frequency shift keying
FTA	fixed time of arrival

ACRONYMS AND ABBREVIATIONS (CONTINUED)

G	Goldstone Tracking Station - NASA DSN gravitational acceleration
g	gravity
G&A	general and administrative
GCC	ground control console
GFE	government furnished equipment
GHE	ground handling equipment
GMT	Greenwich mean time
GSE	ground support equipment
GSFC	Goddard Space Flight Center
H	Haystack Tracking Station - NASA DSN
HFFB	Ames Hypersonic Free Flight Ballistic Range
HPBW	half-power beamwidth
htr	heater
HTT	heat transfer tunnel
I	current
IA	inverter assembly
IC	integrated circuit
ICD	interface control document
IEEE	Institute of Electrical and Electronics Engineering
IFC	interface control document
IFJ	in-flight jumper
IMP	interplanetary monitoring platform
I/O	input/output
IOP	input/output processor
IR	infrared
IRAD	independent research and development
IRIS	infrared interferometer spectrometer
IST	integrated system test
I&T	integration and test
I-V	current-voltage

ACRONYMS AND ABBREVIATIONS (CONTINUED)

JPL	Jet Propulsion Laboratory
KSC	Kennedy Space Center
L	launch
LD/AD	launch date/arrival date
LP	large probe
LPM	lines per minute
LPTTL	low power transistor-transistor logic
MSI	medium scale integration
LRC	Langley Research Center
M	Madrid tracking station - NASA DSN
MAG	magnetometer
max	maximum
MEOP	maximum expected operating pressure
MFSK	M'ary frequency shift keying
MGSE	mechanical ground support equipment
MH	mechanical handling
MIC	microwave integrated circuit
min	minimum
MJS	Mariner Jupiter-Saturn
MMBPS	multimission bipropellant propulsion subsystem
MMC	Martin Marietta Corporation
MN	Mach number
mod	modulation
MOI	moment of inertia
MOS LSI	metal over silicone large scale integration
MP	maximum power
MSFC	Marshall Space Flight Center
MPSK	M'ary phase shift keying
MSI	medium scale integration
MUX	multiplexer
MVM	Mariner Venus-Mars

ACRONYMS AND ABBREVIATIONS (CONTINUED)

NAD	Naval Ammunition Depot, Crane, Indiana
N/A	not available
NiCd	nickel cadmium
NM/IM	neutral mass spectrometer and ion mass spectrometer
NRZ	non-return to zero
NVOP	normal to Venus orbital plane
OEM	other equipment manufacturers
OGO	Orbiting Geophysical Observatory
OIM	orbit insertion motor
P	power
PAM	pulse amplitude modulation
PC	printed circuit
PCM	pulse code modulation
PCM-PSK-PM	pulse code modulation-phase shift keying-phase modulation
PCU	power control unit
PDA	platform drive assembly
PDM	pulse duration modulation
PI	principal investigator proposed instrument
PJU	Pioneer Jupiter-Uranus
PLL	phase-locked loop
PM	phase modulation
p. m.	post meridian
P-MOS	positive channel metal oxide silicon
PMP	parts, materials, processes
PMS	probe mission spacecraft
PMT	photomultiplier tube
PPM	parts per million pulse position modulation
PR	process requirements
PROM	programmable read-only memory
PSE	program storage and execution assembly

ACRONYMS AND ABBREVIATIONS (CONTINUED)

PSIA	pounds per square inch absolute
PSK	phase shift key
PSU	Pioneer Saturn-Uranus
PTE	probe test equipment
QOI	quality operation instructions
QTM	qualification test model
RCS	reaction control subsystem
REF	reference
RF	radio frequency
RHCP	right hand circularly polarized
RHS	reflecting heat shield
RMP-B	Reentry Measurements Program, Phase B
RMS	root mean square
RMU	remote multiplexer unit
ROM	read only memory rough order of magnitude
RSS	root sum square
RT	retargeting
RTU	remote terminal unit
S	separation
SBASI	single bridgewire Apollo standard initiator
SCP	stored command programmer
SCR	silicon controlled rectifier
SCT	spin control thrusters
SEA	shunt electronics assembly
SFOF	Space Flight Operations Facility
SGLS	space ground link subsystem
SHIV	shock induced vorticity
SLR	shock layer radiometer
SLRC	shock layer radiometer calibration

ACRONYMS AND ABBREVIATIONS (CONTINUED)

SMAA	semimajor axis
SMIA	semiminor axis
SNR	signal to noise ratio
SP	small probe
SPC	sensor and power control
SPSG	spin sector generator
SR	shunt radiator
SRM	solid rocket motor
SSG	Science Steering Group
SSI	small scale integration
STM	structural test model
STM/TTM	structural test model/thermal test model
STS	system test set
sync	synchronous
TBD	to be determined
TCC	test conductor's console
T/D	Thor/Delta
TDC	telemetry data console
TEMP	temperature
TS	test set
TTL MSI	transistor-transistor logic medium scale integration
TLM	telemetry
TOF	time of flight
TRF	tuned radio frequency
TTM	thermal test model
T/V	thermo vacuum
TWT	travelling wave tube
TWTA	travelling wave tube amplifier
UHF	ultrahigh frequency
UV	ultraviolet

ACRONYMS AND ABBREVIATIONS (CONTINUED)

VAC	volts alternating current
VCM	vacuum condensable matter
VCO	voltage controlled oscillator
VDC	volts direct current
VLBI	very long baseline interferometry
VOI	Venus orbit insertion
VOP	Venus orbital plane
VSI	Viking standard initiator
VTA	variable time of arrival
XDS	Xerox Data Systems

SECTION 7 APPENDICES

- Appendix 7. 1A. Aeroheating of Sphere Cones and Spherical Segment Probes During Venus Entry
- Appendix 7. 1B. Effect of Aerodynamic Coefficients, Inertial Properties, and Roll Rate on the Dynamic Stability of Conical Probes
- Appendix 7. 1C. Wind Tunnel Test Results
- Appendix 7. 2A. Preliminary Evaluation of Teflon as a Reflecting Heat Shield for Venus Entry
- Appendix 7. 4A. Pressure Shell Temperature Gradients with Concentrated Insulation Penetrations
- Appendix 7. 5A. Parachute Sizing Analysis Summaries
- Appendix 7. 6A. Communications and Tracking Using Lognormal Carriers
- Appendix 7. 6B. Discussion on Communications Channel Models
- Appendix 7. 6C. Uncoded Error Probability Performance Comparisons for Lognormal and Rician Channel Models
- Appendix 7. 6D. Performance and Selection of a Coding Method for Pioneer Venus Entry Probes Using PSK/PM Modulation
- Appendix 7. 6E. Multiple Frequency Shift Keying (MFSK) with Convolutional Error Correcting Coding
- Appendix 7. 6F. Radio Absorption and Defocusing Losses in the Venus Atmosphere
- Appendix 7. 6G. Planet Backscatter Multipath Analysis
- Appendix 7. 6H. Telecommunications Design Control Tables for a Thor/Delta Mission
- Appendix 7. 6I. (This Appendix was Deleted)
- Appendix 7. 6J. Antennas Performance Tests with Antenna Mounted on Large Probe Mockup
- Appendix 7. 6K. (This Appendix was Deleted)
- Appendix 7. 6L. Tradeoff Analysis of One-Way Versus Two-Way Doppler Tracing Hardware Implementation
- Appendix 7. 6M. Probe Telecommunications Design Control Tables, Atlas/Centaur Mission 1978 Arrival
- Appendix 7. 8A. Probe Battery Analysis and Selection
- Appendix 7. 8B. Regulated Versus Unregulated Power Bus

APPENDIX 7.1A
AEROHEATING OF SPHERE CONES AND SPHERICAL
SEGMENT PROBES DURING VENUS ENTRY

1. Summary	7. 1A-1
2. Analysis	7. 1A-1
3. LRC Comparison	7. 1A-18
4. Nomenclature	7. 1A-21
5. References	7. 1A-23

APPENDIX 7.1A
AEROHEATING OF SPHERE CONES AND SPHERICAL
SEGMENT PROBES DURING VENUS ENTRY

1. SUMMARY

The procedures for predicting the aeroheating environment of Venus entry probes are outlined herein. After some consideration, a number of assumptions were adopted in order to make the prediction techniques tractable. Among these assumptions are thermochemical equilibrium, uncoupled radiative and convective processes, and uncoupled ablation products effects. The single strip method of integral relations, appropriately constrained, is shown to provide adequate inviscid results as a basis for heating calculations on blunt configurations. Techniques for prediction of the laminar, transitional, and turbulent convective environment are outlined and shown to agree with data. The prediction of radiative heating in C, N, and O gas mixtures is discussed and a practical scheme adopted. A comparison with LRC calculations is made.

2. ANALYSIS

Science measurement requirements dictate high drag shapes for many planetary entry probe missions. A family of forebody configurations that has been extensively studied for this purpose is the large angle sphere cones, including spherical segments (zero length cone) as members of the family. The present discussion will be limited to these geometries. A schematic of a probe and its associated flow field is shown in Figure 7.1A-1. Although most of the computer programs developed for the aerothermochemical analysis are for gases of arbitrary elemental composition, results will be confined to $\text{CO}_2\text{-N}_2$ mixtures with CO_2 the primary component (90-100%). This corresponds to the composition range presently proposed for the Venus atmosphere (Reference 1). The gases are considered to be in thermochemical equilibrium. At the velocities and freestream densities encountered in Venus entry near peak heating times, shock layer gas particle collision frequencies are sufficiently high to ensure chemical equilibrium. Although the proper chemical system and reaction model for nonequilibrium Venus entry analysis is not clear and reaction rate data are uncertain, a recent study (Reference 2) has indicated that the assumption of equilibrium

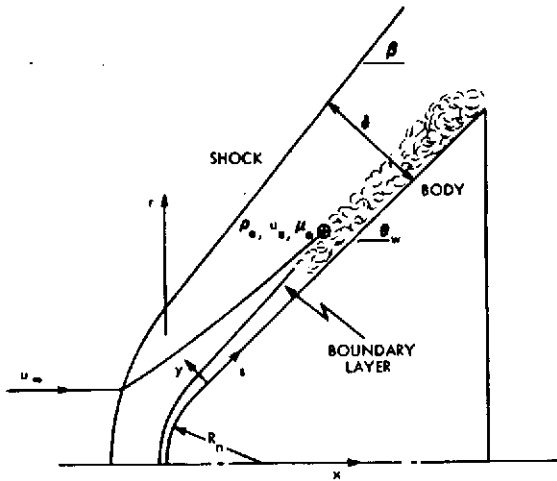


Figure 7.1A-1. Assumed Flow Field Model

chemistry during the maximum heating period is valid. From a convective heating standpoint, this assumption is probably conservative, depending on the wall catalicity used in the boundary layer analysis. Nonequilibrium conditions result in higher temperatures in portions of the shock layer and possible attendant local increases in radiative intensity. As with superorbital entry into earth (Reference 3), nonequilibrium effects are also assumed unimportant for engineering predictions of Venus entry radiative heating. An efficient chemical equilibrium procedure for arbitrary gas mixtures (Reference 4) has been used in most instances to provide the necessary thermochemical data and species population results. The transport properties are evaluated simultaneously with the techniques of Bartlett, et al., (Reference 5) used extensively in complex viscous calculations (Reference 6).

The necessary heating environment results for heat shield design are cold wall, no-blowing convective and radiative heating rate histories. Convection and radiation are computed in an uncoupled manner in the present analysis. The reduction in convective heating due to nonadiabatic shock layer effects is assumed negligible. The radiative calculations, however, are modified to approximately account for these effects. The reduction in incident radiation due to the presence of ablation products is also ignored. Recent studies (Reference 7) show that the modest mass loss rates of a typical carbonaceous material during Venus entry reduce radiative heating by less than 10% for the trajectories of interest.

2.1 Inviscid Calculations

Consider the family of large angle sphere cones. For a sufficiently slender sphere cone, the sonic point on the body occurs on the spherical section and the cone region is entirely supersonic. A number of analytical techniques are available to analyze this situation. Among those for the subsonic regime are the inverse methods (References 8 and 9) where a body shape is determined from a given shock shape. Results from this are coupled with the method of characteristics (Reference 10) for the supersonic portion of the flow. The direct methods, i.e., a given body shape, are represented in part by the method of integral relations (References 11, 12 and 13) and time dependent techniques (References 14 and 15). This last method has perhaps the most promise for analyzing complex shapes and including all the physical processes possibly important in planetary entry such as radiative transport, nonequilibrium chemistry, etc. When the cone angle becomes sufficiently large, the sonic point moves off the sphere and the transition from sub- to supersonic flow occurs in a singular manner at the aft corner. In this case a rapid drop in pressure to the sonic value occurs near the corner. Simple Newtonian results will not predict this drop which can be important both aero- and thermodynamically. In addition, the shock layer may be thicker than approximate calculations based on a supersonic forebody would indicate, with the result that radiative heating to the body might be underestimated. Inverse methods are not easily adapted to the problem because of the corner singularity.

The time dependent procedure is well suited to the problem; however, it is expensive in terms of computing time and no program is presently available that includes the real gas effects currently sought. The method of integral relations is particularly well suited to the present problem, i.e., blunt bodies with sharp sonic corners at zero angle of attack. A number of investigators have addressed this particular problem (References 16, 17 and 18) in each case for an ideal gas. Extension of the technique to an equilibrium gas mixture is straightforward requiring only a sufficiently efficient chemical equilibrium procedure for arbitrary gas mixtures (Reference 4). The basic method (Reference 19), in theory, can be extended to any order of accuracy by dividing the shock layer into enough strips. For a parametric study of planetary entry, the primary shock properties required

are a good representation of the surface pressure distribution for convective heat transfer studies and aerodynamics, and accurate shock layer thickness calculations for radiative heat transfer predictions. Application of the method of integral relations has shown that these two quantities are quite accurately given by the single strip or first approximation to the method of integral relations provided care is taken in the stagnation region. A computer program, SSMIR (Single Strip Method of Integral Relations), has been developed for solution of the appropriate equations for axisymmetric bodies with sharp sonic corners in an equilibrium flow of an arbitrary elemental composition. If the cone angle is low enough so that the body sonic point occurs on the spherical sector, an inverse solution coupled with the method of characteristics in pure CO₂ at chemical equilibrium provides this inviscid flow field results required.

The present programs and results are for axisymmetric bodies at zero angle of attack. Estimates of angle of attack during periods of significant heating during Venus entry indicate that they will be small (less than 5 degrees). Windward and leeward pressure and shock standoff distributions have been approximated with the equivalent cone assumption ($\theta_{c_{\text{eff}}} = \theta_c \pm \alpha$) using the programs just described.

The SSMIR program provides results only to the body sonic point. In order to study the effect of corner radius on the convective environment, a pressure distribution around the corner is required. A procedure was devised for predicting this distribution that involves a matching between the SSMIR results and a Newtonian-like variation to a calculated minimum value. Figure 7.1A-2 compares this prediction procedure with experimental data (Reference 21) for the Apollo shape. The agreement is seen to be quite good, giving confidence that the same matching procedure can be applied to other configurations of interest. Also shown are results from a Prandtl-Meyer expansion analysis. This prediction procedure was not as successful.

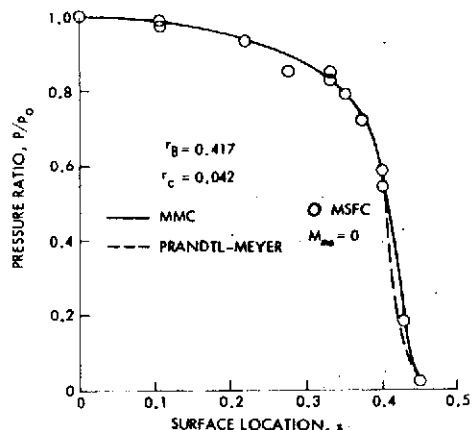


Figure 7.1A-2. A Comparison of Analytical and Experimental Pressure Distribution Results for the Apollo Configuration

2.2 Convective Processes

A common assumption made in calculating convective loads to entry bodies is that the body streamline in an inviscid flow field calculation can be used as a boundary layer edge streamline for predicting the viscous flow field. If the body is sufficiently blunt, the assumption is good; i.e., boundary layer edge properties are properly based on flow that has passed through the normal or near-normal portion of the bow shock. As the boundary layer grows along the body; however, mass is entrained until finally flow that has passed through more oblique sections of the shock enters the boundary layer. In passing through a weaker shock, less energy is lost, and boundary layer edge velocities will be higher. This condition leads to increased boundary layer gradients, and consequently, higher convective heating and shear stress. Earlier studies (References 22 and 23) have indicated the importance of including the effects of this boundary layer swallowing on the convective heating and shear levels during Venus entry.

Basic to the present procedure for estimating the vorticity effect is that the boundary layer equations apply; i.e., the Reynolds number is sufficiently high that the shock layer can be conceptually divided into an inviscid and a viscous layer. The solution of the inviscid flow field provides the edge boundary conditions which (along with the wall conditions) are necessary for solution of the boundary layer equations. No perturbations of the inviscid flow due to boundary layer growth are considered. The effect of bow shock induced vorticity in this case can be accounted for by determining at any body location the boundary layer edge streamline shock

entry point (Figure 7.1A-1) by mass balance considerations. Equating the mass flow rates through the shock and in the boundary layer yields r_s , the edge streamline shock entry radius. With the shock shape and body pressure known from an inviscid solution, conditions behind the shock are found with the shock equations, and a subsequent isentropic expansion to the body pressure leads to the boundary layer edge conditions. This procedure is of course only a first order analysis of viscous-inviscid interaction. However, its application to predictions of convective loads has been extremely useful and has led to quite good results.

For present purposes, locally similar boundary layer solutions are applicable thus simplifying the total problem solution. Considering first laminar flow, the following similarity variables are introduced.

$$\xi = \int_0^s \rho_e \mu_e^{u_e} r_b^{2j} ds$$

$$\eta = R_n^{1/2} \frac{\rho_e u_e r_b^j}{(2\xi)^{1/2}} \int_0^y \frac{\rho}{\rho_e} dy$$

where, as noted in the Nomenclature, all distances are normalized by the nose radius. From the mass balance equations

$$r_s = \left[\frac{j+1}{\rho_\infty u_\infty} \frac{(2\xi)^{1/2}}{R_n^{1/2}} (f_e - f_w) \right]^{1/j+1}$$

or

$$r_s = \left[(j+1) 2.266 \frac{\mu_e r_b^j}{\rho_\infty u_\infty R_n} Re_\theta \right]^{1/j+1}$$

where the definition of the momentum thickness Reynolds number is

$$Re_\theta = R_n^{1/2} \frac{(2\xi)^{1/2}}{\mu_e r_b^j} \int_0^{\eta_e} f' (1-f') d\eta$$

and the modified Blasius value for the integral is used.

In evaluating the heat transfer and shear stress at the wall there is

$$q^c = h_c (H_r - H_w)$$

$$\tau_w = \text{Pr}^{2/3} h_c u_e$$

where the modified Reynolds analogy has been used. For laminar flow, the heat transfer distribution of Lees (Reference 24) is applied, i.e.

$$\frac{h_L}{h_{Lo}} = F_L = \frac{\rho_e \mu_e u_e r_b^j}{\left[(j+1) \rho_o \mu_o \frac{du_e}{ds} \right]_o^{1/2} (2\xi)^{1/2}}$$

Any of the well known correlations (e.g., References 25, 26, 27 and 28), may be used to evaluate the stagnation point heat transfer coefficient h_{Lo} . The correlation of Hoshizaki (Reference 25) is used in the present work. It is a careful study of stagnation point heat transfer in pure CO_2 at hypersonic velocities and is given by

$$\frac{q_o^c}{H_o - H_w} = h_{Lo} = 70.55 \left[\frac{P_o}{R_n} \frac{du_e}{ds} \right]_o^{1/2} u_\infty^{1.69}$$

For present purposes the value of f_w in the shock radius equation is assumed zero, i.e., there is no mass transfer through the wall. Note that, because of the negative sign in the wall stream function equation, the effect of blowing mass transfer is to increase the vorticity effect by thickening the boundary layer.

The locally similar solution of Bromberg et al., (Reference 29) as modified by Hearne (Reference 30) is used for the turbulent calculation. From these analyses, using the modified Reynolds analogy and the integral energy equation, there is

$$\xi = \int_0^s \rho_e \mu_e^{1/4} u_e r_b^{5j/4} ds$$

and

$$r_s = \left[\frac{(j+1)}{\rho_\infty u_\infty} \frac{0.186}{R_n^{1/5} Pr^{8/15}} (2\zeta)^{4/5} \right]^{1/(j+1)}$$

or

$$r_s = \left[9(j+1) \frac{\mu_e r_b^j}{\rho_\infty u_\infty R_n} Re_\theta \right]^{1/(j+1)}$$

with

$$Re_\theta = 2.07^{-2} \frac{R_n^{4/5}}{Pr^{8/15}} \frac{(2\zeta)^{4/5}}{\mu_e r_b^j}$$

The distribution of turbulent heat transfer coefficient over the body is

$$F_T = \frac{\rho_e \mu_e^{1/4} u_e r_b^{j/4}}{\left[(j+1) \rho_o \mu_o^{1/4} \left(\frac{du_e}{ds} \right)_o \right]^{4/5} (2\zeta)^{1/5}}$$

The reference value of turbulent heat transfer coefficient h_{To} is given by

$$h_{To} = \frac{3.31^{-2}}{R_n^{1/5}} \left[(j+1) \rho_o \mu_o^{1/4} \left(\frac{du_e}{ds} \right)_o \right]^{4/5}$$

with

$$h_T = h_{To} F_T / Pr^{8/15}$$

Determination of the beginning of boundary layer transition is a difficult problem. No reasonable transition criterion can possibly include all of the pertinent variables that effect the transition process. A common criterion for the beginning of transition is a critical value of laminar momentum thickness Reynolds number. A criterion especially for blunt body, low Mach number flow fields has been developed (Reference 31) in which the critical Re_θ has been correlated from ground and flight test data as a function of edge Mach number M_e and a shock induced vorticity parameter Nv_L defined herein as

$$Nv_L = \frac{1}{\rho_\infty u_\infty R_n^{1/2}} \left[(j+1) \rho_o \mu_o \left(\frac{du_e}{ds} \right)_o \right]^{1/2}$$

This parameter, an inverse Reynolds number, decreases during entry. The criteria is depicted in Figure 7.1A-3. The increased boundary layer stability with increasing Mach number for all Nv_L is noted. The effect of shock induced vorticity is seen to be destabilizing as the critical Reynolds number increases with decreasing Nv_L . A constant value of Re_θ independent of other parameters has also been used as a transition criterion.

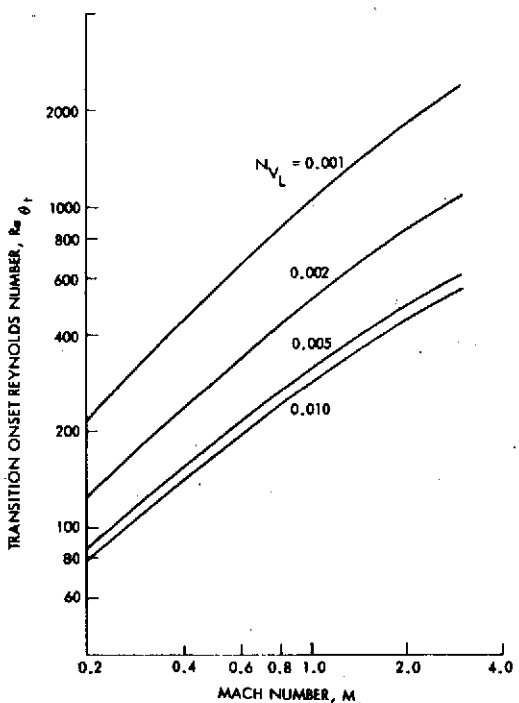


Figure 7.1A-3. Blunt Body Boundary Layer Transition Criterion

The convective heating in the transition regime is determined by the extension of Emmons spot theory (Reference 32) as outlined by Chen and Thyson (Reference 33). In this procedure an intermittancy factor is defined as

$$\gamma = 1 - \exp \left[-R_n^2 G_t r_t \int_{s_t}^s \frac{1}{r} ds \int_{s_t}^s \frac{1}{u_e} ds \right]$$

where the subscript t denotes the start of transition and G_t is the spot formation rate parameter. Following the development of Reference 33, this parameter can be represented by

$$R_n^2 G_t = \left(\frac{Re_n}{A} \right)^2 \frac{u_e}{Re^{8/3}}$$

where

$$A = 60 + 4.68 M_{e_t}^{1.92}$$

The heat transfer rate is then determined from the relation

$$q^c = q_L^c + (q_T^c - q_L^c) \gamma$$

The intermittency is also used to calculate r_s , τ_w and Re_θ in the transition regime.

The procedure is then straightforward. An initial value of r_s is obtained from a stagnation point limiting analysis. Starting at the stagnation point, ξ and ζ are obtained by integration along the body and r_s , the edge streamline shock entry radius, is found from the appropriate relation. With this value of r_s , the shock angle β is determined, a shock solution performed, and an isentropic expansion made to the known body pressure thus establishing the boundary layer edge conditions. The procedure is continued down the body using the shock radius extrapolated from the previous point to evaluate edge properties. A computer program SHIV (Shock Induced Vorticity) has been developed to perform these operations for a gas of arbitrary elemental composition in equilibrium.

The axisymmetric analog (Reference 34) has been used for a number of years to obtain approximate solutions to the three-dimensional boundary layer equations. To apply the procedure, the metric h describing the streamline divergence must be determined and used to replace r, the radial coordinate in the appropriate flow equations. The difficulty lies in that h is a function of the inviscid flow and not geometry alone. In flows for which there is a plane of symmetry, e.g., the windward or leeward generators of the present probes, considerable simplification occurs and a complete three-dimensional inviscid solution is not required. Techniques for determination

of h are well developed (Reference 35) including the effects of boundary layer swallowing (References 30 and 31). Design angle of attack calculations will include these procedures. Sensitivity studies, however, have been conducted with equivalent cone procedures (Reference 36), that is, without including the crossflow terms. The correct trends, if not exact values, can be predicted. The most notable result of the study was the effect on boundary layer transition, delaying it on the windward and promoting it on the leeward side.

Application of the foregoing procedure using the SHIV program to recent ground test data (Reference 37) is demonstrated in Figure 7.1A-4. Shown are nondimensional cold wall heat transfer distributions on the spherical section of a slender sphere cone configuration. The basic study reported on in the reference was one of transitional and turbulent heat transfer measurements on a yawed blunt conical nosetip. At the highest freestream Reynolds number based on nose radius [$(10.1 \cdot 10^6)$], data from the entire angle of attack range (0 - 21 degrees) are included in the data band as measured from the most forward body point. The data on the spherical section should be self similar in this coordinate system. Transition in the SHIV program was forced at the point determined from the data. It is noted in the reference that premature transition, evidently caused by surface roughness, occurred at the lowest Reynolds number [$2.42 \cdot 10^6$] shown. It is felt that the SHIV results provide a reasonable, slightly conservative, representation of the data. Although entropy swallowing was included, its effect was small, less than a 5% increase in heating at the farthest aft position shown. The transitional heating procedure gives an adequate prediction of the distribution. The artificially tripped data are matched most successfully.

Results from the SHIV program when applied to a contemplated Pioneer Venus large probe configuration are given in Figure 7.1A-5. Both cold wall no-blowing heating rate and shear stress distributions are depicted. The freestream conditions provide a more severe environment than present launch dates would support but were chosen to demonstrate the convective environment prediction procedure. The basic analysis is denoted by the most prominent solid line. Comparing this result with those of an isentropic boundary layer edge shows the large effect of shock induced vorticity.

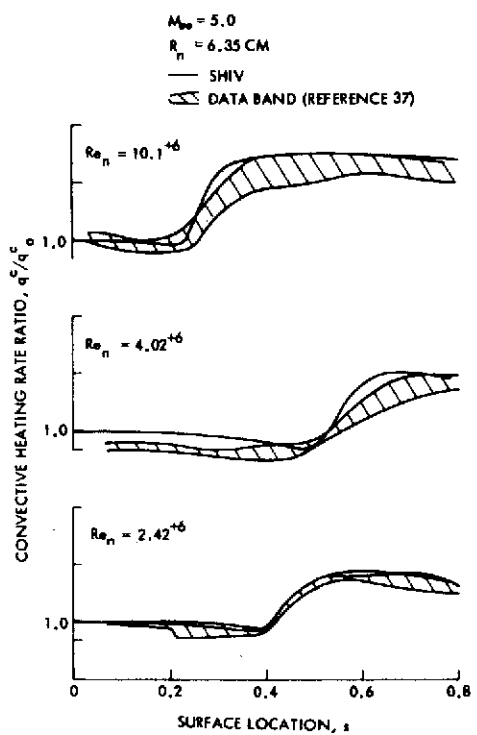


Figure 7.1A-4. Comparison of Analytical and Experimental Convective Heating Distributions on a Spherical Segment

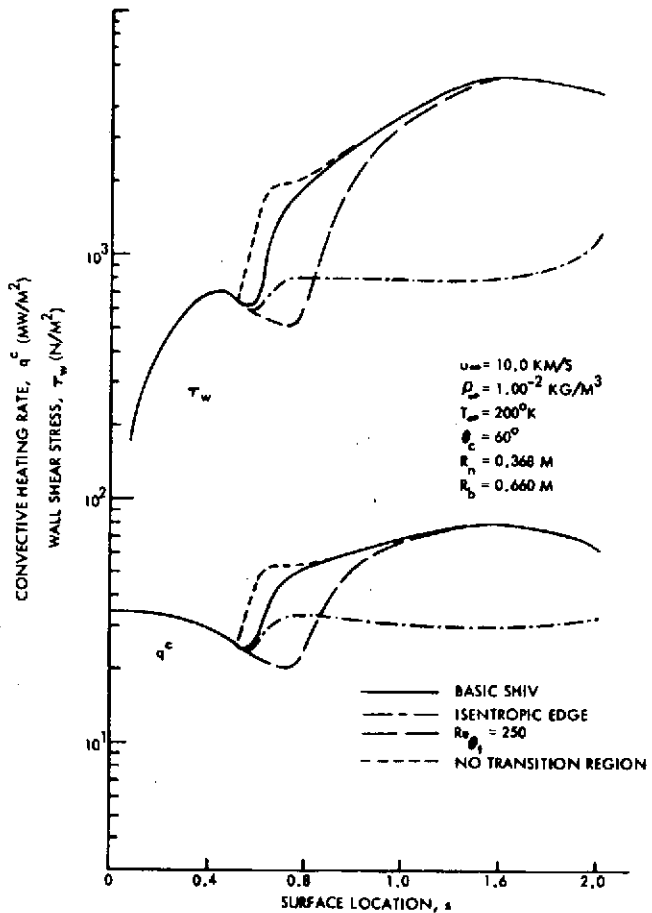


Figure 7.1A-5. Distribution of Cold Wall No-Blowing Convective Heating Rate and Shear Stress

While the laminar nose is affected little at these freestream conditions by boundary layer swallowing, the much larger growth rate of the turbulent boundary layer leads to a large vorticity effect. Peak heating rates aft on the body are more than twice as large and shear stress (even more sensitive to edge velocity) nearly five times as large as those values computed with an isentropic edge. A zero length transition region serves only to alter the distribution until fully developed turbulent heating is established. A transition criterion of $Re_\theta = 250$ independent of edge Mach number leads to later transition in this case. Peak heating on the body is still unaffected. Note that while the isentropic edge results show the expected increase in both heating and shear as the pressure drops near the body base to the sonic point, the values including boundary layer swallowing do not exhibit a rise but instead follow the pressure distribution. The large edge velocity in the latter case leads to a lower potential for high edge velocity gradients in the corner region. The higher convective environment expected at the corner may not exist. Initial corner results have been obtained for the Apollo configuration at the time of peak stagnation point heating. This geometry was chosen for the initial study because of the experimental results for both pressure and heating distribution that were available (Reference 21). The pressure prediction was already shown to be in good agreement with the data (Figure 7.1A-2). Two different analytical procedures were used to predict the heating distribution. The first is the SHIV program and the second technique is the BLIMP computer code (Reference 6), a detailed solution of the nonsimilar boundary layer equations. The second procedure should be more accurate, particularly in regions of large pressure gradient such as those that occur at the aft corner. The results from the two calculations are compared with the experimental data in Figure 7.1A-6. Within the data scatter either technique provides a reasonable comparison. The greatest discrepancy between the two calculations is in the corner region where the BLIMP code predicts higher values. With this configuration the flow remained laminar on the body and vorticity effects were small.

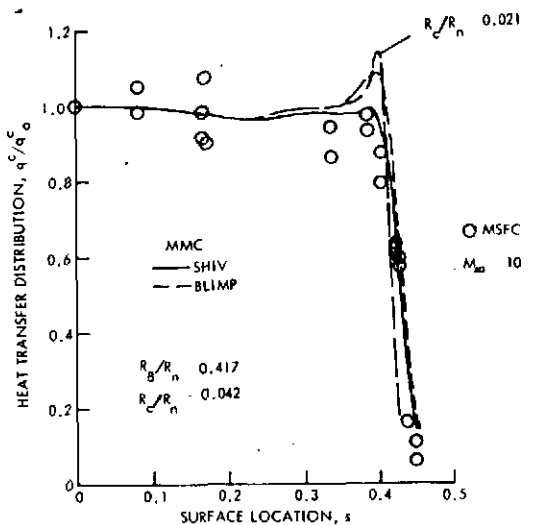


Figure 7.1A-6. Comparison of Analytical and Experimental Convective Heating Distributions for the Apollo Configuration

The effect of a change in corner radius on the convective environment for the same configuration was calculated with the BLIMP program. The results for a corner radius one half of the nominal value are also shown in Figure 7.1A-6. As expected, the smaller corner radius with its attendant higher pressure gradients experiences a more severe environment.

2.3 Radiative Heating

The ultimate in predicting the heating environment experienced by an entry vehicle would be a computer code for solving the coupled viscous three-dimensional shock layer conservation equations of mass, momentum, energy, and non-gray radiative transport for an arbitrary reacting gas mixture. Such a code does not presently exist and would be prohibitively expensive to run in a design effort if it did. A presently accepted method of predicting the environment for a Venus entry probe is to uncouple the radiation and fluid mechanics and calculate the radiative heating from a slab of gas of thickness equal to the adiabatic shock stand-off distance and with constant equilibrium thermochemical properties. Subsequently, this radiative heat flux is modified by a cooling factor which accounts in part for the actual decay in temperature across the shock layer and the thinning of the layer itself. A computer code is now available to calculate in great detail the radiative heating for a slab of arbitrary pressure, temperature and elemental composition in chemical equilibrium. The calculation includes emission and absorption for all the known important radiating

processes in gas mixtures of C, N, and O and their molecules and ions (Reference 38). This computer code is used to provide the required isothermal slab radiation. Recently, a computer program was developed by W. A. Page of NASA Ames for calculating the stagnation point coupled conservation equations and has been applied to Venus entry problems (Reference 39). The code is restricted by the radiative transport data available to a 90% CO₂ -10% N₂ atmospheric mixture and two postshock pressures, 1.0 and 10 atm. The non-gray radiative transport model is a multiband treatment modeled after those used for air calculations (Reference 40) with additional bands to account for the important processes resulting from the addition of carbon. This model is well suited to iterative numerical calculations and six bands are presently included. The selection of the bands and calculation of the appropriate absorption coefficients is a formidable task.

At the request of MMC, Page (References 41 and 42) provided the coupled radiative heating results obtained from the Ames program, making additional runs where necessary so that a complete matrix of cases of interest to Venus entry was obtained. This matrix included for each pressure possible (1.0 and 10 atm) freestream velocities from 7 to 12 km/sec and adiabatic shock stand-off distances of 0.3, 1.0, 3.0, and 10 cm. With the band model results as provided by Page, the corresponding isothermal slab heating was calculated. The ratio of the coupled results and the isothermal slab results from Page's model is the radiative cooling factor necessary for design calculations. The radiative cooling parameter is defined as

$$\Gamma = \frac{2q_{ad}^r}{\frac{1}{2} \rho_\infty u_\infty^3}$$

the ratio of the isothermal radiative heat flux in all directions to the total flow energy. This parameter has been used in previous attempts at correlation of the cooling factor as it appears as the coefficient of the flux divergence term in the normalized energy equation.

The cooling factor is plotted against the radiation cooling parameter in Figure 7.1A-7. The solid line is the suggested correlation of these numerical data. The dashed line is a correlation for air. At values of the cooling parameter usually obtained in the predictions (0.004 - 0.040), the present correlation provides further relief of from 6 to 14% over the air correlation. This difference is primarily due to the optically thin-optically thick aspects of the present emission spectrum as compared to those of air. Although the present correlation was developed for a cold gas mixture of 90% CO₂-10% N₂, its use with mixtures containing even less N₂ can be made with confidence since the radiation is dominated by processes involving the C and O species in all these cases. It is emphasized that the six-band model has been used only for the development of the cooling factor correlation.

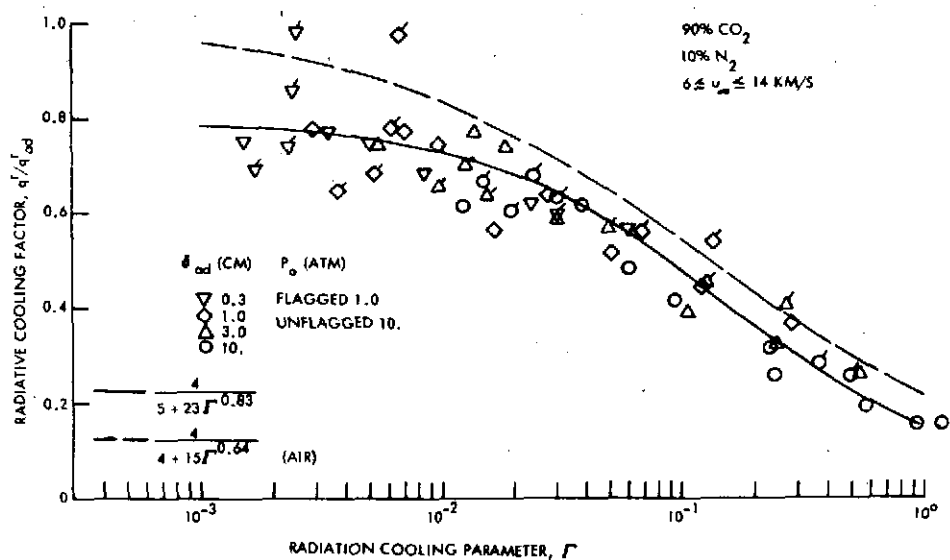


Figure 7.1A-7. Radiative Cooling Factor for Venus Entry

The following procedure is applied to determination of the radiative distribution along the probe. The adiabatic standoff distance is determined from the inviscid calculations outlined previously. The slab pressure is assumed to be the local body pressure and the cold gas composition that of the freestream. Choice of the appropriate temperature for the isothermal slab calculation is difficult, particularly away from the stagnation region. With the strong dependence of radiation on the temperature, use of the postshock value is not appropriate because of the entropy layer influence on

the short blunt bodies. For design purposes, the isothermal slab calculation is performed at the boundary layer edge temperature as calculated in the convective analysis and including boundary layer swallowing. This is a conservative approach but less so as the local body angle increases. The isothermal slab radiative flux to the body is calculated with the detailed procedure of Reference 38.

In determining the radiation cooling factor to be applied, the radiation cooling parameter is assumed to be

$$F = \frac{2q_{ad}^r}{\frac{1}{2} \rho_\infty u_\infty^3 \sin^3 \theta_w}$$

which reduces to the previous value at the stagnation point. The angle modification leads to a relatively greater cooling effect aft on the body.

An equivalent cone procedure has been used to determine the sensitivity of cone radiative heating to angle of attack (Reference 37). Two effects are seen to be important. First, as previously seen, the shock layer tends to thicken as the cone angle increases with the radiation increasing nearly proportionately. More important, however, is the strong dependence of radiative heating on temperature and the increase in the appropriate temperature with effective cone angle.

2.4 Base Region Heating

A conservative approach has been adopted in studies of base heating. Because of the strong influence of boundary layer turbulence on the base region convective environment (Reference 43), the base heating is estimated as some fraction of the aft corner environment. For probes with a relatively flat base, this fraction is assumed to be 0.03 after study of test data from other planetary probe studies (Reference 44). For probe shapes in which the slope of the afterbody from the corner is less than 70 degrees, the fraction is assumed to be 0.05 (Reference 45). In each case the heating is assumed constant over the afterbody and the same fraction is applied to both the convective and radiative heating rates.

3. LRC COMPARISON

Some results from the studies underway at LRC in support of the Pioneer Venus Project have recently been received. The initial release (Reference 46) contained the results from a computer code for calculation of the radiative inviscid flow about blunt bodies using a time asymptotic technique. Subsequently, results from an analysis coupling the inviscid outer layer with an inner viscous layer including steady-state ablation of a carbon phenolic material were obtained (Reference 47). The chemical equilibrium and radiative transport subroutines used in the LRC analyses are the same as those discussed previously. A comparison of the LRC and MMC results then should provide an estimate of the error involved in uncoupling the various processes and ignoring the ablation mass loss effect on radiative heating.

In Figure 7.1A-8, results from the LRC inviscid study are compared with those obtained in the present work for the 60 degree-sphere-cone. The pressure distributions compare favorably with the exception of the aft corner region. Details of the LRC procedure are lacking, but it seems no special consideration is given to the sonic point occurring at the maximum body radius. This is a particularly difficult region to handle in time-dependent procedures (Reference 15) such as those used by LRC. To properly perform convective calculations, the correct pressure distribution must be used. The MMC results do include the rapid drop in pressure as the sonic corner is approached. The agreement between the shock standoff distance also worsens further back on the body. This could be due to the incorrectly predicted pressure distribution in the corner region by LRC and the thinning of the shock layer by radiation as included by LRC. For the 45 degree-sphere-cone, the body sonic point occurs on the sphere and no special consideration is required at the body maximum radius. As seen in Figure 7.1A-9, both the pressure and shock layer thickness compare very well. Calculation mesh sizes with time-dependent techniques are generally much coarser than those used for the present MMC results. Thus, the LRC results may not accurately describe the overexpansion and subsequent recompression occurring near the sphere cone junction, the region of greatest disagreement.

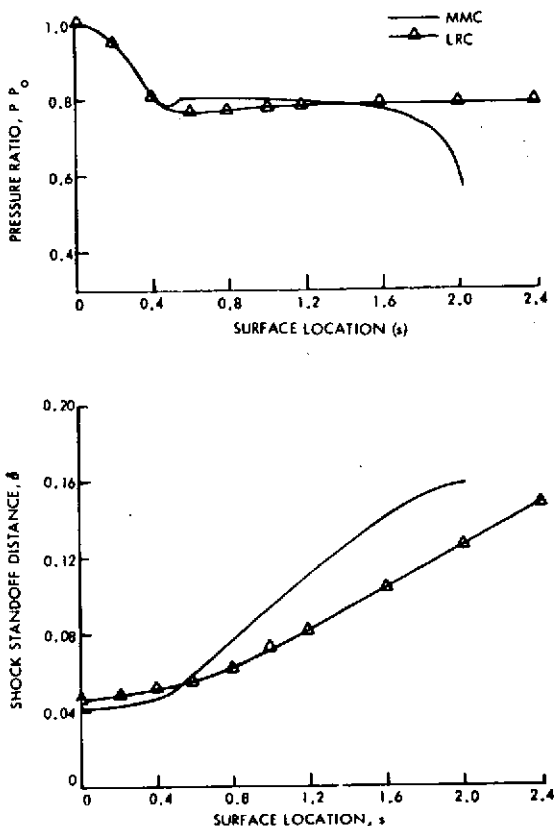


Figure 7.1A-8. Inviscid Analysis Results for the 60° Sphere-Cone Configuration

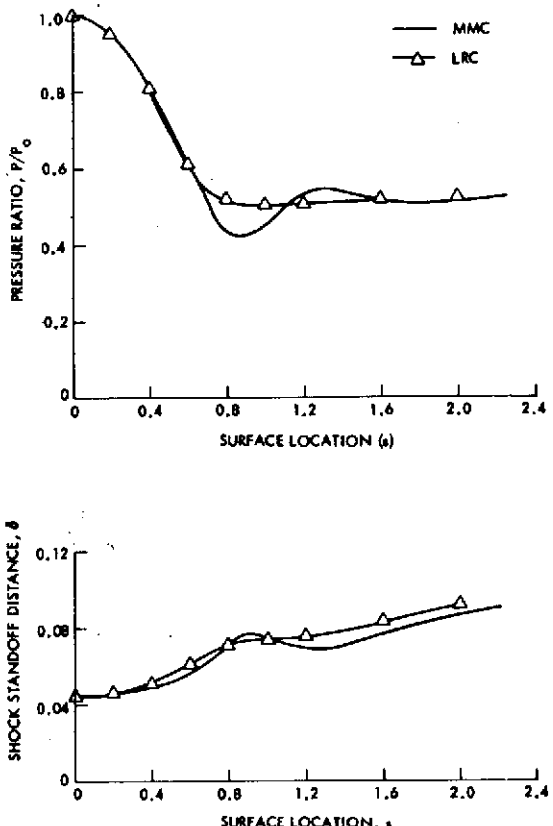


Figure 7.1A-9. Inviscid Analysis Results for the 45° Sphere-Cone Configuration

In Figure 7.1A-10, the radiative heating distributions as obtained by LRC for both the large and small probes are compared with those found with the MMC techniques previously described. Two LRC results are noted for each probe; an inviscid radiative solution, and a fully-coupled solution with steady-state ablation of carbon phenolic. The MMC solution should fall somewhere between these two since an approximation is made for viscous effects but not for the absorption by ablation products. An examination of Figures 7.1A-8 and 7.1A-9 in conjunction with Figure 7.1A-10 explains the differences in final results. First, in regions where the pressure and shock layer thickness from each analysis agree closely, e.g., the spherical section of the small probe, the LRC results do bracket the MMC calculation. On the large probe spherical section, the MMC shock layer thickness is smaller than that predicted by LRC and the radiation heating results are consistent with that fact, i.e., the MMC results fall along the lower limits of the LRC study. On the conical sections of the probe the MMC results

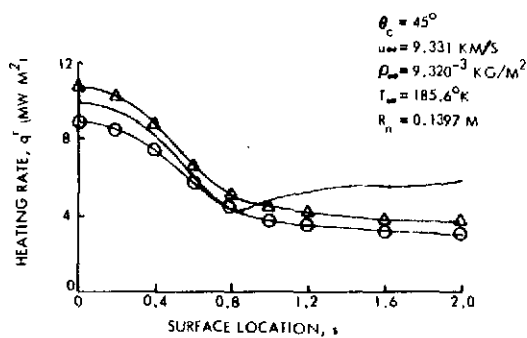
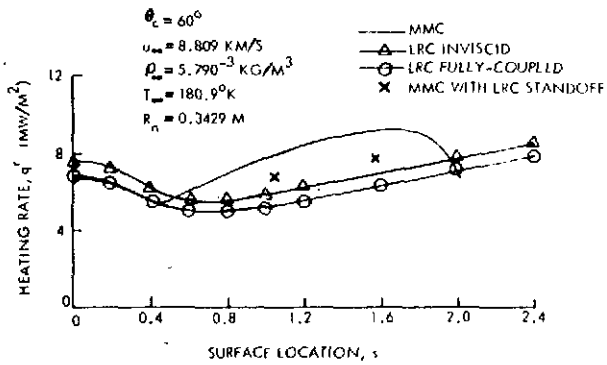


Figure 7.1A-10. A Comparison of Radiative Heating Results

are seen to be strongly dependent on the pressure level which, of course, determines the total population of the radiating species. The minimum cone radiative heating values for each probe occur at the minimum pressure locations; the aft sonic corner for the large probe and the sphere cone junction for the small probe. Since the LRC results do not exhibit these minimum values, the strong dependence of the radiation on the pressure is not as obvious. A conservative procedure has been adopted by MMC in predictions of the cone radiative heating in the choice of the isothermal slab temperature. However, also contributing to the apparent MMC over-prediction of the large probe cone radiation is the significant difference in shock standoff distance prediction. To demonstrate this, a calculation was made at two body locations using the MMC procedure and thermo-chemical data, but using the LRC shock standoff distance (Figure 7.1A-8). The results are shown in Figure 7.1A-10 and are seen to be much nearer those from the LRC analysis. Since the MMC inviscid procedure correctly handles the aft corner sonic point while no special provision is made

for it in the LRC calculation, it is felt that the LRC shock standoff distance is underpredicted on the cone leading to an underestimation of the cone radiative heating.

Another point of comparison is the stagnation point cold wall, no-blowing convective heating rates. The MMC results are 17.9 and 43.3 MW/m^2 for the large and small probes respectively, while the corresponding LRC results are 17.8 and 39.4 MW/m^2 . In general, after consideration of the detailed calculation differences, the agreement between the LRC and MMC results is considered good.

4. NOMENCLATURE

A	Transition extent Reynolds number parameter
F	Convective load distribution functions
f	Dimensionless stream function
f'	Boundary layer velocity ratio
G _t	Turbulent spot formation rate parameter ($1/\text{m} \cdot \text{s}$)
H	Total enthalpy (J/kg)
h	Static enthalpy (J/kg) convective coefficient, ($\text{kg}/\text{m}^2\text{s}$) or streamline divergence metric
j	Flow index; 0 - two dimensional, 1 - axisymmetric
M	Mach number
N _v	Vorticity parameter
Pr	Prandtl number
p	Pressure, (atm or N/m^2)
q	Heating rate (W/m^2)
R _B	Base radius (m)
R _n	Nose radius (m)
Re _θ	Momentum thickness Reynolds number

- r Radial coordinate normalized by the nose radius (Figure 7.1A-1)
 s Body surface coordinate normalized by the nose radius (Figure 7.1A-1)
 T Temperature ($^{\circ}$ K)
 t Time (s)
 u s-component of velocity (m/s)
 u Freestream velocity (km/s)
 v_E Entry velocity (km/s)
 x Axial coordinate normalized by the nose radius (Figure 7.1A-1)
 y Coordinate perpendicular to s normalized by the nose radius (Figure 7.1A-1)
 β Shock angle (Figure 7.1A-1) (degree)
 γ Turbulent intermittency
 γ_E Entry angle (degree)
 δ Shock standoff distance normalized by the nose radius (Figure 7.1A-1)
 ζ Turbulent transformed s-coordinate $[(\text{kg}/\text{m}^2 \text{ s})^{5/4} \text{ m}]^{1/4}$
 η Laminar transformed y-coordinate
 θ Body angle (Figure 7.1A-1) (degree)
 Γ Radiative cooling parameter
 μ Dynamic viscosity ($\text{kg}/\text{m} \cdot \text{s}$)
 ξ Laminar transformed s-coordinate, $[(\text{kg}/\text{m}^2 \text{ s})^2 \text{ m}]$
 ρ Gas density (kg/m^3)
 τ Shear stress (N/m^2)

SUBSCRIPTS

- ad Adiabatic
 B Base
 b Body
 bl Boundary layer

c Cone or corner
e Boundary layer edge
L Laminar
r Recovery
s Shock
T Turbulent
t Transition
w Wall
o Conditions at $s = 0$
 ∞ Freestream

SUPERSCRIPTS

c Convective
r Radiative

5. REFERENCES

1. Anonymous, "Models of the Venus Atmosphere," NASA SP 8011, Review Copy (September 1972).
2. C. Mir-Hosseini, "Venus Entry Nonequilibrium Boundary Layer Analysis," MMC Memorandum (February 1973).
3. J. D. Anderson, Jr., "An Engineering Survey of Radiating Shock Layers," AIAA Journal, Volume 7, No. 9 (September 1969).
4. R. M. Kendall, "A General Approach to the Thermochemical Solution of Mixed Equilibrium - Nonequilibrium, Homogeneous or Heterogeneous Systems," NASA CR-1064 (June 1968).

5. E. P. Bartlett, R. M. Kendall, and R. A. Rindal, "A Unified Approximation for Mixture Transport Properties for Multicomponent Boundary Layer Applications," NASA CR-1063 (June 1968).
6. Anonymous, "Users' Manual-Boundary Layer Integral Matrix Procedure, Version C (BLIMPC)," Aerotherm Report UM-70-20 (June 1970).
7. K. Sutton and R. A. Falanga, "Stagnation Region Radiative Heating with Steady State Ablation during Venus Entry," Paper presented at Symposium on Hypervelocity Radiating Flow Fields for Planetary Entries (January 1972).
8. H. Lomax and M. Inouye, "Numerical Analysis of Flow Properties about Blunt Bodies Moving at Supersonic Speeds in an Equilibrium Gas," NASA TR R-204 (July 1964).
9. M. D. Van Dyke, "The Supersonic Blunt-Body Problem-Review and Extension," JAS, Volume 25, No. 8 (August 1958).
10. M. Inouye, J. V. Rakich, and H. Lomax, "A Description of Numerical Methods and Computer Programs for Two-Dimensional and Axisymmetric Supersonic Flow Over Blunt-Nosed and Flared Bodies," NASA TN D-2970 (August 1965).
11. O. M. Belotserkovskii, "Flow with a Detached Shock Wave about a Symmetrical Profile," JAMM, Volume 22, No. 2 (1958).
12. S. C. Traugott, "An Approximate Solution of the Supersonic Blunt Body Problem for Prescribed Arbitrary Axisymmetric Shapes," MMC RR-13 (August 1958).
13. J. Xerikos and W. A. Anderson, "Blunt Body Integral Method for Air in Thermodynamic Equilibrium," AIAA Journal, Volume 3, No. 8 (August 1965).
14. G. Moretti, and G. Bleich, "Three Dimensional Flow Around Blunt Bodies," AIAA Journal, Volume 5, No. 9 (September 1967).
15. R. W. Barnwell, "Three-Dimensional Flow Around Blunt Bodies with Sharp Shoulders," AIAA Paper 71-56 (January 1971).
16. J. C. South, Jr., "Calculation of Axisymmetric Supersonic Flow Past Blunt Bodies with Sonic Corners, Including a Program Description and Listing," NASA TN D-4563 (May 1968).
17. R. Gold and M. Holt, "Calculation of Supersonic Flow Past a Flat-Headed Cylinder by Belotserkovskii's Method," AFOSR TN-59-199 (March 1959).

18. M. Holt, "Direct Calculation of Pressure Distribution on Blunt Hypersonic Nose Shapes with Sharp Corners," *JAS*, 28, 11 (November 1961).
19. A. A. Dorodnitsyn, "A Contribution to the Solution of Mixed Problems of Transonic Aerodynamics," Advances in Aeronautical Sciences, Volume 2, Pergamon Press (1959).
20. C. T. Edquist, "The Method of Integral Relations for Spherically Blunted Bodies with Sharp Sonic Corners in an Equilibrium Gas Mixture," MMA R72-48671-001 (July 1972).
21. J. J. Bertin, "The Effect of Protuberances, Cavities and Angle of Attack on the Wind-Tunnel Pressure and Heat-Transfer Distribution for the Apollo Command Module," NASA TM X-1243 (October 1966).
22. C. T. Edquist, "Vorticity Effects in Venus Entry," MMC R-70-48671-003 (7 July 1970).
23. C. T. Edquist, "A Technique for Predicting Shock Induced Vorticity Effects During Venus Entry," MMC R-70-48671-006 (August 1970).
24. L. Lees, "Laminar Heat Transfer Over Blunt-Nosed Bodies at Hypersonic Flight Speeds," Jet Propulsion, Volume 26, No. 4 (April 1956).
25. H. Hoshizaki, "Heat Transfer in Planetary Atmospheres at Super-Satellite Speeds," ARS Journal, Volume 130, No. 10 (October 1962).
26. K. Sutton, and R. A. Graves Jr., "A General Stagnation-Point Convective-Heating Equation for Arbitrary Gas Mixtures," NASA TR R-376 (November 1971).
27. J. A. Fay, and F. L. Riddell, "Theory of Stagnation Point Heat Transfer in Dissociated Air," JAS, Volume 25, No. 2 (February 1958).
28. J. G. Marvin, and G. S. Deiwert, "Convective Heat Transfer in Planetary Gases," NASA TR R-224 (July 1965).
29. R. Bromberg, J. L. Fox, and W. O. Ackermann, "A Method of Predicting Convective Heat Input to the Entry Body of a Ballistic Missile," Ramo-Wooldridge Corporation.
30. L. F. Hearne, J. H. Chin, and L. W. Woodruff, "Study of Aero-thermodynamic Phenomena Associated with Reentry of Manned Spacecraft," LMSC Y-78-66-1 (May 1966).
31. Anonymous, "Nose tip Design Analysis and Test Program (NDAT), Final Report," Volume 1, Part 1, LMSC-B133378 (October 1970).

32. H. W. Emmons, "The Laminar-Turbulent Transition in a Boundary Layer - Part I," JAS Volume 18, No. 7 (July 1951).
33. K. K. Chen, and N. A. Thyson, "Extension of Emmons' Spot Theory to Flows on Blunt Bodies," AIAA Journal, Volume 9, No. 5 (July 1971).
34. J. C. Cooke, "An Axially Symmetric Analogue for General Three-Dimensional Boundary Layers," British Aeronautical Research Council R&M 3200 (1961).
35. J. V. Rakich, and G. G. Mateer, "Calculation of Metric Coefficients for Streamline Coordinates," AIAA Journal, Volume 10, No. 11 (November 1972).
36. C. T. Edquist, "Initial Estimates of the Effect of Angle of Attack on Probe Entry Analysis," MMC P71-44487-272 (October 1971).
37. G. F. Widhopf and R. Hall, "Transitional and Turbulent Heat Transfer Measurements on a Yawed Blunt Conical Nosetip," AIAA Journal, Volume 10 (October 1972).
38. W. E. Nicolet, "Users Manual for the Generalized Radiation Transfer Code (RAD/EQUIL)," Aerotherm Report UM-69-9 (October 1969).
39. W. A. Page and H. T. Woodward, "Radiative and Convective Heating During Venus Entry," AIAA Journal, Volume 10, No. 10 (October 1972).
40. W. A. Page, et al., "Radiative Transport in Inviscid Nonadiabatic Stagnation - Region Shock Layers," AIAA Paper 68-784 (June 1968).
41. Personal communication, W. A. Page to J. M. Lefferdo (July 1971).
42. Personal communication, W. A. Page to C. T. Edquist (October 1971).
43. B. M. Bulmer, "Flight Test Correlation Technique for Turbulent Base Heat Transfer with Low Ablation," JSR, Volume 10, No. 3 (March 1973).
44. Anonymous, "Viking Aerophysics Data Book, Revision G," MMC TR-372003 (January 1973).
45. N. S. Vojvodich, "PAET Entry Heating and Heat Protection Experiment," JSR, Volume 10, No. 3 (March 1973).
46. K. Sutton, "Radiative Heating Analysis for Pioneer Venus, Report No. 1," NASA LRC (October 1972).
47. K. Sutton, "Radiative Heating Analysis for Pioneer Venus, Report No. 2," NASA LRC (December 1972).

APPENDIX 7.1B

EFFECT OF AERODYNAMIC COEFFICIENTS,
INERTIAL PROPERTIES, AND ROLL RATE
ON THE DYNAMIC STABILITY OF CONICAL PROBES

1. Large Probe Descent Capsule	7.1B-1
2. Small Probe	7.1B-2
3. Large Probe	7.1B-9
4. Conclusions	7.1B-11

APPENDIX 7.1B

EFFECT OF AERODYNAMIC COEFFICIENTS, INERTIAL PROPERTIES AND ROLL RATE ON THE DYNAMIC STABILITY OF CONICAL PROBES

Coakley's dynamic stability criterion (Reference 1) for a vehicle in six-degree-of-freedom flight is expressed as follows:

$$a + J \left(1 - x^2 \right) - bx > 0 \text{ for stability (convergence of } \alpha) \quad (1)$$

where:

$$a = C_{L\alpha} \frac{md^2}{I_y} \left(C_{m_q} + C_m \dot{\alpha} \right) + \frac{\epsilon md^2}{I_x} C_{l_p} \quad (1a)$$

$$+ (1 - \epsilon) \left(\frac{W \sin \gamma}{qS} - C_D \right) \quad (1b)$$

$$J = \left(\epsilon + \frac{M}{2C_{m_\alpha}} \frac{dC_{m_\alpha}}{dM} \right) \left(\frac{W \sin \gamma}{qS} - C_D \right) \quad (1c)$$

$$- \frac{\epsilon md^2}{I_x} C_{l_p} - \frac{\beta \sin \gamma}{\rho S}$$

$$b = |a - 2c| \quad (1d)$$

$$c = C_{L\alpha} + \frac{md^2}{I_x} C_{m_p} \quad (1e)$$

$$x = 1 / \left[1 - \frac{4 I_y q S d C_{m_\alpha}}{\left(I_x p \right)^2} \right]^{1/2} \quad (1f)$$

The term ϵ is unity for constant roll rate and zero for roll rate proportional to the velocity, such as would occur for a vehicle with canted fins. For the present analysis, the fin angles are given by $\tan^{-1} pd/V$, $dC_{m_\alpha}/dM_\infty = 0$, $C_{m_p} = 0$; and the Venus atmosphere Model I of Reference 2 was used.

1. LARGE PROBE DESCENT CAPSULE

The large probe stages from the parachute at 48 km and requires, for science measurement, a controlled roll rate. Terminal velocities versus altitude for ballistic coefficients of 2.75 and 3.50 are shown in Figure 7.1B-1.

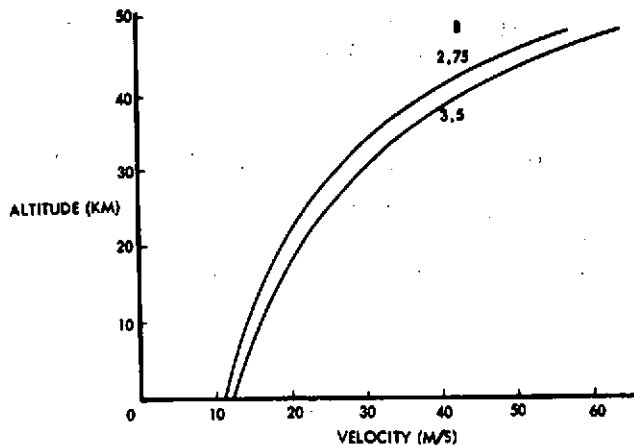


Figure 7.1B-1. Large Probe Descent Capsule Altitude and Velocity for Ballistic Coefficients of 2.75 and 3.5

Figure 7.1B-2 presents the Coakley criterion for the descent capsule as a function of altitude for various roll rates, fin deflection angles, and ballistic coefficients. Descent capsule aerodynamic coefficients and mass properties for this analysis are given in Table 7.1B-1. The C_D , C_{L_a} , and C_{m_a} values shown in Table 7.1B-1 were obtained from tests in the Martin Marietta subsonic wind tunnel. As shown in Figure 7.1B-3, results for the large probe descent capsule are:

- 1) The criterion indicates stability.
- 2) Changing the ballistic coefficient does not significantly influence the stability.

2. SMALL PROBE

The blunted, 45-degree cone with afterbody small probe enters the Venus atmosphere with an initial roll rate of 4.8 rpm, flight path angle, and ballistic coefficient as shown in Figure 7.1B-3, and reaches terminal velocity at about 60 km. The small probe nominal mass properties and aerodynamic coefficients are shown in Table 7.1B-2. Figure 7.1B-4 presents the Coakley parameter versus Mach number for roll rates, $p = 0$ and 4 rad/s.

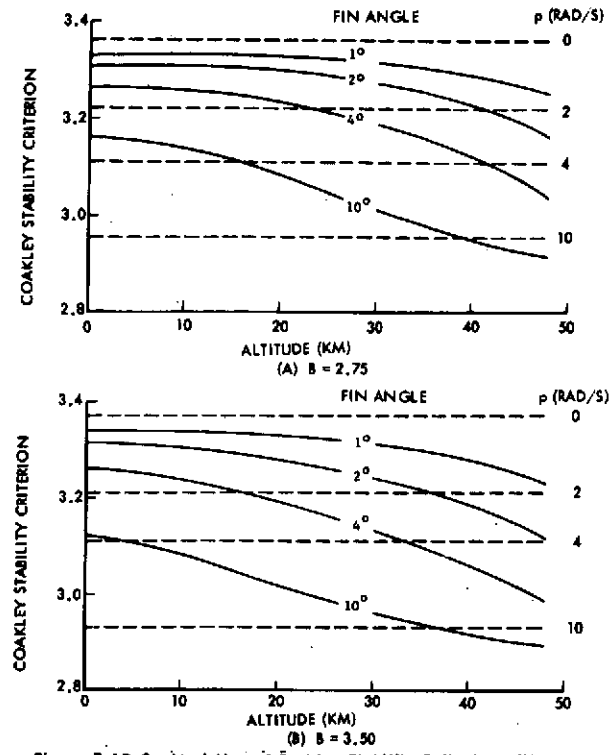


Figure 7.1B-2. Variation of Coakley Stability Criterion with Altitude for the Large Probe Descent Capsule

Table 7.1B-1. Large Probe Descent Capsule Characteristics

$B, \text{KG/M}^2 (\text{SLUGS/FT}^2)$	431.75 (2.75)	549.5 (3.50)
M, KG	88.45	88.45
$I_y, \text{KG-M}^2$	3.98	3.98
$I_x, \text{KG-M}^2$	3.80	3.80
D, M	0.660	0.660
C_D	0.61	0.47
$C_{m_d}, \text{PER RAD}$	-0.057	-0.029
$C_{L_d}, \text{PER RAD}$	1.432	1.432
$C_{m_d} + C_{m_{di}}, \text{PER RAD}$	-0.40	-0.40
C_{I_p}	0	0

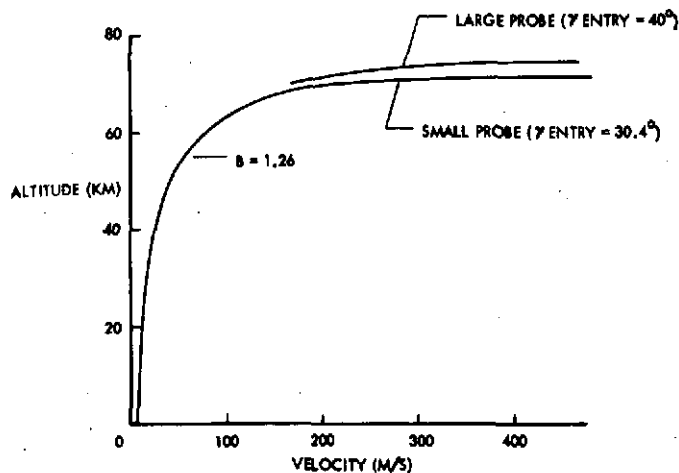


Figure 7.1B-3. Large and Small Probe Altitude and Velocity

Table 7.1B-2. Small Probe Characteristics

MACH NUMBER	$C_L \alpha$	$C_m \alpha$	C_I_p	$C_{m_q} + C_{m_d}$	C_D
0.01	-0.350	-0.229	0	-0.12	0.75
0.30	-0.293	-0.218	0	-0.24	0.75
0.70	-0.366	-0.205	0	-0.40	0.68
1.10	-0.696	-0.183	0	+0.32	1.21
1.35	-0.823	-0.149	0	+0.32	1.28
1.40	-0.832	-0.143	0	-0.36	1.29
2.20	-0.835	-0.138	0	-0.36	1.35
3.00	-0.383	-0.195	0	-0.36	1.30
4.50	-0.325	-0.229	0	-0.36	1.24
100.00	-0.325	-0.229	0	-0.36	1.24

$m, \text{ KG}$ = 25.86
 $I_y, \text{ KG-M}^2$ = 0.3602
 $I_x, \text{ KG-M}^2$ = 0.4129
 $d, \text{ M}$ = 0.4953

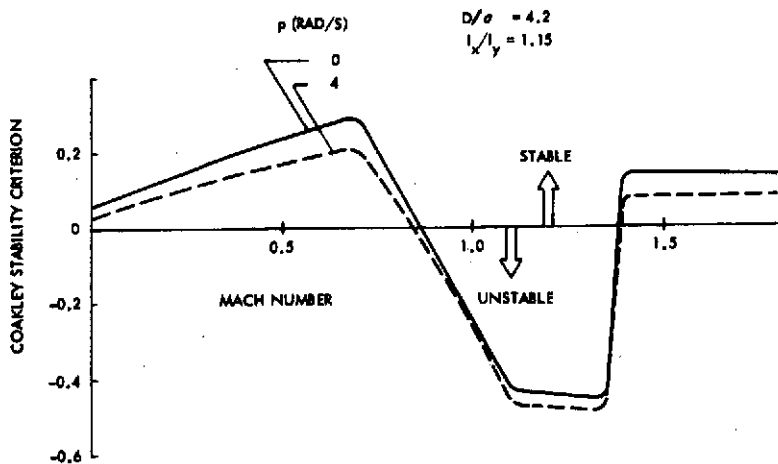


Figure 7.1B-4. Variation of Coakley Stability Criterion with Mach Number

The criterion essentially reflects the pitch damping derivative, shown in Figure 7.1B-5. Figure 7.1B-6 further illustrates the sensitivity of the Coakley parameter to the pitch damping derivative. The square of the diameter to radius of gyration ratio $(D/\sigma)^2 = md^2 I_y$, significantly influences the stability inasmuch as the $(D/\sigma)^2$ term is a multiplier of $C_{m_q} + C_{m_\alpha}$.

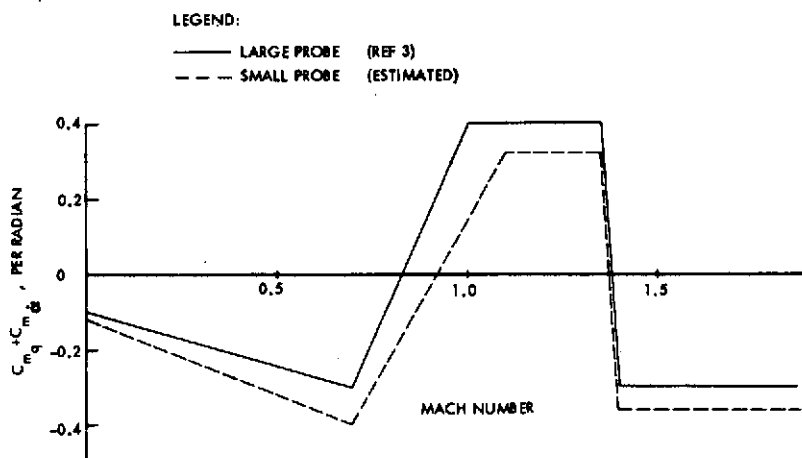


Figure 7.1B-5. Pitch Damping Derivative for the Large and Small Probe

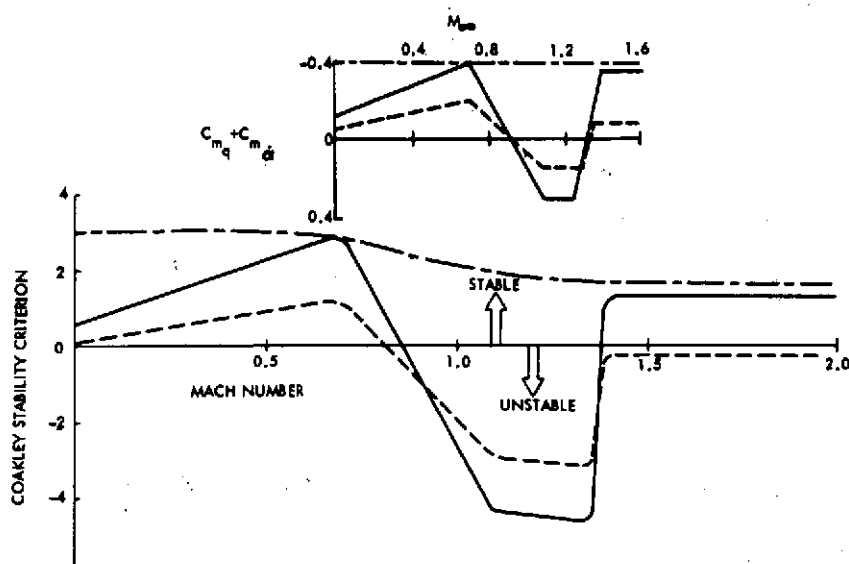


Figure 7.1B-6. Variation of Coakley Stability Criterion with Mach Number for Three Functions of the Pitch Damping Derivative for the Small Probe

The small probe stability parameter versus roll rate for various values of the pitch damping derivative is shown in Figure 7.1B-7. For terminal descent ($h = 0$ to 60 km), the small probe is stable for $\rho < 7.5$ rad/s and $C_{m_q} + C_{m_{\dot{\alpha}}} > -0.5$ per radian.

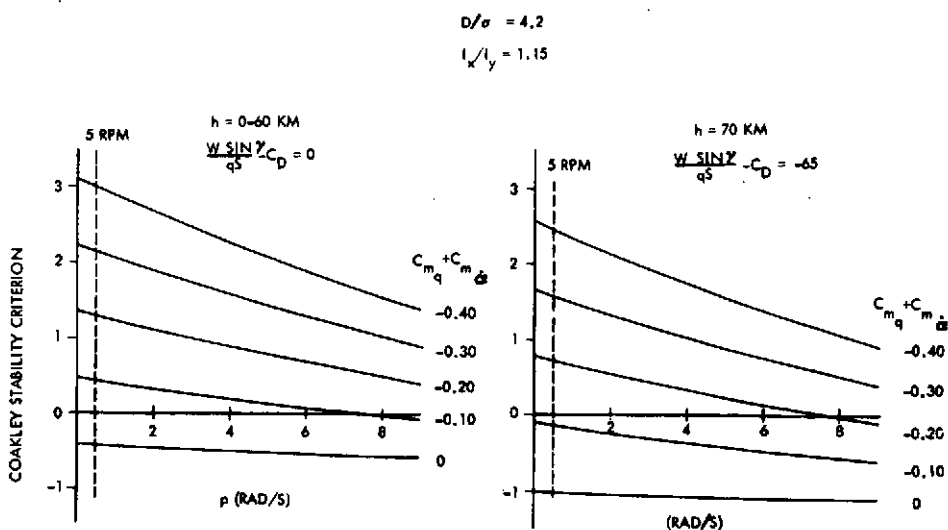


Figure 7.1B-7. Variation of Coakley Stability Criterion with Roll Rate for Various Values of Pitch Damping Derivative

It is interesting to note that for a negative dynamic pressure gradient at $h = 70$ km, shown in Figure 7.1B-7, the Coakley parameter is decreased by approximately $\frac{W \sin \gamma}{qS} - C_D$.

Figure 7.1B-8 illustrates the sensitivity of the parameter for the small probe to the roll-to-pitch moment of inertia ratio. For $p = 5$ rpm, changes in I_x/I_y over a reasonable range, do not significantly influence the stability.

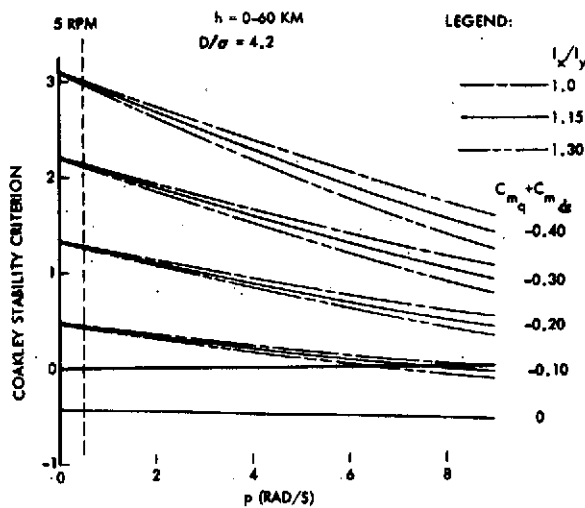


Figure 7.1B-8. Small Probe Coakley Stability Criterion Sensitivity to I_x/I_y Ratio

The effect of varying $C_{L\alpha}$, C_D , $C_{m\alpha}$, and C_{l_p} on the Coakley parameter for the small probe is shown in Figure 7.1B-9. These aerodynamic coefficients were varied independently and, when compared to the effect of the pitch damping derivative shown in Figure 7.1B-6, do not have a significant effect.

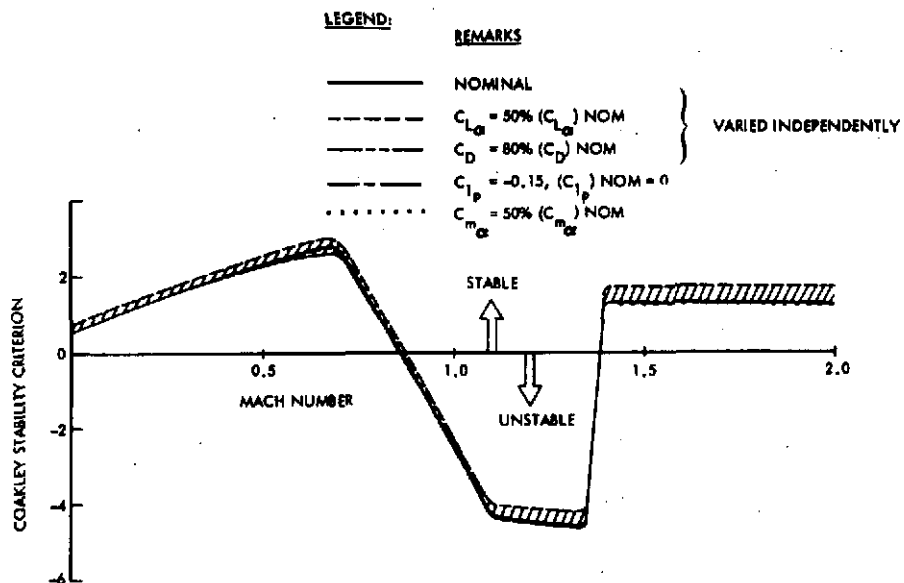


Figure 7.1B-9. The Effect of Varying $C_{L\alpha}$, C_D , $C_{m\alpha}$ and C_{I_p} on the Coakley Stability Criterion for the Small Probe

Figure 7.1B-10 presents stability boundaries for the small probe as functions of pitch damping derivative, roll rate, and altitude. The stable region above about 77 km results primarily from the density term, $\frac{\beta \sin \gamma}{\rho S}$. The unstable bands at approximately 60 to 77 km are due, in part, to the interaction of the drag, gravity, and density terms and correlate to the strong negative gradient following peak dynamic pressure. However, a small change in the damping coefficient, in this case, from -0.10 to -0.15 completely eliminates the unstable band for roll rates less than 6 rad/sec. From 0 to 60 km, the pitch damping derivative and roll rate are reflected in the stability. Also, in Equation (1f), note that the rolling moment of inertia (I_x) and the roll rate (p), appear as multipliers. (The other terms containing I_x are neglected in the present analysis.) Thus, the effects of changes in the I_x or in p will be identical. The implication of this fact is that in Figure 7.1B-10, increasing I_x will have the effect of moving the vertical portion of the stability boundary to the left. The vehicle studied in Reference 3 had $I_x/I_y = 1.8$. Therefore, it is clear why this vehicle was unstable at such a low roll rate.

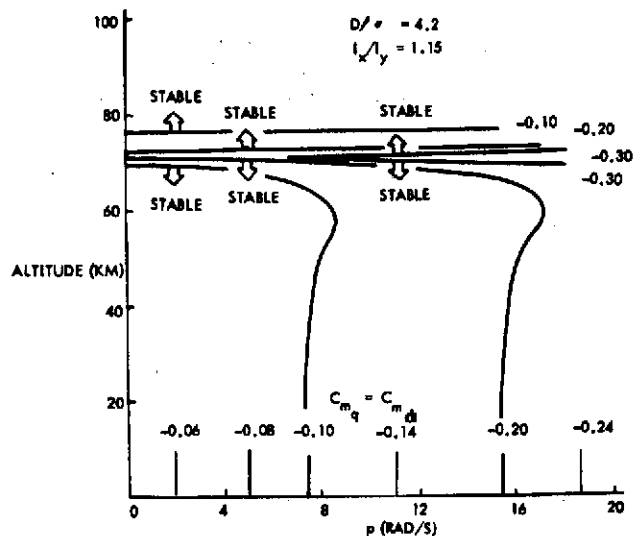


Figure 7.1B-10. Small Probe Stability Boundaries as Functions of Pitch Damping Derivative, Roll Rate, and Altitude

3. LARGE PROBE

The large probe has an initial roll rate of 4.8 rpm. The large probe descent capsule is deployed by parachute from the large probe at approximately 70 km. A portion of the large probe altitude versus velocity trajectory is shown in Figure 7.1B-3. Large probe mass properties and aerodynamic coefficients are shown in Table 7.1B-3.

Table 7.1B-3. Large Probe Characteristics

MACH NUMBER	$C_{L\alpha}$	$C_{m\alpha}$	C_{I_p}	$C_{m_q} + C_{m_d}$	C_D
0.01	-0.774	-0.0688	0	-0.10	0.90
0.60	-0.823	-0.0688	0	-0.27	0.95
0.70	-0.823	-0.0802	0	-0.30	1.00
1.00	-1.112	-0.0802	0	+0.40	1.25
1.25	-1.236	-0.0688	0	+0.40	1.42
1.35	-1.273	-0.0917	0	+0.40	1.48
1.40	-1.270	-0.1031	0	-0.30	1.50
2.00	-1.447	-0.1260	0	-0.30	1.70
4.00	-1.347	-0.1146	0	-0.30	1.60
100.00	-1.347	-0.1146	0	-0.30	1.60

$$\begin{aligned}
 m, \text{ KG} &= 137.6 \\
 I_y, \text{ KG-M}^2 &= 12.04 \\
 I_x, \text{ KG-M}^2 &= 15.48 \\
 d, \text{ M} &= 1.372
 \end{aligned}$$

for $p = 0$ and $4/\text{rad/s}$. Again, the large probe Coakley criterion essentially reflects the pitch damping derivative, shown in Figure 7.1B-5.

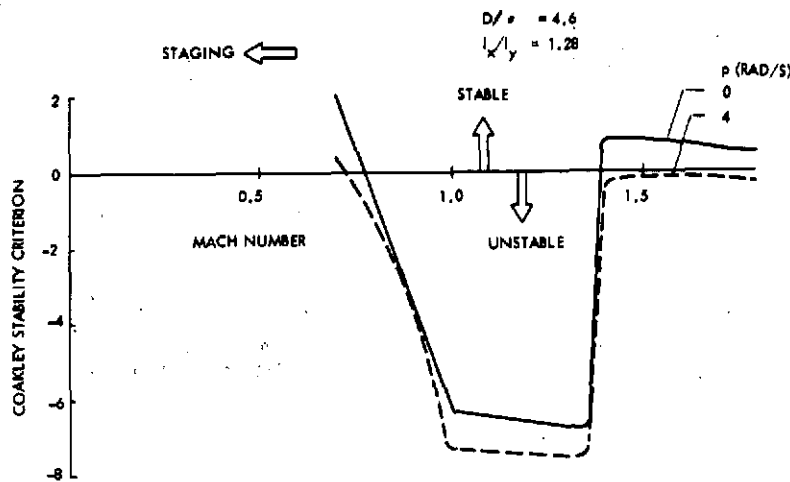


Figure 7.1B-11. Variation of Coakley Stability Criterion with Mach Number for the Large Probe

4. CONCLUSIONS

The Coakley stability criterion has been applied to typical Pioneer Venus large probe descent capsule, large probe entry vehicle and small probe configurations. The stability characteristics of the small probe have been investigated in detail relative to roll rate, aerodynamic coefficients, and roll-to-pitch moment of inertia ratio.

The large probe descent capsule is stable for terminal descent velocities and is not significantly influenced by changes in the ballistic coefficient. The large and small probe stability characteristics are strongly related to the pitch damping derivative--stability increases with more negative values of the pitch damping derivative and decreasing roll rates. The large probe is stable at the time of parachute deployment.

The small probe stability characteristics are summarized as follows for the trajectory considered ($\gamma = 40^\circ$):

- 1) The probe is stable above 77 km, primarily due to the atmosphere scale height term. This corresponds to the period of increasing dynamic pressure.
- 2) Between approximately 60 and 77 km, the instability indicated is dependent on the interaction of the drag, gravity, and density terms, corresponding to the period of rapidly decreasing dynamic pressure and strongly influenced by the pitch damping coefficient.
- 3) In terminal flight the small probe is stable even for very small values of the pitch damping coefficient.

5. NOMENCLATURE

B	Ballistic coefficient, $m/C_D S$
C_D	Drag coefficient
C_{L_α} , C_{m_α}	Lift coefficient curve slope and pitching moment coefficient slope, per rad
C_{l_p}	Roll damping derivative
$C_{m_q} + C_{m_{\dot{\alpha}}}$	Pitch damping derivative, $\frac{2 C_m}{2 \left(\frac{\dot{\theta} d}{2V} \right)} + \frac{2 C_m}{2 \left(\frac{\dot{\alpha} d}{2V} \right)}$
$C_{m_{p_\alpha}}$	Magnus moment stability derivative
d	Reference diameter
g	Acceleration of gravity
h	Altitude
I_x , I_y	Roll and pitch moment of inertia
m	Mass
M	Mach number
p	Roll rate
q	Dynamic pressure, $\rho V^2 / 2$

S	Reference area $\pi d^2/4$
V	Velocity
W	Weight
α	Angle of attack
β	Reciprocal of the atmosphere scale height, $d\rho / \rho dh$
γ	Flight path below the horizon plane
ρ	Atmospheric density
σ	Radius of gyration in pitch

REFERENCES

1. T. J. Coakley, "Dynamic Stability of Symmetric Spinning Missiles," Journal of Spacecraft and Rockets, Vol. 5, No. 10, pp. 1231-1232 (October 1968).
2. NASA: "Models of Venus Atmosphere (1972)," NASA Space Vehicle Design Criteria (Environment), NASA SP-8011, (Revised September 1972).
3. Donna L. Shirley and John E. Misselhorn, "Instability of High-Drag Planetary Entry Vehicles at Subsonic Speeds," Journal of Spacecraft and Rockets, Vol. 5, No. 10, pp. 1165-1169 (October 1968).

APPENDIX 7.1C
WIND TUNNEL TEST RESULTS

- | | |
|--|---------|
| 1. MMC Low-Speed Wind Tunnel Tests | 7.1C-1 |
| 2. Army Meteorological Wind Tunnel at
Colorado State University | 7.1C-7 |
| 3. Ames Research Center, HFFB Water Facility | 7.1C-7 |
| 4. Langley Research Center Spin Tunnel | 7.1C-8 |
| 5. General Discussion | 7.1C-17 |

APPENDIX 7.1C

WIND TUNNEL TEST RESULTS

Several aerodynamic test programs have been conducted under the MMC IRAD Program which supported the selection of preferred probe configurations. These programs have included static force and moment tests, one degree of freedom and six degree of freedom dynamic tests. Descriptions of these tests follow.

1. MMC, LOW-SPEED WIND TUNNEL TESTS

Three component force and moment tests have been conducted on a large number of cone and sphere configurations as shown in Figure 7.1C-1.

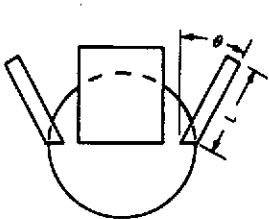
1.1 Conical Models

Aerodynamic coefficients from these tests of the cones with various afterbodies are shown in Figure 7.1C-2. The effect of afterbody shape is seen to be negligible except for the hemisphere, which exhibits an appreciable negative normal force curve slope and positive pitching moment curve slope. In spite of these unusual curves, it is seen in Figure 7.1C-2e that the center of pressure, as indicated by $\partial C_m / \partial C_N$, is identical to those for the other afterbodies.

1.2 Sphere/Fins

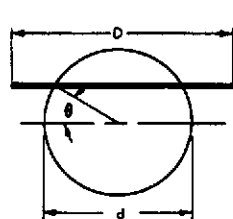
The aerodynamic coefficients, C_L , C_D , and C_m as functions of α are shown in Figure 7.1C-3. A summary of zero lift drag for these configurations is given in Figure 7.1C-3d where it is seen that a wide range of drag coefficients is available from this type of stabilization device. Particular details of interest in these data are:

- 1) All fin configurations produce positive lift-curve slopes.
- 2) C_D is very nearly constant with α up to 30 degrees. (This is a desirable feature for an atmospheric probe.)
- 3) The pitching moment slopes are quite linear. The data show a nonlinearity for the larger fins and fin angles which is probably due to fin deformation.



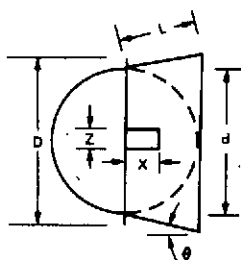
FINNED SPHERE

$L/d = 0.25; \theta = 0^\circ, 10^\circ, 20^\circ, 30^\circ$
 $0.50; \theta = 0^\circ, 10^\circ, 20^\circ, 30^\circ$
 $0.75; \theta = 0^\circ, 10^\circ, 20^\circ, 30^\circ$
 $1.00; \theta = 0^\circ, 10^\circ, 20^\circ, 30^\circ$



SPHERE WITH THIN RINGS

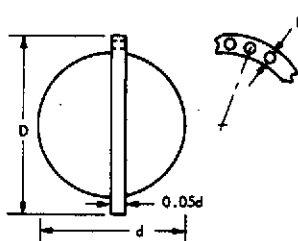
$D/d = 0.807; \theta = 45^\circ$
 $= 1.00; \theta = 45^\circ$
 $= 1.2; \theta = 0^\circ, 15^\circ, 30^\circ, 45^\circ$
 $= 1.4; \theta = 0^\circ, 15^\circ, 30^\circ, 45^\circ$



SPHERE WITH FLARES

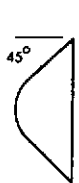
$L/d = 0.5$
 $\theta = 12^\circ$
 $D/d = 0, 1.0375$

NO. OF CUTOUTS	Z/d	X/d
0	0.236	0.213
9	0.05	0.10
24	0.05	0.20
24	0.05	0.30

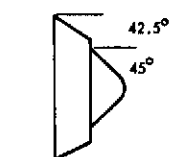


SPHERE WITH PERFORATED RINGS

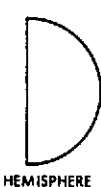
NO. OF HOLES	h/d	D/d
0	0.030	1.08
24	0.030	1.08
48	0.047	1.102
0	0.047	1.115
48	0.047	1.115



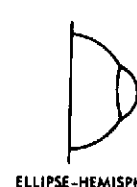
BLUNTED CONES AND AFTERBODIES



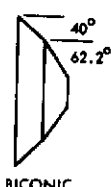
STEPPED BICONIC



HEMISPHERE



ELLIPSE-HEMISPHERE



BICONIC

Figure 7.1C-1. Configurations Tested in the Martin Marietta Subsonic Wind Tunnel

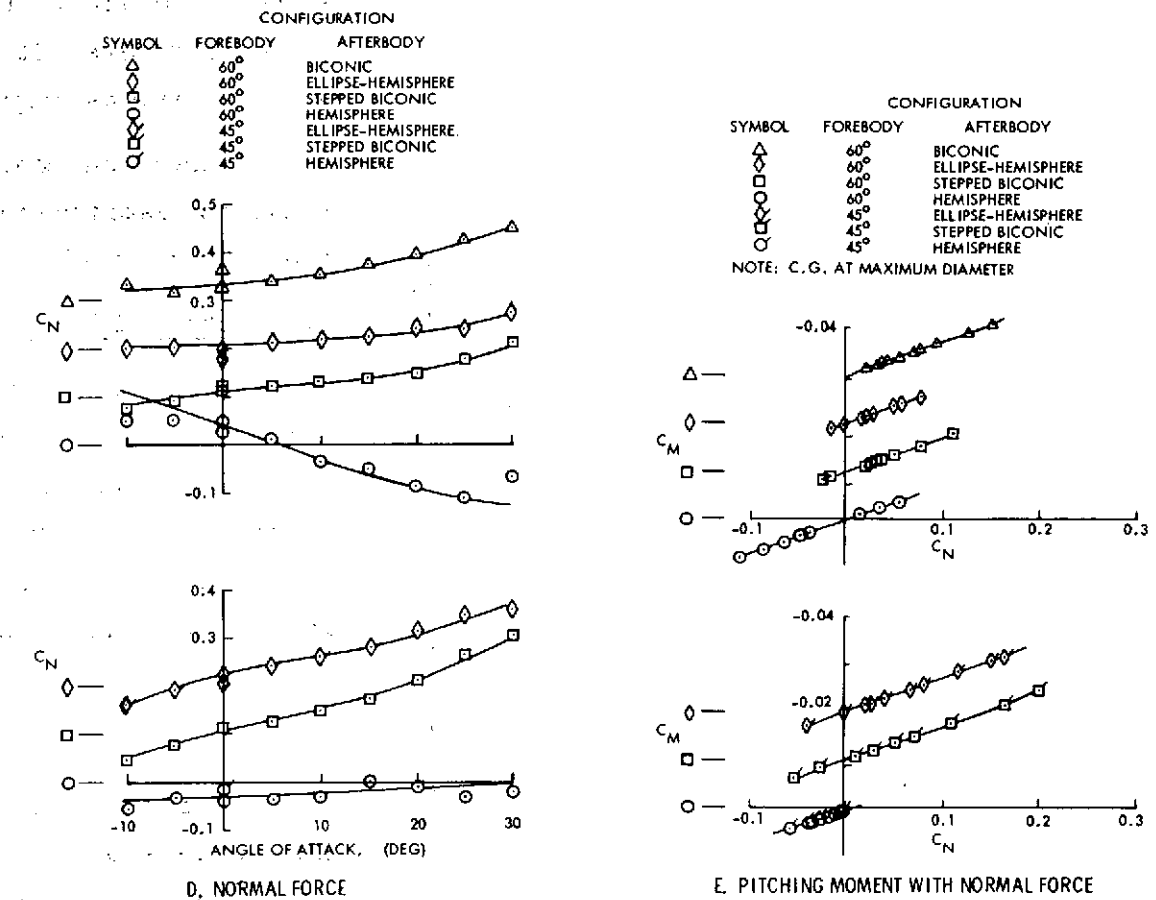
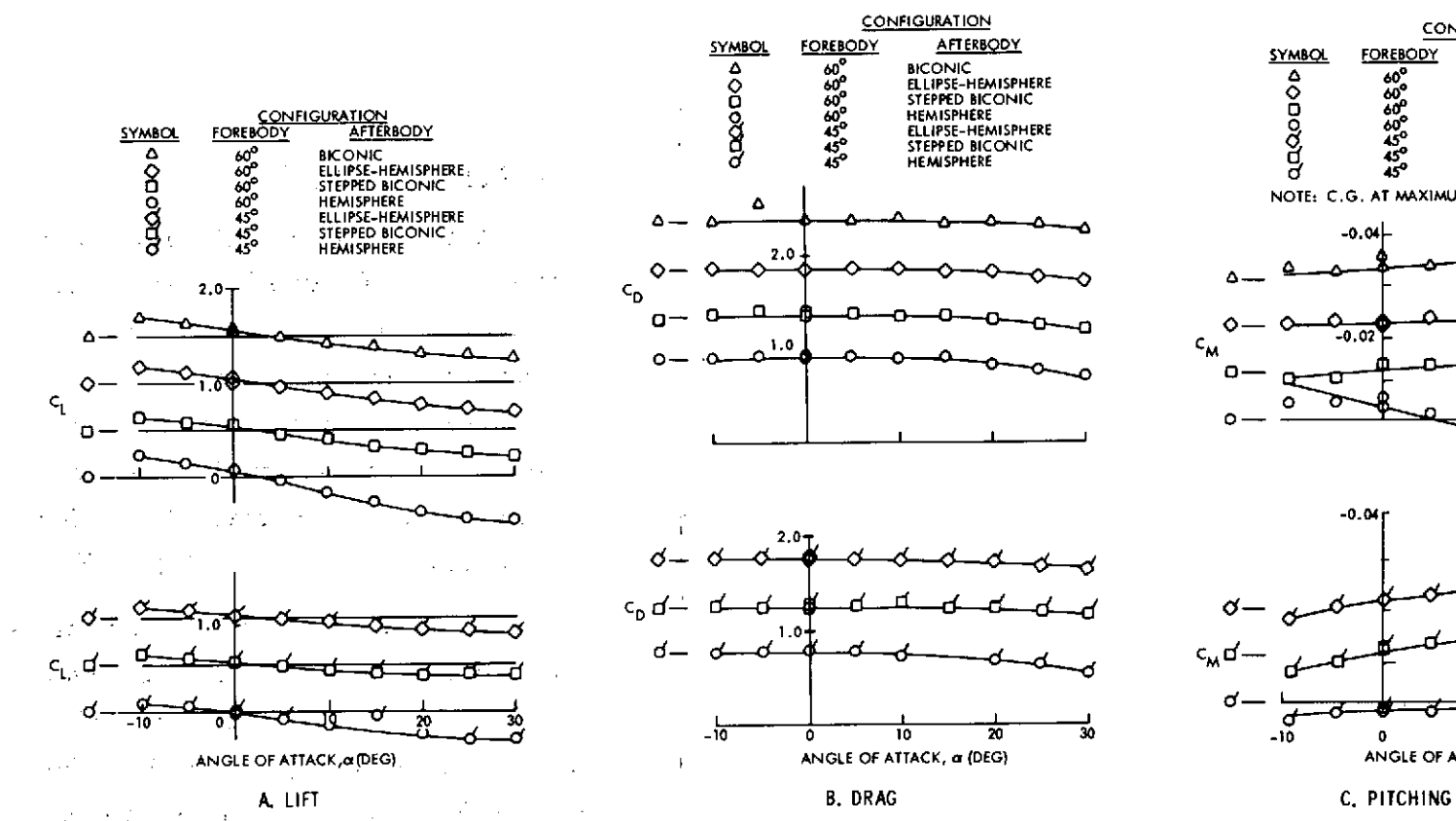


Figure 7.1C-2. Aerodynamic Coefficients for Cone Forebody Models

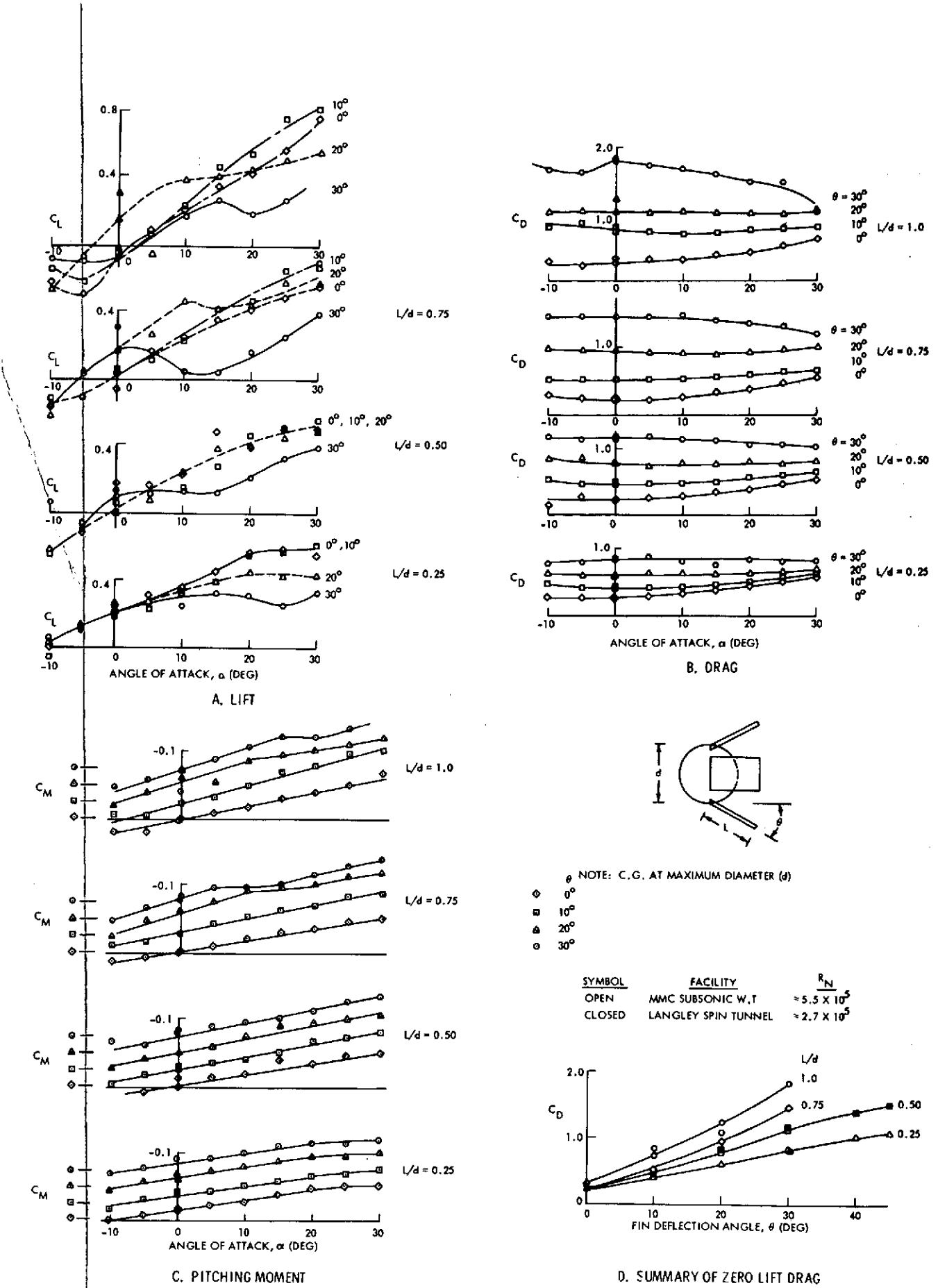


Figure 7.1C-3. Aerodynamic Coefficients for Sphere-Fin Models ($R_N = 5.5 \times 10^5$)

1.3 Sphere/Thin Rings

Lift, drag, and pitching moment data for the thin ring stabilized sphere are shown in Figure 7.1C-4. The effect of ring size is to vary the lift-curve slopes from negative to positive as the D/d varies from 0.8 to 1.4. Also, it appears that the effect of ring location on the lift is small. The effect of ring size and location on drag coefficient is pronounced, as might be expected. The drag increases with ring size and decreases as the ring is moved aft of the maximum diameter. The effect of Reynolds number on the zero angle of attack drag is shown in Figure 7.1C-4d to be negligible over the range tested.

A summary of zero lift drag is shown in Figure 7.1C-4e and compared with spin tunnel data. It appears that the comparison for the $d/D = 1.4$ ring is not very good. This is probably due to the model, which has a very large drag area, shaking in the MMC facility. Also shown in Figure 7.1C-4e are values for the ringed spheres based upon the ring diameter instead of the sphere diameter. The spin tunnel points for the $d/D = 1.2$ and 1.4 cases were used here. It is of interest that the data very nearly collapse to a single curve as might be expected.

The pitching moment curves (Figure 7.1C-4c) indicate that all configurations tested were statically stable and that the stability increases as the ring is moved aft.

1.4 Sphere/Flares

The aerodynamic coefficients for the sphere with 12 degree flares having various vent geometries are shown in Figure 7.1C-5. It is seen that the differences in these static coefficients are very small for the configurations tested. This is not too surprising because all of the vent areas were made equal intentionally to produce the same drag. The major reason for the variations was to study in the spin tunnel the effects on the dynamic stability.

1.5 Sphere/Thick Perforated Rings

Typical plots of the aerodynamic coefficients as functions of angle of attack are shown in Figure 7.1C-6 for ring porosities of 0 and 26 percent. Although there is some scatter in these data, the curves appear to be fairly linear up to $\alpha = 30$ degrees. Aerodynamic derivatives and zero-lift drag are

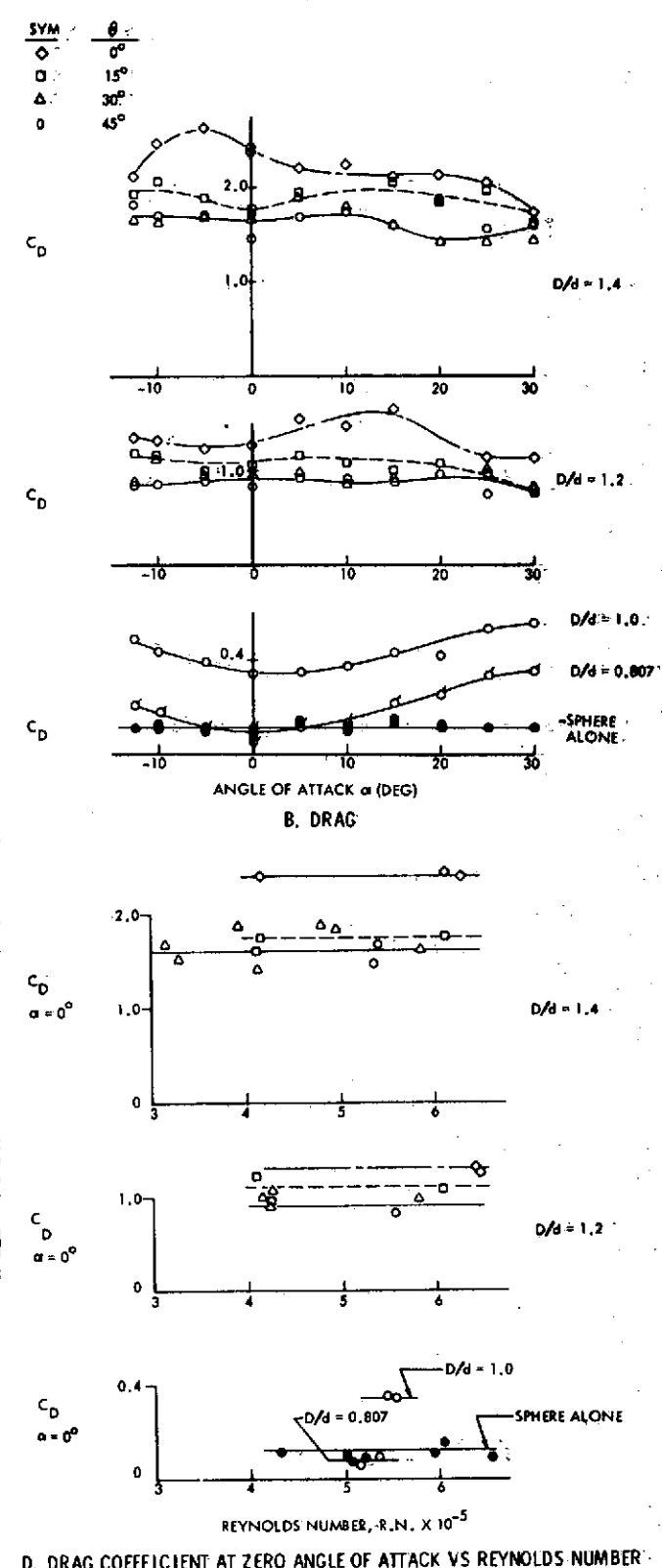
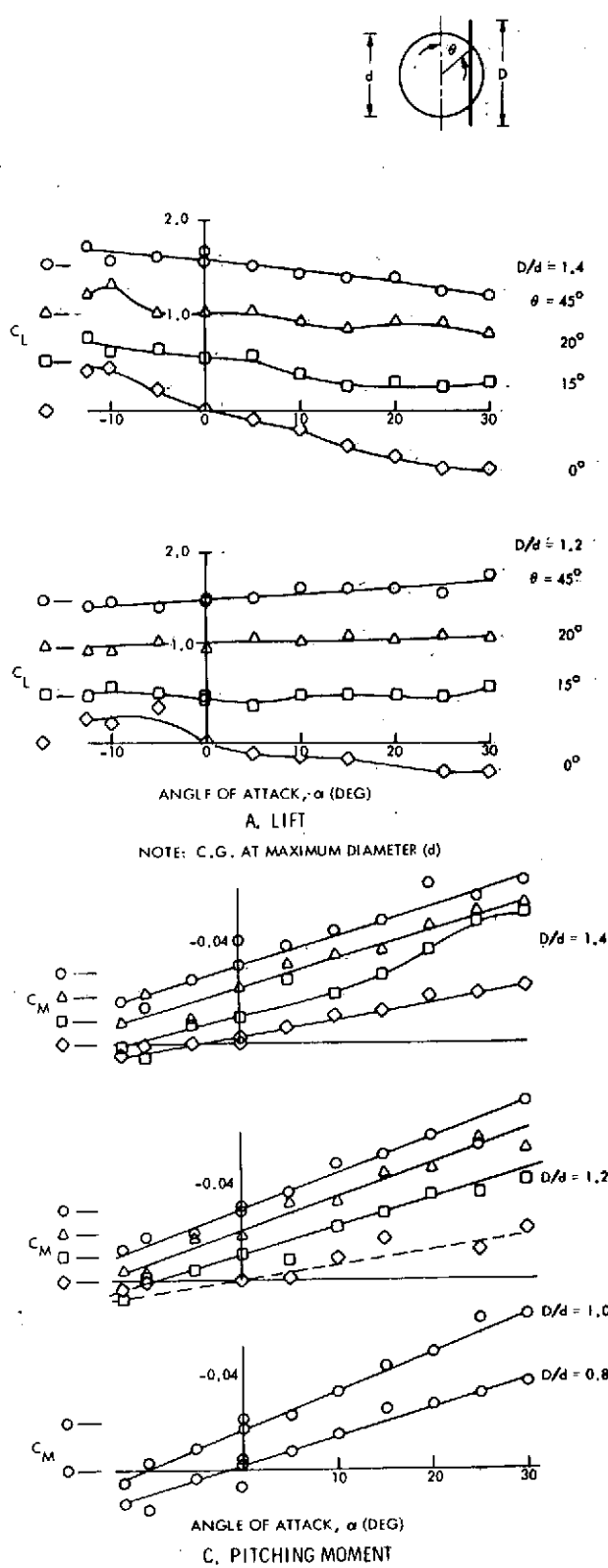


Figure 7.1C-4: Aerodynamic Coefficients for Sphere-Ring Models ($IRN = 5.7 \times 10^5$)

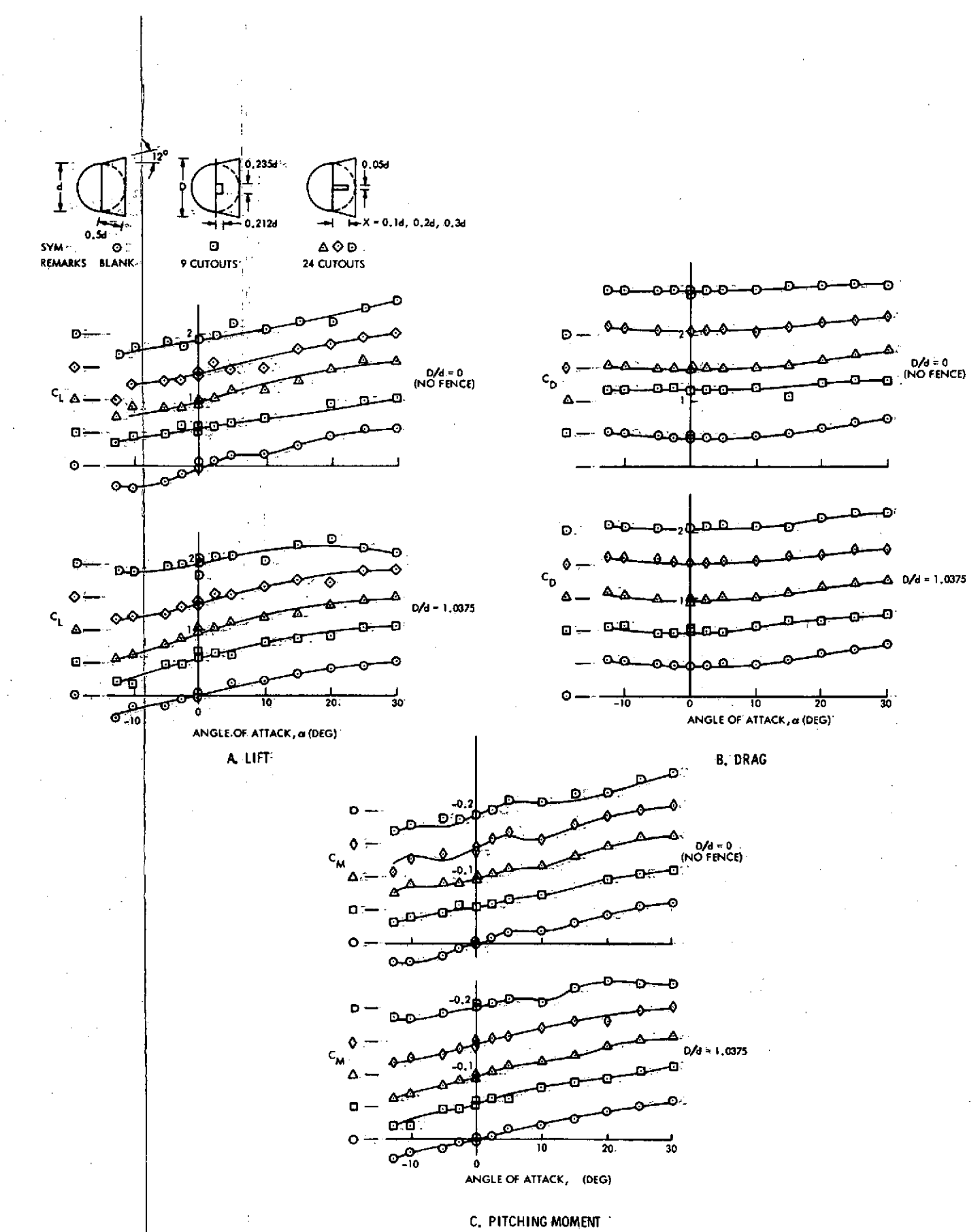
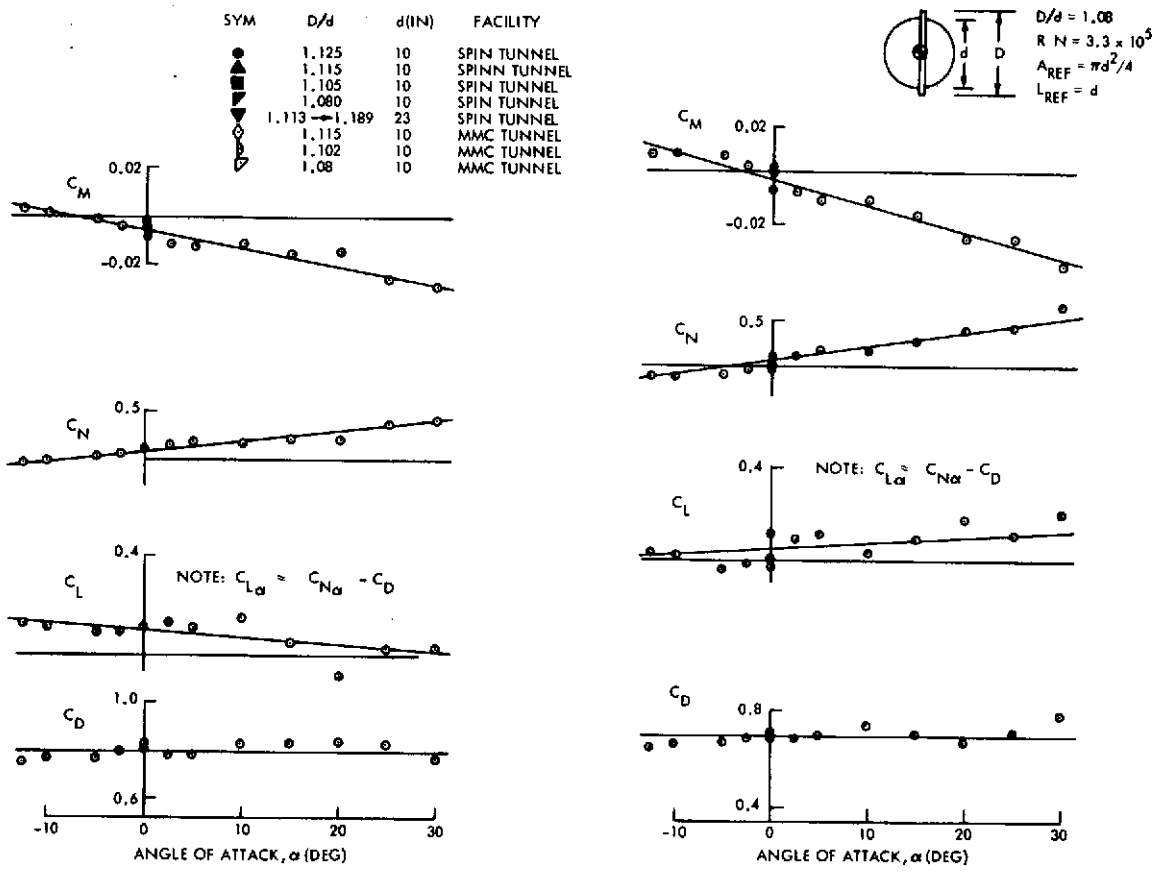
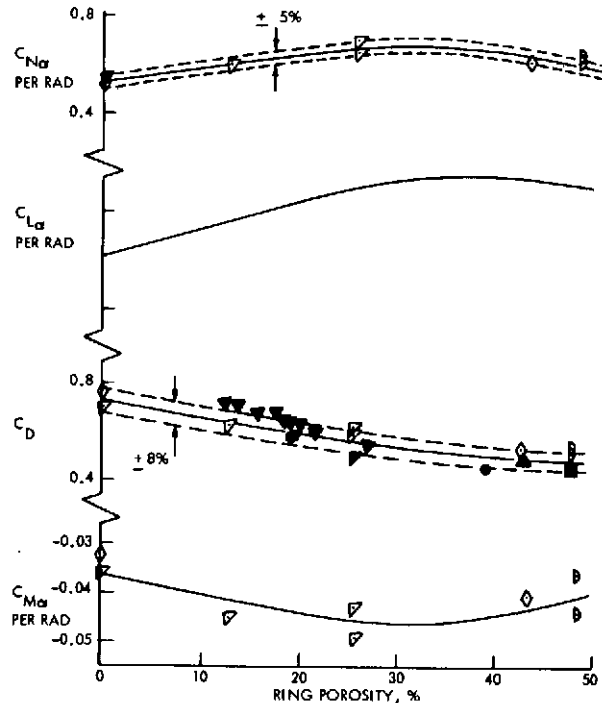


Figure 7.1C-5: Aerodynamic Coefficients for Sphere/Vented Flare Models



A. RING POROSITY = 0

B. RING POROSITY = 26%



NOTE: $C_{L\alpha} \approx C_{N\alpha} - C_D$
ALL VALUES GOOD FOR $-30^\circ < \alpha < 30^\circ$

C. SUMMARY OF AERODYNAMIC DERIVATIVES AND DRAG

Figure 7. IC-6. Aerodynamic Coefficients for Sphere/Thick Ring Configurations

summarized in Figure 7.1C-6c for all of the various ring geometries and porosities tested. Drag data obtained from the spin tunnel tests are also shown.

2. ARMY METEOROLOGICAL WIND TUNNEL AT COLORADO STATE UNIVERSITY

Conical models with various afterbodies and spheres with fins and rings configured as shown in Figure 7.1C-7 were tested for one degree of freedom stability by mounting them in the wind tunnel on a horizontal wire running normal to the air flow and through the center of gravity of the models. The models were perturbed to various degrees and then released into one degree of freedom motion. Motion pictures were made of the motion history. To date only qualitative analysis of these data has been made. The results are summarized in Table 7.1C-1.

All of the finned spheres tested exhibited a stable trim point only at $\alpha = 0$. None of the models would automatically diverge into a tumbling mode; however, as indicated in Table 7.1C-1, those configurations to the left of the dashed line would sustain tumbling if artificially induced. The ring-stabilized spheres would trim at $\alpha = 0$ and 180 degrees and all would sustain tumbling, but only after artificial initiation.

All of the cone models, except for those with the hemispherical afterbody, would automatically tumble. Many of these models would oscillate about $\alpha = 0$ and 180 degrees and the oscillation would diverge into the tumbling mode, indicating that they were statically stable and dynamically unstable at $\alpha = 0$ and 180 degrees. The models with hemispherical afterbodies would not trim at $\alpha = 180$ degrees and would not sustain tumbling if artificially induced.

3. AMES RESEARCH CENTER, HFFB WATER FACILITY

Blunted cone models with half-angles of 45, 55, and 60 degrees, and various afterbody shapes, as shown in Figure 7.1-8, were tested in free fall. The models were fabricated as thin (1/16 in.) aluminum shells with a central screw and weights as shown in Figure 7.1C-9. Various weights and weight locations were used to produce the c.g. and D/σ values indicated in Tables 7.1C-2, 7.1C-3, and 7.1C-4. Data consisted of multiple flash still photographs taken from two orthogonally situated positions. Time has not

permitted thorough analysis of these data; however, the qualitative results are summarized in Table 7.1C-2, 7.1C-3, and 7.1C-4, where it will be seen that the behavior is not clearly correlatable with that observed in the spin tunnel.

Several flights in the water facility with configurations B-E and A-F were partially analyzed by ARC. The drag values deduced from these flights were in fair agreement with those obtained in the Langley spin tunnel and MMC wind tunnel, as indicated:

<u>Configuration</u>	<u>Water Drop Facility</u>	<u>Spin Tunnel</u>	<u>MMC Wind Tunnel</u>
B-E	0.86	0.83	0.86
A-F	0.88	0.72	0.75

The reason for the outstanding value of 0.88 for configuration A-F in the water facility is not understood.

4. LANGLEY RESEARCH CENTER SPIN TUNNEL

A large number of blunted cone models with various afterbody shapes, and spheres with stabilization/drag amplification devices has been tested in the spin tunnel to study their stability characteristics as affected by c.g. location and D/σ . The configurations tested are shown in Figure 7.1C-10 and 7.1C-11. The data obtained consisted of color movies on which readings from a digital clock and a digital wind velocity indicator have been superimposed. The results of the test are summarized in the following paragraphs.

4.1 Spherical Models with Fins, Flares, and Thin Rings

In general, the spherical models with fins behaved similarly to the one DOF case. Those that tumbled in one DOF also tumbled in this case; those that would not tumble when launched inverted would quickly turn over and stabilize.

The models with 12 degree flares having various vent area shapes were all dynamically stable; however, they exhibited an oscillatory behavior that is believed to have resulted from alternating vortex shedding. Installation of a 3/16-inch fence just ahead of the flare improved the behavior but did not eliminate it.

Table 7.1C-1. Qualitative Results of One Degree of Freedom Tests

A. FINNED SPHERES

θ	0.25	0.40	0.50	0.75	1.00
0					
10		NOT TESTED			
20					
30		NOT TESTED			
40					
45					
50					

← → SATISFACTORY

B. RINGED SPHERES

ALL BISTABLE

ALL AUTORotate IF SUFFICIENTLY DISTURBED

C. BLUNTED CONES WITH VARIOUS AFTERBODIES

ALL MODELS TESTED EXCEPT HEMISPHERICAL AFTERBODY WERE DYNAMICALLY UNSTABLE AND DIVERGED INTO AUTOROTATION

Table 7.1C-2. Summary of Results for 45° Conical Forebody Models in ARC Water Facility

C.G.	CODE D/ σ	-0% d		-2.5% d		-5% d	
		B/LC 3.6	B/LC 4.6	B/LC 4.6	LC 3.6	LC 4.6	
A-C				T 3.8	LC 4.6	S 3.6	LC 4.6
A-E ₂							
A-E ₂ -R						LC 3.6	LC 4.6
A-F		LC 3.6	LC 4.6	LC 3.8	S 4.6	S 3.6	S 4.6
A-F-R		LC 3.6	LC 4.6		S 4.6	S 3.6	
A-G		LC 3.6	LC 4.6	LC 3.8		LC 3.8	LC 4.2
A-G-R			LC 4.0		LC 4.0		LC 4.0
A-D	LIFT 3.6	S 4.6	LIFT 3.8	LIFT 4.2	LIFT 4.0	LIFT 4.0	LIFT 4.2

NOTE: SEE FIGURE 7.1-4 FOR CONFIGURATION IDENTIFICATION

B/LC - IMPLIES LIMIT CYCLE $>\pm 15^\circ$ ABOUT $\alpha = 180^\circ$

LC - IMPLIES LIMIT CYCLE $>\pm 15^\circ$ ABOUT $\alpha = 0$

S - IMPLIES STABLE TRIM AT $\alpha = 0$

LIFT - IMPLIES MODEL EXHIBITED LARGE LATERAL OSCILLATIONS, SOMETIMES HITTING SIDE OF TANK

Table 7.1C-3. Summary of Results for 55° Conical Forebody Models in ARC Water Facility

CG		0% d		-5% d		-10% d	
K-M	CODE D/ σ	LLC* 4.4	LLC* 5.4	LLC* 4.4	LLC* 5.4	NOTE 4.4	LLC 5.4
K-L		LLC 4.4	LLC* 5.4	LLC* 4.4	LLC 5.4	LLC 4.4	LLC 5.4
B-M		C* 4.7	LLC* 5.6	LLC 4.7	LLC* 5.6	LLC 4.7	LLC 5.6
B-L	1	C* 4.7	LLC* 5.6	LLC 4.7	LLC* 5.6	LLC 4.7	LLC 5.6

NOTE: MODEL WAS STABLE ON FIRST FLIGHT. SUBSEQUENT FLIGHTS EXHIBITED LLC, BUT AFTER 5 MINUTES WAIT FOR WATER TO SETTLE, A VERY STABLE FLIGHT WAS AGAIN PRODUCED. CONCLUSION REACHED WAS THAT A VERY SMALL DISTURBANCE WAS REQUIRED TO INITIATE THE LLC.

LLC - LARGE LIMIT CYCLE, $30^\circ < \alpha < 45^\circ$

C - CONING $\alpha \approx 30^\circ$

* - WILL EXHIBIT SAME BEHAVIOR BACKWARDS.

Table 7.1C-4. Summary of Results for 60° Conical Forebody Models in ARC Water Facility

CG	CODE D/ σ	0% d		-2.5% d	
		LC 4.3	LC 5.4	LC 4.4	LC 5.5
B-C					
B-E ₂		LC 4.3	LC 5.1		LC 4.4
B-F		LC 4.3	S 5.1	LIFT 4.0	S 5.0
B-F-R		LC 4.3	S 5.1	S 4.0	S 5.0
B-G		LC 3.6	LC 4.7	LC 3.9	LC 4.4
B-G-R		LC 3.6	LC 4.5	LC 4.0	LC 4.3
B-D		LIFT 3.6	LIFT 4.7	LIFT 3.9	LIFT 4.4

NOTE: SEE NOTE ON TABLE 7.1C-2

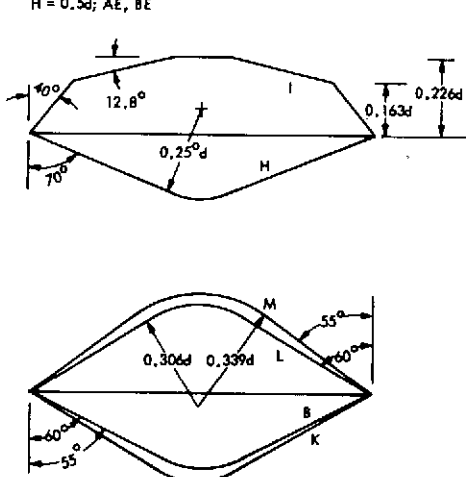
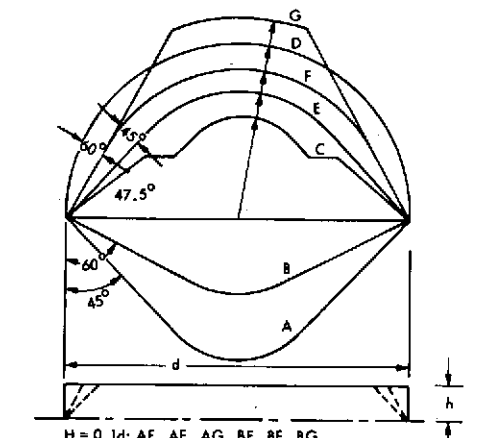
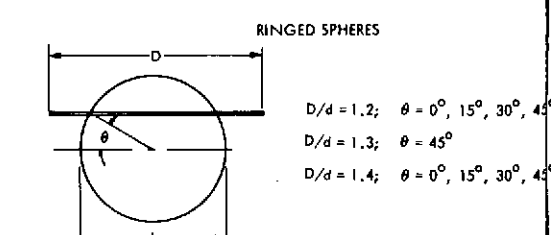
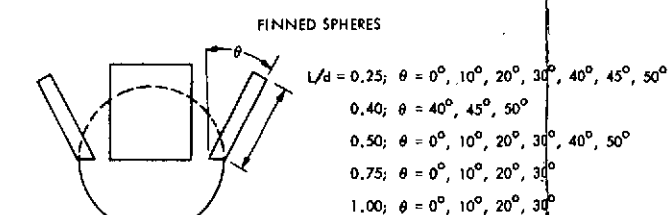


Figure 7.1C-7. Configurations for Army Meteorological Wind Tunnel One Degree of Freedom Tests

Figure 7.1C-8. Configurations Tested in the Ames HFFB Water Tank Showing Identification Code

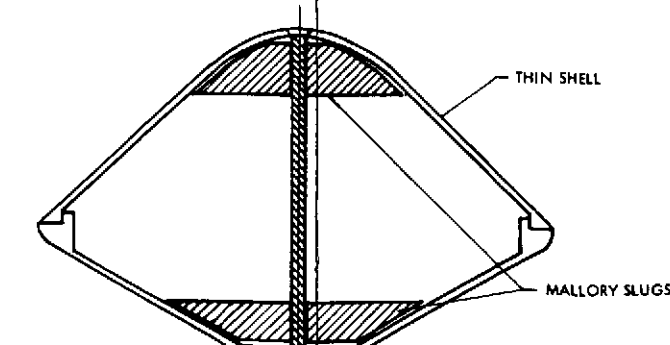


Figure 7.1C-9. Schematic Showing Adjustable Slugs on Central Screw to Facilitate C. G. and Inertia Variations

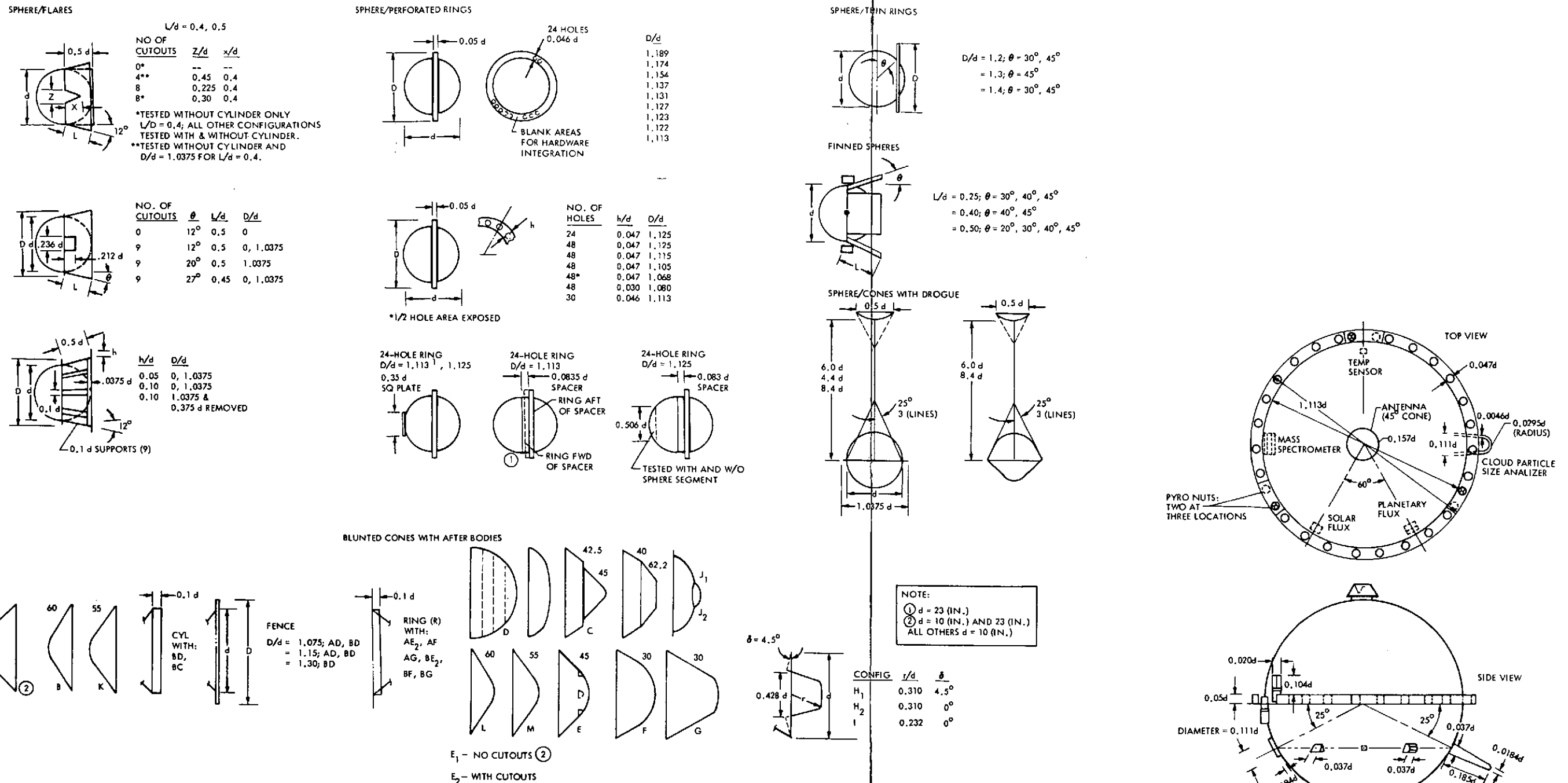


Figure 7.1C-10. Configurations Tested in the NASA Langley Spin Tunnel

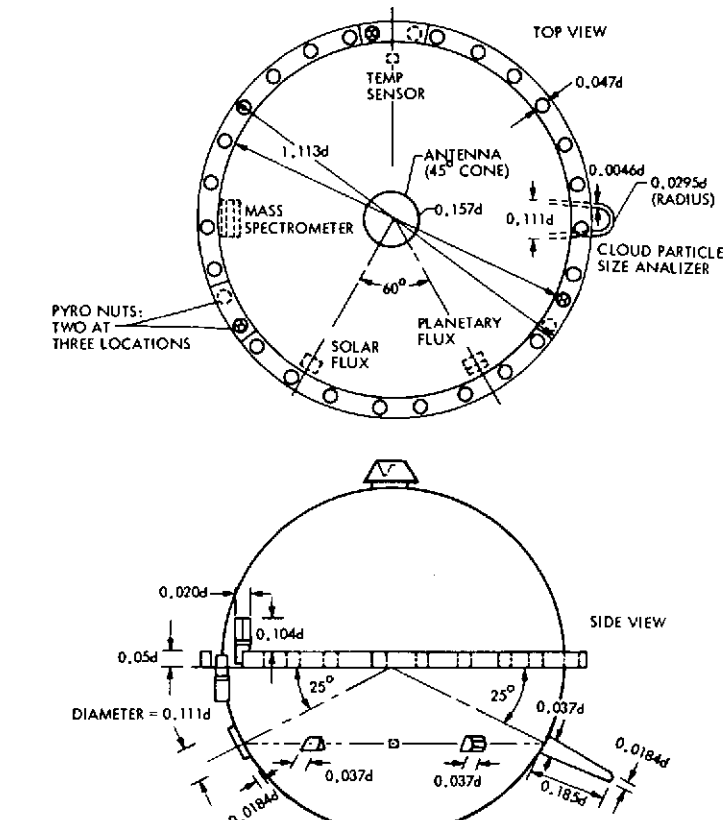


Figure 7.1C-11. Sketch of 23-IN. Sphere with Perforated Ring and Proluberances Tested in the NASA Spin Tunnel

The spherical models with thin rings behaved somewhat differently than in the one DOF tests, i.e., they would not fly inverted (backwards) as they did with one DOF. The models would undergo a divergent oscillation and eventually tumble when launched inverted. The effects on the stability of variations in roll rate were very minor.

4.2 Spherical Models with Perforated, Thick Rings

The results of spin tunnel tests on spherical models with various thick, perforated ring widths and porosities, and various antennas, antenna fairings, and protuberance arrangements are summarized in Table 7.1C-5. These results indicate that the drag coefficient is readily tailored through variations in ring geometry. However, it is also seen that lowering the porosity to 12.8 percent resulted in a limit cycle behavior and reducing the ring width to $D/d = 1.113$ for the 23-inch models (which are 81 percent of full scale), and to $D/d = 1.068$ for the 10-inch models resulting in finite trim angles. This difference has not been resolved. It may be a Reynolds number or a hole geometry effect. The 23-inch model had 30 holes and the 10-inch model had 48.*

The results in Table 7.1C-5 also demonstrate that the effects of several protuberance arrangements on the trim behavior of the sphere were negligible.

The effects of several fairing arrangements designed to accommodate the wind/altitude radar antenna and of simply attaching the antenna to the bottom of the sphere are seen to result in the model being either unstable or developing a finite trim angle. As shown in Table 7.1C-5c the antenna fairing was simulated by placing a cylindrical section between the two model hemispheres. The c.g. was always maintained relative to the lower face of the perforated ring. Thus, inserting the cylinder resulted in moving the center of pressure (c.p.) of the forward hemisphere forward and destabilizing the configuration. The effect of moving the ring fore and aft and of

*In spin tunnel tests it is difficult to distinguish between a limit cycle behavior and a finite trim angle behavior. Sometimes, when the roll rate was very low, a model would tend to limit cycle and, after the roll rate built up, it would settle on a trim angle and fly in a circle.

moving the c.g. is clearly shown in Table 7.1C-5c and it appears that the c.p. was about at the center of the cylinder (0.042d), since the configuration became marginally stable with the c.g. at 0.05d.

The effect of the cylindrical insert in producing transverse motion (lift) in the spin tunnel, as indicated in Table 7.1C-5c, was shown previously to occur also for the conical models. This effect probably results from the extra flat area for the local pressures to act on.

Adding the flat plate antenna to the spherical model (without a cylindrical section) had the effect of producing a finite trim point.

It seems as a result of the spin tunnel tests that the design of the perforated ring for the basic sphere is fairly well in hand and that adding several protuberances has very little effect. However, accommodating the radar antenna has not been resolved. The various effects on c.p. movement discussed above seem to be rather simple, but further testing with other variations on antenna fairings and ring/hole geometry are in order before finalization of the ring or the antenna configurations.

4.3 Roll Devices

The results of studies performed in the spin tunnel on roll devices for the descent capsule are shown in Figure 7.1-12 in terms of helix angle, $\frac{pd}{2V}$, acquired as a function of fin or hole angle. The 4-in.² total area fins are shown to be 64 percent efficient. The 9-in.² total area fins approach 100 percent efficiency. The canted holes, as a roll device on the sphere/perforated ring, exhibit greater than 100 percent efficiency. The canted holes are a more efficient roll device than the fins because in part they probably sense a higher local velocity.

These results indicate that hole angles of 0.54 degrees will produce a roll rate of five revolutions per kilometer for the full scale descent capsule. It should be apparent that the hole angle required for a given roll rate will scale in proportion to the sphere diameter.

4.4 Conical Models

The conical models with various afterbodies, no roll rate, and c.g. located at the maximum diameter ($\approx 0\%d$) stations behaved similarly in the spin tunnel and in the one degree of freedom tests at CSU. Except with the

Table 7.1C-5. Summary of Results
of Sphere/Thick, Perforated Ring
Model Tests in the Spin Tunnel

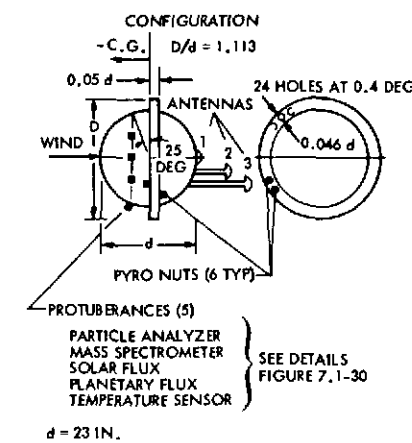
CONFIGURATION

(a) **RING VARIATIONS**

HOLE CONFIGURATION	D/d	h/d	C.G. % d	POROSITY % RING AREA	REF. D C _D	TEST OBSERVATIONS
24 AT 0.8°	1.125	0.047	-5.0	19.9	0.62	0° TRIM, 2° PERTURBATIONS
24 AT 0.8°	1.125	0.047	-3.5	19.9	0.58	0° TRIM, 4° PERTURBATIONS
24 AT 0.8°	1.125	0.047	0	19.9	0.62	0° TRIM, 8° PERTURBATIONS
24 AT 0.8° 24 AT 0°	1.125	0.047	-3.5	39.7	0.44	0° TRIM, 4° PERTURBATIONS
24 AT 0.8° 24 AT 0°	1.115	0.047	-3.5	43.4	0.48	0° TRIM
24 AT 0.8° 24 AT 0°	1.105	0.047	-3.5	47.7	0.45	0° TRIM, 3° PERTURBATIONS
24 AT 0.8° 24 AT 0°	1.068	0.047	-3.5	37.5	0.35	4° LIMIT CYCLE
24 AT 0.4° 24 AT 0°	1.080	0.030	-3.5	26.0	0.49	0° TRIM, 2° PERTURBATIONS
24 AT 0.4°	1.125	0.47	-3.5	19.9	0.58	0° TRIM, 3° PERTURBATIONS
30 AT 0.4°	1.113	0.46	-3.5	27.6	0.54	3° TRIM

(b) **RING VARIATIONS (CONTINUED)**

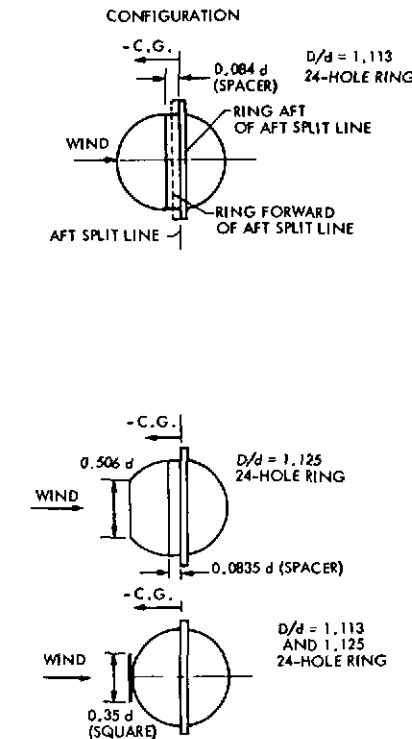
D/d	C.G., % d	POROSITY % RING AREA	C _D REF, D	TEST OBSERVATIONS
1.189	-3.5	12.8	0.71	6° LIMIT CYCLE
1.174*	-3.5	13.9	0.70	0° TRIM, 7° PERTURBATIONS
1.154	-3.5	15.9	0.68	0° TRIM, 5° PERTURBATIONS
1.137	-3.5	18.0	0.68	0° TRIM, 6° PERTURBATIONS
1.131	-1.5	18.8	0.64	0° TRIM, 6° PERTURBATIONS, WEAK DAMPING
1.131	-5.0	18.8	0.64	0° TRIM, 4° PERTURBATIONS
1.131	-6.5	18.8	0.64	0° TRIM, 6° PERTURBATIONS
1.127	-3.5	19.5	0.63	0° TRIM, 5° PERTURBATIONS
1.123	-3.5	20.1	0.62	0° TRIM, 6° PERTURBATIONS
1.122	-3.5	20.4	0.62	0° TRIM, 4° PERTURBATIONS
1.113	-3.5	22.1	0.60	5° TRIM, 7° PERTURBATIONS



CONFIGURATION

(a) **RING VARIATIONS (CONTINUED)**

D/d	C.G., % d	POROSITY % RING AREA	C _D REF, D	TEST OBSERVATIONS
1.189	-3.5	12.8	0.71	6° LIMIT CYCLE
1.174*	-3.5	13.9	0.70	0° TRIM, 7° PERTURBATIONS
1.154	-3.5	15.9	0.68	0° TRIM, 5° PERTURBATIONS
1.137	-3.5	18.0	0.68	0° TRIM, 6° PERTURBATIONS
1.131	-1.5	18.8	0.64	0° TRIM, 6° PERTURBATIONS, WEAK DAMPING
1.131	-5.0	18.8	0.64	0° TRIM, 4° PERTURBATIONS
1.131	-6.5	18.8	0.64	0° TRIM, 6° PERTURBATIONS
1.127	-3.5	19.5	0.63	0° TRIM, 5° PERTURBATIONS
1.123	-3.5	20.1	0.62	0° TRIM, 6° PERTURBATIONS
1.122	-3.5	20.4	0.62	0° TRIM, 4° PERTURBATIONS
1.113	-3.5	22.1	0.60	5° TRIM, 7° PERTURBATIONS



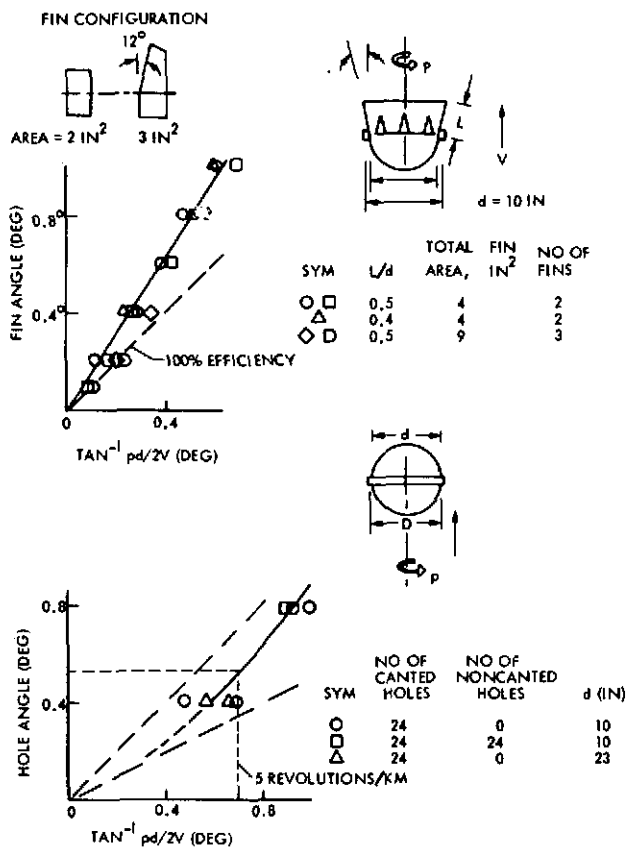


Figure 7.1C-12. Roll Device Angle as a Function of Helix Angle

hemispherical afterbody, they were statically stable and dynamically unstable and would self-excite into a tumbling mode. Moving the c. g. aft increased the self excitation. In the no-roll tests the model behavior was essentially planar.

Of particular interest was the effect of roll rate on the stability of the conical models. As the roll accelerated, a point was reached when the models would enter a divergent spiral mode. It was determined from studying the motion pictures that roll acceleration and not just roll velocity apparently influenced the stability; the instability seemed to be delayed until completion of roll acceleration. Murphy* discussed this phenomenon. Time has not permitted a detailed analysis of the present results in light of Murphy's work; however, the spin rates at which instabilities were observed in the spin tunnel were much higher than those of interest to the Pioneer Venus probes.

*C. H. Murphy, "Response of an Asymmetric Missile to Spin Varying through Resonance", AIAA Journal (November 1971).

With the hemispherical afterbody both of the conical forebodies were dynamically stable at zero roll rate. With roll fins installed, however, these models also would enter a divergent spiral mode at some critical value of roll rate and acceleration. Fences located at the maximum diameter station having heights of $1/8$, $3/8$, $3/4$, and $1-1/2$ inches on the conical models with hemispherical afterbody resulted in decreasing stability. A $1/10$ d cylindrical section in between the 60 degree cone and hemisphere resulted in the model developing a side force and flying into the side wall of the tunnel. With the stepped biconic afterbody the model self-excited into a tumble.

The above discussion pertains to c. g. location in the plane of the maximum diameter station. It can be seen in Tables 7.1C-6, 7.1C-7, and 7.1C-8 that the effect of moving the c. g. forward and of increasing the value of D/σ was to increase dynamic stability markedly. Examination of Table 7.1C-6 indicates that configuration A-F with -4.0 percent d c. g. and $D/\sigma = 4.0$ (the preferred small probe) exhibited the smallest limit cycle angle, and it could be perturbed to about 46 degrees without tumbling. It is interesting that the 23 in. model, which is 81 percent of full scale, exhibited a 0-degree limit cycle compared to 4 degrees for the 10 in. model.* The high degree of stability, the packaging volume availability, and roll-to-pitch inertia ratio (1.18) for this configuration led to its selection as the preferred small probe.

The effects of afterbody shape, c. g. location and D/σ values for the 60 degree large probe candidate configurations are shown in Table 7.1-8. It is seen that the F afterbody with c. g. at -2.5 percent d appears to be best. However, in view of packaging the integration requirements, the E afterbody was deemed to be a satisfactory compromise for the Thor/Delta option. For the Atlas/Centaur option, which incorporates the perforated ring rather than the vented flare for stabilizing the descent capsule, a much smaller afterbody volume is required. Also, because of the larger diameter required by the greater weight, it is possible to package the probe with a more

*This behavior is possibly related to the scale of turbulence in the spin tunnel. It is not thought to be a Reynolds number effect because the drag coefficients, deduced from the equilibrium velocities, were identical for the two models.

Table 7.1C-6. Summary of Spin Tunnel Results for 45° Cones

C.G.		0% d			-2.5% d			40% d		-5.0% d			10.0% d	
A-J ₁	CODE D/ σ		TUMBLE 4.6	TUMBLE 5.4	12-X-30 3.6	6-35-X 4.5	3-25-X 5.3		4-29-40 3.8		5-45-X 5.0			
A-J ₂		TUMBLE 3.8		TUMBLE 5.1	5-38-X 3.6		6-40-X 5.3		5-40-X 3.9		4-40-X 5.1			
A-C		TUMBLE 3.6												
A-E ₁						10-40-X 4.6	6-30-X 5.0		6-24-45 3.6	2-45-X 4.4				
A-E ₂		TUMBLE 3.5		TUMBLE 5.2	9-40-X 3.8	5-44-X 4.6	6-40-X 5.0		10-42-50 3.6	4-25-X 4.4				
A-E ₂ -R			35-X-X 4.3		28-X-X 3.5	12-12-X 4.2			10-X-X 3.4	6-20-X 4.0				
A-F		2-35-X 3.8		4-35-X 4.9	5-40-X 3.6	3-40-X 4.0	5-40-X 4.7	4-45-50 4.0	4-45-X 3.5	5-80-X 3.8	5-45-X 4.6	5-45-X 3.2	4-60-X 3.9	
A-F'								0-30-50 4.0						
A-F-R		6-15-X 3.5	7-32-X 4.2		10-30-X 3.4	7-12-X 4.0			5-36-X 3.3	5-23-X 3.9				
A-G						7-40-X 4.0				12-70-X 3.9				
A-G-R					15-X-X 3.6				15-32-X 3.5					
A-D		15-WILL NOT TUMBLE				LIFT 4.1			LIFT 3.9					

NOTE: BEHAVIOR CODE:

X - X - X

X NO VALUE AVAILABLE

* 24-IN DIAMETER MODEL; ALL OTHERS 10-IN DIAMETER

Table 7.1C-7. Summary of Spin Tunnel Results for 55° Cones

C.G.		-3.5% d		-10.0% d	
K-E	CODE D/ σ	36-X-X 3.6	2-36-48 4.8	0-56-X 3.9	
K-F		4-46-78 3.6	5-49-65 4.6	3-67-X 3.9	
K-H ₂			24-X-37 4.9		

NOTE: SEE NOTE ON TABLE 7.1C-6

Table 7.1C-8. Summary of Spin Tunnel Results for 60° Cones

C.G.		0% d			-2.5% d			-3.5% d		
CONFIG										
B-J ₁	CODE D/ σ							7-23-X 4.6	5-48-X 5.4	
B-J ₂								5-16-X 4.9		
B-C										
B-E ₁		TUMBLE 3.9	8-35-X 4.8	4-41-52 5.6			7-X-65 4.6	5-59-62 5.5		
B-E ₂		TUMBLE 3.9	15-21-38 4.8	6-X-50 5.6	TUMBLE 3.7		5-39-50 4.6	5-X-60 5.5		
B-F		TUMBLE 3.5	10-34-25 4.3	2-40-X 5.5	6-44-50 3.6		2-55-X 4.6	9-44-X 5.4		
B-F-R		20-40-X 3.5	3-38-X 4.6		4-29-X 3.6		5-X-X 4.5			
B-G					15-20-30 3.6		5-20-X 4.6			
B-G-R							7-X-X 4.0			
B-D			10-X-X 4.6		15-X-X 3.5		12-X-X (LIFT) 4.6			
B-H ₁									5-60-68 4.9	
B-H ₂									5-52-58 4.9	
B-I									5-47-X 4.9	

NOTE: SEE NOTE ON TABLE 7.1C-6

forward c. g. location, estimated to be -3.5 percent d, and a relatively large value for D/σ , estimated to be 4.9. These reasons led to a study of the H, H_2 , and I afterbodies. It is seen in Table 7.1C-8 that these configurations all exhibited satisfactory stability in the spin tunnel.

5. GENERAL DISCUSSION

Two particular events occurred during these tests that probably would not have happened in a short duration test such as free-flight in a wind tunnel or ballistic range, or even in an air drop. Some models exhibited a double limit-cycle behavior. The second (larger) limit usually occurred only after disturbing the model significantly. Another model exhibited a limit-cycle behavior over a long period of time, but then, quite suddenly, after being disturbed, apparently by an eddy in the wind stream, it diverged into a tumbling mode.

Because of the utility and flexibility of the spin tunnel and also as a result of the previously described behavior, it is believed that the long flight time available for models in the spin tunnel makes this type of testing mandatory in the final proof test of a particular configuration.

APPENDIX 7.2A
PRELIMINARY EVALUATION OF TEFLON
AS A REFLECTING HEAT SHIELD FOR VENUS ENTRY

1. Radiation Scattering Theory	7.2A-2
2. Radscan Computer Program	7.2A-7
3. Teflon Analyses	7.2A-11
4. Conclusions and Recommendations	7.2A-20

APPENDIX 7.2A

PRELIMINARY EVALUATION AS TEFLON AS A REFLECTING HEAT SHIELD FOR VENUS ENTRY

A probe entering the atmospheres of Venus and the outer planets (Jupiter, Saturn, and Neptune) will experience entry heating very much larger than that of previous entry environments, primarily as a result of the high velocities of typical entry probes. A substantial fraction of the entry heating will be caused by shock-layer radiation. If this radiation could be totally reflected, the net energy delivered to the heat shield surface could be greatly reduced and entirely convective in nature. The result of such a radiation blocking process would be a decreased heat shield weight requirement and, thus, an increased scientific instrument package. This is the concept behind a reflecting heat shield (RHS, also called a radiation scattering heat shield).

The principle of a RHS is very similar to that of white paint. Paint typically is composed of a scattering pigment dispersed in a transparent vehicle or "binder." Scattering is accomplished by reflections and refractions at the interface between the pigment and the binder. This process is most efficient when the difference in the index of refraction between the pigment and the binder is large. White paint appears white because the scattering process is equivalent for all wavelengths in the visible spectrum. Neither the pigment nor the binder is white in itself; in fact, ideally they should be transparent.

Shock-layer radiation during planetary entry covers a broad range of the electromagnetic spectrum. The exact spectral distribution is a strong function of the atmospheric composition and entry conditions. Typically for Venus entry, a substantial fraction is in the ultraviolet region. For maximum efficiency, a RHS must show small absorption and large scattering ability over the spectral range that is particular to a given entry environment.

To analyze the concept of reflective heat shields for planetary entry, a computer program was developed during 1972 under MMC IRAD effort (Reference 1). This program, called RADSCAT, is described in detail in Section 2 and 3 of this Appendix. Because it has been proposed that Teflon

could be used as a reflective ablator (References 2, 3, and 4), analyses were made using RADSCAT to analyze Teflon's performance. The results of these analyses are presented in Section 4 of this Appendix.

1. RADIATION SCATTERING THEORY

Before writing the RADSCAT computer program, various mathematical models were evaluated to determine the best radiation scattering calculation procedure. For a 10-wavelength band analysis, the radiation subroutine would have to be called approximately 1000 times per problem by the main program, an important consideration in choosing the calculation method. The radiation routine would have to give good accuracy, but at the same time, not be unnecessarily costly to operate. Previous papers on radiation scattering ablators (References 4 and 5) advocated the use of the Kubelka-Munk (K-M) method. These papers presented some experimental work which was done on reflecting materials, and K-M absorption and scattering coefficients for these materials, which had been obtained by analytical correlation of the test results.

The literature survey that was conducted in the initial stages of the 1972 IRAD work indicated that the recently developed "many-flux" (M-F) method of Mudgett and Richards (Reference 6) is one of the most accurate methods available for doing multiple scattering calculations. For RHS applications, the K-M method gives results that are just as good as those of the M-F method and is much less costly in computer time. (The K-M method is described in this Section 1A.) When doing radiation scattering calculations by the K-M method, certain restrictions must be followed:

- 1) RHS must extend over a region very large compared to its thickness;
- 2) Incident radiation must be nonpolarized;
- 3) Incident radiation must be entirely diffuse.

The first restriction results from the "one dimensional" nature of the K-M theory. The analysis assumes that any radiation scattered in a sidewise direction is compensated for by equal radiation scattered from adjacent regions. The second restriction is imposed because it is difficult to predict the Fresnel reflection coefficient (described in this Section 1.2) when the radiation is polarized. It should be pointed out that these

first two restrictions apply to the M-F method as well. The third restriction essentially defines the major difference between the K-M analysis and the M-F analysis. The Kubelka-Munk method is not as accurate as the "many-flux" method when incident radiation is collimated. The most accurate analyses by the K-M method are obtained when the incident radiation is entirely diffuse.

It is convenient that radiation scattering heat shield applications are within the range of usefulness of the Kubelka-Munk method. Generally, the RHS thickness will be very small compared to the region over which it extends. The shock-layer radiation produced during atmospheric entry is probably one of the best examples of radiation that is entirely diffuse. The radiation is predicted to be nonpolarized as well. Meeting these three requirements, however, is difficult to achieve in laboratory tests, and care must be taken in conducting tests and in the interpretation of the test results.

1.1 Kubelka-Munk Theory

According to the K-M method, the radiant energy within a RHS can consist of two components; a radiant flux being transmitted through the RHS toward the backface, the I flux; and a radiant flux caused by back-scattering by the RHS directed the front face, the J flux. These radiant fluxes are visually demonstrated in Figure 7.2A-1. The change in intensity of I and J with distance through the heat shield, x , is expressed by the following set of K-M simultaneous differential equations:

$$\frac{dI}{dx} = - (S+K) I + SJ \quad (1)$$

$$\frac{dJ}{dx} = + (S+K) J - SI \quad (2)$$

In these equations, S and K are the scattering and absorption coefficients, respectively, in units of reciprocal length. At the front face of the heat shield, $x = 0$, and at the backface, $x = \bar{X}$, where \bar{X} is the thickness of the heat shield.

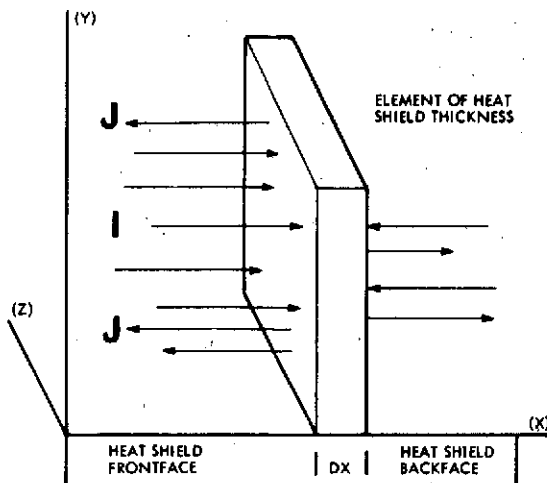


Figure 7.2A-1. Schematic Representation of Kubelka-Munk Analysis

To find solutions to these equations, it is convenient to make the substitutions $a = (S+K)$, $b = (S)$, and $d = (d/dx)$. Equations (1) and (2) can then be expressed as follows:

$$(D+a) I = + bJ \quad (3)$$

$$(D-a) J = - bI \quad (4)$$

Equation (3) is operated on with $(D-a)$, Equation (4) with (b) , and then Equation (4) is subtracted from Equation (3) to give Equation (5).

$$\begin{aligned} (D-a)(D+a)I &= b(D-a)J && \text{(3) times } (D-a) \\ -b^2 I &= b(D-a)J && \text{(4) times } (b) \\ \hline [(D-a)(D+a) + b^2] I &= 0 \end{aligned} \quad (5)$$

Solving Equation (5) and making the substitution $P = \sqrt{a^2 - b^2}$ gives Equation (6):

$$I = C e^{+Px} + C' e^{-Px} \quad (6)$$

This equation is an expression for the intensity of the I radiation at any point in the heat shield. C and C' are arbitrary constants which are dictated by the imposed boundary conditions.

To obtain a similar expression for the J radiation, Equation (6) is operated on with (D) to form Equation (7) and operated on with (a) to form

Equation (8):

$$DI = CPe^+ Px - C'Pe^- Px \quad (7)$$

$$aI = Ca e^+ Px + C'a e^- Px \quad (8)$$

Equations (7) and (8) are added together to form Equation (9):

$$(a+D) I = C(P+a)e^+ Px = C'(P-a)e^- Px \quad (9)$$

Using Equations (3) and (9) and making the substitution $A = (P+a)/b$, $B = (P-a)/b$, it is possible to solve for J , which is given by Equation (10).

$$J = CAe^+ Px - C'Be^- Px \quad (10)$$

Thus, Equation (6) and (10) are solutions to the Kubelka-Munk differential equations, and express the intensity of the I and J radiation at any point in the heat shield as a function of x .

1.2 Fresnel Reflection

Fresnel reflection is an electromagnetic radiation phenomena that occurs at the smooth boundary between optically dissimilar media. The magnitude of the reflection is proportional to the difference in index of refraction of the two media. The reflection coefficients are designated as:

R_E = external reflection, front surface

R_I = internal reflection, front surface

R_B = internal reflection, back surface

The physics of R_I can be explained quite easily. When light travels from a medium of higher refractive index (e.g., the RHS) to one of lower refractive index (e.g., the atmosphere), the angle between the normal to the surface and the light ray is made larger. Figure 7.2A-2 demonstrates that when this angle reaches a certain value, the critical angle, the refracted light ray is, in fact, refracted into the surface of the material. Any angle larger than the critical angle causes light to be refracted back into the medium of higher refractive index, resulting in internal "reflection." Since the internally incident light is coming from every direction (i.e., diffuse radiation), due to backscattering by the material, a constant percentage of light will have an incidence angle greater than the critical angle and will be reflected. The percentage makes up the major part of the internal

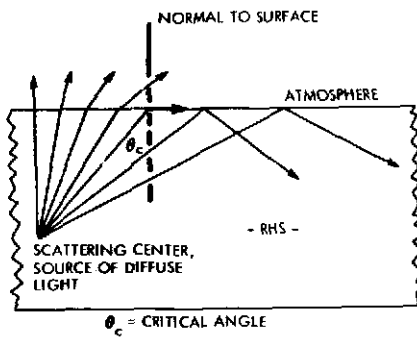


Figure 7.2A-2, Fresnel Reflection

reflection coefficient, R_I . Because the refractive index is a function of wavelength and temperature, so also is R_I .

This situation does not apply to R_E where the externally incident light is traveling into a medium of higher refractive index and its angle with the normal to the surface is made smaller. There is, however, a small external reflection, the magnitude of which depends on the degree of polarization of the incident light and the variation of intensity with angle of incidence. The physical explanation of this reflection requires some detail and will not be given here. Suffice to say that whenever a light wave falls on to a boundary between two homogeneous and optically dissimilar media, some of it is reflected, even when nonpolarized and entirely diffuse.

If the back surface of the RHS were free-standing and not attached to a substructure, then internal reflection at the back surface would be the same as at the front surface. In other words, R_B would equal R_I . However, the magnitude of R_B is controlled to a large extent by the reflectance of the substructure, the smoothness of the interface, and the method of attachment. It is difficult to accurately predict a value for R_B from theory; usually it must be determined by experiment.

If the externally incident radiation is nonpolarized and entirely diffuse, and the external medium has a refractive index of approximately 1.0, R_E and R_I can be estimated by Equations (11) and (12) given below. In these equations, n is the index of refraction of the RHS.

$$R_E = 1/2 + \left[\frac{(n-1)(3n-1)}{6(n+1)^2} \right] + \left[\frac{n^2(n^2-1)^2}{(n^2+1)^3} \right] \ln \left[\frac{(n-1)}{(n+1)} \right] - 2n^3 \left[\frac{(n^2+2n-1)}{(n^2+1)(n^4-1)} \right] + \left[\frac{8n^4(n^4+1)}{(n^2+1)(n^4-1)^2} \right] \ln(n) \quad (11)$$

$$R_I = 1 - \frac{1}{n^2} + \frac{R_E}{n^2} \quad (12)$$

Table 7.2A-1 gives values for R_E and R_I calculated for different indices of refraction using Equations (11) and (12).

Table 7.2A-1. Fresnel Reflection Coefficient As A Function of Refractive Index

R _E AND R _I COMPUTED FROM EQUATIONS (7.2A-11) AND (7.2A-12)		
N	R _E	R _I
1.050	0.00992	0.10197
1.100	0.01760	0.18810
1.150	0.02431	0.26223
1.200	0.03051	0.32674
1.250	0.03644	0.38332
1.300	0.04223	0.43327
1.350	0.04796	0.47762
1.400	0.05366	0.51718
1.450	0.05938	0.55262
1.500	0.06511	0.58449
1.700	0.08831	0.68454
1.900	0.11180	0.75396
2.100	0.13527	0.80392

The three reflection coefficients are used in setting up the boundary conditions for the solution of Equations (6) and (10), as described in the next Section 2.

2. RADSCAT COMPUTER PROGRAM

The RADSCAT computer program is a modified version of the MMC explicit finite difference digital thermochemical ablation program, T-CAP III. The one-dimensional ablator model in this program consists of up to four material phases: virgin plastic, pyrolysis zone, char, and pyrolysis vapor. The aeroheating environment is described by time-dependent curves of convective and radiant heating rates, velocity, and altitude. Surface heating is accommodated by conduction into the ablator, convective blocking due to mass injection into the boundary layer, reradiation from the

surface, and surface chemical reactions. Material removal due to surface reactions, vaporization, sublimation, and spallation may be computed.

The radiant energy absorbed by each ablator element is combined with the enthalpy transitions due to temperature changes, pyrolysis reactions, and transpiring pyrolysis vapors, to determine the heat shield thermal conduction and internal temperature response.

In addition, the thermal response of a substructure consisting of up to six different nonablating materials can be computed, by means of a three-dimensional conduction and radiation heat transfer routine.

The radiation scattering subroutine in RADSCAT divides the heat shield into two zones: a "hot" and a "cold" zone. Figure 7.2A-3 demonstrates the analytical model. The hot zone is the front part of the heat shield where the temperature is everywhere higher than T_{trans} . The variable T_{trans} is pre-loaded for a given material and is the temperature at which the scattering ability of the heat shield material is greatly reduced because of a change in microstructure. Many of the materials that will be considered for use as a radiation-scattering heat shield lose their scattering ability at elevated temperatures. "Melting" of the crystalline scattering centers results in a loss of scattering ability. With Teflon, for instance, opacity maintains until about 603°K (330°C), at which point the crystalline centers melt and the material becomes transparent. The cold zone in RADSCAT is the region at the backface of the heat shield where the temperature is everywhere below T_{trans} . In addition to being broken up into two zones, the heat shield is divided into a large number of independently sized elements, for heat transfer analysis by finite difference methods. Each of the two zones is made up of an integral number of these finite difference elements. Because the elemental temperatures vary with time, the boundary between the hot and cold zones moves with time. The thickness of each element is X_L where L indicates the element number. The total heat shield thickness is \bar{X} . N is the total number of heat shield elements, and M is the number of hot zone elements. The element at the surface of the ablator is a zero mass and zero volume element which is used in an energy balance calculation.

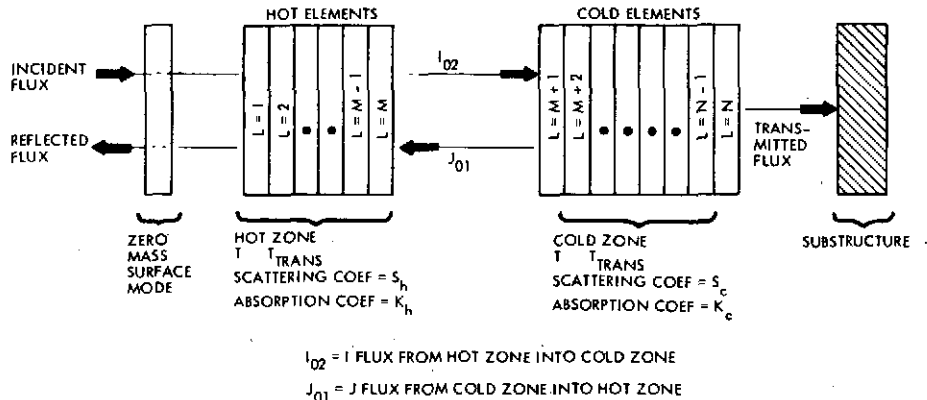


Figure 7.2A-3. RADSCAT Model

In the RADSCAT radiation routine the absorption and scattering coefficients, K and S, are preloaded as functions of wavelength. The routine does a complete set of radiation transfer calculations for each wavelength band and then sums the results over all the bands. Any number of bands can be input, but presently the maximum number being used is ten. The K and S values are input in two arrays, in addition to being functions of wavelength. A "hot" array is input for the K and S in the hot zone, and a "cold" array is input for the cold zone. The subscript h is used to designate the hot zone and the subscript c for the cold zone; thus K_h , S_h , and K_c , S_c . Every variable could also be subscripted with a j to indicate the band number. This is done in the program but would be too cumbersome to do in this discussion. Therefore, subscript j is implicit in all that follows.

The radiation transfer equations in RADSCAT have a closed-form solution. No iterations are performed on the radiation fluxes between the elements. The derivation of the closed form solution is given at this point. As previously presented by Equation (6) and (10), the general solutions to the Kubelka-Munk differential equations are the following:

$$I = Ce^{+Px} + C'e^{-Px}$$

$$J = ACe^{+Px} - BC'e^{-Px}$$

The closed-form solution requires that boundary conditions be specified for three regions of the heat shield: (1) the frontface of the hot zone; (2) the boundary between the hot zone and the cold zone; (3) the backface of the cold zone. The boundary condition at (1) is that the intensity of the I radiation at the frontface is equal to a fraction $(1-R_E)$ of the

externally incident radiation (I_o), plus a fraction (R_I) of the backscattered J radiation at the frontface:

$$I|_{x=0} = I_o(1-R_E) + JR_I$$

The boundary conditions at (2) states that all the I radiation that comes out of the hot zone goes into the cold zone, and all the J radiation from the cold zone goes into the hot zone. The boundary condition at (3) states that a fraction ($1-R_B$) of the I radiation at the backface of the cold zone is transmitted to the substructure, and a fraction (R_B) is reflected back into the heat shield as J radiation.

When the above boundary conditions are imposed, they produce the following six simultaneous equations in six unknowns:

$$C_h(1-R_I A_h) + C'_h(1+R_I B_h) = I_0(1-R_E) \quad (13)$$

$$C_h A_h e^{+ P_h \bar{X}_h} - C'_h B_h e^{- P_h \bar{X}_h} = J_{01} \quad (14)$$

$$C_h e^{+ P_h \bar{X}_h} + C'_h e^{- P_h \bar{X}_h} = I_{02} \quad (15)$$

$$C_c + C'_c = I_{02} \quad (16)$$

$$C_c A_c - C'_c B_c = J_{01} \quad (17)$$

$$C_c(A_c - R_B)e^{+ P_c \bar{X}_c} - C'_c(B_c + R_B)e^{- P_c \bar{X}_c} = 0 \quad (18)$$

In the above equations, \bar{X}_h and \bar{X}_c are the total thicknesses of the hot and cold zones, respectively. The six unknowns that must be solved for are J_{01} , I_{02} , C_h , C'_h , C_c and C'_c . The solutions can easily be obtained by standard matrix inversion and multiplication subroutines. Instead of putting these matrix subroutines into RADSCAT, however, it was decided that it would be less costly to put a closed-form solution of the above equations in RADSCAT.

In a typical RADSCAT analysis, the radiation scattering subroutine sums up the thicknesses of the hot elements to determine the thickness of the hot zone and then sums the thicknesses of the cold elements to determine the thickness of the cold zone. Next, it solves for the constants I_{02} , J_{01} , C_h , C'_h , C_c and C'_c . After these constants have been solved for, it calculates the I and J flux at the frontface and the backface of each element by using Equations (6) and (10). The rate at which energy is absorbed by each element, designated E_L , is equal to I at the frontface of the element, plus J at the backface, minus I at the backface, minus J at the frontface. The rate at which energy is transmitted to the substructure, I_{trans} , is I at the backface of the Nth element times $1-R_B$. The rate at which energy is "reflected" from the frontface of the RHS, J_{refl} , is R_E times the externally incident radiation, plus the J radiation at the frontface of the 2nd element times $1-R_I$. This process is repeated for each wavelength band and the rate at which energy is absorbed, transmitted, and reflected is summed over all the bands.

3. TEFLON ANALYSES

It has been proposed that using a Teflon-reflecting heat shield on the Pioneer Venus entry probes would be competitive with reradiative systems and could possibly be lighter, as a result of Teflon's ability to scatter the incident shock-layer radiation. Therefore, analyses were made using RADSCAT to quantitatively evaluate Teflon's performance and compare it with the performance of other reradiative ablators. These analyses were made for the stagnation point of a blunted Venus probe with the following entry conditions:

$$\gamma_E = -40^\circ$$

$$V_E = 11.16 \text{ km/sec}$$

$$\beta = 78.5 \text{ kg/m}^2$$

Two probe configurations were considered in the analyses. One was a sphere-cone forebody with a nose radius (R_N) of 36.8 cm, and the other was a spherical segment forebody, similar to the Apollo design, with a nose radius of 158.5 cm. The major criteria on the heat shield performance was

that it maintain the heat sink structure supporting the heat shield at a temperature below 422°K for stagnation pressures greater than $1.01 \times 10^4 \text{ N/m}^2$ and below 589°K for stagnation pressures less than $1.01 \times 10^4 \text{ N/m}^2$. The substructure heat sink (aluminum) thickness and ablator thickness were parametrically varied to meet the above temperature criteria. Note that all analyses described are nominal; no design margins are included in the unit weights to accommodate uncertainties. It was assumed in the Teflon analyses that 30% of the MMC-calculated radiant heating was absorbed by the ablating boundary layer (see Section 3.2). The reradiative ablators, however, were analyzed assuming 100% of the MMC-calculated radiation was absorbed at the surface, with no reflection or absorption in the boundary layer. Teflon thermophysical properties are shown in Table 7.2A-2.

3.1 Gray-Body Teflon Analysis

Initially, analyses were conducted using the Teflon radiation scattering model presented in Reference 4. This reference predicts Teflon's scattering and absorption coefficients to be 10 cm^{-1} and 0.01 cm^{-1} , respectively. These coefficients were derived from reflectometer experiments on Teflon at room temperature and tests of ablating Teflon under high intensity radiation from an argon radiation source. It is assumed in this model that the Teflon is optically a gray body, with constant absorption and scattering coefficients over all wavelengths. This model for Teflon will be referred to as the "gray-body (G-B) Teflon model."

Figure 7.2A-4 presents the results of the analyses of G-B Teflon at the stagnation point of the sphere-cone probe and compares them with the predicted unit weights of ESA 5500 M3. The total weight of the ablator plus substructure heat sink is plotted, because a finite (and in some cases substantial) heat sink is required to accommodate the transmitted energy in the G-B Teflon analysis. It is interesting to note the strong influence of backface reflectance on the G-B Teflon system weight. If a perfect backface reflectance is achieved ($R_B = 1.0$), G-B Teflon is competitive with the ESA 5500 M3. With a less than perfect backface reflectance, the heat sink substructure absorbs a significant fraction of the incident radiation. For a backface reflectance of 0.9, which is a realistic coefficient for broad-band reflection, the system weight is nearly twice the weight of a system with $R_B = 1.0$. To the left of the minimum weight point in the G-B Teflon curve,

Table 7.2A-2. Teflon Thermophysical Properties

DENSITY	-	2150 KG/M ³
VAPOR MOLECULAR WEIGHT	-	45.36 KG/MOLE
HEAT OF VAPORIZATION	-	1.74 MJ/KG
<u>THERMAL CONDUCTIVITY TEMPERATURE</u>		
T, °K	K, JOULE/M SEC °K	
0.0	0.05168	
297.8	0.05168	
323.9	0.07475	
348.7	0.07752	
383.9	0.07752	
407.8	0.09298	
418.9	0.09436	
600.0	0.07752	
10 000.0	0.07752	
<u>SPECIFIC HEAT TEMPERATURE</u>		
T, °K	C _P , JOULE/KG °K	
0.0	258.4	
300.0	310.1	
761.1	426.4	
10 000.0	426.4	
<u>SUBLIMATION VAPOR PRESSURE</u>		
1/T, °K ⁻¹	P (GAS) N/M ²	
0.00018	7.72 × 10 ¹¹	
0.00180	1.692 × 10 ⁰	
0.00198	2.09 × 10 ⁻⁴	
0.00225	2.09 × 10 ⁻⁴	
10 000.0	2.09 × 10 ⁻⁴	

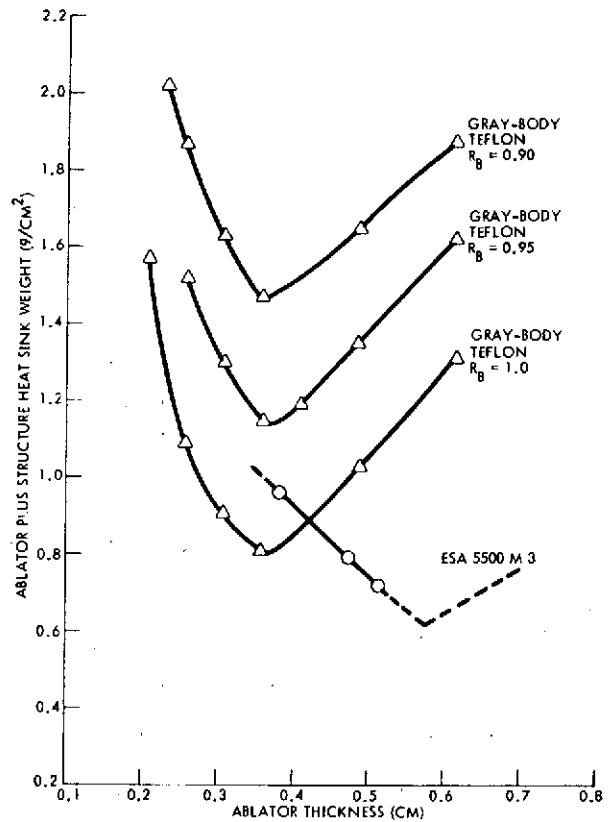


Figure 7.2A-4. Heat Shield System Weight versus R_B - GB Teflon

the steep increase in weight is due to a combination of high transmitted energy and conducted energy from the hot ablating surface. To the right of the minimum weight point, the conduction from the hot ablating surface has little influence on the substructure temperature, and the increase in weight is due to the increase in ablator thickness. In this region of the curve, only small reductions in transmitted energy occur with increasing G-B Teflon thicknesses, and thus only small reductions in the heat sink weight. For ESA 5500 M3 (and G-B Teflon with R_B = 1.0) the minimum weight corresponds to a zero heat sink thickness.

Figure 7.2A-5 shows the sensitivity of the energy transmitted to the backface as a function of the backface reflectance and G-B Teflon thickness, and shows why a high backface reflectance is required to minimize the transmitted energy (and structure temperature rise).

The ablator-heat sink substructure weight versus the substructure thickness, for G-B Teflon and for several reradiative ablators, is presented in Figure 7.2A-6. In addition to the skin thickness weight and

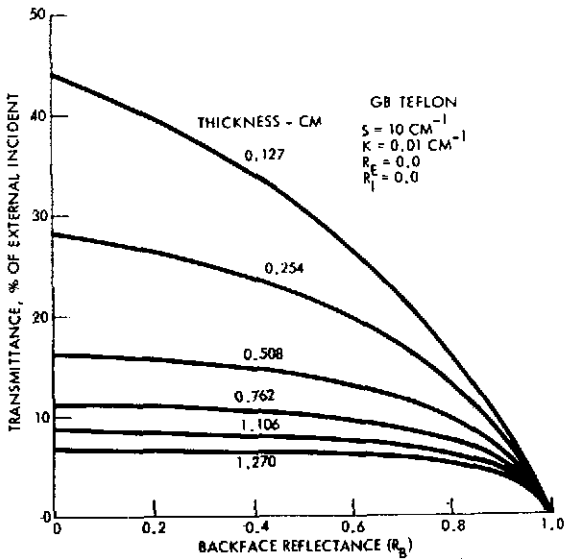


Figure 7.2A-5. Transmittance versus Thickness, R_B - GB Teflon

ablator weight, the structural stiffener weight should also be included in the total weight, to give a true system weight. The effect of stiffeners is to increase the weight more at low substructure thicknesses, dependent only upon the load and temperature criteria, and independent of the ablator system; therefore, a comparison of ablator performance is valid with the present data. Figure 7.2A-6 shows, as previously stated, that the minimum weight of those ablators which do not transmit radiant energy corresponds to a zero substructure thickness. On the other hand, when the backface is less than perfect, very thick heat sink structures are required to absorb the transmitted energy.

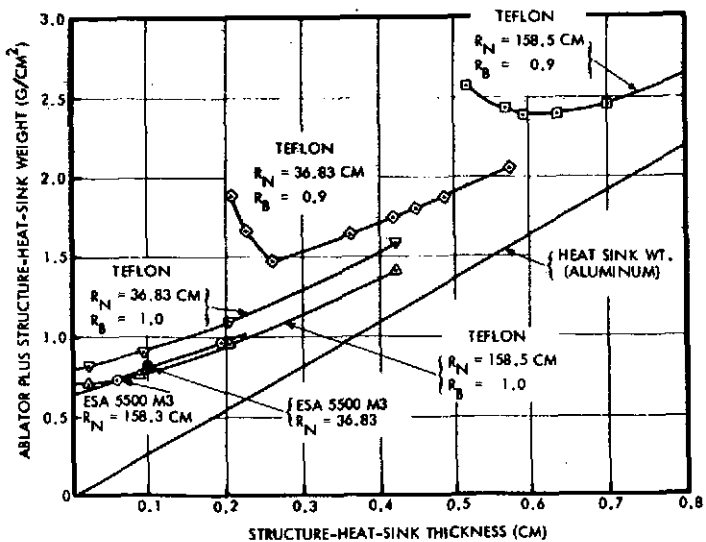


Figure 7.2A-6. Heat Shield Substructure Weight Versus Substructure Thickness - GB Teflon Model

Also shown in Figure 7.2A-6 are the system weights for the blunter, 158.5 cm nose radius Apollo configuration. It has been suggested that going to a blunter vehicle would be advantageous with a reflective ablator, since the convective environment would be reduced (resulting in less mass loss), and the radiation would be increased, but would also be reflected. This hypothesis is shown to be true, if the G-B Teflon heat sink structure interface is a perfect reflector. However, with an interface reflectance of 0.9, the blunter configuration requires a substantially greater system weight ($\sim 60\%$) than the sphere-cone probe, due to the extra mass needed to accommodate the increased transmitted energy. The ESA 5500 M3, on the other hand, is relatively insensitive to the entry configuration. The reduction in net convective heating is offset by the increase in radiant heating for the Apollo shape, and materials which accommodate the energy by reradiation are essentially independent of the entry shape for Venus entry.

Since the heat sink substructure is a significant fraction of the G-B Teflon total system weight, the weight penalty above the ESA 5500 M3 weight can be reduced by using a more efficient heat sink. Figure 7.2A-7 shows that significant weight reductions can be achieved with a beryllium heat sink, but the system weight is still greater than more efficient re-radiative ablators such as Quartz Nitrile Phenolic and ESA 5500 M3.

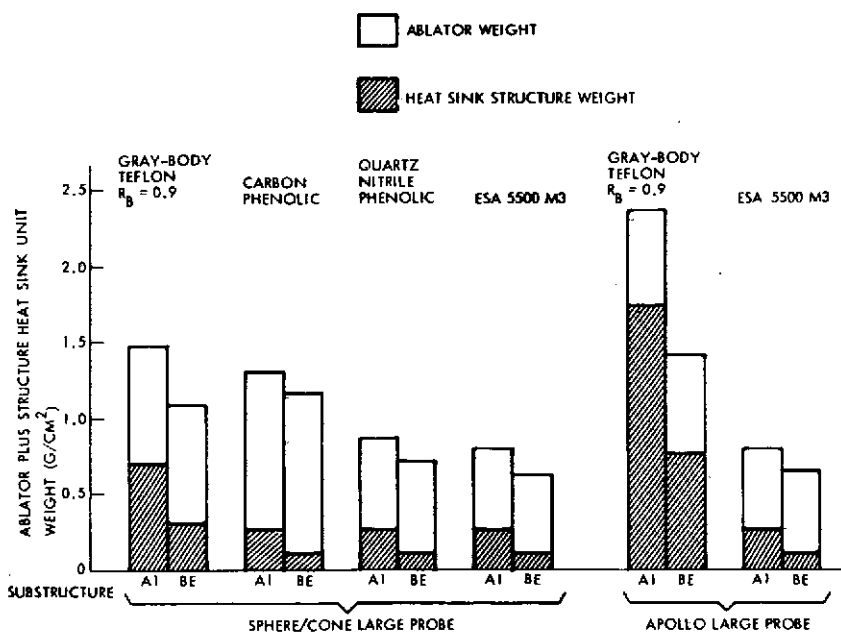


Figure 7.2A-7. Reduction in Heat Shield System Weight with Beryllium

The minimum point in the curve of heat shield-substructure weight versus substructure thickness in Figure 7.2A-6 was chosen for the G-B Teflon system weights. For the reradiative ablators, the minimum system weight corresponds to the unrealistic zero substructure thickness. Therefore, 0.1 cm aluminum was assumed to be representative of typical aeroshell skin thicknesses, and was used as the basis for calculating reradiative ablator system weights for Figure 7.2A-7.

3.2 Non-Gray-Body Teflon Analysis

An examination of the spectral distribution of the shock-layer radiation shows that for Venus entry, the major fraction of the energy is in the ultraviolet. Figure 7.2A-8 compares the spectral radiation from MMC calculations (Reference 7) with those of Sutton and Falanga (Reference 8). Both sources use the same radiating models. The differences in results are attributed to differences in the methods of calculating fluxes, and gas composition, velocity, gas density, and vehicle nose radius. The results plotted are for the continuum processes and molecular band radiation only. No atomic line radiation is included in the plots, but is included in the heating used in the ablation analyses. The MMC calculations are for a self-absorbing, isothermal, adiabatic layer. Sutton and Falanga include non-adiabatic and nonisothermal effects. To account for the nonadiabatic, non-isothermal effects in the ablation analyses, the MMC radiation is multiplied by a time varying "cooling factor" (Reference 9). Sutton and Falanga performed more detailed analyses, which included absorption by the ablation mass injection. The spectral distribution of the net flux to an ablating wall is also shown in Figure 7.2A-8. As can be seen, there is a significant reduction in heat flux to the wall in the vacuum UV, but no effect in the near UV, visible, or infrared. Most of the absorption is due to the cooler boundary layer, with very little additional reduction in radiation caused by the ablation mass injection. The analyses of absorption by ablation mass injection were performed for steady-state ablation of high density nylon phenolic, $(\rho V)_w = 0.371 \text{ kg/m}^2\text{-sec}$. This is approximately equal to the mass loss rate of G-B Teflon ($0.458 \text{ kg/m}^2\text{-sec}$) and ESA 5500 M3 ($0.640 \text{ kg/m}^2\text{-sec}$) at peak heating.

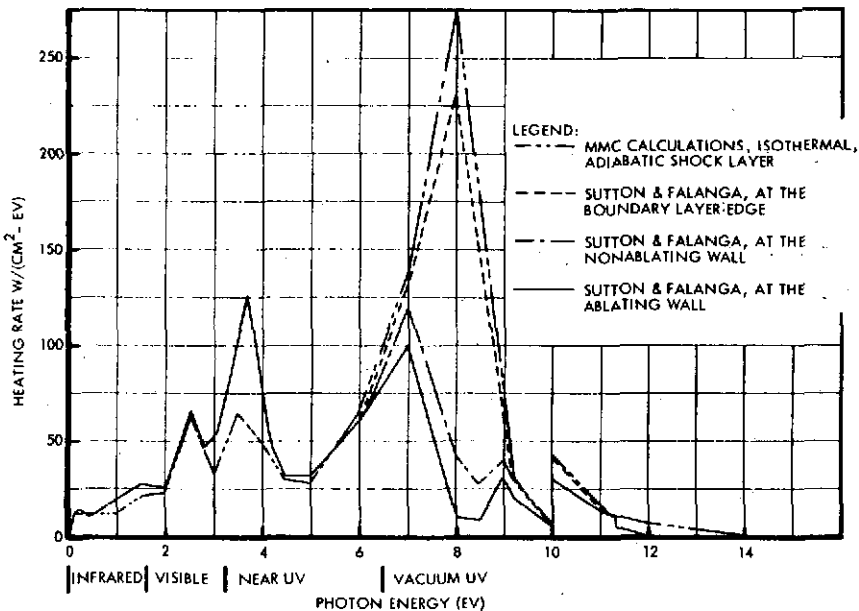


Figure 7.2A-8. Boundary Layer and Ablation Effects on Venus Entry Radiation

For the Teflon analyses (with both the G-B Teflon and the non-gray-body model described further on), it was assumed that 30% of the MMC nonadiabatic isothermal slab radiation is absorbed in the boundary layer, approximating the predictions of Sutton and Falanga for the net flux to an ablating wall.

No increase in convective heating due to boundary layer absorption was assumed, although Sutton and Falanga maintain that "absorption of radiation in the boundary layer can increase the convective heating by 5 to 15 percent." In the ESA 5500 M3, consistent with previous analyses, it was assumed that none of the MMC calculated radiation is absorbed in the boundary layer.

It is concluded, based upon the Sutton and Falanga analyses, that the boundary layer and ablation products will attenuate only a fraction of the incident energy in the ultraviolet, and the remainder must either be absorbed/scattered by the Teflon or reflected from the Teflon-substrate interface. At around 5 eV, Teflon absorption increases significantly; therefore, the radiation in the vacuum UV, which reaches the ablator surface, will be absorbed near the Teflon surface, increasing the Teflon weight required, and reducing the energy transmitted to the substructure.

Radiation properties derived from experiments with radiation energy levels less than 5 eV may yield unrealistic results. Figure 7.2A-9 compares the spectral distribution from a xenon arc lamp (Reference 10) with the net spectral distribution predicted for Venus entry by Sutton and Falanga. It can be seen that the xenon arc lamp emits primarily in the visible, and infrared, with a small fraction in the near ultraviolet, and none in the vacuum ultraviolet. Argon arcs have similar spectral distributions. It can be seen, therefore, that misleading results can occur if Teflon is tested in an inert gas arc lamp. Over the lamp spectral range, Teflon has low absorption, and metals show reasonably good reflection, so good performance is anticipated. However, analyses show that Teflon transmits too much radiation in the spectral range over which its absorption is low. Tests confirm this, as is shown in Figure 7.2A-10. This figure presents the results of tests conducted in the AEHS facility at NASA-Ames. The test models consisted of equal weight of ablator (1.15 g/cm^2) over polished aluminum, 0.236 cm thick. Test time was 2.65 seconds. At the conditions tested, reradiative ablators are fairly insensitive to increasing radiation; surface ablation and reradiation increase to accommodate the incident radiation, with little change in peak backface temperature. Teflon performs differently, with little change in surface mass loss, consistent with previous results (Reference 2). Rather than absorbing the radiation, the Teflon reflects or transmits the radiant energy. These tests indicate that approximately 5% of the incident lamp radiation is transmitted to the substructure with a polished aluminum backface. Less transmission may be achieved with a polished silver backface, which has better reflection below 2.2 eV (Reference 11). This could be optimistic, however, since between 2.2 eV and 5 eV Teflon is expected to be approximately as transparent as below 2.2 eV, and the silver reflectance drops to about 0.10 at 3.9 eV, while aluminum can retain a reflectance on the order of 0.90 into the vacuum UV.

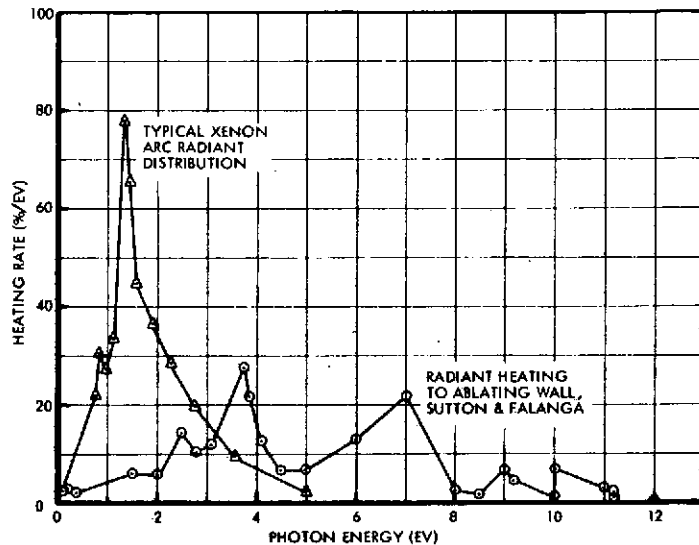


Figure 7.2A-9. Radiant Heating Spectral Distribution - Xenon Arc Versus Venus Entry

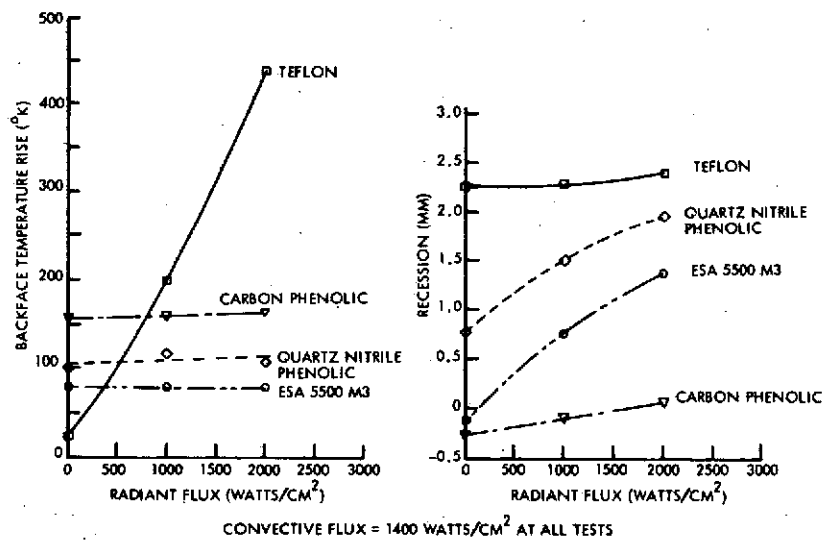


Figure 7.2A-10. Ablator Performance in Tests at NASA Ames

For an accurate analysis of Teflon (or any other reflective ablator), the scattering and absorption coefficients and ablator-heat sink structure reflectance must be known as a function of wavelength. An approximate analysis, however, can be made which better describes the behavior of Teflon in radiation with a vacuum ultraviolet component. An analytical model was setup which assumed that for the radiation in the infrared and visible, Teflon has the scattering and absorption coefficients 10 cm^{-1} and 0.01 cm^{-1} , respectively, consistent with the available data. In the near UV, the test data indicates that Teflon has a very small optical depth (References 3, 12); therefore, the absorption and scattering takes place

near the front surface. Based upon this information, it was assumed that 15% of the incident near UV is absorbed in the Teflon surface and the remaining 85% is reflected; none of the incident near UV is transmitted to the substructure. All the incident vacuum UV is absorbed in the Teflon surface.

Figure 7.2A-11 compares the computed Teflon system weights for this non-gray-body model with the G-B model predicted weights. As in Figure 7.2A-7, 0.1 cm aluminum was assumed the minimum heat sink substructure thickness for the reradiative ablators. As can be seen, with the non-gray-body model, significant increases in Teflon weight over the G-B model are required, due to greater surface mass loss; but substantially less heat sink substructure is required, because of the small fraction of transmitted energy. This trade in heat accommodation modes, while it does reduce total system weights, does not bring Teflon down to the unit weights of efficient reradiative ablators.

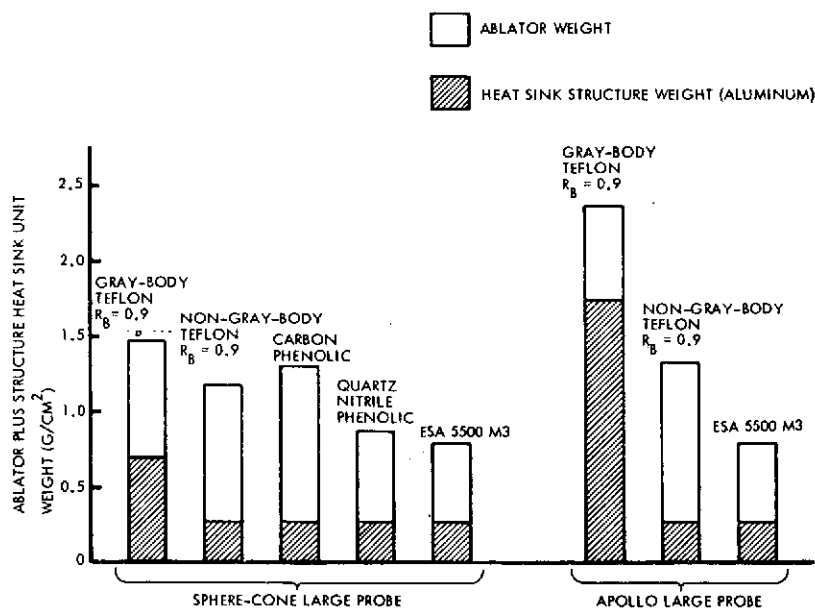


Figure 7.2A-11. Comparison of NGB Teflon with GB Teflon and Other Ablators

4. CONCLUSIONS AND RECOMMENDATIONS

A computer program has been written which accurately models the pertinent physical phenomena associated with radiation scattering heat shields. Analyses of Teflon with this computer program, using radiation properties presented in other publications, indicate that for scattering and absorption coefficients of 10 cm^{-1} and 0.01 cm^{-1} , Teflon transmits

substantial fractions of incident radiant energy. This transmission of radiant energy requires significant heat sink structure weight, which makes a Teflon heat shield system heavier than other efficient ablative systems such as ESA 5500 M3 and Quartz Nitrile Phenolic. Evaluating the spectral distribution of incident radiation from a Venus entry probe shock layer indicates that gray-body Teflon analyses are not correct since a substantial fraction of the radiation is in the vacuum UV where Teflon is a strong absorber. Approximate analyses including absorption of the UV predict that Teflon heat shield system weights are very competitive with carbon phenolic, but are still significantly greater than efficient reradiative ablatives. The absorption of UV by the Teflon reduces the heat sink sub-structure weight, but increases the surface mass loss.

An improved radiation scattering heat shield with efficiency greater than reradiative ablatives may be achieved if a material is developed that has greater heat of sublimation (reducing surface mass loss), and a higher scattering coefficient, while maintaining the insulation efficiency of Teflon. Such a material has yet to be demonstrated, but should be pursued with emphasis on outer planet entry.

REFERENCES

1. W. M. Congdon, "Radiation Scattering Heat Shields, 1972 Final Report," MMC IRAD Report R-72-48691-001 (December 1972).
2. P. R. Nachtsheim, D. L. Peterson, and J. T. Howe, "Reflecting Ablative Heat Shields for Radiative Environments," AAS Paper pp 71-147 (1971)
3. D. L. Peterson and W. E. Nicolet, "Heat Shielding for Venus Entry Probes," Preliminary Data, to be published.
4. J. T. Howe, M. J. Greene, and K. Weston, "Thermal Shielding by Subliming Volume Reflectors in Convective and Intense Radiative Environments," unpublished and updated NASA paper.
5. K. C. Weston, J. T. Howe, and M. J. Greene, "Approximate Temperature Distribution for a Diffuse, Highly Reflecting Material," AIAA Journal, Vol. 10, No. 9, 1252 (September 1972).
6. P. S. Mudgett and L. W. Richards, "Multiple Scattering Calculations for Technology," Applied Optics, Vol. 10, No. 7, 1485 (July 1971).
7. Memorandum from C. T. Edquist to J. R. Mellin, "Preliminary Pioneer Venus Convective and Radiative Results," MMC P73-44432-058, January 11, 1973.
8. K. Sutton and R. A. Falanga, "Stagnation Region Radiative Heating with Steady State Ablation during Venus Entry," paper presented at Symposium on Hypervelocity Radiating Flow Fields for Planetary Entries, January 14-15, 1972.
9. Memorandum from C. T. Edquist to J. R. Mellin, "Radiative Cooling Factor for Venus Entry Environment Predictions," MMC P71-44498-292, 24 November 1971.
10. Data from Tamarak Scientific Company, Orange, California.
11. Y. S. Touloukian and D. P. DeWitt, Thermophysical Properties of Matter, Volume 7, "Thermal Radiation Properties Metallic Elements and Alloys," (Plenum Press, 1970).
12. Personal communications from P. R. Nachtsheim, D. L. Peterson, NASA ARC, January 16, 1973.

APPENDIX 7.4A

**PRESSURE SHELL TEMPERATURE GRADIENTS
WITH CONCENTRATED INSULATION PENETRATIONS**

APPENDIX 7.4A

PRESSURE SHELL TEMPERATURE GRADIENTS WITH CONCENTRATED INSULATION PENETRATIONS

The preferred Atlas/Centaur large probe design is such that all pressure vessel penetrations are located in a single band offset slightly from the equator of the spherical pressure vessel. These penetrations include science windows, electrical feedthroughs, and structural members. All of these pressure vessel penetrations are also insulation penetrations and represent a concentrated heat transfer path from the environment to the pressure vessel wall. This causes a concern relative to the possibility of having large spatial temperature gradients along the pressure vessel walls. If large gradients do exist they could give rise to thermal stress problems and, further, would cause inaccuracies in our design calculations which assume the pressure vessel is isothermal at any given instant of time.

In order to investigate this problem, a 17-node thermal model of the large probe was constructed to determine the magnitude of the temperature gradients in the pressure shell during the descent phase. The probe shell was divided into five sections as sketched in Figure 7.4A-1. Nodes 1 and 5 were spherical end caps and nodes 2, 3, and 4 were spherical segments. All payload equipment and all science penetrations were attached to shell node number 4. High conductance, circumferential flanges were located at the junction of nodes 3 and 4 and at the junction of nodes 4 and 5.

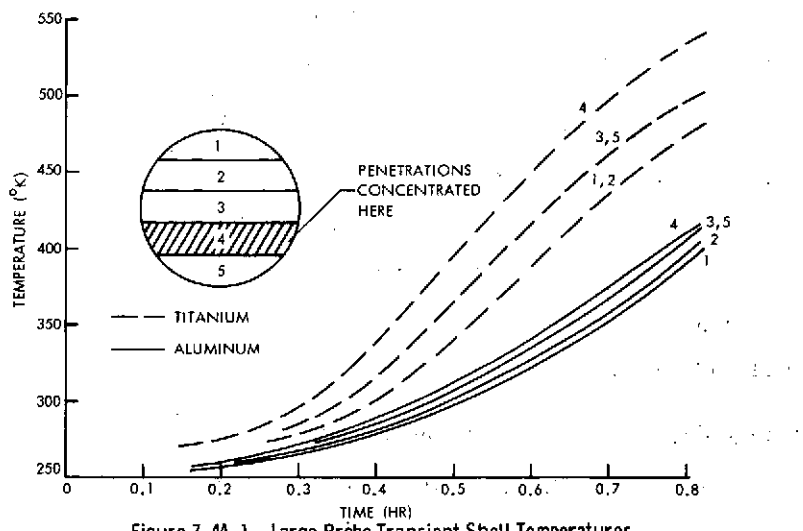


Figure 7.4A-1. Large Probe Transient Shell Temperatures

The actual time-temperature profiles for these 5 nodes are shown in Figure 7.4A-1 for a 0.53-cm (0.21-inch) thick aluminum shell covered with a 2.54-cm (1-inch) layer of MIN-K insulation and a 0.33-cm (0.13-inch) thick titanium shell covered with a 1.5-cm (0.59-inch) layer of MIN-K insulation. The temperature differences between adjacent nodes are shown in Figure 7.4A-2 for the same descent profile.

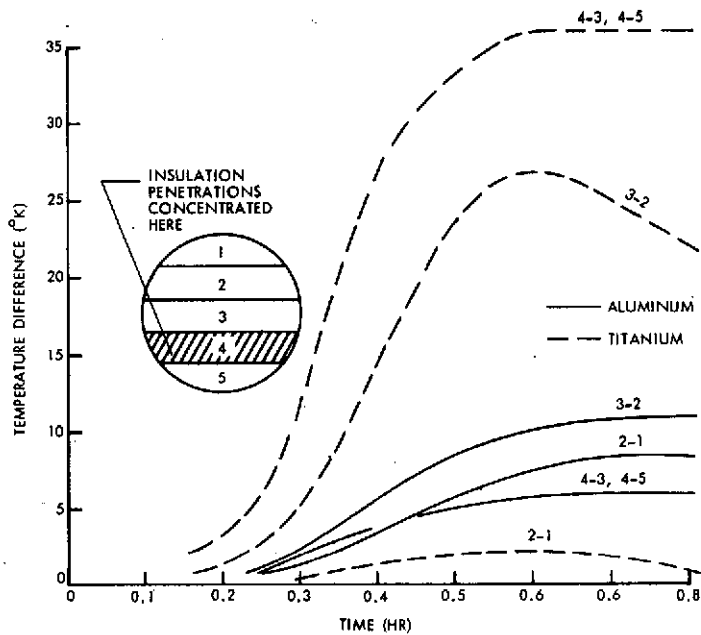


Figure 7.4A-2. Temperature Gradients in Large Probe Pressure Shell

These analyses indicate that the 1.5-cm layer of insulation results in a titanium shell temperature of 540°K at the end of the descent. In addition, the high heat flux plus the thin wall thickness and the low thermal conductivity of the titanium shell compared to the aluminum shell produce temperature gradients up to 35°K per foot of circumferential length.

Increasing the insulation thickness to 2.54 cm plus changing the shell material to aluminum and increasing the wall thickness from 0.33 cm to 0.53 cm reduces the maximum shell temperature to 420°K . In addition, the increased thermal conductivity and cross-sectional conduction area reduce the temperature gradients in the shell to less than 11°K per foot of circumferential length.

These results show that thermal stress is not an important consideration, particularly for an aluminum shell. Also, the assumptions of an isothermal pressure shell is shown to be reasonable.

APPENDIX 7.5A

PARACHUTE SIZING ANALYSIS SUMMARIES

APPENDIX 7.5A
PARACHUTE SIZING ANALYSIS SUMMARIES

1. SUMMARY OF SIZING CALCULATIONS

1.1 Main Parachute

Required $\beta = 7.85 \text{ kg/m}^2$ (0.05 slug/ft 2)

Descent weight, $W = 216 \text{ kg}$ (475 lb)

Use RGS canopy: $C_D = 0.8$ (based on inflated diameter)

$$\text{Required area, } S = \frac{W}{\beta \cdot C_D} = \frac{216}{7.85 (.8)}$$

$$= 34.4 \text{ m}^2 (369 \text{ ft}^2)$$

$$\text{Required diameter, } D_p = \sqrt{\frac{4S}{\pi}} = \sqrt{\frac{4(34.4)}{\pi}}$$

$$= 6.62 \text{ m (21.7 ft)}$$

$$\text{Drag area, } C_D S = 0.8 (34.4) = 27.5 \text{ m}^2 (295 \text{ ft}^2)$$

$$\text{Canopy loading} = \beta = 7.85 \text{ kg/m}^2, q = 77 \text{ N/m}^2$$

$$\text{Descent velocity at } h = 42.9 \text{ km, } v = \sqrt{\frac{2q}{\rho}}$$

$$\rho = \frac{3.855 (10^{-3}) \text{ gm/cm}^3}{2(77)}$$

$$v = \sqrt{\frac{3.855 (10^{-3}) (10^3)}{3.855 (10^{-3}) (10^3)}} = \sqrt{39.9} = 6.32 \text{ m/s (20.7 fps)}$$

$$\text{Opening force, } F_o = X q_o C_D S$$

$$X = 1.1 (\text{hdbk}), q_o = 1820 \text{ N/m}^2 (38 \text{ psf})$$

$$F_o = 1.1 (1820) (27.5) = 55000 \text{ N (12400 lb)}$$

$$\text{Chute D/forebody (aeroshell) } d = 6.62/1.75 = 3.78 \text{ (good ratio)}$$

1.2 Pilot Parachute

Criteria: Apply minimum 10g force for main chute extraction or make

$$\beta = 0.6 (7.85) = 4.70 \text{ kg/m}^2.$$

Use the larger size

Assumptions: Inflation $q = 1296 \text{ N/m}^2$ (25 psf) and $C_D = 0.4$ as a worst case condition

Extraction $F = gw; g = 10, W = 9.80 \text{ kg}$ (from weight estimates)

$$F = 10 (9.80) (9.806) = 960 \text{ N (214 lb)}$$

$$\begin{aligned} \text{Area required, } S &= \frac{F}{q \cdot C_D} = \frac{960}{1296 (.4)} \\ &= 1.83 \text{ m}^2 (19.7 \text{ ft}^2) \end{aligned}$$

$$\text{Diameter (inflated RGS)}, D = \sqrt{\frac{4(1.83)}{\pi}}$$

$$= 1.52 \text{ m (5.00 ft)}$$

$$\text{Using } \beta = 4.70 \text{ kg/m}^2 (0.03 \text{ slug/ft}^2)$$

$$\begin{aligned} \text{Required } C_D S &= m/\beta; M = \text{weight of aft cover and pilot} \\ D &= 5.91 \text{ kg (from weight estimates)} \end{aligned}$$

$$C_D S = \frac{5.91}{4.7} = 1.26 \text{ m}^2 (13.5 \text{ ft}^2)$$

$$S = 1.26/0.4 = 3.15 \text{ m}^2 (33.8 \text{ ft}^2)$$

$$D = \sqrt{\frac{4(3.15)}{\pi}} = 2.0 \text{ m (6.58 ft)}$$

$$D/\text{aeroshell d} = 2.0/1.75 = 1.14 \text{ (fair ratio)}$$

Use 2.0 m diameter RGS pilot

$$F_o = X q_o C_D S = 1.1 (1820) 1.26 = 2520 \text{ N (565 lb)}$$

1.3 Pilot Mortar

$$\text{Use pack density} = 641 \text{ kg/m}^3 (40 \text{ lb/ft}^3)$$

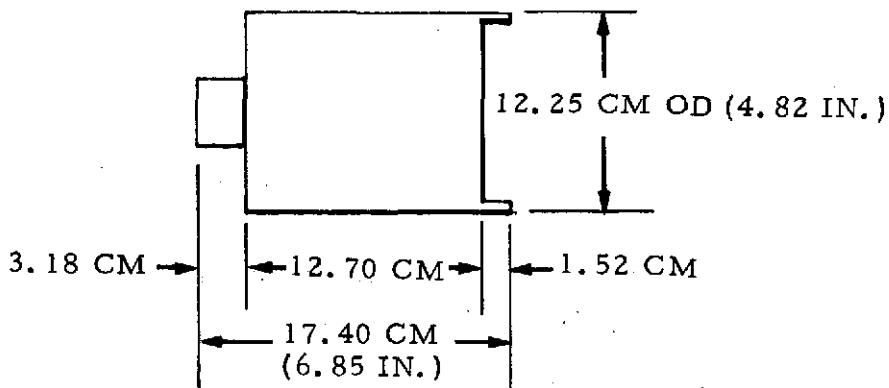
$$W = 0.82 \text{ kg (1.8 lb) from weight estimates}$$

$$\begin{aligned} \text{Volume required} &= 0.82/641 = 0.00127 \text{ m}^3 \\ &= 1270 \text{ cm}^3 (77.6 \text{ in.}^3) \end{aligned}$$

$$\text{Use stroke/bore ratio} = 1.0 \text{ ("square" mortar)}$$

$$\begin{aligned} \text{bore} = \text{stroke} &= \sqrt[3]{\frac{4(\text{vol})}{\pi}} = \sqrt[3]{\frac{4(1270)}{\pi}} = \sqrt[3]{1620} \\ &= 11.72 \text{ cm (4.62 in.)} \end{aligned}$$

Overall dimensions:



Mortar Reaction Force and Impulse:

Ejected weight, $M_e = 1.05 \text{ kg}$; including pilot and covers (2.3 lb)

Ejection velocity = 18.3 m/s (60 fps) = v

Stroke, s = 0.117 m (0.38 ft)

$$\begin{aligned} \text{Energy} &= \frac{1}{2} M_e V^2 = \frac{1}{2} (1.05) (18.3)^2 \\ &= 175 \text{ N-m} (128 \text{ ft-lb}) = KE \end{aligned}$$

Assuming an "inefficiency" factor = 1.3:

$$\text{Energy} = 1.3 (175) = 228 \text{ N-m} = KE'$$

$$\begin{aligned} \text{Reaction force} &= KE'/s = 228/.117 \\ &= 1950 \text{ N} (440 \text{ lb}) \end{aligned}$$

Impulse:

$$\text{Operating time} = \frac{2s}{V} = \frac{2 (.117)}{18.3} = 0.0128s = t$$

$$\text{Average force} = KE/s = 175/0.117 = 1495 \text{ N} = F$$

$$\text{Impulse} = F_t = 1495 (0.0128) = 19.1 \text{ N-s} (4.3 \text{ lb-s})$$

2. SUMMARY OF WEIGHT ESTIMATES

Note: Weights are based on (1) handbook data, (2) calculations, and (3) estimates from available hardware information.

Main Parachute:

Canopy and lines (handbook and calculations)	8.15 kg
Deployment bag (estimate)	0.32 kg
Swivel (estimate)	<u>0.91 kg</u>
	<u>9.39 kg</u>

Bridle calculations:

Total load on 3 legs = 55 000 N

Leg angle = 0.436 rad (25°)

Overall design factor (handbook) = 2.5

$$1 - \text{leg load} = P = \frac{55\ 000}{3 \cos 0.436} = 20\ 200 \text{ N} (4550 \text{ lb})$$

$$\text{Required } P = 2.5 (20\ 200) = 50\ 500 \text{ N} (11\ 400 \text{ lb})$$

Use 2-ply, 40 000 N (9000 lb) b.s. nylon webbing at 10/gm/m (3.25 oz/yd)

Leg Length = 0.615 m (2.0 ft)

1 - leg weight (10% allowance) = 1.1 (2) (101) 0.0615 = 136 gm

Total = 3 (136) = 408 gm = 0.41 kg (0.9 lb)

Main chute total = 9.39 + 0.41 = 9.80 kg

Pilot parachute, including bridle (handbook and calculation)	0.82 kg
Pilot mortar (calculation)	0.59 kg
Main chute container (calculation)	1.72 kg
Extraction bridle (calculation)	0.18 kg
Main parachute pack	<u>9.80 kg</u>
System total	13.11 kg
	(28.9 lb)

APPENDIX 7.6A
COMMUNICATIONS AND TRACKING USING
LOGNORMAL CARRIERS

1.	Introduction and Summary	7. 6A-1
2.	Telecommunication System Model	7. 6A-5
2. 1	Channel Model Based Upon Turbulence Theory and the Lognormal Process	7. 6A-7
2. 2	The Rician Channel Model and Its Interconnection with the Lognormal Model	7. 6A-18
2. 3	The Channel Output Equation	7. 6A-21
2. 4	Characterization of Channel Multipath Due to Planetary Backscatter	7. 6A-22
3.	Characterization of a Phase-Locked Loop Receiver Performance in the Presence of Planetary Multipath and Turbulence (Lognormal Channel)	7. 6A-24
3. 1	The Loop Equations for Both One-Way and Two-Way Operation	7. 6A-26
3. 2	The Data Channel Equation	7. 6A-27
3. 3	Error Probability Performance	7. 6A-29
3. 4	Tracking Loop Analysis (Limiter Absent)	7. 6A-35
4.	Tracking Loop Analysis when a Limiter Precedes the Loop: Backscatter and Turbulence Present	7. 6A-49
4. 1	Static Phase Error Build Up Due to the Doppler Profile	7. 6A-54
4. 2	Doppler Variance in the Transponder Loop and Suppression on the Downlink Carrier Due to Uplink Effects	7. 6A-55
5.	Performance of Two-way Links in the Presence of Multipath and Turbulence	7. 6A-57
6.	Conclusions	7. 6A-61
7.	Addendum	7. 6A-63
	References	7. 6A-74

APPENDIX 7.6A
COMMUNICATIONS AND TRACKING USING LOGNORMAL CARRIERS

1. INTRODUCTION AND SUMMARY

This appendix addresses problems peculiar to communications systems designed to transmit information from a probe descending through the Venus atmosphere. The problem of modeling one-way and two-way coherent links is emphasized by identifying the appropriate system parameters that affect the development of accurate design control tables.

From the outset, characterization of the channel multipath, turbulence, and absorption phenomena has presented the single most important and tedious technical problem area. Careful analysis and various study efforts were devoted to arriving at a channel model that could be justified on the basis of compatible theoretical evidence as well as experimental observations. The base of knowledge central to the channel fading effects has developed around the Rician and lognormal fading phenomenon.

Initially, deWolf (References 1, 2, 3) produced a theory based upon a multiple scattering model which indicated that the depth of fading was sufficiently severe to produce a first-order Rician density in the received signal amplitude fluctuations. Later, Tatarskii (Reference 4, pp. 388) pointed out that deWolf's derivation of the statistics of the amplitude fluctuations were incorrect owing to the fact that he had omitted certain connections in the Feynman diagram. Moreover, it is shown in the addendum of this appendix that the derivation of the zero crossing properties of the envelope developed by deWolf (Reference 2, Equation 5) are incorrect. However, deWolf used this theory to "justify" the magnitude of the outer scale size of turbulence which was conjectured earlier by Kolosov, Yakovlev and Yefimov (Reference 5). According to Lawrence and Strohbehn (Reference 6), deWolf now (Reference 7) seems to favor the lognormal distribution found by Tatarskii (References 4, 8) using Rytov's method to solve the wave equation. A physical discussion pointing out the differences in the two approaches (deWolf and Tatarskii) is given by Strohbehn (Reference 10). The primary difference stems from the fact that severe depths of fading lead to the Rician density, while small fluctuations lead to small fading depths and lognormal fluctuations in the received signal.

amplitude. Strohbenhn's (Reference 10) discussions tend to favor the lognormal fluctuations and so does Ishimaru (Reference 11), Woo and Ishimaru (Reference 12), and Croft, Eshleman, Marouf, Tyler (Reference 13).

Various data taken from the Veneras 4, 5, 6 and 7 spacecraft, and the Mariner V flyby spacecraft, have been analyzed to determine the depth of fading and the fading rate (References 12, 14, 15). The consensus developed from their observations seems to indicate the depth of fading is small and, therefore, distributed in accordance with a lognormal distribution. Various other experimental evidence is quoted in the appendices predicting lognormal fading.

The applicability of the complex lognormal turbulence model with a relatively weak fading amplitude follows essentially from two sources of experimental data. The first is the analysis of the experimental data for Venera 7 (the latest Russian probe data published) by Yakovlev (Reference 14) based on the usual entry probe turbulence model used for Venera 4, 5 and 6. The second is the application of Mariner-5 data to a different flyby model developed and analyzed by Woo and Ishimura (Reference 12). The results of Woo and Ishimura indicates good agreement with the results of Woo (Reference 15) in applying Yakovlev's results (Reference 14) to the case of Pioneer-Venus. In private communications Woo indicates that the worst-case results for the variance of amplitude and phase fluctuations given in Reference 15 will be smaller upon final assessment of Mariner-5 data.

Based on the work of Tartaskii (References 4, 8), which predicts a complex lognormal channel response for small fluctuations, Woo (Reference 15) presented a survey of the various propagation studies pertaining to the Pioneer-Venus channel. He also summarized and derived pertinent characteristics needed in determining basic communication system interface parameters and frequency spectra. Woo (Reference 15) and Woo and Ishimura (Reference 12), on the other hand, present pertinent data (derived primarily from processed Venera and Mariner flyby data) needed in characterizing the parameters of the lognormal density and in preparing the design control theory.

On the basis of the existing turbulence theory and experimental data, it was recommended that the mathematical model for the probe telecommunication system be based upon a lognormal channel. A lognormal channel is defined here

to imply that its response to a sinusoidal carrier produces a lognormal carrier, i.e., if $A_0 \sin [\omega_0 t + \theta(t)]$ is transmitted, then the channel output is given by $A(t) \sin [\omega_0 t + \phi(t) + \theta(t)]$ where $A(t) = A_0 \exp [x(t)]$, with $\{x(t)\}$ a gaussian process and with the phase process $\{\phi(t)\}$ also gaussian. The design control tables are prepared under the above assumptions.

In order to prepare accurate design control tables, for probe communication systems, it has been necessary to construct a theory which accounts for the affects which lognormal carriers produce on the performance of one-way and two-way phase-coherent tracking and data-acquisition systems. Since this theory has not been completely developed, it has been necessary to construct (to the extent possible) a theory which accounts for degradations in tracking system performance as well as in the data channel. One major contribution of the study is that it has led to this development. This theory is presented by first developing a mathematical model of one-way and two-way probe link channels, then carrying out the necessary analysis. Included in the analysis are the effects of planetary backscatter on performance as well as the development of how the channel amplitude fluctuation affects the performance of a phase-locked system preceded by a bandpass limiter.

At the outset, it was felt that the body of theory that presently exists in the literature for designing systems which must combat Rician fading could be used; however, by making a careful analysis and comparisons of the theory developed here for lognormal fading with that for Rician fading, it was found that even though the amplitude fluctuations are small, the two theories yield considerably different losses. Appendix 7.6C outlines the differences for uncoded PSK communications. It turns out that, for a fixed depth of fading, the Rician fading fluctuations are more difficult to combat than are fading fluctuations having lognormal statistics. For example, using the data given by Woo (Reference 15) for Venera 4, the theory predicts a fading loss of approximately 11 decibels for Rician fading and 2.2 decibels for lognormal fading at the surface. Using Venera 7 data at the surface and a bit error probability of 10^{-3} (Reference 15), the Rician fading loss is approximately 5.3 decibels, while the lognormal fading loss is about 0.7 decibels for zenith propagation angles. For very small variances in the amplitude fluctuations, the difference between the lognormal and Rician density functions is small.

However, it is important to note that even though the values of the variance of amplitude fluctuations seem small, as determined by Woo (Reference 15) for the Pioneer-Venus channel, they are not small enough to make Rician fading appear lognormal or vice versa. For large fluctuations, the lognormal density is markedly different from a Rice density. This means that the theory developed for each channel model would give highly different results. On the other hand, if the amplitude fluctuations are large, then the lognormal density, as predicted by Rytov's method of solving the wave equation, no longer remains valid for the Venus channel.

In developing the theory for use in preparing the design control tables, several difficult problems have arisen; for example, the performance of a phase-locked system whose input signal component is fading. A summary of the efforts and key results developed to date are given in this appendix. It should be pointed out here that although the problem cannot be considered as completely solved close approximations have been obtained.

In order to assess the degradations in performance, it has been necessary to model and characterize the behavior of coherent tracking systems in the presence of lognormal carriers. This appendix summarizes and presents mathematical models and investigations, within the time constraints, of the deleterious effects produced on tracking performance as well as the data detection process. Although the work cannot be considered as complete, it has been shown, for the lognormal fading expected on the probes and for uncorrelated amplitude and phase components, that the random phase-characteristic can be tracked by the loop. The random phase-characteristic will however affect the ability to measure doppler accurately, and the theory to assess the degradation is given. It has been difficult to assess, exactly, the effects of the amplitude process on tracking performance; however, for small amplitude fluctuations, the degradation in loop signal-to-noise has been characterized and shown to be less than 0.2 decibel. The effects of correlation between the amplitude and phase process were not fully investigated. It appears that the correlation effects manifest themselves by producing an unsymmetric carrier spectrum for the loop to track. This effect is a curious one and should receive further study in order to assess the degradations (if any) and effects on tracking performance as well as on the performance of the data detector.

Moreover, it is probably safe to conclude that the theory developed to determine the effective loop signal-to-noise ratio does not serve to tell the complete story.

An analysis required to assess the effects of planetary back-scatter on the ground receiver and transponder performance is given in Appendix 7.6G. Further detailed work needs to be done, using the theory given here, in order to accurately determine its effects; however, a preliminary investigation reveals that they are small.

While this appendix presents the theory for determining the degradations which the lognormal amplitude has on the error probability, we have not been able to produce a complete set of design curves for determining the effects which lognormal carriers have on the performance of systems which employ convolutional codes, however, preliminary results are given in Appendices 7.6 and C. This is an important problem area which needs further study owing to the impact the results will have on the specification of accurate design control tables. Computer simulations offer one method for obtaining and validating any theoretical results.

Finally, a linear theory is given which can be used to determine the static phase-error buildup in both one-way and two-way systems where lognormal carriers and high doppler shifts are present. This includes the effects of tuning the voltage-controlled oscillator with and without predicts. Furthermore, a linear theory has been presented which can be used to specify the variance of the doppler and phase-error in one-way and two-way systems where lognormal carriers are present. Some further numerical work is recommended here.

2. TELECOMMUNICATION SYSTEM MODEL

In a coarse sense, we shall begin our discussion of the telecommunication system model (for both the large and small probes) from its simplest representation given in Figure 7.6A-1. It consists of the transmitter (including the encoder and modulator), the channel (including a random time-varying filter), and the receiver (including the demodulator and decoder). For convenience, we have illustrated the source and user as blocks outside the above three elements. The major blocks which have an impact on the

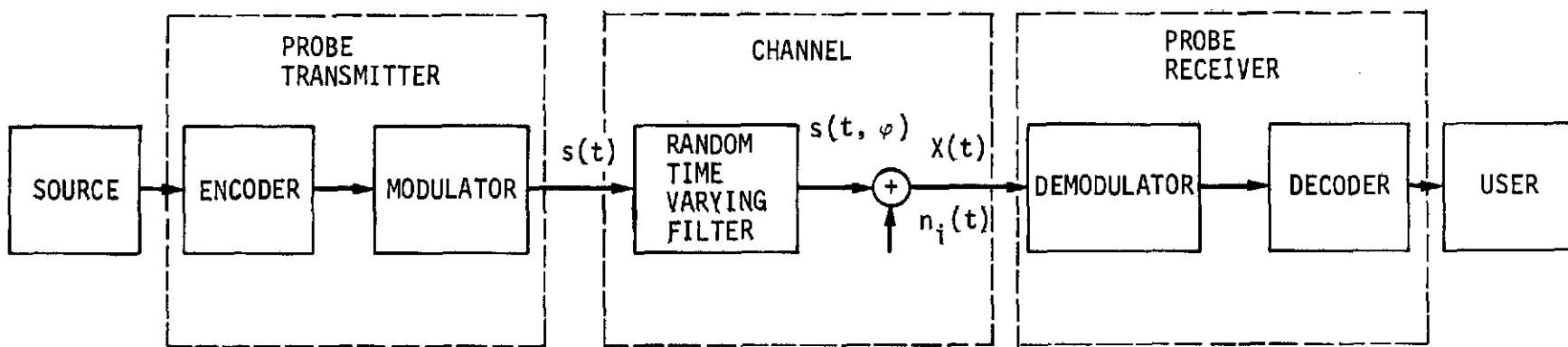


Figure 7.6A-1. Simplest Telecommunication System Model

design and analysis include: the choice of an encoding technique, the modulation technique, the channel model (which includes a statistical characterization of the attenuation and turbulence using the body of theory given in Reference 1 to 15), synchronization, demodulation, and the decoding technique.

For the present, however, we shall characterize the signals $s(t)$, $s(t, \Phi)$, $n_i(t)$ and the received signal $x(t)$ since for all analysis these signal representations, modulation formats, etc. enter into the analysis and design. A general representation for the transmitted signal is given

$$s(t) = \sqrt{2A_0} \sin [\omega_0 t + M(t) + \psi_1(t)] \quad (7.6A1)$$

where

$P = A_0^2$ Represents the total transmitted power

$f_0 = \omega_0/2\pi$ Carrier frequency

$M(t)$ = Represents angle modulation (phase or frequency)

$\psi_1(t)$ = Transmitter oscillator instabilities both long and short term

When two-way transmission is considered, the model for $s(t)$ will change as a result of the up-link multipath, up-link noise, backscatter from the planet, etc.; however, for the present we shall neglect considering their effects and introduce them at the appropriate time.

2.1 Channel Model Based Upon Turbulence Theory and the Lognormal Process

Owing to random fluctuations in the refractive index or dielectric constant of the Venusian atmosphere caused by random winds, thermal currents, and pressure variations, turbulence theory (References 1-15) purports to model the amplitude fluctuations induced by the random time-varying filter as lognormal. What this implies is that the amplitude fluctuations $A(t)$, emerging from the random channel filter output when $s(t)$ serves as its input, are characterized by

$$A(t) = A_0 \exp [x(t)] \quad (7.6A2)$$

where $[x(t)]$ is a gaussian random process which will be assumed stationary. In summary, for plane-wave propagation, Tatarski (Reference 4) has shown by the use of a perturbation approximation to the wave equation (called the Rytov approximation) that the amplitude $A(t)$ of the received electromagnetic

field has the first-order probability density function*

$$p \frac{A}{A_0} = \frac{A_0}{A} \frac{1}{\sqrt{2\pi\sigma_x^2}} \exp \left\{ -\frac{[\ln(A/A_0) - m_x]^2}{2\sigma_x^2} \right\} \quad (7.6A3)$$

for $0 \leq A \leq \infty$. The parameter m_x determines the asymmetry while σ_x controls the spread. The nth moment of the lognormal probability density functions about the origin is given by

$$E[A^n] = A_0^n \exp \left[n m_x + (n^2 \sigma_x^2)/2 \right].$$

The lognormal probability density function results from multiplicative events, i.e., there exist multiplicative central limit theorems (Reference 16), which show that the asymptotic probability density function of the product of n independent random variables tends to be lognormal for large n. The statistics of the probe channel appear primarily to be of a multiplicative nature.

The skewness and shape of the lognormal probability density function can be easily adapted, see Figure 7.6A-2, to provide a good initial approximation to a broad class of non gaussian probability density functions defined over $[0, \infty]$. Other experimental investigations (References 4, 16, 17, 18, 19, 20, 21, 22, 23, 24) have, to an extent, substantiated that the underlying statistics are lognormal for various communication channels.

* For a short discussion of the interconnection between a random variable with a Rician and lognormal probability density functions see the end of Section 2.2.

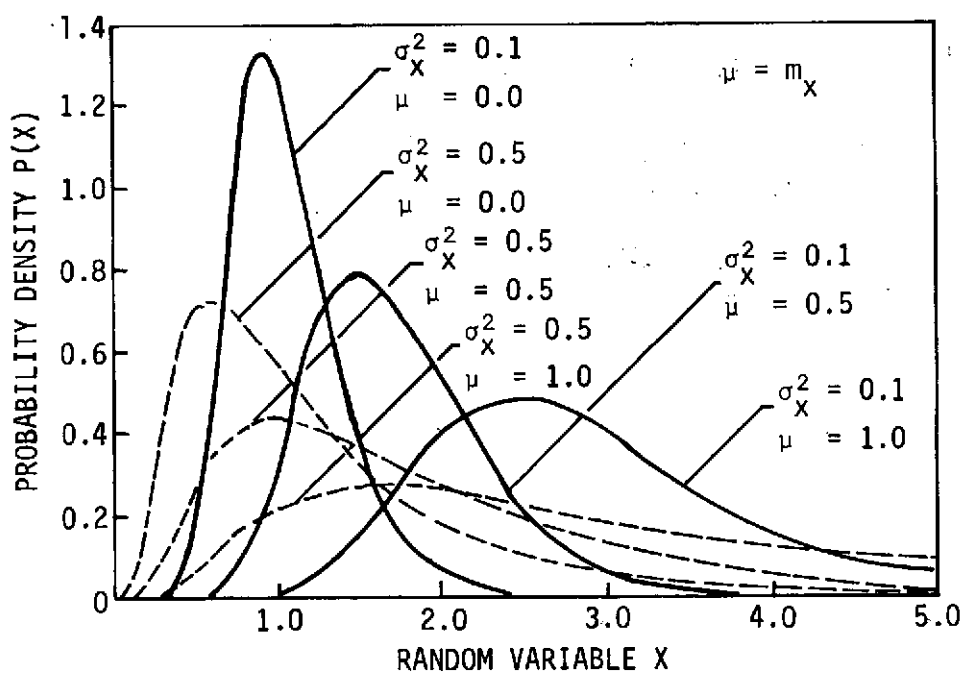


Figure 7.6A-2. Effects of the Variation of m_x on the Shape of the Lognormal Probability Density Function

One can express the mean m_A and variance σ_A^2 of the amplitude fluctuations (channel gain) as

$$\begin{aligned} A_0^{-1}m_A &= E(A) = \exp \left[m_x + \sigma_x^2 / 2 \right] \\ \sigma_A^2 &= E \left[(A - m_A)^2 \right] = 2m_A^2 \exp \left(\sigma_x^2 / 2 \right) \sinh \left(\sigma_x^2 / 2 \right) \\ &= 2A_0^2 \exp \left[2(m_x + 3\sigma_x^2 / 4) \right] \sinh \left(\sigma_x^2 / 2 \right) \end{aligned} \quad (7.6A3)$$

When the amplitude turbulence $x(t)$ has zero mean then the moments of the channel gain become

$$m_x = 0 \begin{cases} A_0^{-1}m_A = \exp \left(\sigma_x^2 / 2 \right) \\ A_0^{-2}\sigma_A^2 = 2 \exp \left(\frac{3}{2} \sigma_x^2 \right) \sinh \left(\sigma_x^2 / 2 \right) \end{cases} \quad (7.6A4)$$

Under a "conservation-of-power", i.e., $E(A^2) = A_0^2$, argument it is easy to show that $m_x = -\sigma_x^2$ so that (7.6A3) reduces to

$$m_x = -\sigma_x^2 \begin{cases} A_0^{-1}m_A = \exp \left(-\sigma_x^2 / 2 \right) \\ A_0^{-2}\sigma_A^2 = 2 \exp \left(-\sigma_x^2 / 2 \right) \sinh \left(\sigma_x^2 / 2 \right). \end{cases}$$

It is interesting to note that the ratio of the mean of the lognormal distribution to its mode M_{mode} is given by

$$\frac{M_{\text{mode}}}{m_A} = \left[\frac{1}{\exp \left(\sigma_x^2 / 2 \right)} \right]^3$$

and that the peak value of the probability density function is given by

$$p = \frac{M_{\text{mode}}}{A_0} = \frac{\exp \left[\sigma_x^2 / 2 - m_x \right]}{2 \sqrt{\pi \sigma_x^2 / 2}}$$

Hence

$$\lim_{\sigma_x \rightarrow \infty} M_{\text{mode}} = 0$$

$$\lim_{\sigma_x \rightarrow \infty} p \left(\frac{M_{\text{mode}}}{A_0} \right) \rightarrow \infty$$

which demonstrate the behavior of the lognormal probability density function for large σ_x .

Furthermore

$$P \left(\frac{A}{A_0} > \epsilon \right) = \int_{\epsilon}^{\infty} p \left(\frac{A}{A_0} \right) \frac{dA}{A_0}$$

$$= \frac{1}{\sqrt{\pi}} \int_G^{\infty} \exp(-z^2) dz,$$

where

$$z \triangleq \frac{\ln \left(\frac{A}{A_0} \right) - m_x}{\sqrt{2 \sigma_x^2}}$$

and

$$G = \frac{\ln \epsilon - m_x + \exp \sigma_x^2 / 2}{\sigma_x}$$

Then, if ϵ is fixed we have

$$\lim_{\sigma_x \rightarrow \infty} P \left[\frac{A}{A_0} > \epsilon \right] = 0,$$

which would seem to imply that the error probability in a coherent system approaches one-half for binary signals and a finite signal-to-noise ratio $A_0^2 T / N_0$. Furthermore, turbulence theory (Reference 8) points out that the random channel filter also disturbs the phase characteristic of the transmitted signal. This suggests that the transmitted wave will be further perturbed by random phase fluctuation $\phi(t)$ which is characterized as a zero-mean gaussian random process. Thus the output of the randomly time-varying filter is conveniently

characterized from turbulence theory as

$$s(t, \phi) = \sqrt{2} A \sin \phi(t) \quad (7.6A5)$$

where the channel phase function is defined by

$$\phi(t) \stackrel{\Delta}{=} \omega_0 t + M(t) + \phi(t) + \theta_w(t) + \psi_1(t) + \theta_B(t) + d(t) + \theta_0$$

$A(t)$ - Amplitude fluctuations due to turbulence = $A_0 \exp[x(t)]$

$\phi(t)$ - Turbulence phase fluctuations

θ_0 - A random epoch uniformly distributed on $[-\pi, \pi]$

$\theta_w(t)$ - Transient modulation due to probe oscillations (zero on small probes) after parachute opens

$M(t)$ - Angle modulation (PSK or MPSK)

$\theta_B(t)$ - Backscatter multipath in a two-way link (zero in one-way case)

$d(t)$ - Doppler profile in radians.

In long hand notation this implies that the received signal $X(t)$ can be characterized as

$$\begin{aligned} X(t) &= \sqrt{2} A_0 \exp[x(t)]. \\ &\quad \sin[\omega_0 t + M(t) + \phi(t) + \theta_w(t) + \psi_1(t) + d(t) + \theta_B(t) + \theta_0] \\ &\quad + n_i(t) \end{aligned} \quad (7.6A6)$$

where $n_i(t)$ is the additive narrowband gaussian noise process which we characterize as (Reference 25, Chapter 3)

$$n_i(t) = \sqrt{2} [n_c(t) \cos \omega_0 t - n_s(t) \sin \omega_0 t] \quad (7.6A7)$$

where $n_c(t)$ and $n_s(t)$ are banlimited white gaussian noise processes of single-sided spectral density N_0 watts/Hz.

In what follows, it will be convenient to break the signal $s(t, \phi)$ into two components, a resultant specular or fixed term due to turbulence, and a random or fluctuating component due to the turbulence. This will be required to carry out a detailed analysis in what follows. There is no loss in generality in doing so. If we ignore, for the moment, the angle modulation $M(t)$ then it can be shown using results in Appendix I, Chapter 13 of Reference 25, that the autocorrelation function of the channel output signal is given by

$$R_s(\tau) = E[s(t, \phi)s(t + \tau, \phi_\tau)] \\ = A_0^2 \exp[2m_x + \sigma_x^2 - \sigma_\phi^2] + R_x(\tau) + R_\phi(\tau) \cos \omega_0 \tau \quad (7.6A8)$$

with $x = x(t)$, $x(t + \tau) = x_\tau$ and

$$R_x(\tau) = E[x x_\tau] - m_x^2 \\ R_\phi(\tau) = E[\phi \phi_\tau] - m_\phi^2 \quad (7.6A9)$$

are defined to be the covariance functions of $\{x(t)\}$ and $\{\phi(t)\}$ respectively. In the above, one assumes that the processes $\{x(t)\}$ and $\{\phi(t)\}$ are stationary, statistically independent with $\{\phi(t)\}$ having a zero mean. While it is a fact that $\{x(t)\}$ and $\{\phi(t)\}$ are slightly correlated (Reference 4), we have neglected this in carrying out the above analysis. With a little patience this correlation can be included and it would be interesting to determine its effects on system performance. From (7.6A8) we can find the power A_{sp}^2 in the fixed or specular term; in particular, the power in the periodic component at frequency ω_0 is given by

$$A_{sp}^2 \stackrel{\Delta}{=} \lim_{\tau \rightarrow \infty} R_s(\tau) = A_0^2 \exp[2m_x + \sigma_x^2 - \sigma_\phi^2] = \text{Power in specular term.} \quad (7.6A10)$$

On the other hand, the power A_R^2 in $s(t, \phi)$ which can be considered in the random component when turbulence alone is considered, is given by

$$A_R^2 = R_s(0) - A_{sp}^2 = A_0^2 \exp[2m_x + \sigma_x^2] [\exp \sigma_x^2 - \exp(-\sigma_\phi^2)] \\ A_R^2 = m_A^2 [\exp(\sigma_x^2) - \exp(-\sigma_\phi^2)]. \quad (7.6A11)$$

Taking the ratio of specular power to random power produces the result

$$\gamma^2 \stackrel{\Delta}{=} \frac{A_{sp}^2}{A_R^2} = \frac{\exp[-(\sigma_x^2 + \sigma_\phi^2)/2]}{2 \sinh[(\sigma_x^2 + \sigma_\phi^2)/2]} \quad (7.6A12)$$

If $\sigma_x^2 + \sigma_\phi^2 \ll 1$ then

$$\gamma^2 \approx \frac{1}{\sigma_x^2 + \sigma_\phi^2} \quad (7.6A13)$$

Equation (7.6A12) is plotted in Figure 7.6A-3.

Using Woo's (Reference 15) estimate for Pioneer-Venus based on the value of c_n (the structure constant) obtained from Venera 7 data $\sigma_x^2 = 0.014$ at the surface and using the Woo-Kolmogorov-von Karman combination for σ_ϕ^2 it turns out that, at the surface Venus, $\sigma_\phi^2 = 0.0558$, so that

$$\gamma^2 = \frac{1}{e^{0.0698} - 1} = \frac{1}{0.0725} = 13.8 \text{ (Venera 7)} \quad (7.6A14)$$

From (7.6A12) and with $m_x = 0$ we note

$$\begin{aligned} \frac{A_{sp}^2}{A_0^2} &= \exp[-0.0418] = 0.959 \\ \frac{A_R^2}{A_0^2} &= \exp(0.028) - \exp[0.0418] - 0.0698 \\ &= 0.0698 \end{aligned} \quad (7.6A15)$$

along the zenith. On the other hand, Woo (Reference 15) used the Venera 4 data which revealed stronger turbulence, from which the worst-case numbers turned out to be $\sigma_\phi^2 = 0.2232 \text{ rad}^2$ and $\sigma_x^2 = 0.056$. For this worst-case, with $m_x = 0$, and along the zenith

$$\begin{aligned} \frac{A_{sp}^2}{A_0^2} &= \exp[-0.1672] = 0.846 \\ \frac{A_R^2}{A_0^2} &= \exp(0.112) - \exp(-0.1672) = 0.272, \end{aligned} \quad (7.6A16)$$

and

$$\gamma^2 = 3.11 \text{ (Venera 4),}$$

for a "worst-worst" case.

It is also interesting to know the power spectral density of the channel output. In theory this can be accomplished by taking the Fourier transform of the covariance function

$$R_s(\tau) = [R_s(\tau) - R_s(\infty)]. \quad (7.6A17)$$

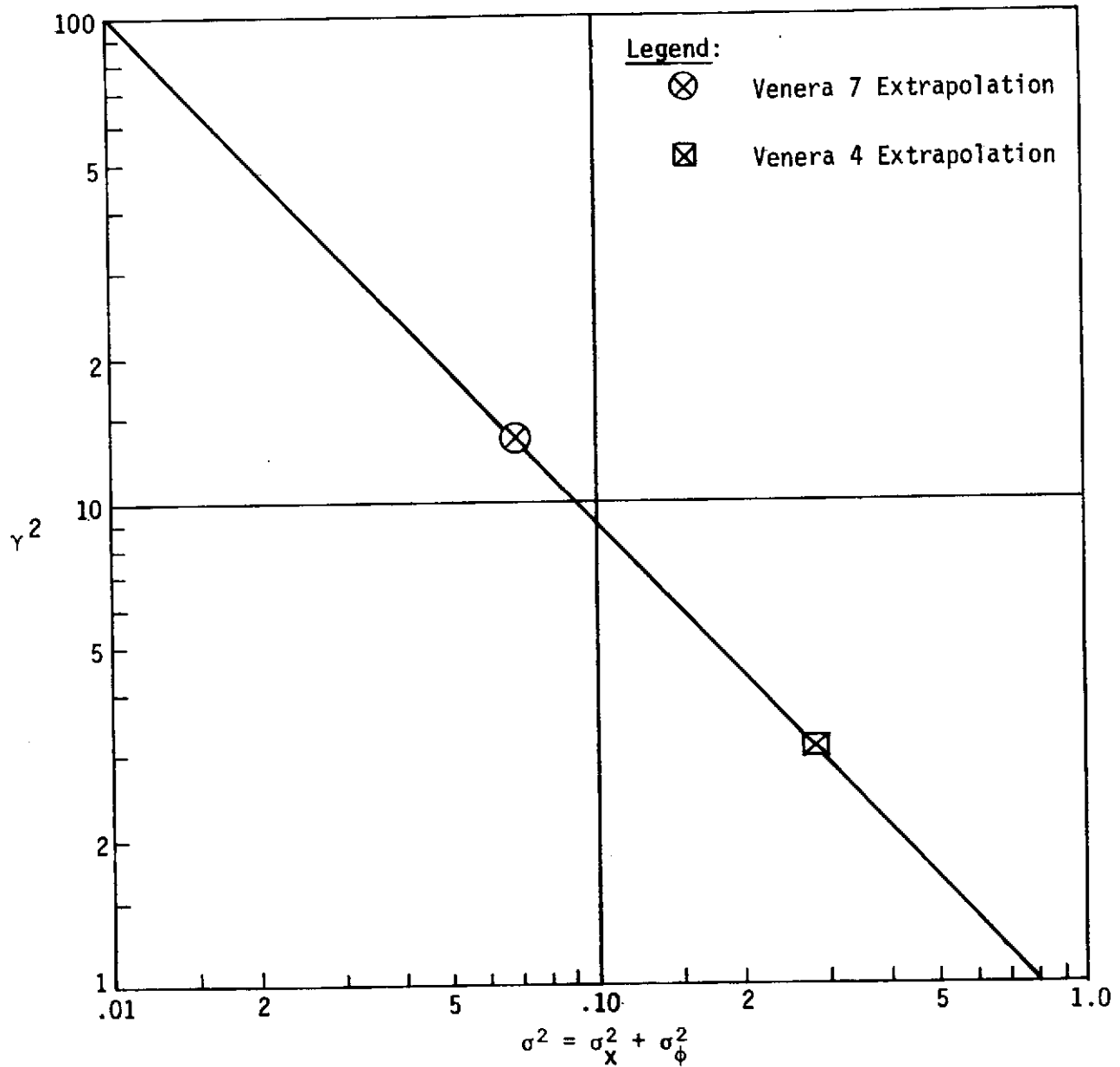


Figure 7.6A-3. Ratio of Power in Specular Component to That of the Random Component Due to Turbulence

Writing this in the form

$$R_s(\tau) = r(\tau) \cos \omega_0 \tau,$$

where

$$r(\tau) \stackrel{\Delta}{=} A_0^2 \exp\left(2m_x + \sigma_x^2 - \sigma_\phi^2\right) \left[\exp\left(R_x(\tau) + R_\phi(\tau)\right) - 1 \right], \quad (7.6A18)$$

then the Fourier transform of (7.6A18) can, in principle, be obtained by expanding $r(\tau)$ in a Taylor series about the normalized covariance function

$$\rho_{x+\phi}(\tau) \stackrel{\Delta}{=} \rho_x(\tau) + \rho_\phi(\tau), \quad (7.6A19)$$

with $\rho_x(\tau) \stackrel{\Delta}{=} R_x(\tau)/\sigma_x^2$ and $\rho_\phi(\tau) = R_\phi(\tau)/\sigma_\phi^2$. Then

$$\begin{aligned} r(\tau) &= A_{sp}^2 \left[\exp\left(\sigma_x^2 \rho_x(\tau) + \sigma_\phi^2 \rho_\phi(\tau)\right) - 1 \right] \\ &= A_{sp}^2 [\exp\{\rho(\tau)\} - 1], \end{aligned} \quad (7.6A20)$$

where

$$\rho(\tau) \stackrel{\Delta}{=} \sigma_\phi^2 \left[\frac{\sigma_x^2}{\sigma_\phi^2} \rho_x(\tau) + \rho_\phi(\tau) \right]. \quad (7.6A21)$$

The Fourier transform $\mathcal{F}[r(\tau)/A_{sp}^2]$ can then be written in terms of multiple convolutions of $\rho(\tau)$. In fact

$$A_r(\omega) = A_{sp}^2 \left\{ S_\rho(\omega) + \sum_{n=1}^{\infty} \frac{1}{n!} (S_\rho(\omega) * S_\rho(\omega))^n \right\}, \quad (7.6A22)$$

where $(x * x)^n$ denotes an n-fold convolution of $x(\omega)$ with itself. From the above we can then write an expression for the power spectral density

$$S_r(\omega) = \mathcal{F}[r(\tau)] = A_{sp}^2 \mathcal{F}[\exp\{\rho(\tau)\} - 1]$$

of the channel output when turbulence only is considered, i.e.,

$$S_s(\omega) = S_r(\omega - \omega_0) + S_r(\omega + \omega_0) \quad (7.6A23)$$

where we have assumed that $r(\tau)$ is narrowband. If we take only the first two terms owing to the smallness of the spectra as determined by Woo (Reference 15), then

$$S_s(\omega) \approx A_{sp}^2 \left\{ S_p(\omega) + S_\phi(\omega) + (S_x(\omega) + S_\phi(\omega)) * (S_x(\omega) S_\phi(\omega)) \right\}. \quad (7.6A24)$$

The root mean square bandwidth of the channel output can be obtained from

$$W_{rms} \stackrel{\Delta}{=} \int_{-\infty}^{\infty} \frac{f^2 S_r(f)}{A_{sp}^2 [e^{\rho(0)} - 1]} df, \quad (7.6A25)$$

which can be written in terms of the covariance function of the channel output, viz.,

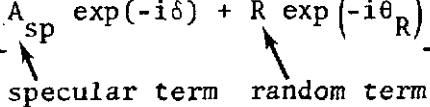
$$\begin{aligned} W_{rms} &= - \frac{(2\pi)^{-2}}{A_{sp}^2 [e^{\rho(0)} - 1]} \left. \frac{\partial^2 r(\tau)}{\partial \tau^2} \right|_{\tau=0} \\ W_{rms} &= - \frac{(2\pi)^{-2} \exp[\rho(0)]}{[\exp[\rho(0)] - 1]} \left\{ \left. \frac{\partial^2 \rho(\tau)}{\partial \tau^2} + \left(\frac{\partial \rho(\tau)}{\partial \tau} \right)^2 \right\} \right|_{\tau=0} \\ &= - \left(\frac{1}{2\pi} \right)^2 \left. \frac{\partial^2 \rho(\tau)}{\partial \tau^2} \right|_{\tau=0} \end{aligned} \quad (7.6A26)$$

In the above $f = \omega/2\pi$ represents the frequency variable. The parameter W_{rms} will be needed when the performance of a phase-locked loop is given. This parameter provides a theoretical estimate for the signal frequency spread seen at the output of the channel due to atmospheric turbulence. Obviously, to work the problem further, one could consider the spectra $W_\phi(\omega)$ and $W_x(\omega)$ as developed in Woo (Reference 15). However, it is readily seen that the problem would become quite complex owing to the nature of the numerical integrations involved. If one were to idealize the spectra illustrated by Woo (Reference 15) and replace them by idealized rectangulairs of appropriate 3 decibel frequencies (on the order of 2 to 3 Hertz for amplitude and 1 Hertz for the phase) then an "approximate" bandwidth of the order of 2 to 4 Hertz seems to a rough rule-of-thumb for the bandwidth of the random turbulence component. Further details of the developments should be pursued with the passage of time; in particular, the additional effects superposed on the carrier due to the cross-correlation function $\rho_{x\phi}(\tau)$ and, in addition, W_{rms} at various angles along the zenith.

2.2 The Rician Channel Model and Its Interconnection with the Lognormal Model

On the basis of the previous discussions, we now consider the problem of remodeling the channel output such that it will interface, in an approximate sense, with certain studies which have been performed for fading channels. As pointed out earlier, deWolf (Reference 1, 2, 3) advanced the hypothesis that the probe channel was Rician; however, it seems as though he has since retracted his position. For simplicity in modeling we begin by neglecting all random modulations other than that due to turbulence, i.e., we consider the response of the random channel filter of Figure 7.6A-1 when the input is a sine wave of A_0^2 watts. Under a Rician hypothesis, see Figure 7.6A-4, the output of the random time-variant filter consists of two terms, viz., a specular term $A_{sp} \exp[i\omega_0 t - i\delta]$ (a phasor of amplitude A_{sp} and fixed phase δ) and a Rayleigh phasor $R \exp[i\omega_0 t - i\theta_R]$ which consists of the sum of two independent normal quadrature phasors of zero mean and variance σ^2 . Thus in phasor notation, the response of the channel filter to $\sqrt{2} A_0 \exp[i\omega_0 t + i\theta_0]$ is

$$s[t, \Phi] = \sqrt{2} \left[A_{sp} \exp(-i\delta) + R \exp(-i\theta_R) \right] \exp[i\omega_0 t + i\theta_0] \quad (7.6A27)$$



which can be combined to give

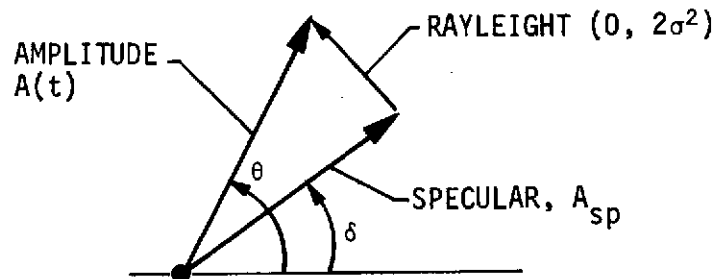
$$s(t, \Phi) = \sqrt{2} A(t) \sin[\omega_0 t + \theta(t)]. \quad (7.6A28)$$

The joint probability density function $p(A, \theta)$ is characterized by

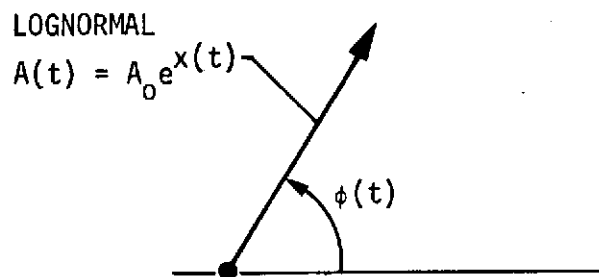
$$p(A, \theta) = \frac{A}{2\pi\sigma^2} \exp \left[-\frac{A^2 + A_{sp}^2 - 2AA_{sp} \cos(\theta - \delta)}{2\sigma^2} \right] \quad (7.6A29)$$

for $0 \leq A \leq \infty$ and $|(\theta - \delta)| \leq \pi$. The parameters A_{sp} and σ in (7.6A-29) may be given physical interpretations. The quantity A_{sp}^2 may be considered to be the power in the specular component while $2\sigma^2$ is the sum of the mean-squared value of the in-phase ($R \cos \theta_R$) and quadrature ($R \sin \theta_R$) components which characterize the Rayleigh vector. For convenience we define

$$\gamma^2 \triangleq \frac{A_{sp}^2}{2\sigma^2} \quad (7.6A30)$$



(a) RICE VECTOR, $A_{sp} \exp(-i\delta) + R \exp(-i\theta_R)$



(b) Lognormal Vector, $A_0 \exp [x(t) + i\phi(t)]$

Figure 7.6A-4. Vector Channel Models

as the ratio of the average power received via the specular component to the random component. The probability density function is given by

$$p\left[A_n \triangleq \frac{A}{\sigma}\right] = A \exp\left[-\frac{A^2}{2} - \gamma^2\right] I_0\left(\sqrt{2\gamma^2 A_n^2}\right) \quad (7.6A31)$$

for $0 \leq A_n \leq \infty$. The mean of the channel gain is given by

$$\begin{aligned} E(A_n) &= \exp(-\gamma^2) \left[(1 + \gamma^2) I_0\left(\frac{\gamma^2}{2}\right) + \gamma^2 I_1\left(\frac{\gamma^2}{2}\right) \right] \\ E(A) &= \sigma E(A) \end{aligned} \quad (7.6A32)$$

where $I_k(x)$ is a modified Bessel function of imaginary argument. The mean squared value is given by

$$\begin{aligned} E(A_n^2) &= 2(1 + \gamma^2) \\ E(A^2) &= 2\sigma^2(1 + \gamma^2). \end{aligned} \quad (7.6A33)$$

When γ is large $I_k(x) \sim \exp(x)/\sqrt{2\pi x}$ then

$$E(A_n) \approx \frac{1 + 2\gamma^2}{\sqrt{\pi\gamma^2}} \sim \frac{2}{\sqrt{\pi}} \gamma \quad (7.6A34)$$

or

$$E(A) \sim \sqrt{2/\pi} A_{sp}$$

while

$$E(A^2) = A_{sp}^2. \quad (7.6A35)$$

It is also known that for large γ the probability density function is approximately gaussian with probability density function

$$p(A) \approx \frac{1}{\sigma} \sqrt{\frac{A}{2\pi A_{sp}}} \exp\left[-\frac{(A - A_{sp})^2}{2\sigma^2}\right] \quad (7.6A36)$$

for $A_{sp} A \gg \sigma^2$. On the other hand, the probability density function $p(\theta)$ is given by

$$p(\theta) = \frac{\exp(-A_{sp}^2)}{2\pi} \left[1 + 2\sqrt{\pi} A_{sp} \cos \theta \left(\frac{1 + \operatorname{erfc}\left[\gamma \cos A_{sp}\right]}{2} \right) \exp[\gamma^2 \cos^2 \theta] \right] \quad (7.6A37)$$

which for large γ is approximated by

$$p(\theta) \approx \frac{1}{2\pi} \sum_{n=0}^{\infty} \varepsilon_n \cos n\theta \left[1 - \frac{n^2}{2\gamma^2} \right] \quad (7.6A38)$$

With the above approximation in mind, then it would seem that the lognormal channel with reasonable large phase fluctuations and a large specular term can be approximated by a Rician channel when γ^2 is reasonably large, perhaps $\gamma^2 > 100$.

It should be noted, however, that the values of γ^2 obtained using the numbers given by Woo (Reference 15) yield values for γ^2 less than 20. It would seem that the Rice probability density function does not provide an adequate approximation to the lognormal fading expected. In fact, it is important to note that a lognormal distributed random variable can be used to approximate a noncentral chi-square random variable. The noncentral chi-squared distribution is defined to be the sum of N independent Rician random variables. If there are enough degrees of freedom in the composition then the noncentral chi-squared random variable is distributed like that of a lognormal random variable. For the details see the notes by Ohta and T. Koizumi, Reference 26 and Clark and Karp, Reference 27. Other interesting details relative to lognormal variates are given in Reference 28.

2.3 The Channel Output Equation

With this in mind then the output of the channel (including thermal noise) when modulation and all other uncertainties involved is modeled as

$$\begin{aligned} X(t) &= \sqrt{2} A_0 e^{x(t)} \sin \Phi(t) + \sqrt{2} A_B(t) \sin \Phi_B(t) + n_i(t) \\ &= \underbrace{\sqrt{2} A_{sp} \sin[\tilde{\Phi}(t)]}_{\text{specular component}} + \underbrace{\sqrt{2} x_m(t) \sin \tilde{\Phi}(t) + \sqrt{2} y_m(t) \cos \tilde{\Phi}(t)}_{\text{multipath component due to turbulence}} \\ &\quad + \underbrace{\sqrt{2} A_B(t) \sin \Phi_B(t) + n_i(t)}_{\text{planetary backscatter}}, \end{aligned} \quad (7.6A39)$$

where

$$\begin{aligned}\tilde{\phi}(t) &\stackrel{\Delta}{=} \omega_0 t + d(t) + M(t) + \psi_1(t) + \theta_{\omega}(t) + \theta_0 \\ &= \omega_0 t + \theta(t)\end{aligned}\quad (7.6A40)$$

$d(t)$ - Doppler profile

$M(t)$ - Angle modulation (PSK or MFSK)

$\psi_1(t)$ - Oscillator instabilities

$\theta_{\omega}(t)$ - Transient modulation due to probe oscillation

θ_0 - Random epoch uniform $(-\pi, \pi]$

and $A_B(t)$ and $\phi_B(t)$ are, respectively, the resultant channel amplitude and phase processes due to planetary backscatter (zero or small probes). The additive thermal noise is characterized in (7.6A7). In (7.6A40) the specular power is characterized in (7.6A10) while the power in the multipath component due to turbulence is characterized in (7.6A11) with m_A given in (7.6A3).

It would be of interest to further characterize the zero-crossing properties of both the lognormal and Rician envelope, i.e., characterize the average number of times per second the envelope crosses its mean and mean-squared values, as well as the average duration between crosses. These were evaluated incorrectly by deWolf (References 2, 3) for the Rician channel; however, a correct mathematical development is given in the addendum at the end of this appendix.

2.4 Characterization of Channel Multipath Due to Planetary Backscatter

Multipath not only arises due to the scattering of the incident rays due to the atmospheric inhomogeneities, but also because unscattered rays of the signal arrive via different path lengths. This results in time-spreading of the received signal, and is frequently related to the channel memory time. Brookner (Reference 28) discusses the problem from a propagation physics point of view. This would determine whether intersymbol interference exists as a result of the different path lengths. It appears that this effect is negligible.

If one considers further the problem of evaluating the power reflected into a spacecraft receiver when planetary multipath or backscatter is present, and if one assumes that the doppler shift is consistent, then the reflected or backscatter signal can be modeled as

$$s_B(t) = \sqrt{2} A_B(t) \sin[(\omega_0 + \omega_d)t + \theta_B(t)], \quad (7.6A41)$$

where

- f_d - Doppler shift assumed constant for simplicity of analysis
- $A_B(t)$ - Amplitude backscatter
- $\theta_B(t)$ - Phase backscatter.

Then assuming the backscatter process $s_B(t)$ is stationary, the autocorrelation function of $\{s_B(t)\}$ is written as

$$R_s(\tau) = E[s_B(t) s_B(t + \tau)]$$

$$R_s(\tau) = \exp[2m_z + \sigma_z^2 - \sigma_{\theta_B}^2 + R_z(\tau) + R_{\theta_B}(\tau)] \cos(\omega_0 + \omega_d)t, \quad (7.6A42)$$

where $z(t) = e^{\lambda n} A_B(t)$ and

$$R_z(\tau) = E[z(t) z(t + \tau)] - m_z^2$$

$$R_{\theta_B}(\tau) = E[\theta_B(t) \theta_B(t + \tau)] - m_{\theta_B}^2 \quad (7.6A43)$$

are the covariance functions of $\{z(t)\}$ and $\{\theta_B(t)\}$ respectively. From this we can easily deduce the power, if any, in a fixed term at frequency $f_0 + f_d$ Hertz. In fact, if we denote the power in and reflected fixed component as A_f^2 then

$A_f^2 \triangleq$ Power in specular component of planetary backscatter at $f_0 + f_d$ Hz

$$= \exp[2m_z + \sigma_z^2 - \sigma_{\theta_B}^2] \quad (7.6A44)$$

while

$A_r^2 \triangleq$ Power in random component of planetary backscatter at frequency $f_0 + f_d$ Hz

$$= \exp[2m_z + \sigma_z^2] \left[\exp(\sigma_z^2) - \exp(-\sigma_{\theta_B}^2) \right] \quad (7.6A45)$$

and the ratio becomes

$$\left(\frac{A_f}{A_r} \right)^2 = \frac{1}{\exp[\sigma_z^2 + \sigma_{\theta_B}^2] - 1}. \quad (7.6A46)$$

Once σ_z^2 and $\sigma_{\theta_B}^2$ have been determined, the curve given in Figure 7.6A-3 can be applied with σ^2 now equal to $\sigma_z^2 + \sigma_{\theta_B}^2$. In an actual design, characterization of the total power reflected from the planetary surface as a function of antenna gain, incident power, etc. is what is required. This involves modeling the "roughness" of the planet as well as its radar cross-section, and using these to determine the total power reflected. This has been done in Appendix 7.6 G.

3. CHARACTERIZATION OF A PHASE-LOCKED LOOP RECEIVER PERFORMANCE IN THE PRESENCE OF PLANETARY MULTIPATH AND TURBULENCE (LOGNORMAL CHANNEL)

Consider the communication system model illustrated in Figure 7.6A-5. The terms in the signal $s(t, \phi)$, as characterized in (7.6A5), can be regrouped and $X(t)$ of (7.6A39) can be rewritten as

$$X(t) = \sqrt{2} A(t) \sin[\phi(t)] + \sqrt{2} A_B(t) \sin \phi_B(t) + n_i(t), \quad (7.6A47)$$

where the planetary backscatter term will be present only on two-way links. It should be noted that when the planetary backscatter term is present, one has the problem of determining the response of a phase-locked receiver to two narrowband processes located at two different center frequencies. We shall return to this question later as it will be of concern on the large probe.

In Equation (7.6A48) $\phi(t)$ and $A(t)$ are characterized as follows:

$A(t) = A_0 e^{x(t)}$ - random channel gain process

$\phi(t) = \omega_0 t + d(t) + \psi_1(t) + \phi(t) + M(t)$

$d(t)$ - Doppler phase function

$\psi_1(t)$ - Transmitter oscillator instabilities

$M(t)$ = Phase modulation = $\text{H} X_d(t) S(t)$

H = $(\cos^{-1} m)$ = modulation index

$S(t)$ = Subcarrier

$X_d(t)$ = Data modulation

$\phi(t)$ - Channel phase characteristic

$A_B(t)$, $\phi_B(t)$ - Planetary backscatter

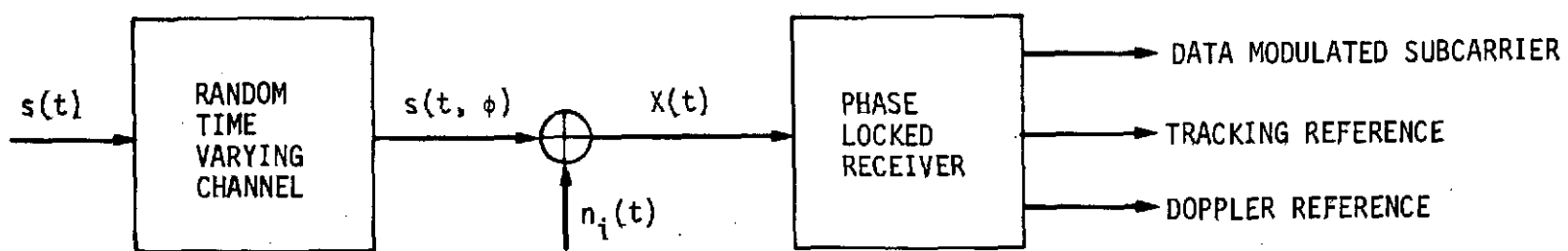


Figure 7.6A-5. Coherent Communication System Model

3.1 The Loop Equations for Both One-Way and Two-Way Operation

Things are now in tact such that the model considered in Reference 25, page 74, Figure 3-3, applies directly. If one characterizes the reference signal in the loop as $r(t, \hat{\Phi}) = \sqrt{2} K_1 \cos [\hat{\Phi}(t)]$ and define the total loop phase error φ as

$$\varphi + M = \Phi - \hat{\Phi} \quad (7.6A48)$$

Then the loop equation becomes (see Reference 25, pages 76-86) with the time variable suppressed:

3.1.1 One-Way System

$$\begin{aligned} \varphi = d + \psi_1 + \phi - \frac{mKF(p)}{p} & [A \sin \varphi + A_B \sin \varphi_B + N(t, \varphi)] \\ & - \psi_2 - K_V e/p \end{aligned} \quad (7.6A49)$$

3.1.2 Two-Way System (Up-Link)

$$\varphi = d + \psi_1 + \phi + I - \frac{mKF(p)}{p} [A \sin \varphi + N(t, \varphi)] - \psi_2 - K_V e/p \quad (7.6A50)$$

where, for the link involved, we have the following signal components:

$d(t)$ - Doppler phase function

$\psi_1(t)$ - Transmitter oscillator instabilities

$\phi(t)$ - Turbulence phase function

$I(t)$ - Planetary backscatter

$A(t) - A_0 \exp[x(t)]$ - amplitude process due to turbulence

$N(t, \varphi)$ - Equivalent phase noise process (Reference 25)

$A_B(t), \Phi_B(t)$ - Planetary backscatter process

ψ_2 - Receiver oscillator instabilities

K_V - VCO gain

e - Acquisition voltage

p - $\frac{d}{dt}$ Heaviside operator

K - Open loop gain

m - Modulation factor

From the above equations we see that the total system phase error φ is due to many different effects. Later we shall characterize these and assess the degradation on system performance. Furthermore, for the present we shall neglect the effects of the limiter and treat that under a separate subsection as it represents a slightly more complex problem.

3.2 The Data Channel Equation

The demodulated signal passed to the subcarrier demodulator assembly (SDA) is characterized by

$$u(t) = A_2(t) X_d(t) S(t) \cos \varphi + N(t, \varphi) \quad (7.6A51)$$

with $A_2(t) = (\sqrt{1 - m^2}) A(t)$. (See Figure 7.6A-6 for a system model which excludes the limiter.) The limiter analysis will be included later on in this sequel.

If the effects of subcarrier tracking loop are to be accounted for, then the reference subcarrier signal can be modeled as $\hat{S}(t)$. Then it is reasonable to approximate the baseband signal to the symbol detector as

$$y(t) = A_2(t) X_d(t) S(t) \hat{S}(t) \cos \varphi + n_w(t). \quad (7.6A52)$$

The product

$$S(t) \hat{S}(t) = \begin{cases} \cos \phi_s \text{ sine wave subcarriers} \\ 1 - \frac{2}{\pi} |\phi_s| \text{ square wave subcarriers} \end{cases},$$

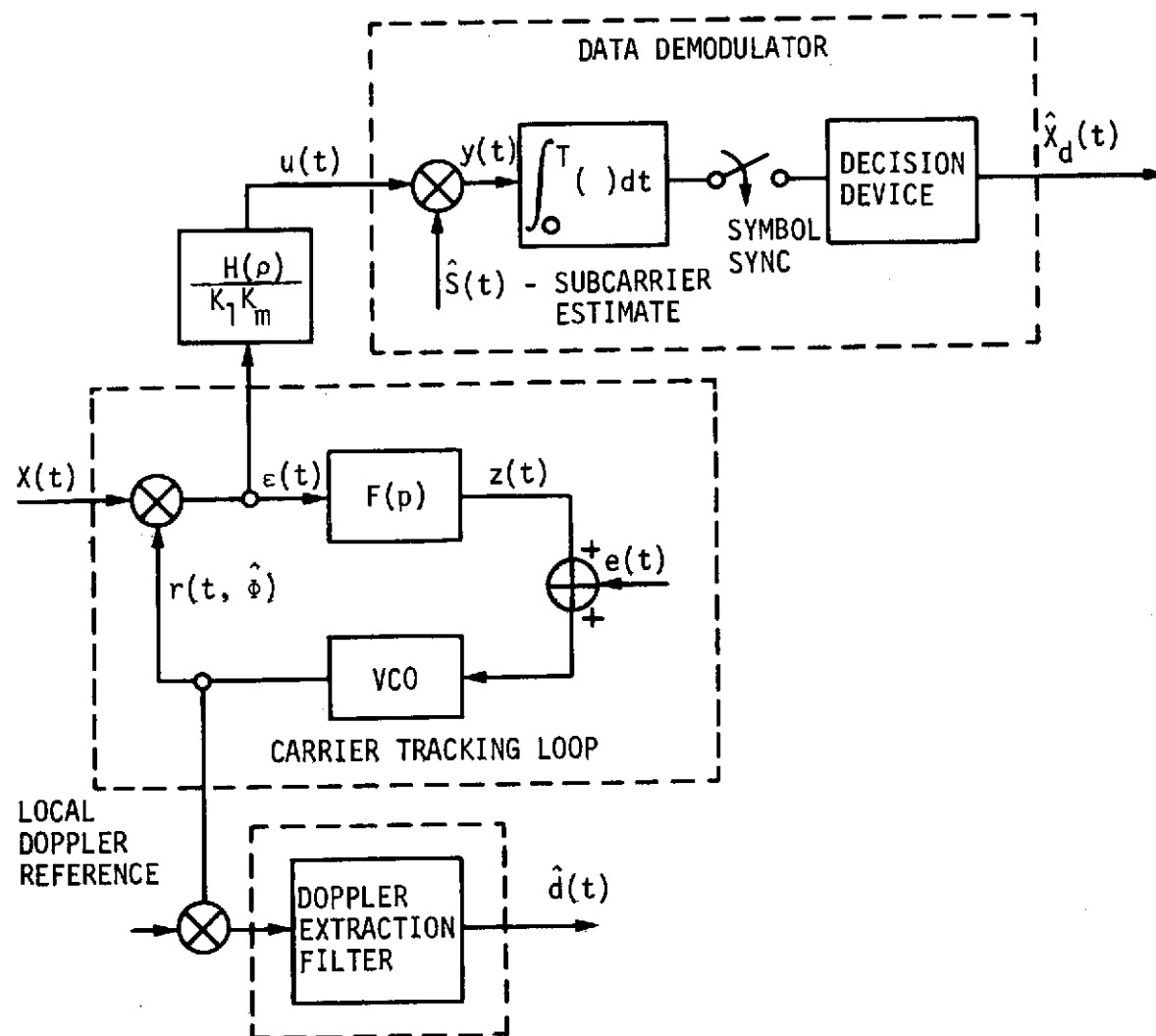


Figure 7.6A-6. Carrier Tracking Doppler and Phase Modulation Extraction (Limiter Absent)

where ϕ_s is the phase error in the subcarrier tracking loop. For simplicity in what follows, we shall assume the sine wave subcarrier case so that

$$y(t) = A_2(t) X_d(t) \cos \varphi \cos \phi_s + n_w(t), \quad (7.6A53)$$

where $n_w(t)$ is white gaussian noise. The data detector produces the random variable (infinite quantization assumed)

$$q \stackrel{\Delta}{=} \int_{\tau}^{T+\tau} y(t) X_d(t) dt \quad (7.6A54)$$

where T is the symbol time and τ represents the symbol synchronization jitter. The decoder of Figure 7.6A-5 works with the quantized variable $V[q]$

$$V[q] = \left[\int_{\tau}^{T+\tau} \left[A_2(t) X_d(t) \cos \varphi(t) \cos \phi_s(t) + n_w(t) \right] dt \right] \quad (7.6A55)$$

or

$$= \left[\int_{\tau}^{T+\tau} \left[A_2(t) X_d(t) \cos \varphi(t) \left[1 - \frac{2}{\pi} |\phi_s| \right] + n_w(t) \right] dt \right]$$

Thus the data detection process is degraded by the channel multipath, $A_2(t)$, the phase error in the carrier tracking loop including: the phase fluctuations due to the channel multipath, and turbulence, the doppler profile, oscillator instabilities, the subcarrier phase error ϕ_s and the symbol synchronization jitter. In the two-way mode of operation one must also include degradations in the transponder due to the up-link thermal noise, any oscillator instabilities, up-link doppler, planetary backscatter.

3.3 Error Probability Performance

To evaluate the error probability one needs an expression for the conditional bit-error probability $P_E(\varphi, \phi_s, \tau, A_2)$ to produce the average bit error probability

$$P_E = \iint_{R \tau} \int_{\phi_s} \int_{\phi} P_E(\varphi, \phi_s, \tau, A_2) P(\phi, \phi_s, \tau, R) d\varphi d\phi_s d\tau dR \quad (7.6A56)$$

Obviously, some reasonable and simplifying assumptions must be made to carry out any analysis.

Our approach to this end has been to compute the losses separately more or less in the approximation, and use the "principle-of-superposition" to get their combined effect. (See the detailed design control tables and other technical memos dealing with these design aspects.)

In order to indicate the problems involved we consider first the effects due to the amplitude fluctuations $A(t)$. If we let $P_E(A)$ denote the conditional symbol error probability due to the channel amplitude fluctuations, then one can argue that the average error probability is given by

$$P_E = \int p(A) P_E \left[Y \sqrt{(1 - m^2) T / N_0} \right] dA \quad (7.6A57)$$

where $p(A)$ is characterized in (7.6A4) and

$$Y \triangleq \frac{1}{T} \int_0^T A(t) dt \quad (7.6A58)$$

with T being the symbol time. Assuming that the correlation time τ_A of the amplitude fluctuation is much less than T (slow amplitude fluctuations) then $Y \approx A$ and one can easily show that the symbol error probability for an uncoded PSK system is given by

$$P_E = \frac{1}{2\sqrt{\pi}} \int_{-\infty}^{\infty} \exp(-z^2) \operatorname{erfc} \left[\sqrt{R} \exp \left(\sqrt{2}\sigma_x z + m_x \right) \right] dz \quad (7.6A59)$$

where $R = (1 - m^2) A^2 T / N_0$ and

$$\operatorname{erf}(z) \triangleq \frac{2}{\sqrt{\pi}} \int_0^z \exp(-t^2) dt$$

$$\operatorname{erfc}(z) = 1 - \operatorname{erf}(z). \quad (7.6A60)$$

Equation (7.6A59) has been evaluated on the digital computer for the case where $m_x = -\sigma_x^2$. The degradations due to atmospheric turbulence are assessed in terms of the loss factor L in Figure 7.6A-7. This plot represents the extra signal-to-noise ratio (decibel) required above that needed to overcome the additive noise of the system and to compensate for the adverse effect of turbulence. Using the value $\sigma_x^2 = 0.014$ (Venera 7 data at the surface)

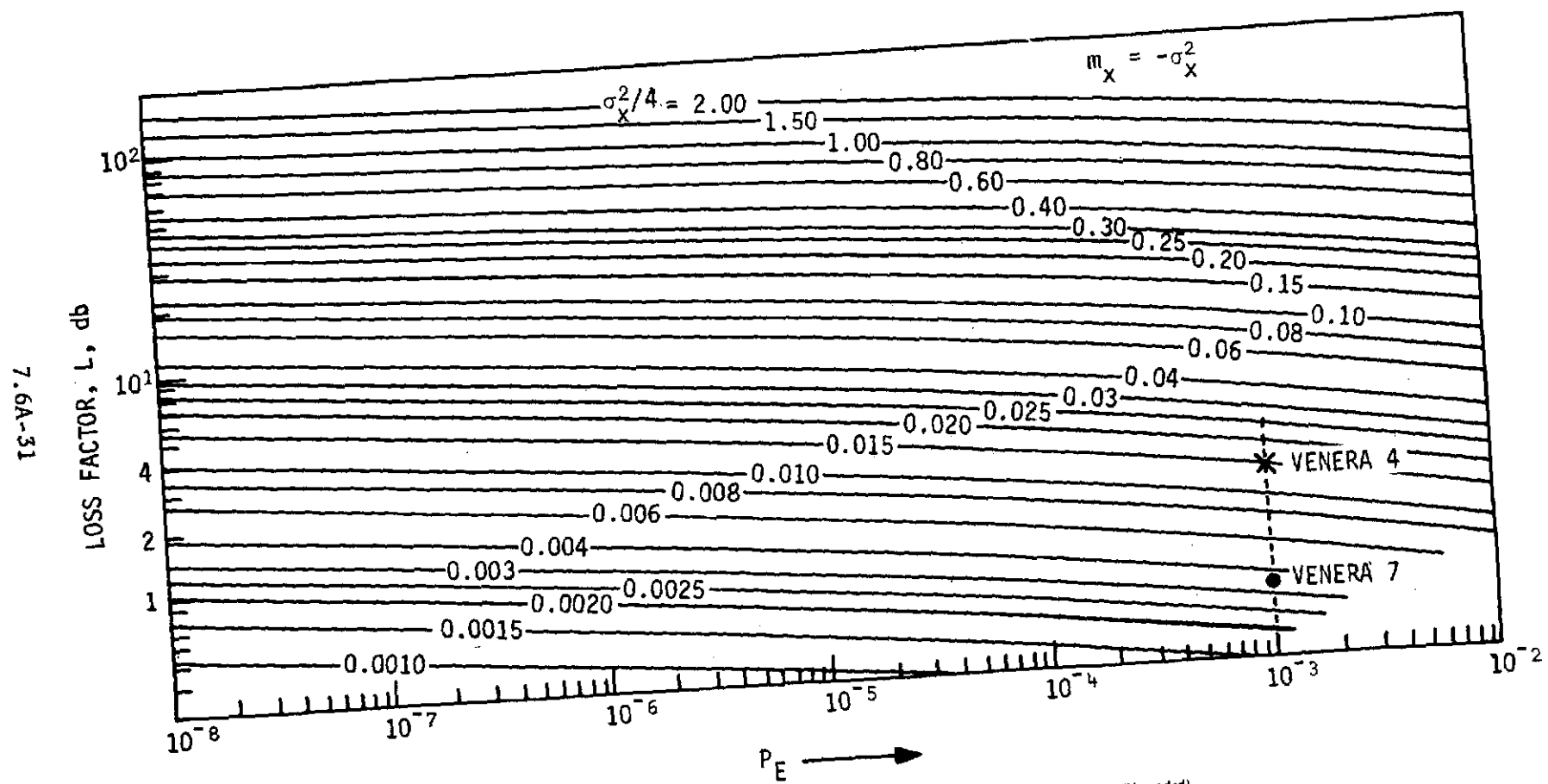


Figure 7.6A-7. Fading Loss Factor, L , vs Error Probability for Lognormal Fading (Uncoded)

the loss due to atmospheric turbulence alone is approximately 2.2 decibels at $P_E = 10^{-3}$. For $\sigma_x^2 = 0.056$ the loss is approximately 2.2 decibels at $P_E = 10^{-3}$. Other plots of equation (7.6A59) are given in Appendix 7.6C.

Generally speaking, analytical expressions for the bit-error probability achievable when using a sequential decoding or maximum-likelihood decoding algorithm in connection with convolutional codes, is practically impossible to achieve owing to the mathematically-nontractable nature of the problem. Aside from this fact, the case in point here presents other difficulties, namely, owing to the slow variations in channel gain, the decisions made on the symbols are correlated, i.e., the channel possesses memory. The memory effects manifest themselves as slow fades due to the noisy synchronization references and due to channel gain variations. In certain cases interleaving techniques can be used to help alleviate the problem and the amount of "help" is usually dependent on the data rate as well as the number of frames of interleaving.

To account for the bit error probability, short of computer simulations of the combined effects (Reference 29), one can degrade the idealized coded performance, as obtained by computer simulations in the presence of thermal noise. This degradation can be accounted for in the form of an integration over the curve fit $P_E(A) = f[A\sqrt{T(1 - m^2)/N_0}]$ to the simulation data for the bit error probability. In this case, we have that the bit error probability is

$$P_E \approx \int_0^\infty p(A) f[A\sqrt{T(1 - m^2)/N_0}] dA \quad (7.6A61)$$

and the approximate sign is due to the fact that the decisions made on the symbols are correlated. In Appendix 7.6D, Equation (7.6A61) is plotted for various values of m_x and σ_x^2 . Computer simulation results are needed to verify the region of validity of the approximations as the rate of variations in $A(t) = mA_0 \exp[x(t)]$ may produce correlated decisions on the symbols.

To account for the noisy reference losses for the coded case, one can provide approximate results by arguing that the amplitude (see 7.6A55) of the baseband signal is effected by $\cos \varphi (1 - \frac{2}{\pi} |\phi_s| \cos \phi_s)$ and produce an integration over the probability density function $p(\varphi)$ of the phase error. Using this approximation, three cases of interest arise:

- (I) Phase error varies slowly with respect to bit time
- (II) Phase error varies rapidly over the bit time
- (III) Phase error varies moderately over the bit time

Various studies, References 29, 30, 31, 32, 33, 34, 35, 36, have been made for both one-way and two-way systems coded and uncoded, and deal with both the coded and uncoded cases. Reference 30 studies the noisy reference losses, via computer simulation techniques, for sequential decoding with phase-locked demodulation in the presence of white noise. References 31 and 32 treat uncoded coherent communication system performance due to noisy reference losses in the presence of white noise for all three of the above mentioned rates of phase error variations. Reference 33 studies the noisy reference problem in white noise for convolutional codes and Viterbi decoding; both one-way and two-way results are available. Heller and Jacobs (Reference 34) have demonstrated how to calculate the noisy reference loss for the white noise case using short constraint length codes. The noisy carrier reference loss has been studied in References 35 and 36 for one-way and two-way systems which use block codes and work in the presence of white gaussian noise. While the above mentioned references do not completely exhaust the noisy reference problem studies, they are typical of the contributions made. For brevity we do not draw conclusions or reproduce any of the curves based upon the above studies contained therein. In any case, the above mentioned analysis or simulations do not account for the channel turbulence and generally neglect the problem of correlated symbol decisions when convolutional codes are used. It appears at this point that, if one is to accurately account for and assess the combined effects due to atmospheric turbulence and additive noise, further working of the problem is necessary.

At least two fruitful avenues are available: characterize the joint probability density function $p(A, \varphi)$ and average over the conditional bit-error probability $P_E(A, \varphi)$ for the three rates (discussed above) of variation, in φ and A or perform computer simulations which account for the combined effects which produce losses and compare the results. From either of these results one can assess the system losses for various probe attitudes and zenith angles. We now demonstrate the two approaches.

For uncoded communications an approximate theory which accounts for the combined effects can be derived. For Case I, the BEP can be approximated by

$$P_E = \int_0^\infty \int_{-\pi}^{\pi} P_E(A, \varphi) p(A, \varphi) d\varphi dA$$

when the data rate is large compared to the loop bandwidth and the fading bandwidth. Here

$$P_E(A, \varphi) = \frac{1}{\sqrt{2\pi}} \int_{\sqrt{\frac{A^2 T}{N_0}} \cos \varphi}^{\infty} \exp(-x^2/2) dx$$

$$p(\varphi | A = A_0 e^x) = \frac{\exp[\rho e^{2x} \cos \varphi]}{2\pi I_0(\rho e^{2x} \cos \varphi)} \quad |\varphi| < \pi,$$

and $\rho = 2A^2/N_0 W_L$ represents the loop signal-to-noise ratio.

For Case II the phase error varies rapidly over the symbol time and the BEP is approximated by

$$P_E = \int_0^\infty P_E(A) p(A) dA$$

where

$$P_E(A) = \frac{1}{\sqrt{2\pi}} \int_{\sqrt{\frac{A^2 T}{N_0}} (\overline{\cos \varphi})}^{\infty} \exp(-z^2/2) dz$$

and

$$\overline{\cos \varphi} = E[\cos \varphi | A] = \frac{(I_1 \rho e^{2x})}{(I_0 \rho e^{2x})}$$

For the case of coded communication, the effects of atmospheric turbulence and additive noise on the BEP can be assessed in an approximate theory by replacing the $P_E(A, \varphi)$ and $P_E(A)$, for Cases I and II, by functions which have

been obtained via computer simulation and produce averages. This approach is discussed in Reference 33.

3.4 Tracking Loop Analysis (Limiter Absent)

As seen from the loop equation of operation (7.6A50) there are several deleterious effects which must be accounted for in the design of the tracking system. Several of these effects are different from previous deep space missions. These include: high doppler, doppler rate, and doppler accelerations, etc., turbulence effects, planetary backscatter in two-way mode, perhaps oscillator instabilities, all combined with low signal-to-noise ratios.

In consideration of (7.6A49) it is clear that the equation of operation represents a formidable equation (nonlinear, stochastic, integrodifferential with time-varying coefficients) to deal with even when the loop is linearized. If linearized, we see that the equation is a linear differential equation with randomly time-varying coefficients. Consequently, one must resort to introducing approximations in order to proceed with an analysis. Based upon the work of Woo and Tartarski (References 4, 15), two extreme cases immediately suggest themselves. As far as the envelope of the channel multipath and turbulence characteristic is concerned: (I) If the correlation time τ_A is small in comparison with the bandwidth of the loop (i.e., $A(t)$ of bandwidth, say W_A is smaller than W_L or $W_A \ll W_L$, then one can approximate the probability density function $p(\varphi|A)$ and average over the probability density function of A to find the required $p(\varphi)$; (II) If the correlation time τ_A is large in comparison with the loop bandwidth, i.e., $\tau_A \gg 1/W_L$, then $A(t)$ represents a fast fluctuation and the loop filter passes, in the approximation, the average value $m_A = E(A) = \exp[m_x + \sigma_x^2/2]$. Therefore, for these two cases, the loop equation can be approximated by:

Case I: $W_A \ll W_L$

$$\varphi = d + \psi_1 + \phi + I - \frac{m K F(p)}{p} [A \sin \varphi + A_B \sin \varphi_B + N(t, \varphi)]$$

$$-\psi_2 = K_V e/p \quad (7.6A62)$$

Case II: $W_A \gg W_L$

$$\varphi = d + \psi_1 + \phi + I - \frac{mKF(p)}{p} \left[A \sin \varphi + A_B \sin \varphi_B + N(t, \varphi) \right] \\ -\psi_2 - K_V e/p \quad (7.6A63)$$

where, for one-way transmission $I = 0$ and $A_B = 0$. Another case of interest, in theory, would be the case where the turbulence effects have fast and slow varying components. In this case one can expand the channel output into two sets of components excluding perhaps any specular term. This includes components which are slowly varying (with respect to W_L) and components which are varying rapidly with time. In this case, the envelope fluctuations $A(t)$ can be decomposed into two terms, i.e.,

$$A(t) = A_s(t) + A_f(t) \quad (7.6A64)$$

where $A_s(t)$ characterizes the slowly varying terms and $A_f(t)$ represents fast variations. For this decomposition one can write the hybrid of the above equations as:

Case III.

$$\varphi = d + \psi_1 + \phi + I - \frac{mKF(p)}{p} \left[(\bar{A}_f + A_s) \sin \varphi A_B \sin \varphi_B + N(t, \varphi) \right] \\ -\psi_2 - K_V e/p \quad (7.6A65)$$

where we have suppressed the time variable. One then solves the Fokker-Planck equation for $p(\varphi|A_s)$ and then averages over the probability density function of A_s .

It should be noted at this point that based upon the results of Woo (Reference 15), Case I represents the case of interest here. Thus to obtain the probability density function $p(\varphi)$ one solves the Fokker-Planck equation for $p(\varphi|A)$ and then averages over $p(A)$ given in (7.6A4).

There are several methods for approximating the probability density function of the phase error (or conditional probability density function) depending on the parameters of the channel model (Reference 25). In either case, the solution will be considerably complicated owing to the facts that $A(t)$ is changing randomly with time, etc. In fact, the above equation (Case I) indicates

the complicated nature of the system operation. Even if the thermal noise is zero, the equation still represents a stochastic differential equation of operation, and even when linearized, the coefficients remain randomly time-varying owing to the random channel effects. Thus any theory which has been developed in the absence of noise remains largely invalid owing to channel multipath effects. For example, the static phase error calculated in the usual way does not have meaning because the notion of singularities has meaning only for deterministic-type differential equation. This is particularly bad for the problem at hand, in that at certain points in time the doppler profile possesses first, second and higher order derivatives as opposed to the usual case wherein one has to contend primarily with doppler offsets. In fact, for the case under study the "equivalent" channel doppler signal which the loop sees is

$$D(t) \stackrel{\Delta}{=} d(t) + \psi_1(t) + \phi(t) + I(t) - \psi_2(t) \quad (7.6A66)$$

and is truly stochastic process owing to the channel turbulence phase characteristics, oscillator instabilities, etc. Another point worth mentioning is that as a consequence of the channel multipath, the equation which governs loop behavior does not "enjoy" the usual simplification which takes place when the noise vanishes. By linearizing the loop, a formidable problem remains in that the closed loop transfer function becomes meaningless owing to the channel multipath and turbulence. While one can carry out a loop design on the basis of the white noise background theory, it is difficult to obtain loop performance, in general, without making simplifying assumptions suggested by studying the propagation physics of the medium (References 1, 11). Most of the effects of interest enter into the system equations in a nonlinear way, and as a result, the use of intuition becomes, in general, suspect when attempting to assign numbers to the various side effects produced by the many disturbing processes.

In what follows an attempt is made to characterize the most needed probability density function $p(\varphi)$. To accomplish this we first linearize the loop; later we shall characterize the nonlinear effects.

3.4.1 Linearized Analysis ($\sin \varphi \approx \varphi$) of a Second Order Loop

In order to produce a linear analysis using the stochastic differential equation developed thus far, it will be necessary to observe that the correlation time τ_A of the channel amplitude fluctuations is long in comparison

with the correlation time τ_φ of the phase error process, Reference 11. The implication is that one can carry out an approximate analysis by producing ensemble averages over the fast fluctuating terms and then averaging over the remaining slow fluctuations.

If the loop equation is linearized then the equation of operation becomes, in operator form,

$$\begin{aligned}\varphi &= \frac{p}{p + mKF(p)A} \left[d + \psi_1 + \phi + I - \psi_2 - \frac{K_V e}{p} \right] \\ &\quad - \frac{1}{A} \frac{mKAF(p)}{p + mKF(p)} \left[A_B \sin \varphi_B + N(t, \varphi) \right]\end{aligned}\quad (7.6A67)$$

which clearly shows that the system phase error is due to many effects. When the amplitude, A , fluctuations are taken into account the loop transfer functions becomes

$$H_\varphi(p, A) \stackrel{\Delta}{=} \frac{mKAF(p)}{p + mKF(p)A} \quad (7.6A68)$$

$$1 - H_\varphi(p, A) \stackrel{\Delta}{=} \frac{p + mKF(p)A - mAF(P)}{p + mKF(p)A} \quad (7.6A69)$$

which differs from the case for which the theory has been developed. If however, the correlation time τ_A is much less than the reciprocal of the loop filter bandwidth then one can assume that

$$F(p)A(t) \approx A(t)F(p), \quad (7.6A70)$$

in which case the loop equation is approximated by

$$\begin{aligned}\varphi &\approx [1 - H_\varphi(p|A)] \left[d + \psi_1 + \phi + I - \psi_2 - \frac{K_V e}{p} \right] \\ &\quad - H_\varphi(p|A) \left[A_B \sin \varphi_B + N(t, \varphi) \right]\end{aligned}\quad (7.6A71)$$

where

$$H_\varphi(p|A) \stackrel{\Delta}{=} \frac{mKAF(p)}{p + mKAF(p)}. \quad (7.6A72)$$

The assumption that $A(t)$ is slowly varying has been addressed in Woo (Reference 11). For brevity of notation in what follows we write

$$H_\varphi(p) \stackrel{\Delta}{=} H_\varphi(p|A). \quad (7.6A73)$$

Assuming $e = 0$ (under control by the operator) then the total mean square phase error, conditional upon the slow fluctuations, is given by*

$$\sigma^2(A) = \sigma_d^2(A) + \sigma_d^2(A) + \sigma_{\Delta\psi}^2(A) + \sigma_\phi^2(A) + \sigma_I^2(A) + \sigma_B^2(A) + \sigma_\varphi^2(A) \quad (7.6A74)$$

where $\Delta\psi \stackrel{\Delta}{=} \psi_1 - \psi_2$ where we have assumed statistically independent processes.

The first term represents the mean-square tracking error defined by

$$\sigma_d^2(A) \stackrel{\Delta}{=} \frac{1}{2\pi i} \int_{-i\infty}^{i\infty} |1 - H_\varphi(s)|^2 E[|\tilde{d}(s)|^2] ds \quad (7.6A75)$$

where $E[\cdot]$ denotes the expected value of the Laplace transform of $d(t)$. The contribution due to the oscillator instabilities is defined by

$$\sigma_{\Delta\psi}^2(A) \stackrel{\Delta}{=} \frac{1}{2\pi i} \int_{-i\infty}^{i\infty} |1 - H_\varphi(s)|^2 S_{\Delta\psi}(s) ds \quad (7.6A76)$$

where $S_{\Delta\psi}(s)$ represents the "power spectral density" of $\Delta\psi$. The third term represents a conditional variance due to the phase characteristics of the atmospheric turbulence and is defined by

$$\sigma_\phi^2(A) \stackrel{\Delta}{=} \frac{1}{2\pi i} \int_{-i\infty}^{i\infty} |1 - H_\varphi(s)|^2 S_\phi(s) ds \quad (7.6A77)$$

where $S_\phi(s)$ represents the "power spectral density" of the phase process $\{\phi(t)\}$. The fourth term in σ_I^2 represents a variance component on the down-link signal due to those up-links components tracked in the transponder. Thus

$$\sigma_I^2(A) = \frac{1}{2\pi i} \int_{-i\infty}^{i\infty} |1 - H_\varphi(s)|^2 S_I(s) ds \quad (7.6A78)$$

* At this point we have assumed that the processes $\{x(t)\}$ and $\{\varphi(t)\}$ are statistically independent. It would be interesting to consider the effects (if any) which the cross-correlation produces on the loop's tracking ability.

where $S_I(s)$ characterizes the power spectral density of the interference, e.g., up-link thermal noise, up-link multipath, up-link doppler, which the transponder sees. This term is zero for one-way operation. The variance term σ_B^2 present only in the transponder, is due to planetary backscatter and is a term which must be considered in evaluating the performance of the transponder loop. Its effects are defined by

$$m^2 A^2 \sigma_B^2(A) = \frac{1}{2\pi i} \int_{-i\infty}^{i\infty} |H_\phi(s)|^2 S_B(s) ds \quad (7.6A79)$$

where $S_B(s)$ represents the power spectral density of the effective multipath signal $A_B \sin \phi_B$. Finally, we have that

$$m^2 A^2 \sigma_\phi^2(A) = \frac{1}{2\pi i} \int_{-i\infty}^{i\infty} |H_\phi(s)|^2 S_N(s) ds \quad (7.6A80)$$

represent a conditional variance owing to the thermal noise fluctuations.

This reduces to

$$\sigma_\phi^2(A) = \frac{N_0 W_L(A)}{2A^2} \triangleq \frac{1}{\rho(A)} \text{ where } \rho(A) \triangleq \frac{2A^2}{N_0 W_L(A)} \quad (7.6A81)$$

where the "conditional loop bandwidth" is defined by

$$W_L(A) \triangleq \frac{1}{2\pi i} \int_{-i\infty}^{i\infty} |H_\phi(s)|^2 ds. \quad (7.6A82)$$

The unconditional variance of the total phase error can be found by averaging $\sigma^2(A)$ over the probability density function $p(A)$, i.e.,

$$\sigma^2 = \int_{-\infty}^{\infty} \sigma^2(A) p(A) dA \approx \sigma^2(\bar{A}) \quad (7.6A83)$$

which serves to characterize the spread of $p(\phi)$ in the region of operation where $\sin \phi \approx \phi$. The approximation applies when σ_x is small enough that $p(A) \approx \delta(A - \bar{A})$.

3.4.2 The Effect of Thermal Noise on the Total Loop Phase Error

Notice that when $W_L(A)$ is not appreciably affected by the amplitude fluctuations (this will be determined by the limiter suppression factor to be considered shortly), then the average loop signal-to-noise ratio is

$$\rho \stackrel{\Delta}{=} \int_{-\infty}^{\infty} \rho(A) p(A) dA \approx \int_{-\infty}^{\infty} \rho(A) \delta(A - \bar{A}) dA$$

$$\rho = \frac{2m^2 [E(A)]^2}{N_0 W_L(\bar{A})} \quad (7.6A84)$$

and from (7.6A3) we have, under a conservation of power assumption,

$$\rho \approx \frac{2m^2 A_0^2 \exp(-\sigma_x^2)}{N_0 W_L(\bar{A})} \quad (7.6A85)$$

or small σ_x . With $\sigma_x^2 = 0.056$, the normalized signal-to-noise ratio becomes

$$\left(\frac{\rho}{2m^2 A_0^2} \right) \approx 0.945 < 0.1 \text{ dB} \quad (7.6A86)$$

The above function should be studied further for other locations along the zenith.

3.4.3 The Effect of Doppler on the Total Loop Phase Error

To evaluate the remaining conditional variances one must evaluate various tedious integrals listed above. We omit the details.

When $d(t)$ is characterized by a simple doppler offset (we shall treat the more complicated problem of doppler rate and acceleration later) and $F(p) = (1 + \tau_2 p)/(1 + \tau_1 p)$ then (Reference 25)

$$\sigma_d^2(A) = \frac{\tau_1 \tau_2 \Omega_0^2}{2mrAK} \left[1 + \frac{\pi^2 mAK}{3\tau_1 \Omega^2} \right]. \quad (7.6A87)$$

When $mAK/\tau_1 \Omega_0^2 \ll 1$ then

$$\sigma_d^2(A) \approx \frac{\Omega_0^2}{2r^2} \left[\frac{r+1}{2W_L} \right]^3 \quad (7.6A88)$$

and for $\sigma_x \ll 1$

$$E[\sigma_d^2(A)] \approx \frac{\Omega_0^2}{2r^2} \left[\frac{1+r}{2W_L} \right]^3 \approx \sigma_d^2(\bar{A}). \quad (7.6A89)$$

3.4.4 The Effect of Oscillator Instabilities on the Total Phase Error

Electing to model the oscillator instabilities as in Reference 25, then

$$S_{\Delta\psi}(\omega) = N_{ov} + \frac{2\pi N_{ov}}{|\omega|} \quad (7.6A90)$$

and

$$\sigma_{\Delta\psi}^2(A) = \left(\frac{r+1}{4r} \right) \frac{N_{ov}}{W_L} + G(r) \frac{N_{ov}}{W_L^2} \quad (7.6A91)$$

where $r^2 = 4\xi$ (ξ - loop damping) and $G(r)$ is defined in Reference 25, p. 1.51. For particular oscillators this effect can be evaluated.

3.4.5 The Effect of the Channel Phase Characteristics Due to Turbulence on the Total Phase Error

The next component in the phase-error budget is due to the channel phase fluctuation produced by turbulence. If one characterizes these fluctuations as RC filtered white noise, then the spectrum of $\{\phi(t)\}$ can be approximated by (Reference 11)

$$S_\phi(s) \approx \frac{2a\sigma_\phi^2}{a^2 - s^2} \quad (7.6A92)$$

where a is the 3-decibel radian frequency and σ_ϕ^2 is the variance of the fluctuations. Without going into the tedious details it can be shown that

$$\begin{aligned}\sigma_{\phi}^2(A) &= 2a\sigma_{\phi}^2 \left[\frac{d_1 c_2^2 + c_1^2 d_3}{2d_3(d_1 d_2 - d_0 d_3)} \right] \\ &\approx a\sigma_{\phi}^2 \left[\frac{d_1 c_2}{(d_1 d_2 - d_0 d_3)} \right]\end{aligned}\quad (7.6A93)$$

where

$$\begin{aligned}c_1 &= \frac{\mu}{\alpha_0 K}, \quad c_2 = \frac{\mu}{r_0} \left(\frac{r_0 + 1}{2W_{L0}} \right)^2 \\ d_0 &= a, \quad d_1 = \left[a \left(\frac{r_0 + 1}{2W_{L0}} \right) + \frac{\mu}{\alpha_0 K} \right] + 1 \\ d_2 &= \left[\frac{\alpha_0 \mu}{r_0} \left(\frac{r_0 + 1}{2W_{L0}} \right)^2 + \left(\frac{r_0 + 1}{2W_{L0}} \right) + \frac{\mu}{\alpha_0 K} \right] \\ d_3 &= \frac{\mu}{r_0} \left(\frac{r_0 + 1}{2W_{L0}} \right)^2.\end{aligned}$$

The factors μ , r_0 and W_{L0} are defined in Reference 25 from pages 153 to 156. Substitution of the above results into Equation (7.6A94) and simplifying, leads to

$$\begin{aligned}\sigma_{\phi}^2(A) &\approx \mu\sigma_{\phi}^2 \left(\frac{r_0 + 1}{r_0} \right) \left(\frac{a}{2W_{L0}} \right) \\ &= \mu\sigma_{\phi}^2 \left(\frac{r_0 + 1}{r_0} \right) \left(\frac{\pi f_{3dB}}{W_{L0}} \right)\end{aligned}\quad (7.6A94)$$

where f_{3dB} has been determined by Woo, Reference 3. When σ_x is small then

$$0 < E[\sigma_{\phi}^2(A)] \approx \sigma_{\phi}^2(\bar{A}) < \sigma_{\phi}^2. \quad (7.6A95)$$

3.4.6 The Effect of the Up-Link on the Ground Receiver's Total Phase Error

Turning now to the component of phase error due to up-link effects on the performance of the ground receiver $\sigma_I^2(A)$, one can easily show that

$$\begin{aligned}\sigma_I^2(A) &= 2\pi B_I \sigma_I^2 \left[\frac{d_1 c_2^2 + c_1^2 d_3}{d_3(d_1 d_2 - d_0 d_3)} \right] \\ &\approx \mu \sigma_I^2 \left(\frac{1 + r_0}{r_0} \right) \frac{\pi B_I}{W_{L0}}\end{aligned}\quad (7.6A96)$$

where B_I represents the 3dB frequency of the process $\{I(t)\}$. When $\sigma_x \ll 1$, then

$$\begin{aligned}\sigma_I^2 &= \int p(A) \sigma_I^2(A) dA \\ &\approx \sigma_I^2(\bar{A}).\end{aligned}\quad (7.6A97)$$

The exact effect on the loop phase error is bounded by

$$0 \leq E[\sigma_I^2(\bar{A})] \leq \sigma_I^2 \quad (7.6A98)$$

when σ_x is small.

3.4.7 The Effect of Planetary Backscatter on the Total Phase Error*

The variance due to planetary backscatter requires modeling the spectrum of the backscatter process $A_B(t) \sin[\phi_B(t) - \hat{\phi}_B(t)]$. For sake of argument, assume that the power spectrum of the multipath backscatter can be modeled as a narrowband process centered around $2\pi f_d$ where f_d represents the doppler shift present on the backscattered signal (see Figure 7.6A-8). If we characterize the backscatter spectrum as

$$S_B(\omega) \approx \frac{\sqrt{2}\pi\sigma_B^2}{2\beta} \left[\exp\left(-\frac{(\omega - \omega_d)^2}{2\beta^2}\right) + \exp\left(-\frac{(\omega + \omega_d)^2}{2\beta^2}\right) \right] \quad (7.6A99)$$

where σ_B^2 represents the variance of the backscatter as a function, 3 decibel radian frequency β , then, by assuming that the PLL operates as an ideal filter, (Figure 7.6A-8) of bandwidth $W_L = 2B_L$ Hertz, then

* The theory should apply to determining the effects which planetary multipath produces in the spacecraft and/or ground receivers.

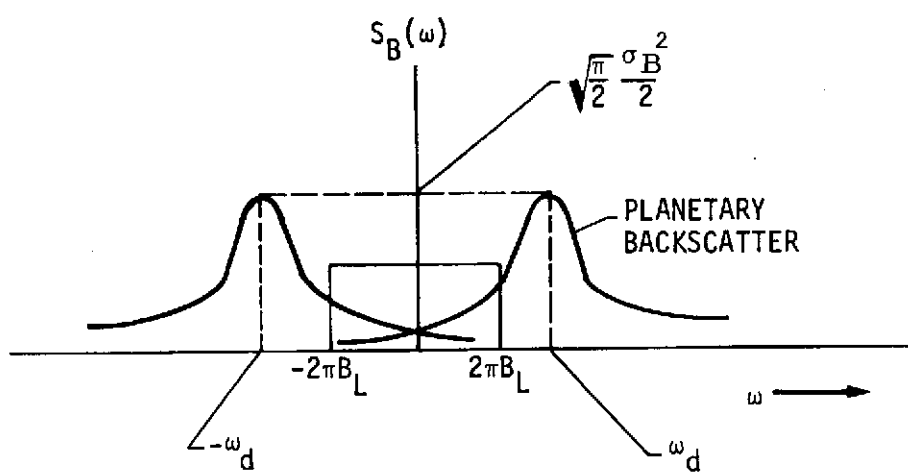


Figure 7.6A-8. Spectrum of Planetary Backscatter and Its Effects on the Transponder Loop

$$m^2 A^2 \sigma_B^2(A) = \frac{1}{2\pi} \int_{-2\pi B_L}^{2\pi B_L} S_B(\omega) d\omega. \quad (7.6A100)$$

Substitution leads to

$$m^2 A^2 \sigma_B^2(A) \approx \sigma_B^2 \left\{ \operatorname{Erfc}\left[\frac{2\pi B_L - \omega_d}{\beta}\right] + \operatorname{Erfc}\left[\frac{2\pi B_L + \omega_d}{\beta}\right] \right\} \quad (7.6A101)$$

where

$$\operatorname{Erf} x \triangleq \frac{1}{\sqrt{2\pi}} \int_0^x \exp(-z^2/2) dz \quad (7.6A102)$$

and

$$\operatorname{Erf} x = -\operatorname{Erf}(-x). \quad (7.6A103)$$

Now if $\omega_d \gg 2\pi B_L$ ($f_d \gg B_L$), then

$$\sigma_B^2(A) \approx 0. \quad (7.6A104)$$

On the other hand, if $f_d \ll B_L$, then

$$m^2 A^2 \sigma_B^2(A) \approx 2\sigma_B^2 \operatorname{Erf}\left[\frac{2\pi B_L}{\beta}\right]. \quad (7.6A105)$$

In addition, when $2\pi B_L \gg \beta$ and $f_d \ll B_L$, then

$$m^2 A^2 [\sigma_B^2(A)] \approx \sigma_B^2 \quad (7.6A106)$$

and when $2\pi B_L \ll \beta$ and $f_d \ll B_L$, then

$$\sigma_B^2(A) \approx 0. \quad (7.6A107)$$

Therefore, the backscatter effect on the loop phase error is bounded by

$$0 \leq E[\sigma_B^2(A)] \leq \sigma_B^2 / m^2 A^2. \quad (7.6A108)$$

The mean-squared value which the planetary backscatter produces outside the loop bandwidth (additional sideband noise) is given by

$$\sigma_0^2(A) = \frac{\sigma_B^2}{2} \left[\int_{\frac{2\pi B_L - \omega_d}{\beta}}^{\infty} \Phi(z) dz + \int_{\frac{2\pi B_L + \omega_d}{\beta}}^{\infty} \Phi(z) dz \right. \\ \left. + \int_{-\infty}^{-\frac{2\pi B_L - \omega_d}{\beta}} \Phi(z) dz + \int_{-\infty}^{\frac{2\pi B_L - \omega_d}{\beta}} \Phi(z) dz \right]$$

where

$$\Phi(z) \stackrel{\Delta}{=} \frac{1}{\sqrt{2\pi}} \exp(-z^2/2).$$

The parameters β and σ_B^2 can presumably be determined by considering the antenna pattern and the results due to Glenn, Staras, Roth and Rouland in an RCA report, January 1967. They present models of Venus surface roughness, and methodology of determining active scattering areas. Appendix 7.6G generates the appropriate parameters for assessing degradation in the total phase error in the tracking loop of probe and ground receivers.

3.4.8 Bound on the Variance of the Total Phase Error

From the above results we can conclude that (if σ_x is small)

$$\sigma^2 < E[\sigma_d^2(\bar{A})] + E[\sigma_{\Delta\psi}^2(\bar{A})] + \sigma_\phi^2 + \sigma_I^2 + \sigma_B^2 + \frac{1}{\rho} \quad (7.6A109)$$

where the loop signal-to-noise ratio is

$$\rho = \rho_0 \exp[2m_x + \sigma_x^2] = \rho_0 \exp[-\sigma_x^2] \text{ if } m_x = -\sigma_x^2 \quad (7.6A110)$$

and ρ_0 represents the loop signal-to-noise ratio when σ_x and σ_ϕ are zero, i.e., no turbulence.

3.4.9 Nonlinear Analysis of a Second-Order Loop in the Presence of Multipath and Turbulence

To produce an analysis which gives the conditional probability density function $p(\psi|A = A_0 e^X)$ we shall begin by assuming that $d(t) = \theta_0 + \Omega_0 t$ and neglect the planetary backscatter term. The assumption about $d(t)$ is of no trouble since we shall study it in its more general nature later; however, including the planetary backscatter term $A_B \sin \phi_B$ in any nonlinear analysis

creates formidable problems as we shall see. Without going into pages of details, it can be shown, under rather general assumptions (Reference 25, Chapter 11, 12) that the conditional probability density function $p(\phi|A)$ is given by

$$p(\phi|A = A_0 e^x) = C_0 \exp[-U_0(\phi)] \int_{\phi}^{\phi+2\pi} \exp[U_0(x)] dx \quad (7.6A111)$$

where we have assumed that the bandwidth of $\{x(t)\}$ is much smaller than the loop bandwidth with

$$\begin{aligned} U_0(\phi) &\stackrel{\Delta}{=} \frac{2}{K_{00}} [\Omega_0 - AKF_0 \sin \phi + E[y_1|\phi] \\ &+ E[\phi|\phi] + E[I|\phi] + E[\Delta\psi|\phi]] \end{aligned} \quad (7.6A112)$$

where K_{00} is defined in Reference 25, page 482, and y_1 is defined in Reference 25, page 481. The remaining terms are conditional expectations which must be approximated in order to produce the conditional probability density function $p(\phi|A)$. If one uses the conditional expectation method to approximate these then

$$U_0(\phi) = -\beta'(1) - \alpha'(1) \cos \phi \quad (7.6A113)$$

where

$$\beta'(1) = \beta(1) - \frac{2 \overline{\sin \phi}}{K_{00} \sigma_G^2} [\sigma_\phi R_{\phi\theta}(0) + \sigma_{\Delta\psi} R_{\Delta\psi G}(0) + \sigma_I R_{IG}(0)] \quad (7.6A114)$$

$$\alpha'(1) = \alpha(1) - \frac{2}{\sigma_G^2 K_{00}} [\sigma_\phi R_{\phi G}(0) + \sigma_{\Delta\psi} R_{\Delta\psi G}(0) + \sigma_I R_{IG}(0)] \quad (7.6A115)$$

and $\alpha(1)$ and $\beta(1)$ are defined on page 537 of Reference 16. Here $\sigma_G^2 = E[(\sin \phi - \overline{\sin \phi})^2]$ and $R_{xy}(0)$ represents the value of the cross-correlation function between the process $x(t)$ and $y(t)$ at zero shift. To carry the analysis further, one must evaluate these coefficients which represent detailed calculations. In order to effect a careful and rather accurate noisy reference loss study, the above details should be investigated further.

When the planetary backscatter is included in the nonlinear analysis then the restoring force in the loop becomes (from 7.6A62)

$$A \sin \varphi + A_B(t) \sin(\varphi + \Delta\Phi) = A \sin \varphi + A_B(t)$$

$$[\sin \varphi \cos \Delta\Phi + \cos \varphi \sin \Delta\Phi] \quad (7.6A116)$$

where $\Delta\Phi \stackrel{\Delta}{=} \Phi_B - \Phi$. If the processes are slowly varying then the probability density function $p(\varphi | A, A_B, \Delta\Phi)$ is given by (7.6A111) with $U_0(\varphi)$ characterized by

$$U_0(\varphi) = -\beta'(1) - \alpha'(1) \left[(A + A_B \cos \Delta\Phi) \cos \varphi + A_B \sin \Delta\Phi \sin \varphi \right] \quad (7.6A117)$$

The resulting $p(\varphi)$ can then be obtained, in theory, by averaging over the joint probability density function $p(A, A_B, \Delta\Phi)$. To access the degradation in tracking loop performance at low signal-to-noise ratios, the above analysis should be pursued further. We shall not proceed with this here; however, we turn to the problems one is faced with when a limiter is present.

4. TRACKING LOOP ANALYSIS WHEN A LIMITER PRECEDES THE LOOP: BACKSCATTER AND TURBULENCE PRESENT

We now turn to addressing the problem of developing the behavior of a PLL when it is preceded by a bandpass limiter (BPL). We assume the lognormal channel model discussed earlier and include at a later time the planetary backscatter effects. The input signal to the BPL can be modeled as

$$x(t) = \sqrt{2} A_0 \exp[x(t)] \sin[\omega_0 t + M(t) + \theta_r(t)] + n_i(t)$$

where

$$\theta_r(t) \stackrel{\Delta}{=} d(t) + \psi_1(t) + \phi(t) + I(t).$$

It is convenient to expand the noise about $\theta_r(t)$. It can be shown (Reference 2, Chapter 3) that

$$n_i(t) = \sqrt{2} N_c(t) \cos [\omega_0 t + \theta_r(t)] - N_s(t) \sin [\omega_0 t + \theta_r(t)],$$

where

$$N_c \stackrel{\Delta}{=} n_c \cos \theta_r + n_s \sin \theta_r$$

$$N_s \stackrel{\Delta}{=} n_s \cos \theta_r - n_s \sin \theta_r.$$

Thus

$$x(t) = \sqrt{2} \left\{ A_0 \exp[x(t)] \cos M - N_s \right\} \sin(\omega_0 t + \theta_r(t)) \\ + \sqrt{2} \left\{ A_0 \exp[x(t)] \sin M + N_c \right\} \cos(\omega_0 t + \theta_r(t)).$$

If we define

$$\gamma(t) \triangleq \tan^{-1} \left[\frac{\sqrt{2} A_0 \exp(x(t)) + \sqrt{2} N_c}{\sqrt{2} A_0 \exp(x(t)) - \sqrt{2} N_s} \right],$$

then the output of the first zone (limiter is characterized by (Reference 37)

$$z(t) = \frac{4}{\pi} \sin[\omega_0 t + \gamma(t) + \theta_r(t)].$$

Since the power in the first zonal output is $P_1 = 8/\pi^2$ and constant, we have

$$z = \sqrt{2P_1} \left[\cos \gamma \sin \phi_r + \sin \gamma \cos \phi_r \right]$$

where

$$\phi_r(t) = \omega_0 t + \theta_r(t),$$

with

$$\sin \gamma \triangleq \frac{\sqrt{2} A \sin M + \sqrt{2} N_c}{\sqrt{\dots}}$$

$$\cos \gamma \triangleq \frac{\sqrt{2} A \cos M - \sqrt{2} N_s}{\sqrt{\dots}}$$

$$\sqrt{\dots} \triangleq \sqrt{2} (A \sin M + N_c)^2 + 2 (A \cos M - N_s)^2$$

and $A = A_0 \exp(x)$. It is convenient to expand the output in terms of a signal component and a noise component. Thus, in the first zone of the limiter output we have, time suppressed,

$$z = \sqrt{2P_1} \left[\overline{\cos \gamma} \sin \phi_r + \overline{\sin \gamma} \cos \phi_r + N_A \sin \phi_r - N_B \cos \phi_r \right]$$

where

$$N_A \triangleq \frac{2\sqrt{2}}{\pi} (\sin \gamma - \overline{\sin \gamma})$$

$$N_B \triangleq \frac{2\sqrt{2}}{\pi} (\cos \gamma - \overline{\cos \gamma}).$$

It is easy to show (Reference 2) that

$$\overline{N_c N_{c\tau}} = \overline{N_s N_{s\tau}} = r(\tau) \approx \frac{N_0}{2} \delta(\tau)$$

$$\overline{N_c N_{s\tau}} = -\overline{N_s N_{s\tau}} \approx 0$$

so that the loop's phase detector output is given by

$$e = K_1 K_m \sqrt{P_1} \left\{ [\overline{\cos \gamma} \sin \varphi + \overline{\sin \gamma} \cos \varphi] + N_A \cos \varphi - N_B \sin \varphi \right\}$$

where

$$\varphi \triangleq d + \psi_1 + \phi + I - \hat{\theta}$$

so that the loop equation of operation can be rewritten as

$$\varphi = d + \phi + I + \psi_1 - \frac{K\sqrt{P_1}F(p)}{p} \left[\overline{\cos \gamma} \sin \varphi + \overline{\sin \gamma} \cos \varphi + N_e(t, \varphi) \right]$$

$$= \psi_2 - \frac{K_V e}{p}$$

where

$$N_e(t, \varphi) \triangleq N_A \cos \varphi - N_B \sin \varphi.$$

Now with a great deal of algebra one can show that

$$\sqrt{P_1} \overline{\cos \gamma} = \frac{4}{\pi} \sqrt{m^2 \alpha^2(x)}$$

and

$$\sqrt{P_1} \overline{\sin \gamma} = \frac{4}{\pi} \sqrt{(1 - m^2) \alpha^2(x)} M(t)$$

where the conditional limiter suppression factor is defined by

$$\alpha(x) \triangleq \sqrt{\frac{\pi}{2}} \sqrt{\rho_i \exp(2x)} \exp\left[-\frac{\rho_i \exp(2x)}{2}\right] \left\{ I_0(\rho_i \exp(2x)) + I_1(\rho_i \exp(2x)) \right\}$$

and $\rho_i = 2A_0^2 N_0 W_i$ represents the signal-to-noise at the output of the IF filter. Since the data modulated subcarrier is designed to lie outside the bandpass of the loop filter we can write the loop equation of operation as

$$\psi = d + \phi + I + \psi_1 - \frac{KF(p)}{p} \left[m\alpha(x) \sin \varphi + N_e(t, \varphi) \right] - \psi_2 - \frac{K_V e}{p}.$$

Comparing this equation with the one developed earlier, when no limiter was present, we see that A has been replaced by $\alpha(x)$ and $N(t, \varphi)$ by $N_e(t, \varphi)$. If one assumes that the loop is narrowband with the equivalent spectral density of $N_e(t, \varphi)$ at the origin, conditioned upon x , then one can approximate this by

$$N_{oe}(x) = \frac{N_0}{\Gamma_p(x)}$$

where (Reference 2)

$$\Gamma_p(x) \approx \frac{1 + \rho_i \exp(2x)}{\Gamma_H^{-1} + \rho_i \exp(2x)}$$

where $\{x(t)\}$ is the amplitude process and Γ_H is defined in Reference 25, page 197 (usually taken to be around 0.9). Using the above formulas and material in Chapter 4 of Reference 25, the formulas developed in Section 3 can easily be generalized to the case where a limiter is present. We omit the details here.

If we now include the multipath effects due to planetary backscatter, things become a bit more difficult to carry out owing to the fact that the center frequency is not $\omega_0 + d\theta_r/dt$; however, a worst-case analysis can be carried out by assuming that the planetary backscatter process can be expanded as

$$A_B(t) \sin \Phi_B(t) = \sqrt{2} n_{Bc}(t) \cos \omega_0 t - \sqrt{2} n_{Br}(t) \sin \omega_0 t$$

in which case, with time suppressed,

$$n_i = \sqrt{2} (n_c + n_{Bc}) \cos \omega_0 t - \sqrt{2} (n_s + n_{Bs}) \sin \omega_0 t.$$

Without going into the tedious details, the conditional limiter suppression factor reduces to

$$\alpha(x) = \sqrt{\frac{\pi}{2}} \sqrt{Q(x)} \exp \left[-\frac{Q(x)}{2} \right] \left\{ I_0 \left(\frac{Q(x)}{2} \right) + I_1 \left(\frac{Q(x)}{2} \right) \right\}$$

where

$$Q(x) \triangleq \frac{A^2}{\sigma_n^2 + \sigma_B^2} = \frac{A_0^2 \exp(2x)}{\sigma_n^2 + \sigma_B^2}$$

and $\sigma_n^2 = N_0 W_i / 2$, W_i - if filter bandwidth, σ_B^2 is the variance of the planetary backscatter. If we define $\rho_i \triangleq 2A_0^2 / N_0 W_i$ then

$$Q(x) = \frac{\exp(2x)}{\left[1/\rho_i + \sigma_B^2/A_0^2 \right]}$$

assesses the effect on the limiter suppression factor due to multipath and turbulence.

If we now average over $Q(x)$ we find that

$$E[Q(x)] = \frac{\rho_i \exp[2m_x + \sigma_x^2]}{1 + \rho_i/\rho_m}$$

where $\rho_m \triangleq A_0^2 / \sigma_B^2$ represent the SNR the signal-to-noise ratio due to backscatter. If $m_x = -\sigma_x^2$ then

$$E[Q(x)] = \frac{\rho_i \exp(-\sigma_x^2)}{1 + \rho_i/\rho_m}$$

represent the average signal-to-noise ratio affecting the limiter suppression factor.

When $\sigma_x \ll 1$ then one can approximate

$$p(\varphi) = \int p(\varphi|A)p(A)dA$$

$$\approx p(\varphi|\bar{A})$$

so that, to a good approximation, all the above limiter formulas hold when $Q(x)$ is replaced by $E(Q(x))$ and A is replaced by $m_A = E(A)$.

4.1 Static Phase Error Build Up Due to the Doppler Profile

For a second-order loop preceded by a BPL, the transfer function for slowly varying amplitude variations is given in Reference 25, page 156. When the gain of the loop is not assumed to be infinite, then

$$1 - H_\varphi(s) = \frac{\left(\frac{\mu}{\alpha_{10}K}\right)s + \frac{\mu}{r_0} \left(\frac{r_0 + 1}{2W_{L0}}\right)^2 s^2}{1 + \left(\frac{r_0 + 1}{2W_{L0}} + \frac{\mu}{\alpha_0 K}\right)s + \frac{\mu}{r_0} \left(\frac{r_0 + 1}{2W_{L0}}\right)^2 s^2}$$

so that the steady-state phase error becomes

$$\varphi_{SS}(t) = \frac{\mu}{\alpha_{10}K} \dot{d}(t) + \frac{\mu}{r_0} \left(\frac{r_0 + 1}{2W_{L0}}\right)^2 \ddot{d}(t)$$

where

$$\mu = \frac{\alpha_{10}}{\alpha_1}$$

is the limiter suppression factor and $\alpha_{10}K$ represents the loop gain at the loop design point. Let $\dot{d}(t) = 2\pi f(t)$ where $f(t)$ is the instantaneous frequency of doppler then

$$\varphi_{SS}(t) = \mu \left[\frac{2\pi f(t)}{\alpha_{10}K} + \frac{2\pi}{r_0} \left(\frac{r_0 + 1}{2W_{L0}}\right)^2 \dot{f}(t) \right].$$

By appropriately choosing the VCO center frequency "during any time interval of interest" then

$$\varphi_{SS}(t) \approx \frac{2\pi\mu}{r_0} \left(\frac{r_0 + 1}{2W_{L0}}\right)^2 \dot{f}(t).$$

For a 10 Hertz loop which has 0.707 damping then

$$\varphi_{SS}(t) \approx 0.0707\mu f(t).$$

And at threshold $\mu = 1$, so that

$$\varphi_{SS}(t) \approx 4.05 f(t) \text{ (degrees)}.$$

From the doppler profile it appears that an average value for $f(t) = 40$ Hertz per second near blackout. Therefore at threshold and entry, $\varphi_{SS}(t) \approx 160$ degrees which is much too large (should be less than 30 degrees at high signal-to-noise ratio) to track with a second-order loop. At entry minus 60 minutes $\varphi_{SS}(t) \approx 12$ degrees and with a loop signal-to-noise of 10 decibels then $\varphi_{SS} \approx 3$ to 5 degrees. It is easy to compute φ_{SS} at any position along the predicted trajectory and with the passage of time further conclusions can be drawn. Later we shall consider the problem of two-way static phase error build-up; see Section 5.

If one desires to study the effects of tuning the VCO with the passage of time, then one replaces $d(t)$ by

$$d(t) = 2\pi f(t) + K_v e(t)$$

where $e(t)$ represents the tuning voltage; see Equation (7.6A49) and Equation (7.6A50).

4.2 Doppler Variance in the Transponder Loop and Suppression on the Downlink Carrier Due to Uplink Effects

In a two-way mode of operation there are four random signal components circulating in the transponder loop which serves to suppress and spread the downlink carrier. For the present, we do not evaluate the resulting correlation function and spectra of the transmitted signal as the results given in Section 2 can be applied directly. The signals which serve to suppress the downlink carrier include: uplink turbulence, uplink thermal noise, planetary backscatter and, if any, oscillator instabilities which are negligible owing to the spectral purity of the transmitted carrier.

The mathematics of the situation can be described using Equation (7.6A62) and assuming that $\sin \varphi \approx \varphi$. Thus the equation of operation which governs the VCO phase modulation is ($e = 0$)

$$\hat{\theta}(A) = H_\phi(p|A) \left[d + \psi_1 + \phi + \frac{A_B \sin \phi_B + N(t, \phi)}{m^2 A^2} \right].$$

So that the mean-squared value of $\hat{\theta}$ due to disturbances other than $d(t)$ itself is

$$\sigma_{\hat{\theta}}^2(A) = \sigma_{\psi_1}^2(A) + \sigma_{\phi}^2(A) + \sigma_B^2(A) + \sigma_\varphi^2(A)$$

where

$$\sigma_{\psi_1}^2(A) = \frac{1}{2\pi i} \int_{-i\infty}^{i\infty} |H_\phi(s|A)|^2 S_{\psi_1}(s) ds$$

$$\sigma_{\phi_d}^2(A) = \frac{1}{2\pi i} \int_{-i\infty}^{i\infty} |H_\phi(s|A)|^2 S_\phi(s) ds$$

and the last two terms are determined by Equations (7.6A80) and (7.6A102). Generally, $\sigma_{\psi_1}^2(A) \approx 0$ is a two-way mode so that one need only determine the first and third terms. In fact, using Equation (7.6A92) in the above produces

$$\sigma_{\phi_d}^2(A) = 2a\sigma_\phi^2 \left[\frac{c_1^2 d_0 - d_2}{2d_0(d_1 d_2 - d_0 d_3)} \right]$$

where

$$c_1 = \frac{r_0 + 1}{2W_{L0}}$$

and d_0 , d_1 , d_2 and d_3 are defined in (7.6A93).

If G represents the static phase gain of the receiver then the carrier suppression on the downlink is given by

$$\tilde{S} = \int p(A) \tilde{S}(A) dA \approx \tilde{S}(\bar{A})$$

if $\sigma_x \ll 1$. Here

$$\begin{aligned}\hat{S}(\bar{A}) &\approx \exp \left[-G^2 \frac{\sigma_x^2(\bar{A})}{\theta} \right] \\ &\approx \exp \left[-G^2 \frac{\sigma_{\psi_1}^2(\bar{A})}{\theta} \right]. \\ &= \exp \left[-G^2 \frac{\sigma_{\phi}^2(\bar{A})}{\theta} \right] \exp \left[-G^2 \frac{\sigma_B^2(\bar{A})}{\theta} \right]. \\ &= \exp \left[-G^2 \frac{\sigma_{\varphi}^2(\bar{A})}{\theta} \right]\end{aligned}$$

Finally, we note that the variance on the doppler measurement is given by

$$\sigma_{\hat{\theta}}^2 \approx \int p(A) \sigma_x^2(A) dA \approx \sigma_x^2(\bar{A})$$

if $\sigma_x \ll 1$.

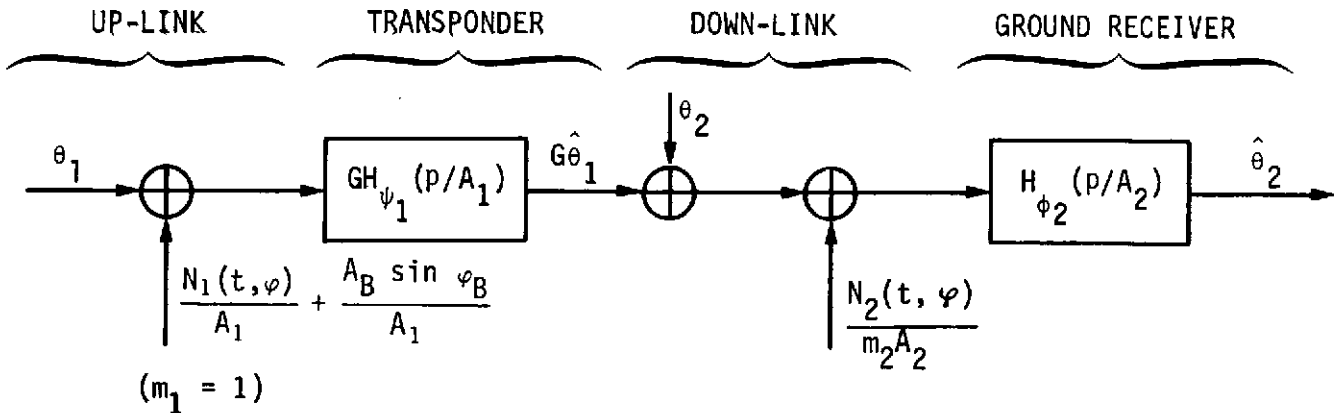
5. PERFORMANCE OF TWO-WAY LINKS IN THE PRESENCE OF MULTIPATH AND TURBULENCE

In what follows, we specify the theory required to obtain the steady-state response of a two-way link. We merely specify the equation of operation and leave the details for later evaluation. Subscripts "one" have to do with uplink variables while subscript "two" implies a downlink variable.

Figure 7.6A-9 depicts a two-way system model, all the disturbances, and basic equations needed for analysis. Previous sections have given the theory for one-way operation; consequently, in what follows we specify the variance of the phase and doppler error. The steady-state phase error, due to "deterministic quantities" can be found from

$$\varphi_{SS}(t) = \lim_{p \rightarrow 0} p \hat{\varphi}_2(p) \quad (7.6A118)$$

Using the basic equations given in Figure 7.6A-9 we have



$$\theta_1 = d_1 + \psi_1 + \phi_1$$

$$\theta_2 = d_2 + \psi_2 + \phi_2$$

$$\hat{\theta}_1 = H_{\psi_1}(p|A_1) \left[\theta_1 + \frac{N_1(t, \varphi)}{A_1} + \frac{A_B \sin \varphi_B}{A_1} \right]$$

$$\hat{\theta}_2 = H_{\phi_2}(p|A_2) \left[G\hat{\theta}_1 + \theta_2 + \frac{N_2(t, \varphi)}{A_2} \right]$$

$$\varphi_1 = \left[1 - H_{\psi_1}(p|A_1) \right] \theta_1 + H_{\psi_1}(p|A_2) \left[\frac{N_1(t, \varphi)}{A_1} + \frac{A_B \sin \varphi_B}{A_1} \right]$$

$$\varphi_2 = \left[1 - H_{\phi_2}(p|A_2) \right] \left[\theta_2 + G\hat{\theta}_1 \right] + H_{\phi_2}(p|A_2) \left[\frac{N_2(t, \varphi)}{m_2 A_2} \right]$$

Figure 7.6A-9. Two-Way Link Model and Basic Equations

$$\begin{aligned}
\varphi_{SS}(t) &= \frac{\mu_2 \dot{d}_2}{\alpha_{20} K_2} + \frac{\mu_2}{r_{20}} \left(\frac{r_{20} + 1}{2W_{10}} \right)^2 \ddot{d}_2 \\
&+ G \left[\frac{\mu_2 \dot{d}_2}{\alpha_{20} K_2} \dot{d}_1 + \frac{\mu_2}{r_{20}} \left(\frac{r_{20} + 1}{2W_{10}} \right)^2 \ddot{d}_1 \right] \\
&+ G \left(\frac{r_{10} + 1}{2W_{10}} \right) \left[\frac{\mu_2 \dot{d}_1}{\alpha_{20} K_2} + \frac{\mu_2}{r_{20}} \left(\frac{r_{20} + 1}{2W_{20}} \right)^2 \ddot{d}_1 \right]
\end{aligned} \tag{7.6A119}$$

as the steady-state error due to the uplink doppler phase function $d_1(t)$ and downlink doppler phase function $d_2(t)$.

Letting $\dot{d}_1(t) = 2\pi f(t) \approx \dot{d}_2(t)$, then

$$\begin{aligned}
\varphi_{ss}(t) &= \frac{(1 + G) 2\pi \mu_2 f(t)}{\alpha_{20} K_2} + \frac{2\pi \mu_2}{r_{20}} \left(\frac{r_{20} + 1}{2W_{10}} \right)^2 \dot{f}(t) \\
&+ \frac{2\pi \mu_2 G}{r_{20}} \left(\frac{r_{20} + 1}{2W_{20}} \right)^2 \dot{f}(t) \\
&+ G \left(\frac{r_{10} + 1}{2W_{10}} \right) \left[\frac{2\pi \mu_2 f(t)}{\alpha_{20} K_2} + \frac{2\pi \mu_2}{r_{20}} \left(\frac{r_{20} + 1}{2W_{20}} \right)^2 f(t) \right].
\end{aligned} \tag{7.6A120}$$

The conditional variance of the two-way phase error is given by

$$\begin{aligned}
\sigma_{\varphi_2}^2(A) &= \frac{1}{2\pi i} \left[\int_{-i\infty}^{i\infty} \left\{ \left| 1 - H_{\varphi_2}(s|A_2) \right|^2 \left[S_{\theta_2}(s) + G^2 S_{\hat{\theta}_1}(s) \right] ds \right. \right. \\
&\quad \left. \left. + \frac{H_{\varphi_2}(p|A_2) S_{N_2}(s)}{m_2^2 A_2^2} ds \right\} \right]
\end{aligned} \tag{7.6A121}$$

while the variance of the two-way doppler measurement is found from

$$\sigma_{\hat{\theta}_2}^2(A) = \frac{1}{2\pi i} \int_{-i\infty}^{i\infty} |H_{\varphi_2}(s|A_2)|^2 \left[G^2 S_{\hat{\theta}_1}(s) + S_{\theta_2}(s) \frac{S_{N_2}(s)}{m_2^2 A_2^2} \right] ds \quad (7.6A122)$$

with $d_1 = d_2 = 0$.

By using the basic equations given in Figure 7.6A9 we find that

$$S_{\theta_2}(s) = S_{d_2}(s) + S_{\psi_2}(s) + S_{\phi_2}(s)$$

$$S_{\hat{\theta}_1}(s) = |H_{\varphi_1}(p|A_1)|^2 \left[S_{\theta_1}(s) + \frac{S_{N_1}(s)}{A_1^2} + \frac{S_B(s)}{A_1^2} \right] \quad (7.6A123)$$

and

$$S_{\theta_1}(s) = S_{d_1}(s) + S_{\psi_1}(s) + S_{\phi_1}(s). \quad (7.6A124)$$

These respective equations can be substituted into $\sigma_{\hat{\theta}_2}^2(A)$ and $\sigma_{\hat{\theta}_2}^2(A)$ to produce conditional variances so that

$$\sigma_{\varphi_2}^2 = \int p(A) \sigma_{\varphi_2}^2(A) dA \quad (7.6A125)$$

$$\sigma_{\hat{\theta}_2}^2 = \int p(A) \sigma_{\hat{\theta}_2}(A) dA$$

to produce the average values of the mean-squared value of the two-way phase and doppler error. The evaluation is straightforward, but tedious.

If $\sigma_x^2 \ll 1$ then

$$\sigma_{\varphi_2}^2 \approx \sigma_{\varphi_2}^2(\bar{A})$$

$$\sigma_{\hat{\theta}_2}^2 \approx \sigma_{\hat{\theta}_2}^2(\bar{A}) \quad (7.6A126)$$

where μ_k represents a_{k0}/a_k and w_{10} and w_{20} represent the design point loop bandwidth of the transponder and ground receiver respectively.

If one desires to drive the ground VCO with a predict, then $d_2(t)$ should be replaced by

$$d_2(t) = 2\pi f_2(t) + K_V e(t)$$

and the effects can be studied from the resulting theory.

6. CONCLUSIONS

This appendix has dealt with problems peculiar to communication systems designed to transmit information through the Venus atmosphere from a space-craft (probe). Since the atmosphere produces lognormal carriers, and large doppler coefficients are present, a number of new problems have arisen which hinder the engineer from directly applying (with confidence) the usual equations and rules-of-thumb in the design.

The first problem concerns channel characterization. This problem deals with specifying the relationship between the communication parameters and the physical parameters of the propagation medium. Therefore, the first part of the appendix deals with identifying the relationship between the communication and propagation parameters arising in the channel. There has been a considerable amount of theoretical work carried out by propagation physicists on the effects of refractive index fluctuations (time and spatial) upon monochromatic signals. Also, there has been a considerable amount of theoretical work by communication engineers on the effects of randomly time-varying channels on the error probabilities of digital communication systems. On the other hand, there has been virtually no work on the effects which randomly time-varying channels have upon the performance of coherent tracking and synchronization systems. Regarding error probabilities, considerable effort has been expended on predicting system performance when the channel model is considered Rician. Virtually no work has been reported which can be used to specify the performance of coherent systems where lognormal carriers are present. This appendix has given preliminary results.

In the study of communications through the Venus atmosphere reported here, two channel models have been considered, viz., the Rician channel, and the lognormal channel. On the basis of this investigation, it appears that the lognormal channel represents a more accurate characterization of the fading characteristics, i.e., if $s(t)$ is transmitted, then exclusive of

additive noise, the lognormal carrier $s(t) \exp[x(t) + i\phi(t)]$ is received. Here both $[x(t)]$ and $[\phi(t)]$ are correlated gaussian processes. Thus, an immediate question arises concerning how the Rice theory does not, in general, directly apply. The primary reason is that a lognormally distributed random variable can be used to approximate a noncentral chi-squared random variable. A noncentral chi-squared random variable, on the other hand, represents the sum of the squares of several Rice-distributed random variables.

Accomplishing coherent communications over the lognormal channel implies that the transmitted signal amplitude is multiplied by $\exp[x(t)]$ while it also undergoes a random phase-shift of $\exp(i\phi(t))$. In order to assess the degradations in performance, it has been necessary to model and characterize the behavior of coherent tracking systems in the presence of lognormal carriers. This appendix has summarized and presented these mathematical models and investigated, to within the time constraints, the deleterious effects produced upon tracking performance. Although the work cannot be considered as complete, it has been shown for the slow lognormal fading expected on the probes and for uncorrelated amplitude and phase components, that the random phase-characteristic can be tracked by the loop. Further, the random phase characteristic will affect the ability to measure doppler accurately and the theory to assess the degradation is given. It has been difficult to assess, exactly, the effects of the amplitude process on tracking performance; however, for small amplitude fluctuations, the degradation in loop signal-to-noise has been characterized and shown to be less than 0.2 decibel. The effects of correlation between the amplitude and phase process were not fully investigated. It appears that the correlation effects manifest themselves by producing an unsymmetric carrier spectrum for the loop to track. This effect is a curious one and should receive further study in order to assess the degradations (if any) and effects on tracking performance as well as the performance of the data detector. Moreover, it is probably safe to conclude that the theory developed to determine the effective loop signal-to-noise ratio does not serve to tell the complete story.

The theory required to assess the effects of planetary backscatter on the ground receiver and transponder performance is given. Further detailed

work needs to be done, using the theory given here, in order to accurately determine its effects; however, a preliminary investigation reveals that they are small.

While this appendix has presented the theory for determining the degradations which the lognormal amplitude has on the error probability, we have not been able to produce a complete set of design curves for determining the effects which lognormal carriers have on the performance of systems which employ convolutional codes. This is an important problem area which needs further study owing to the impact the results will have on the specification of accurate design control tables. Computer simulations offer one method for obtaining these results.

Finally, a linear theory is given which can be used to determine the static phase-error build-up in both one-way and two-way systems where lognormal carriers and high doppler shifts are present. This includes the effects of tuning the VCO with and without predicts. Furthermore, a linear theory has been presented which can be used to specify the variance of the doppler and phase-error in one-way and two-way systems where lognormal carriers are present. Some further numerical work is recommended in this area.

7. ADDENDUM

A Correction of the Errors in deWolf's Fading Rate Analysis

This addendum points out a major error in deWolf's (References 2, 3, 38) analysis using an expression for the fading rate of a Rician envelope. Although the use of the Rician distribution for amplitude fading has been shown to be erroneous, the error in the fading rate does not appear to have been noticed. This can be important since deWolf uses the results from his analysis to predict different results for the fading for Venera 4, 5, and 6 and Mariner-5. In particular, his results indicate that the fading is more severe than indicated by other investigators. Also, it appears that his criticism of the Mariner-5 data is also based in part on his erroneous results. Since some recent assessments of models for relating experimental data to theory still suggest deWolf's method, it appears necessary to present the proper fading rate expressions for both the Rician and lognormal signal amplitudes. The most recent report suggesting deWolf's erroneous

analysis is the SEL report by Croft et al. (Reference 13).

DeWolf (References 2, 3, 38) has made estimates concerning the expected signal fading rate in the atmosphere of Venus due to turbulence. Based on measurements from the Venera 4, 5, 6 and Mariner-5 probes, he tends to conclude that the signal fading rate can be more severe than that measured or predicted by other investigations. deWolf's analyses have all been based on his model of the Rice probability density for the signal amplitude $A(t)$. This is contrasted with the lognormal amplitude distribution obtained from the Rytov approximation which is known to be valid for weak fading. However, deWolf's proof of the validity of Rice distribution (Reference 39) is now known to be incorrect (References 4, 40). For example, on page 388 of Tatarskii's second book (Reference 4), we have the following footnote:

"... A particular case of equation (22) was derived by Shishov/190/ by means of selective summation of Feynman diagrams. deWolf/188, 189/ also tried to derive an expression for Γ_4 , but his results for Γ_4 are definitely erroneous. (In particular, the conclusion regarding the Rayleigh distribution of the intensity fluctuations stems from the unjustified omission of the connected diagrams describing the fourth cumulants of the field u -- see /196/.)"

Also, as pointed out in a discussion of this subject by Lawrence and Strohbehn (Reference 6), deWolf originally predicted the Rice distribution when $\sigma_x^2 > 0.64$; however, he now tends to favor the lognormal in this region (Reference 7). Although the Rice model was used by deWolf to analyze the data from four of the Venus probe missions, the results of these assumptions still appear in the latest assessments of the signal fading expected from atmospheric turbulence on Venus for Pioneer-Venus, the latest being the SEL report by Croft et al. (Reference 13). It should be noted, however, that the range of values for σ_x^2 as determined by Woo (Reference 15) are much less than 0.64. In fact, they appear to be in the weak fluctuation region where the Rytov approximation is valid and the first-order fading distribution is lognormal.

deWolf's investigations (References 2, 3, 38) were directed towards estimating the possibility of atmospheric turbulence on Venus and its effect on microwave signal fading. deWolf seeks an estimate of the dielectric strength which is the variance of the dielectric permittivity* and in his notation was given by $\epsilon^2 \equiv \langle(\delta\epsilon)^2\rangle$. The approach used was to consider the propagation parameter defined by $\sigma_\epsilon^2 = k^2\epsilon^2 L_i L$. (The notation is unfortunate, since σ_ϵ^2 is carelessly used in the SEL report (Reference 13) to represent the propagation parameter as done by deWolf and also to represent the variance of the dielectric permittivity.) The term σ_ϵ is approximately equal to the measured quantity σ_A , defined as the depth of fading. The depth of fading is defined by deWolf by

$$\sigma_A^2 = \frac{\langle A(t)^2 \rangle - \langle A(t) \rangle^2}{\langle A(t) \rangle^2},$$

and in terms of a commonly-measured intensity value $I(t) = A^2(t)$, by

$$\sigma_I^2 \equiv \frac{\langle I^2(t) \rangle - \langle I(t) \rangle^2}{\langle I(t) \rangle^2}.$$

Based on the Rician theory, deWolf (References 2, 3, 38, 39) relates this value to σ_ϵ^2 by

$$\sigma_I^2 = 1 - e^{-4\sigma_\epsilon^2}$$

such that

$$\sigma_A^2 \approx \sigma_I^2 / 2 = \frac{1}{4} \left[1 - e^{-4\sigma_\epsilon^2} \right] \approx \sigma_\epsilon^2,$$

* Unfortunately, deWolf's notation causes some confusion when compared with some more standard work as indicated, for example, in the survey by Strohbehn (Reference 10). It appears that deWolf's δ_ϵ corresponds to the term $\epsilon_1(r,t)$ in Strohbehn's expression on page 1302. $\epsilon(r,t) = \epsilon_0 + \epsilon_1(r,t)$, $\epsilon_0 = \langle \epsilon(X,t) \rangle$. In Strohbehn's notation, we have $C_\epsilon(0) = \langle \epsilon_1(r,t)^2 \rangle_0 = \langle (\delta\epsilon)^2 \rangle$ which corresponds to deWolf's term ϵ^2 . Also, deWolf's expression $\epsilon^2 = 4\langle(\delta n)^2\rangle$ on page 7 of Reference 38 appears to follow from Strohbehn's definition on page 1306 and page 1316, that $\epsilon(r,t) = n(r,t) = (1 + \delta n(r,t))^2 \approx 1 + 2\delta n(r,t)$ with the result that $C_\epsilon(0) = 4\langle(\delta n)^2\rangle$.

or $\sigma_A \approx \sigma_\varepsilon$ for small σ_ε . The other terms in σ_ε^2 are determined by $k = 2\pi/\lambda$, the propagation distance L and by the integral scale L_i ; that is strongly related to the macroscale scale of the turbulence L_o . deWolf's objective is to relate the measured value of σ_A and the fading rate f_A (rate of fading of $A(t)$ below its mean value $\langle A(t) \rangle$) through his Rician theory to determine the macro-scale L_o . This value can be used in turn to determine ε^2 . This value of ε^2 then determines the dielectric strength of the turbulence on Venus. From this value, extrapolations to different frequencies and geometries can be made to predict signal fading conditions.

Unfortunately, the first equation used in deWolf's analysis for f_A is incorrect. In fact, by using the correct expressions for Rician and the log-normal statistics for $A(t)$ derived below, it appears that his analysis must be completely redone. Making certain simplifying approximations for weak fading does not permit justification of his expression for f_A nor the acceptance of his results.

The basic error committed by deWolf was to use Wheelon's formula (2.16) (Reference 41) for level crossing that only applies for gaussian processes. Unfortunately, Wheelon did not give a reference for this formula and did not point out that it applied only for the case of gaussian processes. Since deWolf's model is based on a Rice distribution for $A(t)$ or a noncentral chi-squared distribution with two degrees of freedom for $I(T) = A^2(t)$, his use of Wheelon's formula for the level crossing of $A(t)$ below its mean value is incorrect and the analysis based upon its use is incorrect. After discussing deWolf's and Wheelon's specific formulas we will derive the correct formulas for the Rician and lognormal cases for $A(t)$ and $I(t)$.

deWolf's definition of f_A given by equation (5) in Reference 2 is as follows: "The envelope fading rate f_A is given by the average number of crossings per unit time of $A(t)$ over the mean value $\langle A \rangle$. A well-known expression for f_A [Wheelon, 1967] is

$$\begin{aligned} f_A &= \frac{1}{2\pi} [\langle (dI/dt)^2 \rangle / \langle I^2 \rangle]^{\frac{1}{2}} \\ &= \lim_{\tau \rightarrow 0} \frac{1}{2\pi\tau} \left[2 - 2\langle I(t)I(t + \tau) \rangle / \langle I^2 \rangle \right]^{\frac{1}{2}} \end{aligned} \quad (5)''$$

(See footnotes* and ** concerning this quote.)

Wheelon's equation (2.16) is accompanied by the following statement:
 "To represent the average number of times that the signal crosses its mean value with positive slope per unit time, we adopt the standard definition:

$$N_\alpha = \frac{1}{2\pi} \left[\frac{\langle \dot{\alpha}(t)^2 \rangle}{\langle \alpha(t)^2 \rangle} \right]^{\frac{1}{2}}$$

$$= \frac{1}{2\pi} \left[\frac{\int_0^\infty \gamma^2 W_\alpha(\gamma) d\gamma}{\int_0^\infty W_\alpha(\gamma) d\gamma} \right]^{\frac{1}{2}}$$

or

$$N_\alpha = \frac{\sqrt{2} u}{4\pi} \frac{\int_0^\infty k^3 S(k) dk}{\int_0^\infty k S(k) dk} \quad (2.16)''$$

* It should be noted that the fading rate should be defined as the average number of down crossings of the mean value per second and not by the average number of times it crosses this value since this counts both up and down crossings. However, as used by Wheelon, the corresponding formula is correct except of course that it applies only for a gaussian process.

** We note that the fading rate f_A is expressed in terms of the properties of $I(t)$. We also note that on page 8 of reference 38 f_A is replaced by f_I and on page 27 f_A is used. In the analysis that we will give the crossing rate for $I(t)$ for a level L_L can be expressed in terms of the crossing rate of $A(t)$ by A_L . This allows an easy way to relate to two crossing rates and avoids re-computing joint probability densities for $I(t)$ and $I(t)$. That is $\bar{N}_A(L) = \bar{N}_I(L^2)$.

However, formula (2.16) is the classic result due to Rice (Reference 42) and applies only when $\alpha(t)$ is a gaussian process. Although Wheelon did not state explicitly that the process $\alpha(t)$ was gaussian it is obvious that $\alpha(t)$ has a zero mean. This can be seen as follows, from page 684 and 685 of Wheelon's paper: ---"Models for the turbulence, which decomposes the atmosphere's dielectric constant $\epsilon(r,t)$ into its mean value and a small stochastic fluctuation."

$$\epsilon(r,t) = \epsilon_0 + \Delta\epsilon(r,t) \quad (1.1)$$

--- "The anomalous phase is thus shown to be the line integral of $\Delta\epsilon$ along the (rectilinear) ray path

$$\alpha(t) = \frac{\pi}{\lambda} \int_0^L \Delta\epsilon(x,t) dx. \quad (2.1)''$$

It follows that, since the expected value of $\Delta\epsilon(x,t)$ is zero,

$$\langle \alpha(t) \rangle = \frac{\pi}{\lambda} \int_0^L \langle \Delta\epsilon(x,t) \rangle dx = 0.$$

In general Wheelon's formula (2.16) corresponds to the expected number of up (or down) crossings per second of the level L by the stationary gaussian process $\alpha(t)$ with mean value $\langle \alpha(t) \rangle = \bar{\alpha}$

$$N_\alpha(L) = \frac{1}{2\pi} \sqrt{\frac{\langle \dot{\alpha}(t)^2 \rangle}{\langle \alpha(t)^2 \rangle}} e^{-\frac{(L - \bar{\alpha})^2}{2\langle \alpha(t)^2 \rangle}}$$

When $L = \bar{\alpha}$ we obtain (2.16).

For deWolf's case of a Rician distribution for the envelope $A(t)$, we can obtain the correct expression for f_A directly from Rice's equation (4.8) given on page 125 of reference 42. First we define the received "sine wave plus noise" by

$$v(t) = Q \sin \omega_0 t + n(t)$$

where the narrow band noise process is expressed as

$$n(t) = x(t) \cos \omega_0 t + y(t) \sin \omega_0 t$$

and assuming a symmetric spectrum of $n(t)$ about f_0 we have*

$$E[n^2(t)] = E[x^2(t)] = E(y^2(t)) = \sigma^2.$$

Expressing $v(t)$ in terms of envelope and phase, we have

$$v(t) = A(t) \sin [\omega_0 t + \theta(t)]$$

where

$$A(t) = \sqrt{(Q + y(t))^2 + x^2(t)}$$

and

$$\theta(t) \equiv \tan^{-1} \left(\frac{x(t)}{Q + y(t)} \right).$$

Rice's expression for the average numbers of times per second that $A(t)$ down crosses the level $A(t) = L$ is given by:

$$\begin{aligned} \bar{N}_L(A) &= \sqrt{-\frac{R_x''(0)}{2\pi}} p_A(L) \\ &= \sqrt{-\frac{R_x''(0)}{2\pi R_x(0)}} \frac{L}{\sigma} I_0\left(\frac{LQ}{\sigma^2}\right) e^{-\frac{L^2 + Q^2}{2\sigma^2}} \\ &= \sqrt{-\frac{R_x''(0)}{2\pi R_x(0)}} \sigma p_A(L) \end{aligned}$$

where $p_A(L)$ is the Rician density function of A at $A = L$

* We have previously used the notation $\langle \cdot \rangle$ to denote expectation in order to conform with the quoted results of deWolf and Wheelon. Now we use the more commonly-used expression $E(\cdot)$.

$$p_A(L) = \frac{L}{\sigma^2} I_0\left(\frac{LQ}{\sigma^2}\right) e^{-\frac{L^2+Q^2}{2\sigma^2}}$$

Also we have the following definitions for the quadrature noise terms $X(t)$ and its derivative $X'(t)$ in terms of its correlation function $R_X(t)$ as

$$R_X(0) = E[X^2(t)] = \sigma^2$$

$$R_X''(0) = E[X'(t)]^2$$

For deWolf's case where $L - E[A(t)] = \bar{A}$ we have

$$\bar{A} = e^{-\gamma^2/2} \sqrt{\frac{\pi \sigma^2}{2}} [1 + \gamma^2 I_0(\gamma^2/2) + \gamma^2 I_1(\gamma^2/2)]$$

where the specular-to-random power ratio is defined by

$$\gamma^2 = \frac{Q^2}{2\sigma^2}.$$

It is seen that the expression for $\bar{N}_A(\bar{A})$ is a complicated expression and in no way resembles deWolf's equation (5) (where $f_A \leftrightarrow \bar{N}_A(\bar{A})$).

It is also noted that for the case of the fading rate of $I(t)$ below \bar{I} , f_I , which corresponds to $\bar{N}_I(\bar{I})$, it can be shown that

$$\bar{N}_I(C) = \bar{N}_A(\sqrt{C})$$

so that

$$\bar{N}_I(\bar{I}) = \bar{N}_A(\sqrt{\bar{I}})$$

where

$$\bar{I} = Q^2 + 2\sigma^2.$$

Therefore $\bar{N}_I(\bar{I})$ can be obtained from $\bar{N}_A(L)$ by setting $L = \sqrt{\bar{I}}$.

This expression is easily written down but is cumbersome and provides no insight to the problem in question. We also note that for measurements available on $I(t)$ we should set the threshold of fading level of $I(t)$ at $(\bar{A})^2$ since

$$\bar{N}_A(\bar{A}) = \bar{N}_I((\bar{A})^2).$$

It is of interest to investigate the Rician case for large values of γ . From Appendix 7.6A, values of γ^2 considered were 3.11 and 14. For the case when γ^2 is large, Rice uses the approximation (page 125)

$$A(t) \stackrel{\sim}{=} Q + x(t).$$

The corresponding expression for $\bar{N}_A(L)$ is given by his equation (4.12) as

$$\bar{N}_A(L) \stackrel{\sim}{=} \frac{1}{2\pi} \sqrt{-\frac{R''_x(0)}{R'_x(0)}} e^{-\frac{(L-Q)^2}{2\sigma^2}}.$$

Since

$$L = E[A(t)] = \bar{A} = Q$$

we have for this case

$$\bar{N}_A(\bar{A}) = \frac{1}{2\pi} \sqrt{-\frac{R''_x(0)}{R'_x(0)}}.$$

It is of interest to relate this expression to the second moments of $A(t)$ and $A'(t)$ as in deWolf's expression. For these moments we have

$$E[A(t)]^2 = Q^2 + R_x(0)$$

$$E[A'(t)]^2 = E(X'(t))^2 = -R''_x(0).$$

From deWolf's equation (5) we have in the present notation

$$\bar{N}_A(\bar{A}) = \frac{1}{2\pi} \sqrt{\frac{E[A'(t)]^2}{E[A(t)]^2}} \quad (\text{deWolf})$$

which become upon substitution of the above second moments

$$\bar{N}_A(\bar{A}) = \frac{1}{2\pi} \sqrt{\frac{-R''_x(0)}{Q^2 + R_x(0)}}. \quad [\text{deWolf}]$$

We notice that this last expression differs from the correct expression

$$\bar{N}_A(\bar{A}) = \frac{1}{2\pi} \sqrt{\frac{-R''_x(0)}{R_x(0)}} \quad (\text{correct expression})$$

by the addition term Q^2 in the denominator. However, since we are assuming $Q^2 \gg R_x(0)$, deWolf's expression cannot be directly salvaged for this $\gamma^2 \gg 1$ case.

Actual measurements indicate that the variance of the log amplitude is small. The lognormal amplitude distribution of $A(t)$ appears to be valid. For this case we derive an expression for f_A . For convenience we define

$$\ell(t) \equiv \frac{A(t)}{A_0} = e^{x(t)}$$

Following the usual procedure we define $X(t) = \ln(A(t)/A_0)$ where A_0 is the received amplitude without fading. The process $X(t)$ is gaussian with mean M_x and variance σ_x^2 and $\ell(t)$ is a lognormal envelope process. It is convenient to consider the fading rate of $\ell(t)$, the normalized version of $A(t)$, below the level L .

The general expression for $\bar{N}_\ell(L)$ is given by definition

$$\bar{N}_\ell(L) = \int_0^\infty \ell p(L, \ell) d\ell,$$

and it can be shown that

$$\bar{N}_\ell(1) = \frac{1}{\sqrt{2\pi}} e^{-\frac{1}{2} \left[\frac{\ln L - M_x}{\sigma_x} \right]^2} \sqrt{\frac{-R''_x(0)}{2\pi R'_x(0)}}$$

where the correlation function of $X(t)$ is defined by

$$R_x(\tau) = E(x(t)x(t + \tau)) - M_x^2.$$

Defining the correlation functions of $A(t)/\bar{A}$ by $R_{A/\bar{A}}(\tau)$ it can be shown that

$$R_{A/\bar{A}}(\tau) \equiv E \left[\left(\frac{A(t) - \bar{A}}{\bar{A}} \right) \left(\frac{A(t + \tau) - \bar{A}}{\bar{A}} \right) \right] = e^{R_x(\tau)} - 1$$

where $R_{A/\bar{A}}(0)$ corresponds to n^2 , where n is the usual definition of "depth of fading."

This allows us to obtain the expression for $R_x''(0)$ and $R_x'(0)$ in terms that can be obtained from measurements, namely $\eta^2 = R_{A/\bar{A}}(0)$, and $R_{A/\bar{A}}'(0)$. These expressions are

$$\ln [R_{A/\bar{A}}(0) + 1] = \ln [\eta^2 + 1] = R_x'(0)$$

and

$$R_{A/\bar{A}}'(0) = R_x''(0) e^{R_x'(0)}.$$

For $L = \bar{\ell}$ we have

$$\bar{\ell} = e^{m_x + \frac{1}{2}\sigma_x^2}$$

Using these results we obtain

$$\begin{aligned} \bar{N}_\ell(\ell) &= \frac{1}{2\pi} e^{-\frac{5}{8}\sigma_x^2} \sqrt{\frac{-R_{A/\bar{A}}'(0)}{\ln[R_{A/\bar{A}}(0) + 1]}} \\ &= \frac{1}{2\pi} \frac{\sqrt{R_{A/\bar{A}}'(0)}}{(\eta^2 + 1)^{5/8} \sqrt{\ln(\eta^2 + 1)}}. \end{aligned}$$

Thus the expression for the fading rate of $A(t)$ (normalized by A_0) over its mean value \bar{A} has been obtained for the more meaningful lognormal distribution of the envelope. In order to use deWolf's analysis and its conclusions, it appears that much additional work must be done. This could be important in any assessment of measured data from Venera 4, 5, 6, 7, 8 and Mariner-5.

REFERENCES

1. D. A. deWolf, "Saturation of Irradiance Fluctuations due to Turbulent Atmosphere," Town. Opt. Soc. Amer. 58 pp. 461-466, (1968).
2. D. A. deWolf, "Evidence for Severe Microwave Signal Fading in the Atmosphere of Venus due to Turbulence," J. of Geophys. Research, Vol. 76, No. 7, pp. 1202-1208, (March 1970).
3. D. A. deWolf, "Atmospheric Turbulence on Venus: Venera 4, 5, 6 and Mariner 5 Estimates," J. of Geophys. Research, Vol. 76, No. 13, pp. 3154-3158, (May 1971).
4. V. I. Tatarskii, "The Effects of the Turbulent Atmosphere on Wave Propagation," Naka, Moscow, (1967). Translated and available from the U.S. Dept. of Commerce, Springfield, Va., TT-68-50464.
5. M. A. Kolosov, O. I. Yakovlev, and A. I. Yefimov, "Study of the Propagation of Decimeter Radiowaves in the Atmosphere of Venus with the Aid of AIS Venera-4," Dokl., Adad. Nauk SSR, Geofiz., Vol. 132, No. 1, pp. 93-94, (1968).
6. R. W. Lawrence and J. W. Strohbehn, "A Survey of Clear-Air Propagation Effects Relevant to Optical Communications," Proc. of the IEEE, Vol. 58, No. 10, pp. 1523-1545, (October 1970).
7. D. A. deWolf, "Are Strong Irradiance Fluctuations Lognormal or Rayleigh Distributed?", J. Opt. Soc. Amer. Vol 59, pp. 1455-1460, (1969).
8. V. I. Tatarskii, Wave Propagation in a Turbulent Medium, (McGraw-Hill, New York, 1961).
9. R. S. Kennedy, S. Karp, editors, Optical Space Communications, NASA SP-217, (August 1968).
10. J. W. Strohbehn, "Line-of-Sight Wave Propagation Through the Turbulent Atmosphere," Proc. of the IEEE, Vol. 56, No. 8, pp. 1301-1318, (August 1968).
11. A. Ishimaru "Temporal Frequency Spectra of Multifrequency Waves in Turbulent Atmosphere," IEEE Trans. Antennas & Propagation, Vol 20, No. 1 pp. 10-19, (January 1972).
12. R. Woo and A. Ishimaru, "Remote Sensing of the Turbulence Characteristics of a Planetary Atmosphere by Radio Occultation of a Space Probe," Radio Science, Vol. 8, January 1973.
13. A. C. Croft, et al., "Preliminary Reivews and Analysis of Effects of the Atmosphere of Venus on Radio Telemetry and Tracking of Entry Probes," Final Report SEL Project 3239, Standard Electronics Labs, (October 1972).

14. O. I. Yakovlev, A. I. Efimov, and T. S. Timofeeva, "Venera-7 Space-probe Data on Propagation of Radio Waves Through the Venusian Atmosphere and Through the Interplanetary Plasma, Kosm. Issle., Vol. 9, No. 5, pp. 748-753, (September-October 1971).
15. R. Woo, "Pioneer Venus Propagation Study," to be published in JPL Final Report, (June 1973).
16. J. A. C. Brown, J. Aitchison, "The Lognormal Distribution," Department of Applied Economics, University of Cambridge, England, Mono. 5 (1957).
17. H. B. Jones, et al., "Comparison of Simultaneous Line-of-Sight Signals at 9.6 and 34.5 GHz," IEEE Transactions of Antennas and Propagation, Vol. AP-18, No. 4, (July, 1970).
18. C. Clarke, "Atmospheric Radio Noise-Studies Based on Amplitude-Probability Measurements at Slough, England, During the International Geophysical Year," Proc. IEEE (London), 109, pt. B, pp. 393-404, (September 1962).
19. K. Davies, "Ionospheric Radio Progation," National Bureau of Standards, Mono. 80, (November 1965).
20. L. F. Fenton, "The Sum of Lognormal Probability Distributions in Scatter Transmission Systems," IRE Trans. Communication Systems, Vol. CS-8, pp. 57-67, (March 1960).
21. K. Furutsu and T. Ishida, "On the Theory of Amplitude Distribution of Impulsive Random Noise," J. Appl. Phys., Vol 32, (July 1961).
22. T. Nakai, "The Study of the Amplitude Probability Distributiuons of Atmospheric Radio Noise," Proc. Res. Inst. Atmos. (Japan), Vol. 7, pp. 12-17, (January 1960).
23. A. D. Watt and E. L. Maxwell, "Measured Statistical Characteristics of VLF Atmospheric Radio Noise," Proc. IRE, Vol. 45, pp. 55-62, (January 1957).
24. H. Yuhara, T. Ishida, and M. Higashimura, "Measurement of the Amplitude Probability Distribution of Atmospheric Noise," J. Radio Res. Labs. (Japan), Vol. 3, pp 101-108, (February 1958).
25. W. C. Lindsey, Synchronization Systems in Communication and Control, (Prentice-Hall, Englewood Cliffs, New Jersey, 1972).
26. M. Ohta, T. Korzrimi, "Intensity Fluctuations of Stationary Random Noise Containing an Arbitrary Signal Wave," Proceeding of IEEE, Vol. 57, pp. 1231-1232, (June, 1969).
27. S. Karp, John R. Clark, "Approximations for Lognormally Fading Optical Signals," Proceedings of the IEEE, Vol. 58, No. 12, pp. 1964-1965, (December, 1970).

28. K. S. Miller, R. M. Jones, "On the Multivariate Lognormal Distribution," Journal of Industrial Mathematics Society, Vol. 16, Part 2, (1966).
29. E. Brookner, "Propagation and Channel Model for Laser Wavelengths," IEEE Trans. on Comm. Tech., Vol. COM-18, No. 14, pp. 396-416, (August 1970).
30. G. K. Huth, C. R. Cahn; C. R. Moore, "Simulation of Sequential Decoding With Phase-Locked Demodulation," IEEE Trans. on Comm. Tech., Vol. COM-21, No. 2, (February, 1973).
31. W. C. Lindsey, I. F. Blake, "Effects of Phase-Locked Loop Dynamics on Phase-Coherent Communications," JPL Space Program Summary 37-54, Vol. III, pp. 192-195, (December 31, 1968).
32. W. C. Lindsey, "Performance of Phase-Coherent Receivers Preceded by Bandpass Limiters," IEEE Trans. on Comm. Techn., Vol. COM-16, No. 2, pp. 245-251, (April, 1968).
33. H. M. Merrill, G. D. Thompson, "Designing Communication Systems Using Short Constraint Convolutional Codes," NTC, Houston, Texas, (1972).
34. J. A. Heller, I. M. Jacobs, "Viterbi Decoding for Satellite and Space Communications," IEEE Trans. Comm. Tech., Vol. COM-19, pp. 835-848, (October, 1971).
35. W. C. Lindsey, "Block Coding for Space Communications Systems," IEEE Trans. Comm. Tech., Vol. COM-17, pp. 217-225, (April, 1969).
36. W. C. Lindsey, "Design of Block-Coded Communications Systems," IEEE Trans. Comm. Tech., Vol. COM-15, pp. 525-534, (August, 1967).
37. J. C. Springett, M. K. Simon, "An Analysis of the Phase Coherent-Incoherent Output of the Bandpass Limiter," IEEE Transactions on Communication Technology, Vol. COM-19, No. 1, (1971).
38. D. A. deWolf, J. W. Davenport, "Investigation of Line-of-Sight Propagation in Dense Atmospheres," Final Report, March 1969-May 1970, NASA CR-73440 RCA Labs, Princeton, N. J.
39. D. A. deWolf, "Saturation of Irradiance Fluctuations Due to Turbulent Atmosphere," J. Opt. Soc. Amer. Vol 58, pp. 461-466 (1968).
40. Yu. N. Barabznenkov, et al., "Status of the Theory of Propagation of Waves in a Randomly Inhomogeneous Medium," Usp. Fix. Nank, Vol. 102, pp. 3-42, (September 1970). Translated in Soviet Physics Uspekhi, Vol. 13, No. 5, pp. 551-680, March-April 1971.
41. A. D. Wheelon, "Relation of Radio Measurements to the Spectrum of Tropospheric Dielectric Fluctuations," J. Appl. Phys., 28, p 684, (1967).
42. Steven O. Rice, "Statistical Properties of a Sine-Wave Plus Random Noise," Bell Syst. Tech. Jour., 27, pp. 109-157, (January 1948).

APPENDIX 7.6B

DISCUSSION ON COMMUNICATIONS CHANNEL MODELS

APPENDIX 7.6B

DISCUSSION ON COMMUNICATIONS CHANNEL MODELS

1. SUMMARY

As pointed out in Appendix 7.6A, two of the basic parameters that characterize the lognormal fading characteristics are the variance σ_x^2 of the exponent in the channel amplitude characteristic $A = A_0 e^x$ and the variance of the channel phase characteristic σ_ϕ^2 . Expected values of these parameters for the Venus probe communication links are summarized in Table 7.6B-1. Methods of using these parameters to compute other interface parameters needed for communications system design and analysis are given. The power spectral density of the channel phase and amplitude characteristics are discussed in Woo (Reference 1) and are not repeated here. Certain conclusions relative to the 3 dB bandwidth of these amplitude processes are summarized as a function of altitude.

Table 7.6B-1. γ^2 and 3 dB Frequency for x at
the Subearth Point Based on Venera
4 Data - Log Amplitude and Phase
Fluctuations Data (Reference 1)

L - (km)	γ^2	$f_{3dB, x}$ (Hz)	σ_x	σ_ϕ (rad)
55	16.9	0.43	0.2378	0.472
30	54.6	0.59	0.136	0.367
10	399.0	1.02	0.05	0.22
5	1426.0	1.45	0.026	0.16
1	250,000	3.23	0.006	0.071

2. FADING CHANNEL CHARACTERISTICS

The possibility of signal fading on Venus probe communication links is a major consideration in the system design. We investigated the physical phenomena of fading and some of the more recent work in the area to predict Venus probe communication system performance.

Fading occurs when the propagating electromagnetic wave is partially scattered due to variations in the constituents of the medium through which it is traveling (Reference 2, p. 361). The variations of the atmospheric constituents is random in space and time in the general case so that the wave also acquires random fluctuations in amplitude and phase. One way to model such a wave is to idealize the signal as consisting of two components, one component with nonrandom amplitude-phase characteristics and the other component with random amplitude-phase characteristics. In the absence of fading, the transmitted signal is received entirely in the nonrandom or specular component. When a random component is present, its amplitude and phase or frequency characteristics must be used to optimally design the communication system.

Considering first the amplitude fluctuations, let

$$E_o(\bar{r}) = A_o(F)e^{j\theta_o(\bar{r})}$$

be an unperturbed planewave at $F = r(s, y, z, t)$, and

$$E(\bar{r}) = A(\bar{r})e^{j\theta(F)}$$

be the wave at \bar{r} when the atmospheric perturbations are included.

Inducing the conservation of total power, the total power in $E(\bar{r})$ is the power in the specular component A_s^2 , plus the variance in the random component, σ_R^2 , which approximately equals A_o^2 , i.e.,

$$\overline{A^2} = A_s^2 + \sigma_R^2 \approx A_o^2$$

An often used parameter (Reference 3) is

$$x \triangleq \ln \frac{A}{A_0} \approx \frac{A}{A_0} - 1$$

for small fluctuations which is usually the case of interest. Then,

$$\sigma_x^2 = \frac{\sigma_A^2}{A_0^2}$$

and

$$A_s^2 = A_0^2 (1 - \sigma_x^2)$$

from above if we use

$$\sigma_R^2 \approx \sigma_A^2$$

For Rician fading, see Appendix 7.6A, communication system performance is a function of the ratio of the power in the specular component to the power in the random component, i.e.,

$$\gamma^2 \triangleq \frac{A_s^2}{\sigma_A^2} = \frac{1 - \sigma_x^2}{\sigma_x^2}$$

Once σ_x^2 is known, γ^2 can be computed and when the probability distribution of the received signal is established, the average performance for a given communication system can be computed. The phase behavior must also be properly accounted for with σ_R^2 actually the variance in the received signal when both phase and amplitude are accounted for.

Before going into the statistical distribution of the received signal, let us consider the evaluation of σ_x^2 . The cause of the randomness in the wave is due to random variations in the constituents of the medium, i.e., the index of refraction, n , or the dielectric permittivity, ϵ . These are functions of the atmospheric elements and temperature and humidity, which in turn are affected by winds. Since x is a random

field, the variance of x , σ_x^2 , must be taken with respect to three dimensional space and time in general. The variations due to time change are quite negligible, however, and can usually be ignored. In terms of the index of refraction, n , the Maxwell equation which is required to be satisfied by the \bar{E} field becomes (Reference 3, p. 93),

$$\Delta \bar{E} + k^2 n^2(\bar{r}) \bar{E} = 0$$

for short waves. With turbulence present n will fluctuate rapidly with respect to small space and time dimensions causing corresponding fluctuations in the received E field. The structure constant, C_n , is a factor in the structure function of n , $D_n(\tau)$. $D_n(\tau)$ enters into the autocovariance of n , $B_n(\tau)$, in cases when n is nonstationary. The function $D_n(\tau)$ is defined on a small interval over which n is stationary.

To establish a value of σ_x^2 , either of two parameters can be used, i.e., the variance of n , σ_n^2 , or the structure constant of the medium, C_n . In a random environment this equation is a stochastic differential equation and its solution, \bar{E} , depends on the random field, n . There are a number of equations which can be used to relate σ_x^2 to σ_n^2 or C_n depending upon the wavelength, λ , and assumptions concerning scale factors related to the characterization of the turbulent medium. The basic relations are the following (Reference 3, Chapter 7).

$$\sigma_x^2 = \sigma_\phi^2 = \sigma_n^2 k^2 L L_n$$

where:

$k = 2\omega/\lambda$, the wavenumber

L = propagation distance of the wave through the turbulent medium

L_n = integral scale of turbulence which is the normalized integral of the correlation of n .

This equation is based on the assumptions:

- a) $\lambda L \gg L_o$, L_o = outer scale of turbulence
- b) $\lambda \ll l_o$ = inner scale of turbulence
- c) n is a statistically homogeneous and isotropic random field.

$$\sigma_x^2 = 0.31 C_n^2 k^{7/6} L^{11/6}$$

Assumptions:

- a) $\lambda L \gg l_o$
- b) $\lambda \ll l_o$
- c) n is locally homogeneous with correlation (structure function),

$$D_n(r) = \begin{cases} C_n^2 r^{2/3}, & l_o \ll r \ll L_o \\ C_n l_o^{2/3} \left(\frac{r}{l_o}\right)^2, & r \ll l_o \end{cases}$$

$$\sigma_x^2 = L^3 \quad \text{when} \quad \lambda L \ll l_o$$

$$\sigma_x^2 = L^a \quad l_o \ll \lambda L \ll L_o$$

where a is determined by the form of $D_n(r)$.

It should be noted here that the variance of n , σ_n^2 is sometimes replaced by the variance of the dielectric constant, ϵ , since $\epsilon = n^2$. For small variations in n ,

$$n \approx 1 + \Delta n$$

$$\epsilon \approx 1 + 2 n + \dots$$

$$\sigma_\epsilon^2 \approx 4\sigma_n^2$$

The equation is then written as:

$$\sigma_x^2 = \sigma_\epsilon^2 k^2 L L_n$$

The distribution of the received signal amplitude is required in order to obtain the system performance. There are two statistical distributions that are presently considered in describing the received signal. The amplitude A can be considered to follow a Rician distribution or A/A_0 can be considered to follow a lognormal distribution (i.e., $\ln A/A_0$ is normally distributed). The derivation of either distribution involves invoking the central limit theorem over a large number of independent contributors to the resultant signal. In the case of the Rician distribution the contributors to the randomness affect the signal in an additive manner. In the case of the lognormal distribution, the contributors to the randomness affect the signal in an independent, multiplicative manner so that when the logarithm is taken the effects become additive. Therefore, for the situation in which the signal passes through a thin scattering medium and then travels a great distance before reaching the receiver, the Rician distribution would be appropriate. In the case when the scattering can be considered to occur as the wave passes through sheets of turbulent medium such that each sheet affects the wave independently and multiplicatively, the lognormal distribution would perhaps be more accurate. In the case when the random fluctuations are small there is little difference in either distribution for A since $X = \ln A/A_0 \approx A/A_0 - 1$, which implies that A becomes normal and the Rician distribution is also approximately normal. This is the case when most of the received power is in the specular component.

Experimental evidence tends to substantiate using the lognormal distribution in that the measured normalized variance, $(A - \bar{A})^2/\bar{A}^2$ has exceeded the upper bound of .27 for the Rayleigh variance (Reference 4). In modeling a Rician channel, DeWolf has used (Reference 5, p. 41).

$$E(R) = E_0(R) \left[e^{-\sigma_x^2} + \delta B \right]$$

where $E(R)$ is the wave perturbed by turbulence and δB is a Rayleigh component with:

$$\langle |\delta B|^2 \rangle = A_0^2 \left(1 - e^{-2\sigma_x^2} \right)$$

The power in the specular component is then $A_o^2 \exp(-2\sigma_x^2)$ and

$$\gamma^2 = \frac{\exp(-2\sigma_x^2)}{1 - \exp(-2\sigma_x^2)} \approx \frac{1 - 2\sigma_x^2}{2\sigma_x^2}$$

for σ_x^2 small. This disagrees with the above expression for γ^2 by the 2 factor. However, the more recent work (some by DeWolf) has led most researchers including DeWolf to favor the lognormal distribution in which case

$$\gamma^2 \approx \frac{1 - \sigma_x^2}{\sigma_x^2}$$

We need to be able to compute the fraction of the total received power which is in the specular component in order to compute the system performance. We will show that the approximate expression

$$\gamma^2 = \frac{1 - \sigma_x^2}{\sigma_x^2}$$

is correct when the lognormal distribution is used assuming $\bar{x} = 0$. We need to compute the variance of A , σ_A^2 , as a function of the given parameter σ_x^2 . Let

$$y \Delta A/A_o$$

then:

$$x = \ln y$$

$$y = e^x$$

and

$$E(y) = E(e^x) = M_x(1) = \exp\left[1/2(\sigma_x^2)\right] \quad \text{or}$$

$$E(A) = A_o \exp(1/2\sigma_x^2)$$

where $M_x(t)$ is the moment generating function of the normal variable x (Reference 6, p. 220),

$$M_x(t) = E(e^{xt}) = \exp(m_x t + \frac{1}{2} \sigma_x^2 t^2) = \exp(\frac{1}{2} \sigma_x^2 t^2)$$

$$\text{Var}(y) = E(y^2) - E^2(y) = M_x(2) - M_x^2(1)$$

$$= \exp(2\sigma_x^2) - \exp(\sigma_x^2)$$

Thus:

$$\sigma_A^2 = A_o^2 \left[\exp(2\sigma_x^2) - \exp(\sigma_x^2) \right]$$

and

$$\sigma_A^2 \approx A_o^2 \left[1 + 2\sigma_x^2 - 1 - \sigma_x^2 \right] = A_o^2 \sigma_x^2$$

for σ_x^2 small. Another approach (Reference 4) has been to use $\bar{A}^2 \approx A_o^2$ rather than $\bar{x} = 0$. Then

$$E\left[\left(\frac{A}{A_o}\right)^2\right] = E(e^{2x}) = M(2) = e(2m_x + 2\sigma_x^2)$$

or

$$m_x = -\sigma_x^2$$

Then,

$$E(A) = A_o M(1) = A_o e^{-\frac{1}{2} \sigma_x^2}$$

$$\sigma_A^2 = \bar{A}^2 - \bar{A}^2 = A_o^2 - A_o^2 e^{-\sigma_x^2} = A_o^2 \left(1 - e^{-\sigma_x^2} \right) \approx A_o^2 \sigma_x^2$$

for σ_x^2 small.

$$\gamma^2 = \frac{e^{-\sigma_x^2}}{1 - e^{-\sigma_x^2}} \approx \frac{1 - \sigma_x^2}{\sigma_x^2}$$

Either approach yields the same value when $\sigma_x^2 \approx 0$. The γ^2 with respect to amplitude variations becomes

$$\gamma^2 = \frac{A_s^2}{\sigma_A^2} = \frac{1 + \exp(\sigma_x^2) - \exp(2\sigma_x^2)}{\exp(2\sigma_x^2) - \exp(\sigma_x^2)} \approx \frac{1 - \sigma_x^2}{\sigma_x^2}$$

for σ_x^2 small.

Up to this point the depth of the amplitude fluctuation has been the primary concern. In communication system design the random behavior of the phase as well as the spectrums of the amplitude and phase are important. An exact computation of the amount of power in the random component must account for phase fluctuations as well as amplitude fluctuations (i.e., σ_A^2). It is important to recognize that in the deviations for γ^2 given above only the amplitude fluctuations were included. The effects of the phase fluctuation is given in Appendix 7.6A. The behavior of the phase is also important in that it will affect the performance of a carrier tracking loop used to provide a reference phase for data demodulation. The variance of the phase, σ_ϕ^2 , can be computed using methods similar to those outlined above for σ_x^2 (Reference 3).

The spectrums of x and ϕ are also important. A measured quantity which provides a gross estimation of the typical frequencies (i.e., power spectral content) of A^2 or $x = \ln A/A_0$ is f_I , the number of crossings of A^2 over \bar{A}^2 per unit time. The power spectrums for ϕ and x can be computed from the temporal autocorrelations $R_{\phi, x}(\tau)$ by taking transforms. This has been done for S-band frequencies based on the Venera 4 data.¹ The 3 dB points of the x process are given in Table 7.6B-1.

The fading bandwidth of the amplitude is important in determining the fading effects on the carrier tracking phase lock loop. For the case when the bandwidth of x is small relative to the loop bandwidth, the effect on the loop performance is negligible (Reference 7) if the fading depth is not great. Otherwise, the fading signal will affect the performance of the carrier tracking loop and the data channel and must be accounted for.

In a coherent system the effect of the random phase fluctuations will essentially be that of causing a noisy carrier reference loss (radio loss) in cases when the tracking loop does not track the random phase fluctuations accurately. If the bandwidth of the random phase fluctuations is much greater than the loop bandwidth, the loop will be unable to track the phase. If in addition, the data rate or data bandwidth is much greater than the fading bandwidth the slow fading case will prevail.

This is the situation resulting in the most serious degradation.

REFERENCES

1. R. Woo, "Pioneer Venus Propagation Study," to be published in JPL Final Report, Contract NAS7-100-RD-65, JPL.
2. M. Schwartz, Information Transmission, Modulation and Noise, McGraw-Hill Book Company, New York, 1970.
3. V. I. Tatarski, Wave Propagation in a Turbulent Medium, Dover Publications, Inc., New York, 1961.
4. E. Brookner, "Atmosphere Propagation and Communication Channel Model for Laser Wavelengths," IEEE Tran. Comm. Technology, Vol. 18, No. 4, August 1970.
5. D. A. DeWolf, J. W. Davenport, "Investigation of Line-of-Sight Propagation in Dense Atmosphere: Phase II," Final Report, RCA Laboratories, Princeton, New Jersey, July 1971.
6. E. Parzen, Modern Probability Theory and Its Applications, John Wiley and Sons, Inc., New York 1960.
7. Results published in JPL Interim Report, Contract NAS7-100-RD-65, December 1, 1972, Enclosure I.

APPENDIX 7.6C

**UNCODED ERROR PROBABILITY PERFORMANCE
COMPARISONS FOR LOGNORMAL
AND RICIAN CHANNEL MODELS**

APPENDIX 7.6C

UNCODED ERROR PROBABILITY PERFORMANCE COMPARISONS FOR LOGNORMAL AND RICIAN CHANNEL MODELS

1. SUMMARY

This appendix summarizes the effects of atmospheric turbulence (fading) on the uncoded data performance of a perfectly synchronized phase coherent receiver. Two types of fading are considered, viz., fading characterized by (1) the Rician probability density function (p. d. f.), and (2) the lognormal p. d. f. For the perfectly synchronized receiver two parameters serve to characterize the effects of atmospheric turbulence on the error probability. For example, if the turbulence is characterized by the Rician p. d. f. then the parameter of concern is γ^2 , the ratio of the power in the specular component to the power in the random component (see Appendix 7.6A). For lognormal fading two parameters serve to characterize the fading due to turbulence; namely, the mean m_x and the variance σ_x^2 of the p. d. f.

In the following section results are presented which show that communication receiver performance is very dependent on proper consideration of the effects of atmospheric turbulence and that the loss factors with such turbulence may not be neglected in a system which must operate with a small margin. For an uncoded perfectly synchronized PSK system, it will be shown that atmospheric turbulence can cause losses of the order of 1 to 2 dB for BER's of 10^{-3} when lognormal fading is assumed and the parameters from Table 7.6B-1 of Appendix 7.6B are used.

2. ERROR PROBABILITY FOR LOGNORMAL FADING (PERFECT PHASE SYNCHRONIZATION ASSUMED)

When the fading bandwidth is small in comparison to the reciprocal of the data rate then the bit error probability of a PSK demodulator has

been shown (see Appendix 7.6A) to be given by

$$P_E = \frac{1}{2\sqrt{\pi}} \int_{-\infty}^{\infty} e^{-z^2} \operatorname{erfc} \left[\sqrt{R} \exp(\sqrt{2}\sigma_x z + m_x) \right] dz$$

where

$$R = \frac{A^2 T_b}{N_o}; \quad A = A_o e^x$$

$$= \frac{A_o^2 T_b}{N_o} e^{2x}$$

In order to evaluate the above expression numerically, one needs to provide a rational for determining m_x . By assuming that the variations in the index of refraction are small and possess a zero mean, Tartarski (Reference 1, p. 97) shows that $m_x = 0$. With $m_x = 0$,

$$m_A = E[A] = A_o \exp(\sigma_x^2)$$

On the other hand, under a conservation of power argument, Fried (Reference 2) has shown that

$$m_A = E[A] = A_o \exp(-\sigma_x^2)$$

Figure 7.6B-1 represents a plot of the BER versus $\frac{E_b}{N_o} = A_o^2 T/N_o$ for typical values of σ_x taken from Table 7.6B-1 of Appendix 7.6B. The values of σ_x are based upon a view along the zenith.

With $m_x = -\sigma_x^2$ it can be observed from Figure 7.6C-1 that the degradation in the uncoded PSK system is 0.7 dB at a zenith angle for $\sigma_x = .1189$ and a bit error probability of 10^{-3} . Using $m_x = 0$ the corresponding degradation is 0.45 dB. This is the value for σ_x calculated by Woo and given in Table 7.6B-1 of Appendix 7.6B on the Venus surface at the subearth point based upon the Venera 7 data. At a descending angle of 50 degrees, Croft (Reference 3) et al, have computed σ_x to be about 0.18. This results in degradations of 1.2 dB with $m_x = 0$ and 1.5 dB with $m_x = -\sigma_x^2$ for the uncoded PSK system. It is not clear on the basis of observation or analysis whether $m_x = 0$ or $m_x = -\sigma_x^2$ should be used to provide

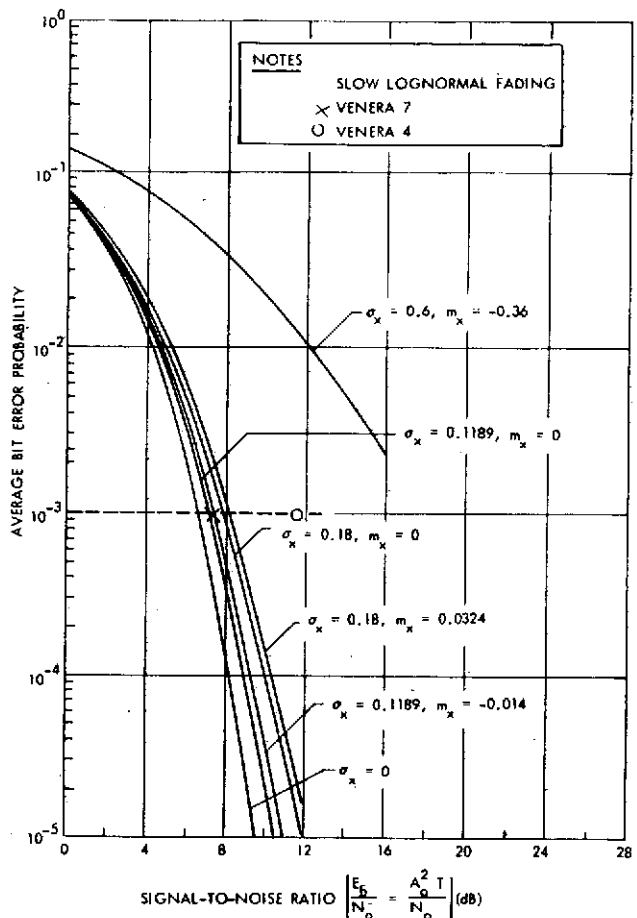


Figure 7.6C-1. Bit Error Probabilities for a Perfectly Synchronized PSK System

correct results. It is our position that the conservation of power argument is valid and the losses based on this position will be used in the design control tables.

3. ERROR PROBABILITY FOR RICIAN FADING (PERFECT PHASE SYNCHRONIZATION ASSUMED)

Communication system performance curves are available in the literature (References 4, 5, 6) for Rician fading. For the perfect phase synchronization the bit error probability is given by (References 4 and 6)

$$P_E = \int_0^\infty x \operatorname{erfc}(\sqrt{\beta}x) e^{-\frac{x^2}{2}} I_0(\sqrt{2}\gamma x) dx$$

where

$$\frac{E_{ave}}{N_o} = (1 + \gamma^2) \beta = (\alpha^2 + 2\sigma^2) \frac{E_b}{N_o}$$

is the total average received energy to noise density and

$$\gamma^2 = \frac{\alpha^2}{2\sigma^2}$$

$$\beta = 2\sigma^2 \frac{E_b}{N_o}$$

with

α = amplitude of specular component

$2\sigma^2$ = average power in random component

This expression is plotted in Figure 7.6C-2.

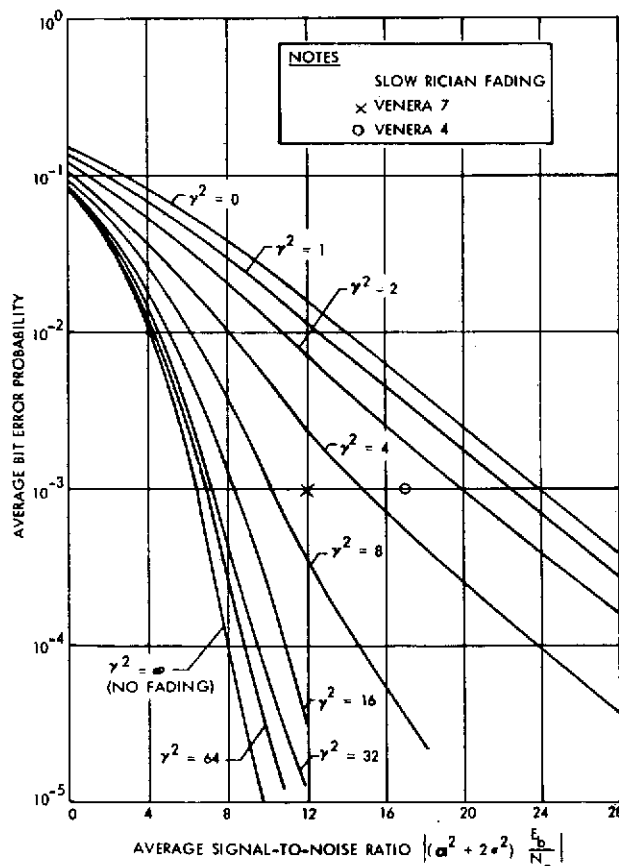


Figure 7.6C-2. Average Error Probabilities for a Perfectly Synchronized PSK System

REFERENCES

1. V. J. Tatarski, Wave Propagation in a Turbulent Medium, Dover Publications, Inc., New York, 1961.
2. D. L. Fried, J. Opt. Soc. Am., 56, p. 1372, 1966.
3. J. A. Croft, et al., "Preliminary Review and Analysis of Effects of the Atmosphere of Venus on Radio Telemetry and Tracking of Entry Probes," Final Report, SEL Project, Stanford Electronics Laboratories, Stanford University, Stanford, California, October 1972.
4. W. C. Lindsey, "Error Probabilities for Rician Fading Multi-channel Reception of Binary and N-ary Signals," IEEE Trans Info Theory, Vol. IT-10, October 1964, pp. 339-350.
5. W. C. Lindsey, "Coded Noncoherent Communications," IEEE Trans Space Electronics and Telemetry, Vol. SET-11, pp. 6-13, March 1965.
6. J. Zelen, et al., "Study and Analysis of Multipath Analysis and Modulation Selection for Relay Radio Links," RCA, Astro-Electronics Division, Radio Corporation of America, Princeton, New Jersey, August 1967.

APPENDIX 7.6D

PERFORMANCE AND SELECTION OF A CODING
METHOD OF PIONEER VENUS ENTRY
PROBES USING PSK/PM MODULATION

1. Data Requirements	7.6D-1
2. Channel and Receiver Effects	7.6D-5
3. Interleaving	7.6D-16
4. System Complexity Considerations	7.6D-17
5. Conclusions	7.6D-18
6. Recommendations for Further Study	7.6D-18
7. References	7.6D-19

APPENDIX 7.6D
PERFORMANCE AND SELECTION OF A CODING
METHOD FOR PIONEER VENUS ENTRY PROBES
USING PSK/PM MODULATION

The most suitable candidates for coding methods to be used on planetary entry probe communications channels are sequential and Viterbi. These coding techniques provide significant reduction in required E_b/N_o at a specified probability of bit error from the uncoded PSK/PM requirements. They also provide superior error rate performance to orthogonal codes as well as block codes of equivalent complexity for nonfading channels. To assess the performance of each of these techniques for a planetary entry and descent probe one must include both fading and receiver synchronization losses. This appendix develops performance data for these non-ideal conditions and provides a rationale for selecting sequential decoding for the Pioneer Venus, essentially on the basis of DSN compatibility. Suitability of the algorithms is discussed in regard to user requirements, channel characteristics, system complexity, and hardware compatibility with the DSN. A basic understanding of the two decoding algorithms is assumed.

1. DATA REQUIREMENTS

The data requirements call for a minimum undetected bit error rate of 10^{-3} with a frame deletion rate of 10^{-2} . The deletion rate is applicable to sequential decoding only. For the small probes, approximately 250 000 data bits will be transmitted and for the large probe, the total number of transmitted data bits will be approximately 560 000.

Let us first consider the coding methods with respect to the undetected bit error rate of 10^{-3} . For the Viterbi decoder this is achieved for $E_b/N_o = 2.3 \text{ dB}$ for a rate 1/3, constraint length, $K = 8$ code or for $E_b/N_o = 2.5 \text{ dB}$ for a rate 1/3, constraint length $K=6$ code as illustrated in Figure 7.6D-1 (Reference 1). For a JPL experimental Fano sequential decoder a bit error rate of 10^{-3} at 2 kbps is achieved for $E_b/N_o = 2.5 \text{ dB}$ with an information rate 1/2 quick-look-in code as the curve labeled B in Figure 7.6D-2 (Reference 2) illustrates. The curves labeled A and C are for systematic and non-systematic codes. The two methods therefore require essentially the same E_b/N_o to achieve an error rate of 10^{-3} when the sequential decoder operates at 2 kbps. The required E_b/N_o for the sequential decoder will be less for 128 bps, however these data are not available at this time.

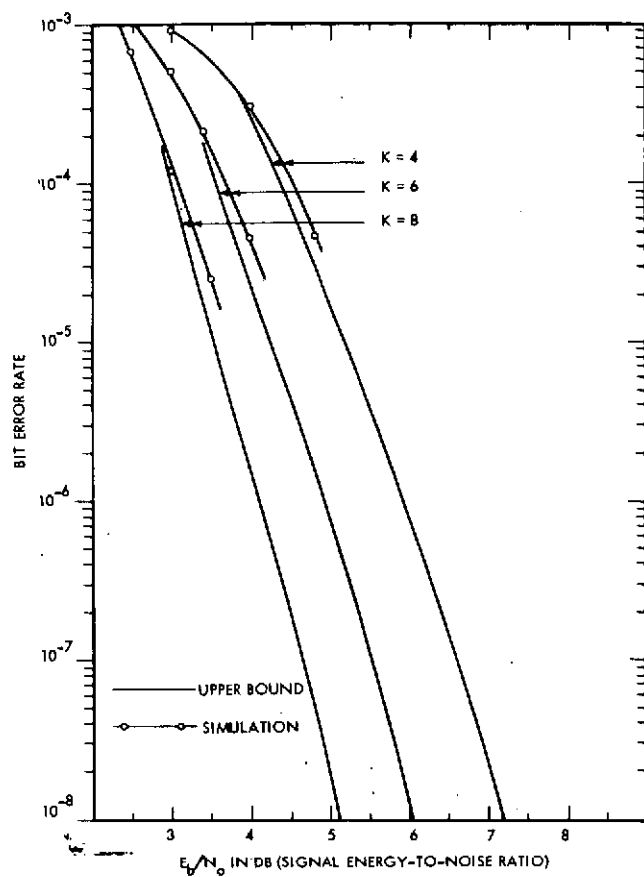


Figure 7.6D-1. Performance of Rate 1/3, K = 4, 6 and 8 Codes with Viterbi Decoding

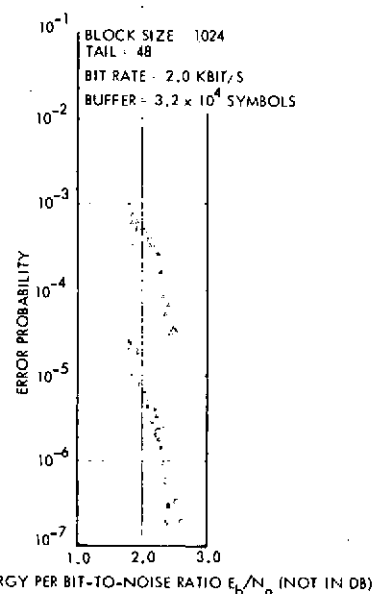


Figure 7.6D-2. Bit Error Probabilities for JPL Experimental Fano Sequential Decoder

Next consider the frame deletion rate of 10^{-2} . Since Viterbi decoding requires no framing, only the bit error rate is meaningful. With sequential decoding the frame deletion rate is an important parameter. From Figure 7.6D-3 (Reference 3) it can be observed that an average deletion rate of 10^{-2} requires an E_b/N_o of 2.2 dB with the DSIF decoders operating at 128 bps. This performance is independent of frame length because the decoder input buffer length is increased with frame length (Reference 3). Performance curves for the corresponding undetected bit error rate are not available. In general, however, the higher the deletion rate the lower the undetected bit error rate in the successfully decoded frames. This is because a high deletion rate implies that few computations were allowed to decode a frame so that only the less noisy bit sequences would not be deleted. This has been substantiated through experimentation (Reference 3). The undetected bit error rate in the 2 kbps case is less by a factor on the order of 10^{-3} than the deletion rate, as can be seen by comparing Figures 7.6D-2 and 7.6D-3. Therefore, a deletion rate of 10^{-2} should assure an undetected bit error rate of 10^{-3} or less at 128 bps, and the deletion rate is the more critical parameter. The required E_b/N_o to meet the data requirements of undetected bit error rate and deletion rate is within 0.3 dB for either coding method with 0.1 dB difference if the $R = 1/3$, $K = 8$ Viterbi decoder is used.

The fact that the amount of data transmitted is small must be taken into account. In the above discussion we have been concerned with average rates. With respect to bit error rates this is quite satisfactory since the number of transmitted bits is large enough to make an average bit error rate meaningful. However, the number of frames in the case of sequential decoding is small enough, particularly for the small probes, so that an average deletion rate is not very meaningful. Since the loss of a few frames is very significant we must explore the probability of such an event as well as the average deletion rate discussed previously. To do this we concern ourselves with the probability distribution function of the number of computations per bit required to decode. This distribution, $P(C \geq N)$, of the probability that the number of computations C required to decode a bit is greater than or equal to a specified number of computations N , is Pareto (Reference 4). Experimental curves for $P(C \geq N)$ based on Pioneer 10 data are shown in Figure 7.6D-4 (Reference 3). Since the curves for $P(C \geq N)$ decrease slowly with N , the variance in the number of computations required to decode a bit is large. Therefore, over a small sample set the probability of

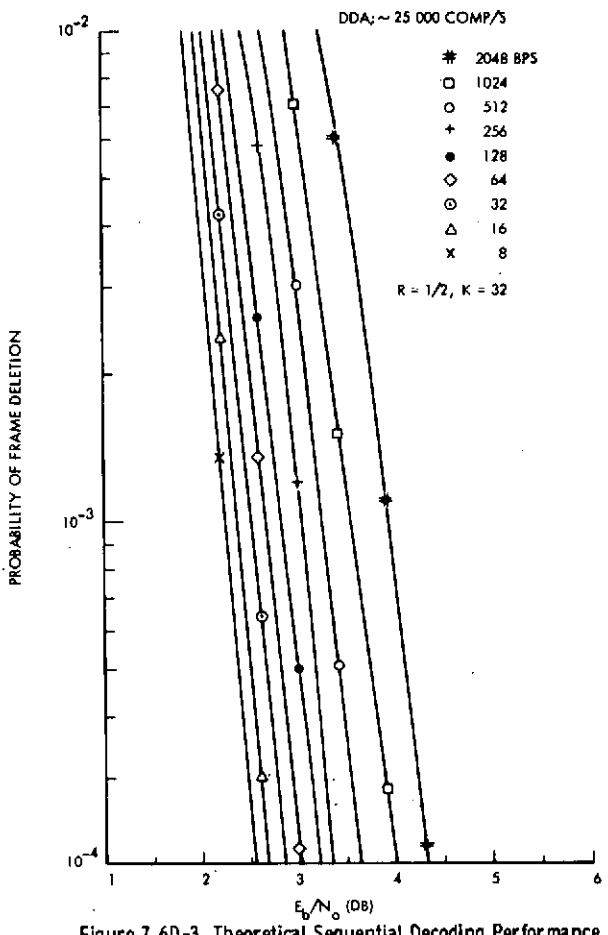


Figure 7.6D-3. Theoretical Sequential Decoding Performance

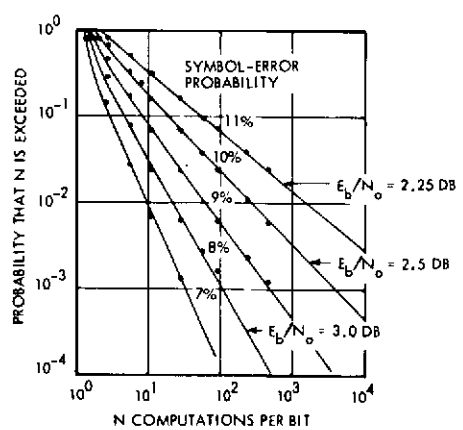


Figure 7.6D-4. Experimental Distribution of Computations for Sequential Decoding of Pioneer 10 Frame

a large deletion rate cannot be ignored, even when a very large amount of computation is used in decoding a frame. For example, at $E_b/N_o = 2.25$ dB the probability that the number of computations per bit required to decode a particular frame exceeds 10 000 is 0.005. If a frame is comprised of 200 bits, two million computations would be required to decode the frame. This is an exorbitant amount of computation and certainly could not be done in real time. If it were decoded off-line, the number of bit errors would be very large. With a Viterbi decoder these data would very likely also be of poor quality, but the two million computations would not have been required to decode this section of data and the undetected bit error rate of 10^{-3} would still be achieved.

The performance of sequential and Viterbi decoding method with respect to the data requirements can therefore be summarized as follows. Sequential decoding provides an undetected bit error rate of 10^{-3} and a deletion rate of 10^{-2} for $E_b/N_o = 2.2$ dB at a transmission rate of 128 bps using a rate 1/2 code. Viterbi decoding provides an undetected bit error rate, with no deletions, of 10^{-3} for E_b/N_o of 2.3 dB to 2.5 dB (depending on the code used), and this could be attained in real time for transmission rates much higher than 128 bps. The Viterbi decoding method is therefore the choice based on data requirements considerations although the choice is somewhat close.

2. CHANNEL AND RECEIVER EFFECTS

The channel characteristics that affect the coded system performance are the fading on the received signal due to propagation effects and the receiver degradation due to synchronization errors. Receiver synchronization errors are caused by a noisy carrier reference and the subcarrier loop. The curves presented here will be used in constructing the design control tables, as well as to aid in the coding method selection.

It is convenient to treat the case of the combined effects of fading and synchronization errors on the coded system performance first. Then the cases with only fading or synchronization errors present can be treated as special cases. The combined effect of additive thermal noise, an erroneous reference phase (radio loss) and a fluctuating signal amplitude due to channel fading, when the latter two effects are assumed to be independent, will be considered. This assumption of independence is quite accurate

if the fading bandwidth is much smaller than the tracking loop bandwidth and the fading depth is not great. Figure 7.6D-5 (Reference 5) shows the effect of slow Rician fading on the phase error probability density function when these conditions are met. It can be observed that the fading has a rather small effect on the phase error density function. Here we are considering lognormal fading rather than Rician fading, however the effect on the phase error will be similar. These conditions of slow fading and small amplitude fluctuations characterized by the lognormal distribution are anticipated to a large degree for signals passing through the atmosphere of Venus based on recent investigations (References 6 and 7).

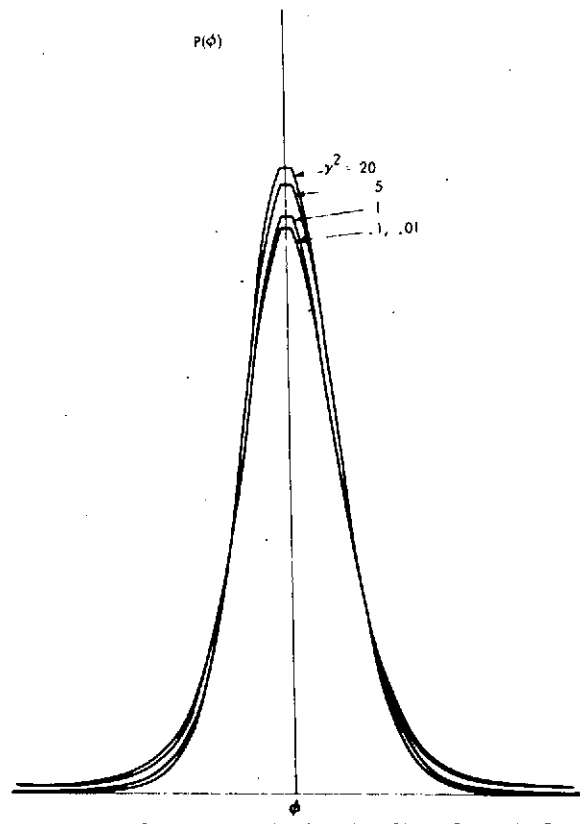


Figure 7.6D-5. Slow Rician Fading (Received Signal Power the Same in Each Case)

The total undetected bit error or frame deletion probability, P_E , is given by

$$P_E = \int_{\phi} \int_A P(E/\phi, A) P_{\phi, A}(\phi, A) d\phi dA$$

where $P(E/\phi, A)$ is the bit error probability or frame deletion probability in the presence of white Gaussian noise, conditioned on the phase error, ϕ , and amplitude value A . Then assuming ϕ and A are independent,

$$\begin{aligned}
P_E &= \int_{\phi} \int_A P_{\phi}(e) P_A(A) \left(\int_{-\infty}^E \frac{p(e, \phi, A)}{p(\phi, A)} de \right) d\phi dA \\
&= \int_{\phi} \int_A \left(\int_{-\infty}^E p(e, \phi, A) de \right) d\phi dA \\
&= \int_A \int_{-\infty}^E \left(\int_{\phi} P(e, A/\phi) P(\phi) d\phi \right) dedA \\
&= \int_A \int_{-\infty}^E P_1(e, A) dedA = \int_A \int_{-\infty}^E P_1(e/A) P_A(A) dedA \\
&= \int_A P_A(A) P_1(E/A) dA,
\end{aligned}$$

where $P_1(e, A)$ represents the joint probability density function of the undetected bit error, e , and amplitude error, A , in the presence of additive white Gaussian noise. $P_1(E/A)$ is the error probability conditioned on A , with phase error effects and additive white Gaussian noise included.

The function $P_1(E/A)$ can be obtained from simulation and analysis. If $P(E)$, the error probability due to white Gaussian (thermal) noise only, is obtained through simulation, then $P_1(E)$, the error probability due to thermal noise and phase errors, is obtained by

$$P_1(E) = \int_{\phi} P(E/\phi) p(\phi) d\phi.$$

The functions $p(\phi)$ and $P(E/\phi)$ can be derived quite accurately from the tracking loop equations. The tracking loop static phase error for a two-way link is given by,

$$P_{\phi}(\phi) = \frac{I_o}{2\pi} \frac{\left[\eta_1 + \eta_2 \exp(j\phi) \right]}{I_o(\eta_1) I_o(\eta_2)}$$

where η_1 and η_2 are the signal-to-noise ratios in the spacecraft and ground tracking loop bandwidths W_{L1} and W_{L2} . These can be found in terms of the loop threshold signal-to-noise ratios in $W_{L10} = 2B_{L10}$ and $W_{L20} = 2B_{L20}$ (Reference 8, p. 110). The probability $P(E/\phi)$ is approximately $P(E)$ degraded by $\cos^2 \phi$ (Reference 9), where $P(E)$ is either the bit error or frame deletion probability which has been obtained through simulations.

If the phase error memory is equal to or greater than the decoder memory the expression is accurate. This is approximately the case for a Viterbi decoder with a 10 Hz loop and a data rate of 200 data bits per second, but is not as accurate for the sequential decoder because of the longer decoder memory. In order that this expression for $P_1(E)$ be accurate it is necessary that

$$\tau_L > MT$$

where M is the decoder memory length in transmitted symbols, T is the symbol period and

$$\tau_L \triangleq 1/W_L$$

is the tracking loop response time. This situation gives the worst-case degradation because when the phase error fluctuates about its zero mean during a decoder memory length the phase error tends to average to zero. This is the same effect as found in uncoded systems, but there the phase error only needs to remain constant over one symbol period to give worst-case degradation.

Similar remarks apply with respect to amplitude variations due to channel fading. For a fading band near 1 Hz, as has been computed by Woo (Reference 6) at the surface of Venus, the Viterbi decoder memory is easily included at 60 data bits per second while for the sequential decoder of constraint length 32, the data rate should be above 80 to 100 bps with the exact number being difficult to compute analytically.

For lognormal amplitude distribution due to fading, the above expression for P_E can be written explicitly as follows. With

$$X = \ln A/A_o \text{ or } A = A_o e^X$$

and

$$R' = E_b/N_o = \frac{A_T^2}{N_o} = \frac{e^{2X} A_o^2 T}{N_o} = e^{2X} R$$

where $\sqrt{2 A_o}$ is the transmitted amplitude and $\sqrt{2 A}$ the received amplitude. Then

$$F(R'^{1/2}) = F(e^X \sqrt{R}) \triangleq P(E/X)$$

where F is the probability of error as a function of received E_b/N_o and $P(E/X)$ is the error probability conditioned on X . Then,

$$P_E = \frac{1}{\sqrt{\pi}} \int_{-\infty}^{\infty} P(E/X) P(X) dX = \\ = \frac{1}{\sqrt{2\pi \sigma_X^2}} \int_{-\infty}^{\infty} \exp\left(-\frac{(X-M_X)^2}{2 \sigma_X^2}\right) F\left(e^{X\sqrt{R}}\right) dX$$

with

$$Z = \frac{X - M_X}{\sqrt{2 \sigma_X^2}}$$

we have

$$P_E = \frac{1}{\sqrt{\pi}} \int_{-\infty}^{\infty} \exp(-Z^2) F\left[\sqrt{R} \exp(\sqrt{2 \sigma_X^2} Z + M_X)\right] dZ$$

The function $F(o)$ can be taken as either bit error or frame deletion probability with or without the noisy carrier reference loss (radio loss). For the case of no radio loss (perfect synchronization), $F(o)$ can be obtained by applying curve fitting methods to Figure 7.6D-1 and 7.6D-3. Figures 7.6D-6 through 7.6D-14 give the coded system performance for various combinations of coding methods and losses. Figure 7.6D-6 (Reference 10) gives the Viterbi decoder performance with noisy carrier reference, $P_1(E)$. Figure 7.6D-7 (Reference 3) gives the sequential decoder deletion rate with all receiver losses (noisy carrier reference plus subcarrier loop losses) included from experimental data at the DSN. Figure 7.6D-7 plots frame deletion probability versus data channel E_b/N_o with the signal-to-noise ratio in $2B_{LO}$ changing with E_b/N_o (i.e. the modulation index is fixed for each data rate). The figure does not contain sufficient data to optimumly choose the loop signal-to-noise ratio (i.e., set the modulation index) for various data rates. Also the performance is for a one-way link, whereas we also are concerned with a two-way link. For these reasons we have computed the deletion rate with noisy carrier reference by the method given above and some of the results are given in Figures 7.6D-8 and 7.6D-9.

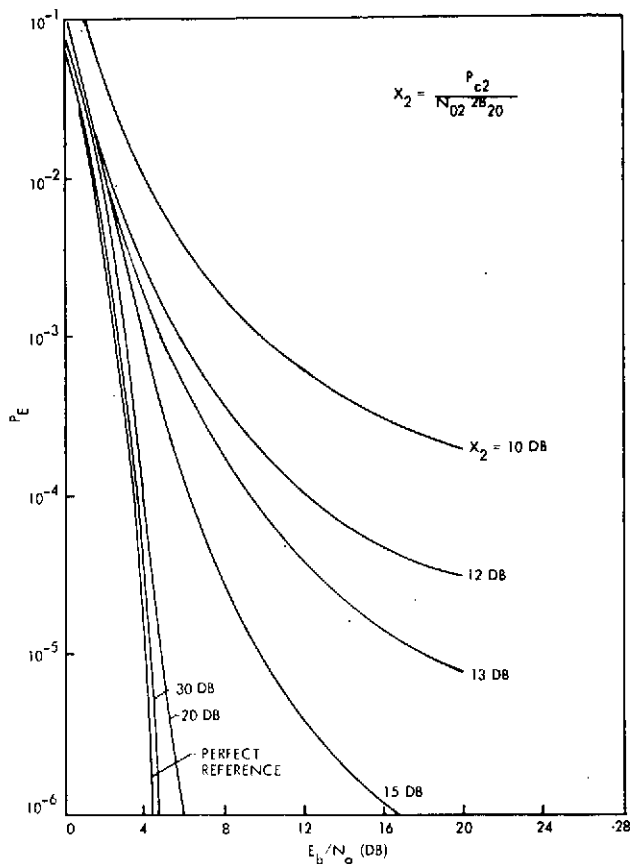


Figure 7.6D-6. Expected Bit Error Rate for Convolutional Code 756617 ($k = 6$, $v = 31$; Two-Way Link: $\rho_1 = 20 \text{ dB}$, Viterbi Decoding)

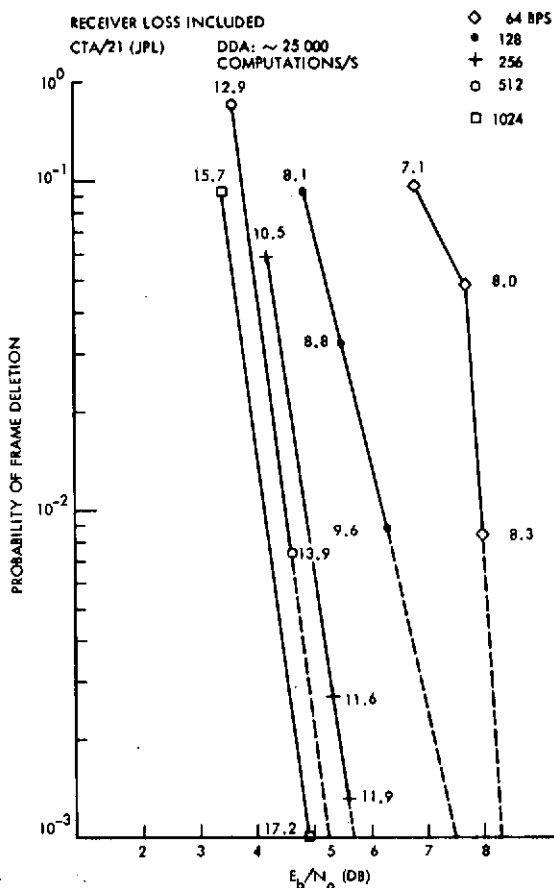


Figure 7.6D-7. Experimental Deletion Rate for Sequential Decoding from Pioneer 10/11 Data

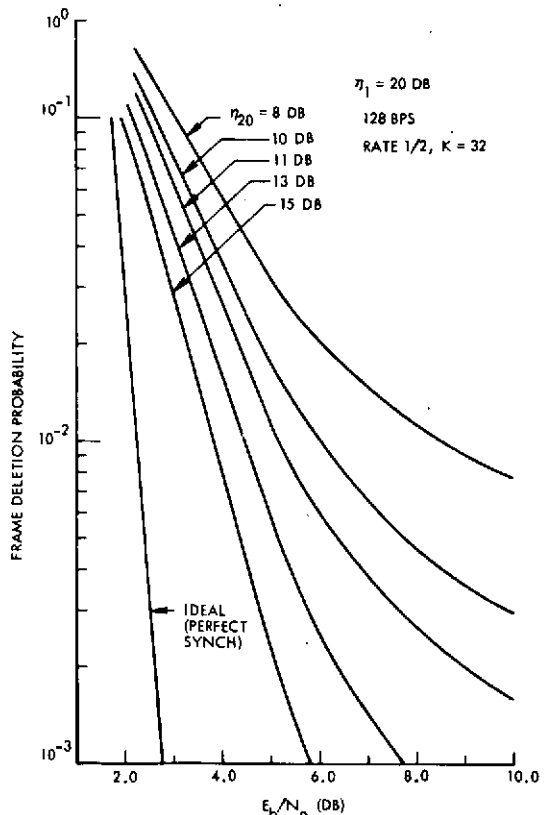


Figure 7.6D-8. Deletion Rate in the Presence of Noisy Carrier Reference for Sequential Decoding for a Two-Way Link

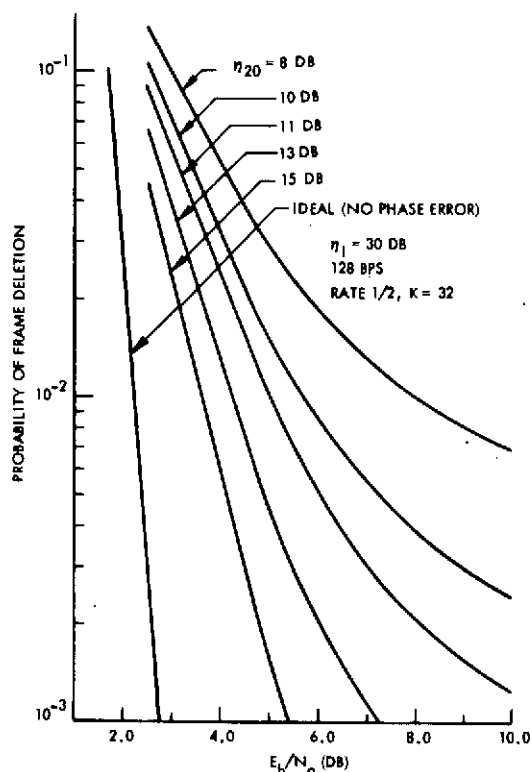


Figure 7.6D-9. Deletion Rate in the Presence of Noisy Carrier Reference for Sequential Decoding for a Two-Way Link

It can be observed from Figure 7.6D-8 that for 13.0 dB in the ground tracking loop $2B_{LO}$ with 20 dB in the spacecraft bandwidth $W_L = 2B_L$, the degradation in deletion rate is 2.23 dB. With 11.0 dB in the ground loop $2B_{LO}$ the degradation is 2.92 dB, which indicates that serious degradation results when less than 13.0 dB is used in the ground loop. Figure 7.6D-9 is useful for the design of the small probe links, since 30.0 dB in the spacecraft loop represents closely a one-way link. There are still two important differences between the experimental curves of Figure 7.6D-7 and the analytical curves of Figures 7.6D-8 and 7.6D-9. The experimental data includes all receiver losses which includes the subcarrier loop (symbol synchronizer, waveform distortion, and demodulator) losses as well as the noisy carrier reference loss. Also the experimental data makes no assumption regarding how long the phase error remains constant. By analyzing the DSN subcarrier loop we can obtain an estimate for the subcarrier losses, which in turn can be used to get an estimate of the inaccuracy of the analytical method due to the constant phase assumption. With this estimate, Figures 7.6D-8 and 7.6D-9 can be used for accurate design purposes.

The parameter values in the experimental and analytical data unfortunately do not allow an exact comparison between the two. To compare a data point from the experimental curve of Figure 7.6D-7 to the analytical curve of Figure 7.6D-9 we first use $N_{20} = 13.0$ dB and frame deletion rate 10^{-1} . From the experimental data the required E_b/N_o is 3.6 dB at 512 bps, while from Figure 7.6D-9 the required E_b/N_o is 2.12 dB at 128 bps. To account for the difference in data rate, Figure 7.6D-3, for the ideal case, can be used by subtracting the difference between the 512 bps curve, and the 128 bps curve, from the experimentally required E_b/N_o of 3.6 dB. This extrapolation gives a required E_b/N_o of 3.1 dB using the experimental data. The difference between the analytical and experimental data is

$$3.1 - 2.12 = 0.98 \text{ dB.}$$

The subcarrier loss has been computed (see Design Control Table Appendix) to be 0.8 dB. This makes the error in the analytical results due to the constant phase assumption to be approximately

$$0.98 - 0.8 = 0.18 \text{ dB}$$

at 128 bps. Notice however, that the experimentally required E_b/N_o for a deletion rate of 10^{-1} is greater than that predicted analytically, if only 0.8 dB is used in the subcarrier loop. We can only assume at this point, that the subcarrier loss is at least 0.98 dB since the constant phase assumption yields worst-case results.

Since subcarrier loop loss depends upon data rate we next take the case of 8.0 dB in $2B_{LO}$, for which a deletion rate of 10^{-1} requires an E_b/N_o of 4.65 dB at 128 bps using the experimental data. The corresponding case from the analytical method requires an E_b/N_o of 3.0 dB with 30 dB in the spacecraft tracking loop. This indicates at least a 1.65 dB subcarrier loss at 128 bps. To clearly establish the degradation in the coded system due to reference phase errors when the phase does not remain constant over the entire decoder memory, a simulation with the subcarrier loop bypassed is required.

Consider next the performance computation when channel fading due to propagation effects are included. Using the methods outlined above, the performance of the Viterbi decoder and the sequential decoder with perfect reference has been computed in Figures 7.6D-10 through 7.6D-13. The log-normal fading model is used (see Appendix 7.6B), which is characterized by the variance σ_x^2 and mean $-\sigma_x^2$. The variance has been computed (References 6 and 7) to be 0.1189 at subearth and 0.18 at a transmitting angle of 50 degrees.

The performance of the coded and uncoded systems in the presence of both reference phase errors and channel fading for the sequential and Viterbi decoders are given in Figures 7.6D-14 through 7.6D-20. The deletion rate for the sequential decoder in Figures 7.6D-14 and 7.6D-15 was obtained by using the experimental results with all receiver losses included (Figure 7.6D-7), and then averaging over the signal amplitude, which is fluctuating due to fading. Figures 7.6D-16 and 7.6D-17 are for deletion rate with noisy carrier reference (no subcarrier losses) and fading only, using the above analytical technique. The Viterbi curve also was obtained analytically by using the curve of Figure 7.6D-6 for the performance of the Viterbi decoder with the noisy reference included and then averaging over the amplitude.

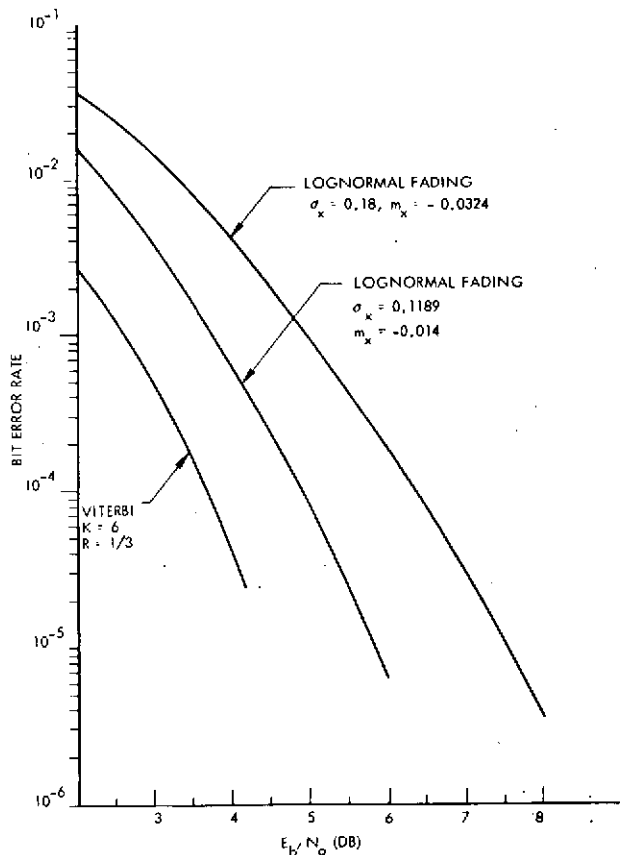


Figure 7.6D-10. Viterbi Decode Performance in the Presence of Lognormal Fading Assuming Slow Fading Relative to Decoder Memory

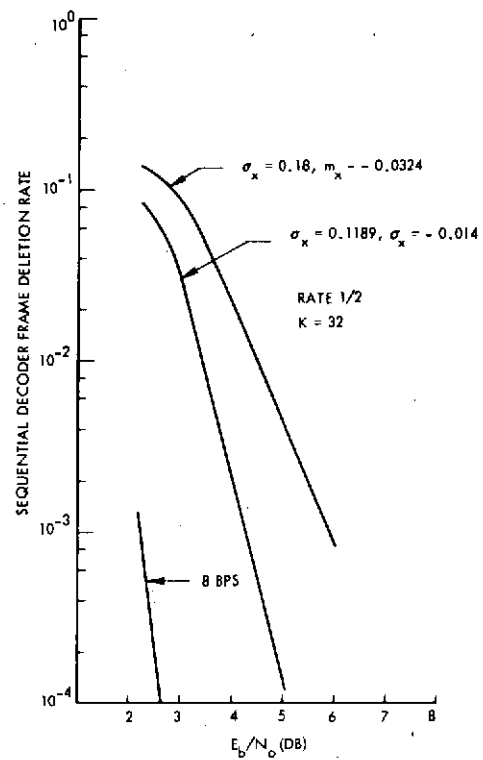


Figure 7.6D-11. Frame Deletion Probability with Sequential Decoding in the Presence of Slow Lognormal Fading Relative to Decoder Memory

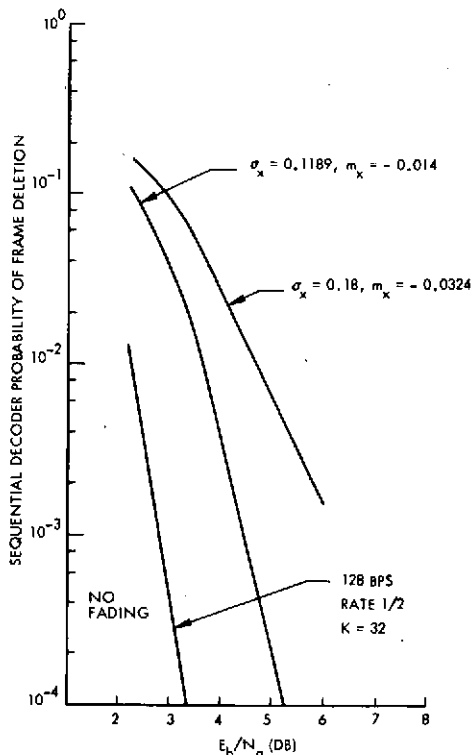


Figure 7.6D-12. Deletion Rate for Sequential Decoding with Slow Lognormal Fading

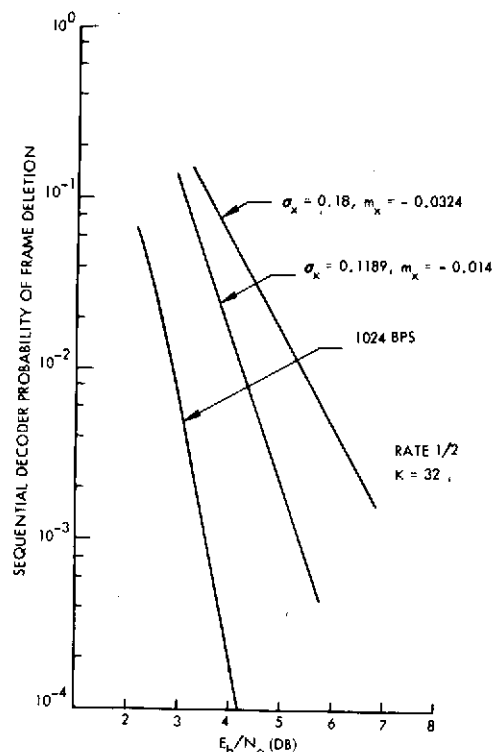


Figure 7.6D-13. Frame Deletion Probability for Sequential Decoding with Slow Lognormal Fading

It can be observed from the figures that a deletion rate of 10^{-2} at 128 bps for sequential decoding with both receiver losses and fading effects included, requires less than 7.5 dB since this is the required E_b/N_o at 512 bps. This is true if the gain in decoder performance achieved by going from 512 bps to 128 bps is greater than the subcarrier loop degradation. If the difference in E_b/N_o between the 512 bps and 128 bps curve for the ideal case is subtracted from the 7.5 dB we obtain a required E_b/N_o of 7.0 dB. This, of course, ignores any difference in the subcarrier losses between the two rates. To be conservative we use 7.1 dB since the subcarrier loss is greater for lower rates. For the Viterbi decoder a bit error rate of 10^{-3} , when both effects are included, requires an E_b/N_o of 6.5 dB. To this number we must add the subcarrier loss which is estimated to be between 0.80 dB and 1.25 dB. This brings the total E_b/N_o required by the rate 1/3, constraint length 6, Viterbi decoder to 7.5 dB, which is 0.4 dB greater than the requirement of the sequential decoder. In both cases the signal-to-noise ratio in the transponder is 20 dB and in the ground loop $2B_{LO}$ is 13.0 dB. To compensate for Doppler effects in the subcarrier loop an estimated 0.2 dB should be added to this total.

The performance for the uncoded PSK system with both reference phase errors and channel fading included is given in Figures 7.6D-19 and 7.6D-20. This was computed by using the performance curve for the uncoded PSK system in the presence of a noisy phase reference (Reference 11) and averaging over the amplitude. The figure can be used for obtaining the coding gain. The required E_b/N_o to achieve a bit error rate of 10^{-3} is observed to be 8.9 dB and when a subcarrier loss of 0.8 dB (this is smaller than the loss used in the coded case because of the higher signal to noise ratio) is added, the total E_b/N_o required is 9.7 dB. The coding gain is the difference between this and 7.1 dB, i.e., 2.2 dB. It can also be observed from Figure 7.6D-16 that the loss in the uncoded system is 2.0 dB, whereas the corresponding loss in the coded system is 4.0 dB. The 2.0 dB difference between these values is the enhancement which could be achieved with the use of interleaving by removing all memory effects, which are greater than one transmitted symbol duration in length between the channel and receiver, and between the receiver and decoder.

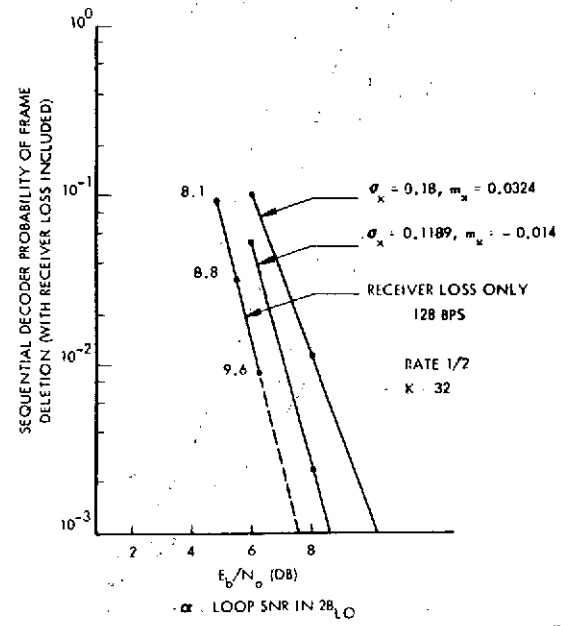


Figure 7.6D-14. Frame Deletion Probability for Sequential Decoding with Receiver Losses and Lognormal Fading Effects Included

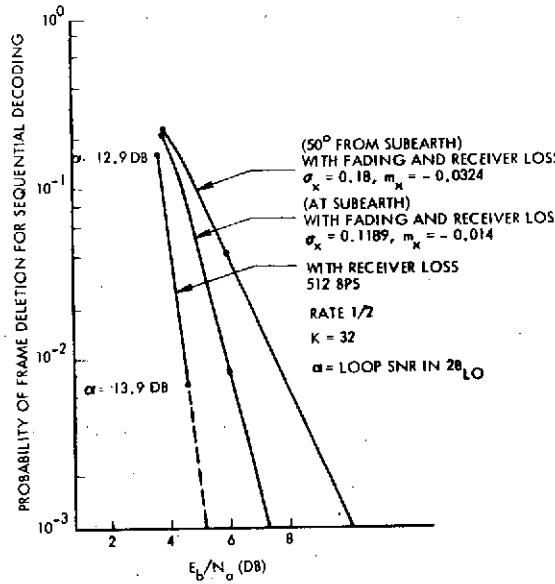


Figure 7.6D-15. Frame Deletion Probability for Sequential Decoding with Receiver Losses and Lognormal Fading Effects Included at the Venus Surface

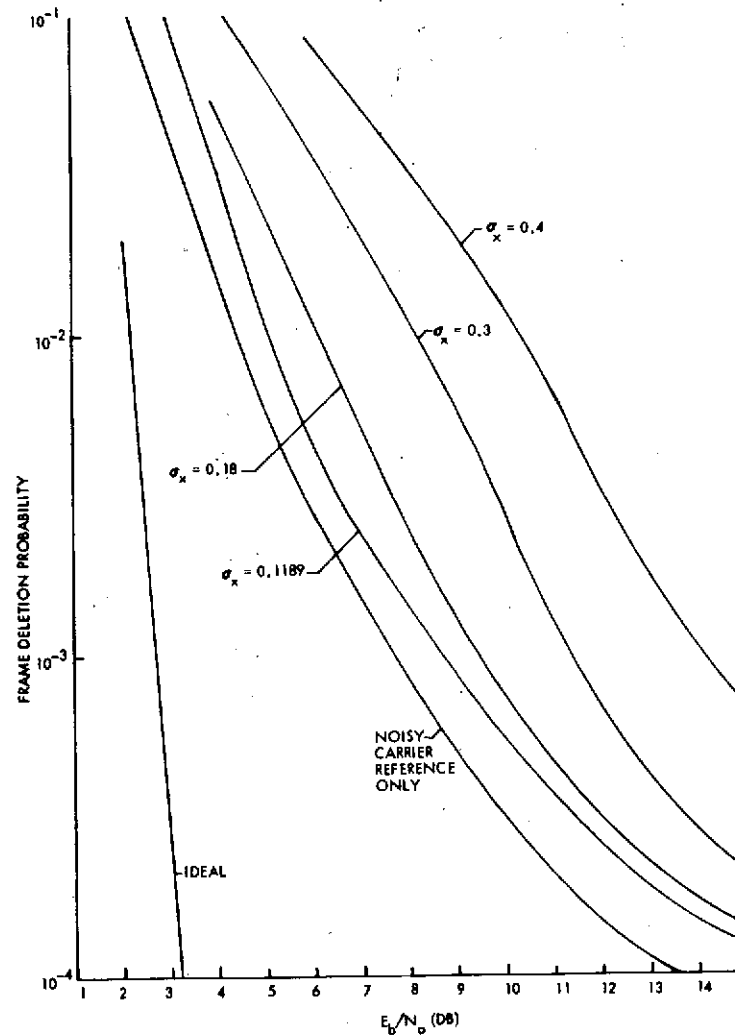


Figure 7.6D-16. Sequential Decoder Frame Deletion Probability versus E_b/N_0 with Noisy Carrier Reference and Lognormal Fading for Two-Way Link with 13.0 dB in Ground Loop $2B_{L0}$ and 20.0 dB in Transponder Loop $2B_L$ at 128 bps

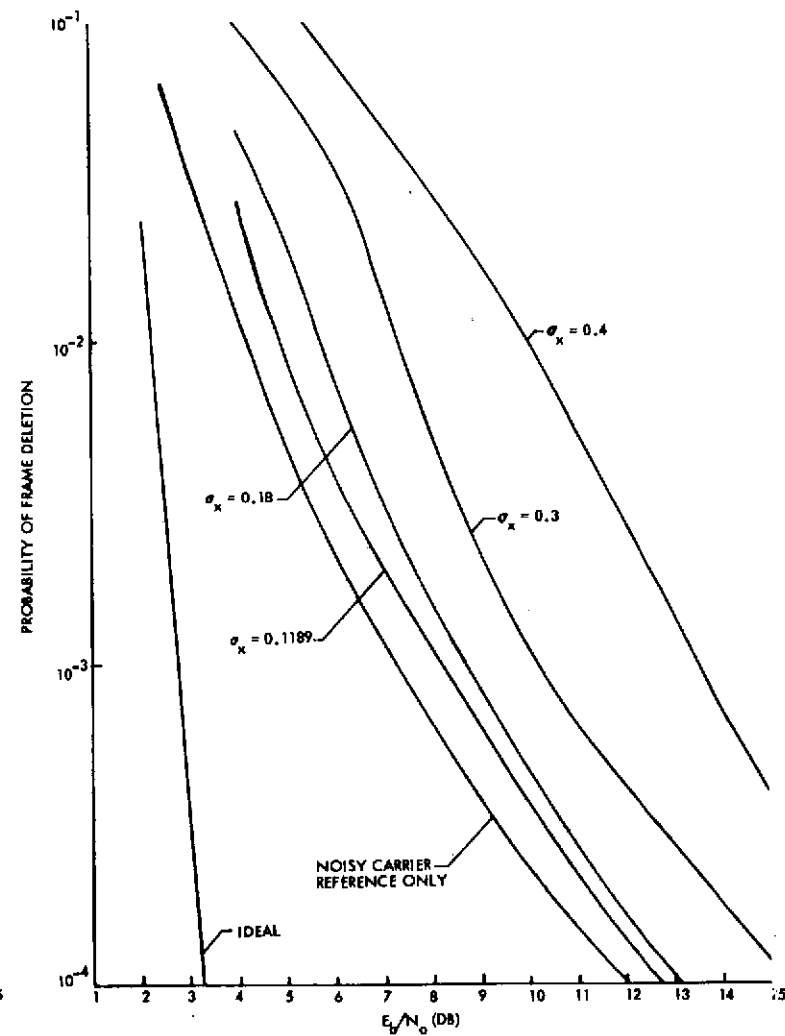


Figure 7.6D-17. Sequential Decoder Frame Deletion Probability versus E_b/N_0 with Noisy Carrier Reference and Lognormal Fading for Two-Way Link with 13.0 dB in Ground Loop $2B_{L0}$ and 30.0 dB in Transponder Loop $2B_L$ at 128 bps

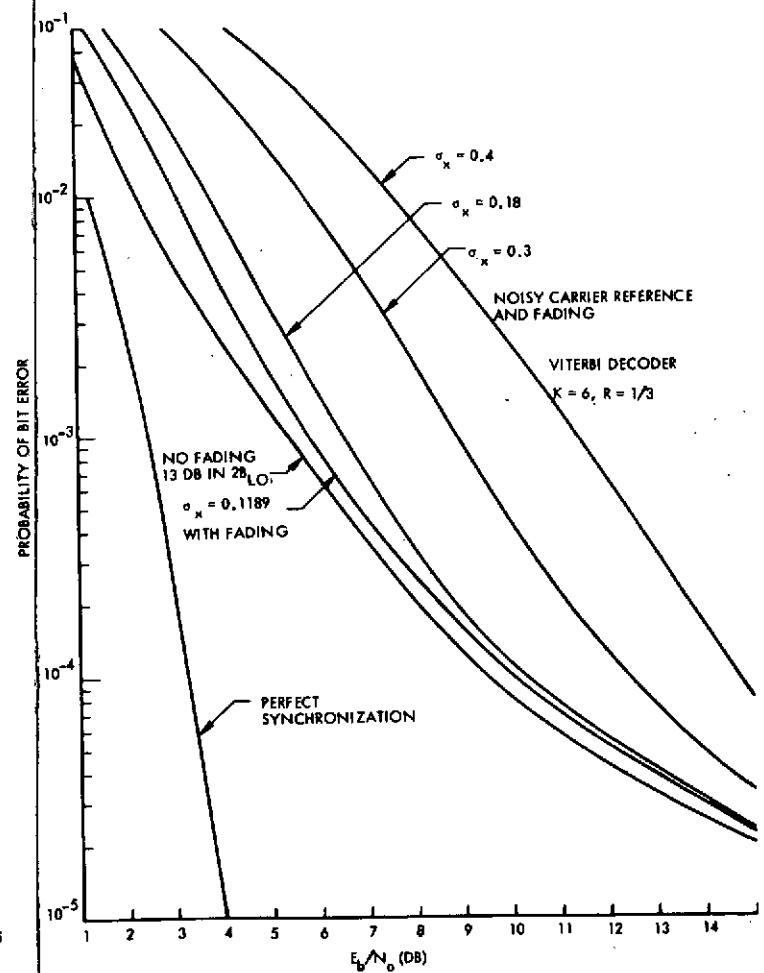


Figure 7.6D-18. Viterbi Decoder Performance in the Presence of Noisy Carrier Reference and Slow Lognormal Fading, Two-Way Link with 20 dB in Transponder Loop

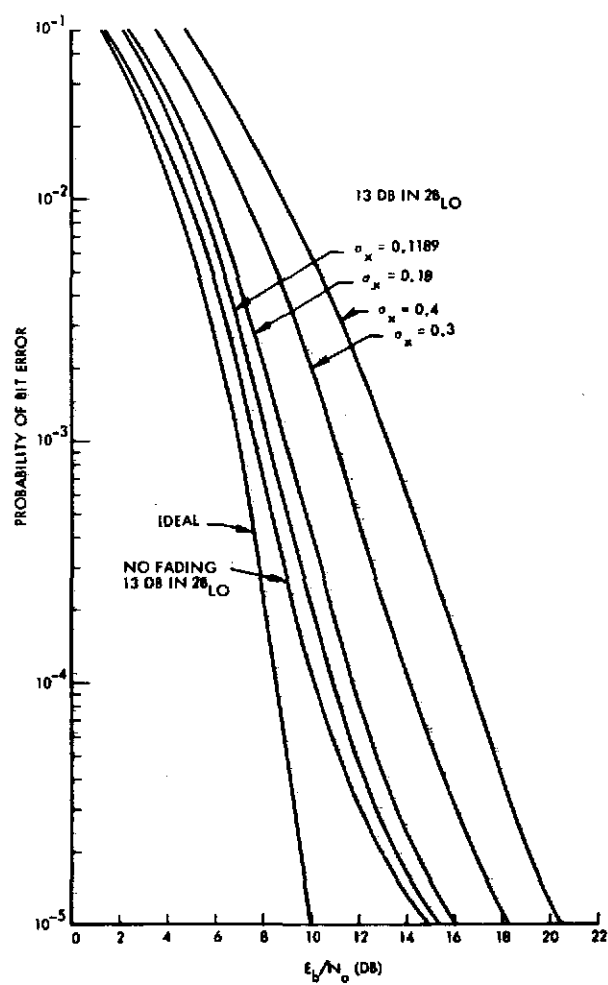


Figure 7.6D-19. Performance of Uncoded PSK in the Presence of Noisy Carrier Reference and Slow Lognormal Fading

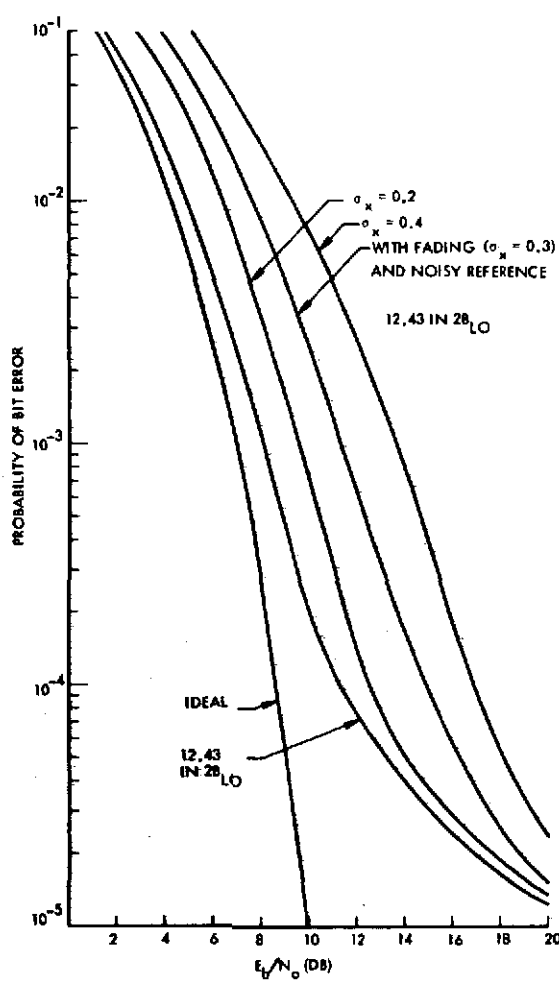


Figure 7.6D-20. PSK Performance in Presence of Noisy Carrier Reference and Slow Lognormal Fading

From this discussion we conclude that there is negligible difference between the performance of the Viterbi and sequential decoders when the effects of channel fading and receiver synchronization errors are included. The coding gain is 2.2 dB.

3. INTERLEAVING

The combined effect of channel fading and noisy carrier reference can be combated using interleaving as a means of providing time diversity to overcome memory effects. As stated above the benefit that could be achieved by the use of interleaving is 2.0 dB. This assumes that the data rate is much greater than the fading bandwidth as well as the tracking loop bandwidth. Since the fading bandwidth has been computed to be approximately 1 Hz on the surface (Reference 6) and the loop bandwidth is designed at 10 Hz, this condition exists for the large probe transmitting at 128 bps. For data rates less than about 100 bps the interleaving gain is decreased from 2.0 dB. For data rates less than about 10 bps there would be no interleaving gain. The interleaving gain for the small probes transmitting at 40 to 100 bps can only be estimated to be between 0.5 dB to 1.5 dB.

The complexity of interleaving must be considered in relation to the gain it can provide. First, the interleaving must be synchronized. Second, the buffer in the transmitting end which is required to accomplish interleaving must be considered. For a fading bandwidth of 2 Hz, the fading time response is 0.5 seconds, which spans 128 transmitted symbols at a data rate of 128 data bits per second with a rate 1/2 code. If adjacent symbols are spread so as to be separated by 128 symbols by using a square matrix type storage, a buffer space of $128 \times 128 = 16\,384$ memory words would be required. The time delay at the transmitter would be extended considerably and this storage implies a potentially great loss of data at impact. In fact this is 5 percent of the total data transmitted from the large probe. This degree of interleaving of course is very elaborate; however, the fading bandwidth might also be smaller, in which case interleaving over a greater time interval would be required. Further investigation is required into designing an interleaving system that achieves not all the 2.0 dB theoretical gain, but a significant portion of this with little complexity.

Since interleaving would provide little advantage on the small probes, and its overall desirability on the large probe is questionable, and since the DSN does not presently have de-interleaving capabilities, its application for Pioneer Venus probe mission is not recommended.

4. SYSTEM COMPLEXITY CONSIDERATIONS

This discussion is not concerned with decoder hardware complexity, but rather with complexity in regards to synchronization and transmission efficiency, i. e., loss of user data due to any decoder overhead. With Viterbi decoding only node or branch synchronization (assigning the appropriate transmitted symbols to each data bit) is required and synchronization is simple. With sequential decoding, frame synchronization is required and a known sequence of 24 bits or more (Reference 3) is required for resynchronization after buffer overflow. Frame synchronization must be acquired before decoding begins, which indicates that a longer framing sequence is required than if data frame acquisition were accomplished on decoded data. With Viterbi decoding all data frame acquisition is accomplished on data that has the protection of the error correcting code since it is done after decoding. We can obtain an estimate for the data loss due to the code frame sequence required in sequential decoding. The length of the data framing sequence

required should be 13 to 15 bits. Allowing an additional overhead in the 24-bit tail for things such as bit count of 6 bits, there is a 3 percent data loss assuming a frame length of 192 bits. For a frame length of 768 bits the data loss is 0.75 percent. Therefore, on an efficiency basis the Viterbi algorithm is superior at high error rates.

5. CONCLUSIONS

Because sequential and Viterbi decoding will provide essentially the same coding gain, but only sequential decoding is DSN compatible, sequential decoding is the recommended method. Although Viterbi decoding is simpler from a system point of view, and involves no deletions, the factor of sequential decoding DSN compatibility is overriding because of economics. Interleaving is not recommended for the Pioneer Venus mission application.

6. RECOMMENDATIONS FOR FURTHER STUDY

Further study is required to establish more clearly the effect of complex lognormal fading on tracking loop behavior. The joint probability density $p(\phi, A, \theta)$ where ϕ is the loop static phase error, A is the received signal amplitude and θ is the received phase fluctuation due to turbulence, is required. This requires further analysis and simulation for various fading rates and depths. Decoder behavior, when amplitude and loop phase error changes occur during a decoder memory length, requires further investigation. This will almost certainly require simulations with noise accurately representing the additive noise as well as the synchronization errors and turbulence effects included. Interleaving with the objective of obtaining a significant portion of the theoretically available interleaving gain for a small degree of complexity is an important area requiring additional study. Finally the analytical results must be compared closely with any experimental data that become available.

7. REFERENCES

1. J. A. Heller, I. M. Jacobs, "Viterbi Decoding for Satellite and Space Communication," IEEE Trans. Comm. Tech., Vol. COM-19, No. 5, pp. 835-848 (October 1971).
2. J. W. Layland, "Information Systems: Multiple-Mission Sequential Decoder - Comparing Performance Among Three Rate 1/2, K-32 Codes," JPL SPS 37-64, Vol. II, pp. 50-52 (August 1970).
3. D. Lumb, Unpublished Data from NASA/Ames.
4. J. M. Wozencraft, I. M. Jacobs, Principles of Communication Engineering, (John Wiley and Sons, Inc., New York, 1967).
5. Results to be published in JPL Final Report, Contract NAS 7-100-RD-65 in June 1973.
6. R. Woo, "Pioneer Venus Propagation Study," to be published in JPL Final Report, Contract NAS7-100-RD-65 (June 1973).
7. J. A. Croft, et al., "Preliminary Review and Analysis of Effects of the Atmosphere of Venus on Radio Telemetry and Tracking of Entry Probes," Final Report SEL Project, Stanford Electronics Laboratories, Stanford University, Stanford, California (October 1972).
8. R. E. Edelson, Telecommunications Systems Design Techniques Handbook, NASA Tech. Memorandum 33-571, JPL, Calif. Inst. of Tech., Pasadena, California (July 1972).
9. W. C. Lindsey, "Block Coding for Space Communications Systems," IEEE Trans. Comm. Tech., Vol. COM-17, pp. 217-225 (April 1969).
10. H. M. Merrill, G. D. Thompson, Jr., "Design of Communications Systems Using Short-Constraint-Length Convolutional Codes," NTC Proceedings (1972).
11. W. C. Lindsey, "Performance of Phase-Coherent Receivers Preceded by Bandpass Limiters," IEEE Trans. Comm. Tech., Vol. COM-16, No. 2 (April 1968).

APPENDIX 7.6E
MULTIPLE FREQUENCY SHIFT KEYING (MFSK)
WITH CONVOLUTIONAL ERROR CORRECTING CODING

- | | |
|--|--------|
| 1. Ideal Performance | 7.6E-1 |
| 2. Uncoded MFSK Performance with Oscillator
Instabilities, Doppler and Channel Fading
Effects Included | 7.6E-4 |
| 3. Off-Line Acquisition and Tracking Methods | 7.6E-9 |

APPENDIX 7.6E

MULTIPLE FREQUENCY SHIFT KEYING (MFSK) WITH CONVOLUTIONAL ERROR CORRECTING CODING

Multiple frequency shift keying (MFSK) modulation for digital communication systems has the desirable attributes that all the transmitter power can be used in the data channel (no carrier is required) and no phase synchronization is required. We have conducted a study of MFSK with convolutional error correcting codes (Viterbi and sequential) to compute the performance when effects of channel fading, oscillator instabilities and Doppler rates are included (Reference 1). To accommodate off-line processing, an algorithm for performing frequency and timing acquisition was derived and evaluated. The performance results were obtained through analysis and computer simulation for $M = 16$ tones in the signal set. For computer simulations, the digital fast Fourier transform (FFT), was used to perform the matched filter (or correlation) tone detection. An important result pointed out the degradation in MFSK at low data rates due to transmitter oscillator frequency instabilities. This MFSK degradation due to frequency synchronization errors, is analogous to the PSK degradation that occurs due to phase synchronization errors at low data rates. Because of these degradations, neither MFSK nor PSK is efficient at low data rates (less than 6 to 8 bps).

1. IDEAL PERFORMANCE

A diagram of the convolutional encoder and modulator is given in Figure 7.6E-1. The data bits are encoded using a rate 1/4 binary convolutional code and the four encoded symbols are used to determine one of 16 frequencies or tones to be transmitted. To choose the number of data bits to shift into the encoder for each tone transmitted with the use of sequential decoding, for an efficient system, the work of Jordan (Reference 2) was used. It was determined that two data bits shifted into the encoding register at a time should be used, making the overall code of rate two, i. e., for each tone transmitted, two data bits are shifted into the encoder. With Viterbi decoding the same encoding procedure was used and encouraging simulation results were obtained. The codes used were binary convolutional codes for long constraint and sequential decoding (Reference 3) and short constraints with

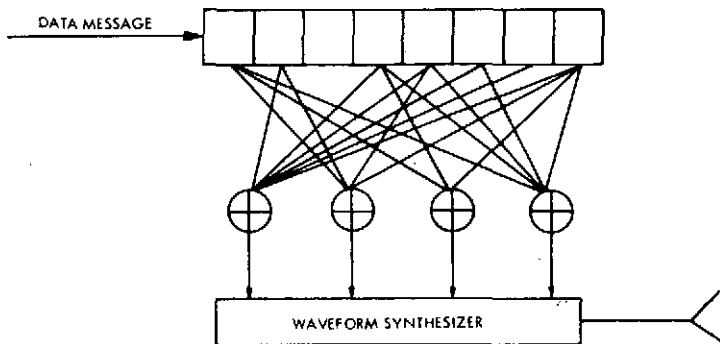


Figure 7.6E-1. Convolutional Encoder and Modulator

Viterbi decoding (Reference 4). A constraint length of 16 was used for sequential decoding of minimum free distance 22 and a constraint length 8 code of minimum weight 22 for Viterbi decoding. In using Viterbi decoding with nonbinary signal sets, others (References 5 and 6) have used an orthogonal coding method that uses a constraint length such that 2^k equals the number of signals in the signal set. We have used the method described above to utilize longer constraint lengths.

The decoding metrics used with the MFSK receiver outputs were;

$$M_j = \log \left[I_0 \left(\sqrt{E r_j / \sigma} \right) \right] - \log \left[\sum_{\ell=1}^{16} I_0 \left(\sqrt{E r_\ell / \sigma} \right) \right]$$

for sequential decoding and

$$M_j = \log \left[I_0 \left(A r_j / \sigma^2 \right) \right]$$

for Viterbi decoding, where

j = tone index,

E = tone energy, $A^2 T / 2$,

r_j = amplitude of receiver output for j th tone,

σ^2 = additive with Gaussian noise variance,

I_0 = modified Bessel function of the first kind of order zero.

Sixteen levels of quantization were used.

Digital computer simulations were carried out and the results are given in Figure 7.6E-2. The curve for the sequential decoder performance is based on 110 000 bits and the curve for Viterbi decoder performance is based on 20 000 bits. The sequential decoder results are based on frames of 1000 data bits and allowing a maximum of 200 000 computations before frame deletion. Adequate data to compute the frame deletion rate for sequential decoding was not obtained. The theory for computational behavior discussed in Appendix 7.6D will be applicable, however.

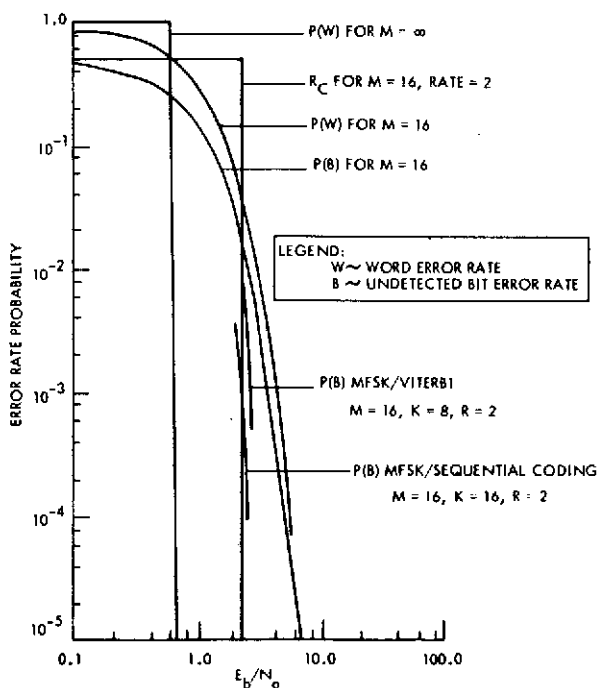


Figure 7.6E-2. MFSK Performance with Sequential or Viterbi Error Correcting Coding

From Figure 7.6E-2 it is observed that the required E_b/N_0 to obtain an undetected bit error rate of 10^{-3} is 2.4 dB using Viterbi decoding. This is 0.2 dB greater than the E_b/N_0 required to obtain a deletion rate of 10^{-2}

using PSK and sequential decoding. It is worthwhile to note that the Viterbi decoder performance is about 1.0 dB inferior to the sequential decoder performance even though the minimum weights of the codes used were identical. Since the Viterbi decoder is "maximum-likelihood" its performance should equal or exceed that of the sequential decoder. This discrepancy could be a result of insufficient data, or the encoding method used with Viterbi decoding, and further simulation is required to resolve this question. The moderate constraint length ($K = 16$) was used with sequential decoding as an attempt to reduce the computations at low signal-to-noise ratios. However, theory and further simulations have verified that the computational behavior is only a weak function of constraint length so that a long constraint length should be used with an increased minimum free distance. This would improve the sequential decoder performance somewhat and it follows that the coded MFSK and coded PSK systems provide equivalent performance to within 0.1 to 0.2 dB. The coding gain in the MFSK system is 2.0 dB using 16 tones, while for PSK the coding gain is about 6.0 dB at a bit error rate of 10^{-4} .

2. UNCODED MFSK PERFORMANCE WITH OSCILLATOR INSTABILITIES, DOPPLER AND CHANNEL FADING EFFECTS INCLUDED

To design an MFSK system it is necessary to take into account the effects of oscillator instabilities, Doppler frequency shift, and channel fading. These will be discussed separately and then the combined effect will be considered.

2.1 Oscillator Instability Effects

In any MFSK system the transmitted frequencies will not be pure tones due to oscillator instabilities in the transmitter. The effect of this is to degrade the bit error performance and the degradation is considerable at low data rates (less than 10 tones per second). Frequency jitter or linewidth results in a decrease in receiver output signal-to-noise ratio. Assuming that the oscillator frequency is a Gaussian random process, $w(t)$, stationary over a tone period T , with mean equal to the carrier frequency and variance σ_w^2 the degradation factor is given by Reference 7,

$$L_s = \frac{\pi}{2} \left[\frac{1}{\sigma T} \operatorname{erf} \frac{\sigma T}{\sqrt{2}} \right]^2$$

This factor is valid provided that the sum frequency $2W_i$, of any i th frequency of the signal set, is not an element of the signal set. The signal-to-noise ratio degradation factor L , is plotted in Figure 7.6E-3. The factor L is a function of the symbol period T and the frequency variance σ^2 , and decreases with T and/or σ^2 , ranging between 1 and 0. As σ^2 approaches 0, L approaches 1. The factor L is symmetrical in σ and T . However, for any physically realizable method of frequency stability measurement, σ^2 will increase as the measuring interval becomes smaller (References 8 and 9). The measuring interval should be the Nyquist sampling interval $1/2WT$ where W is the signal bandwidth. For low data rates these measurement intervals are practical, while for high data rates (data rates ≥ 10 tones per second) the noisy oscillator effect is negligible for any reasonably good oscillator so that the measurements are not critical.

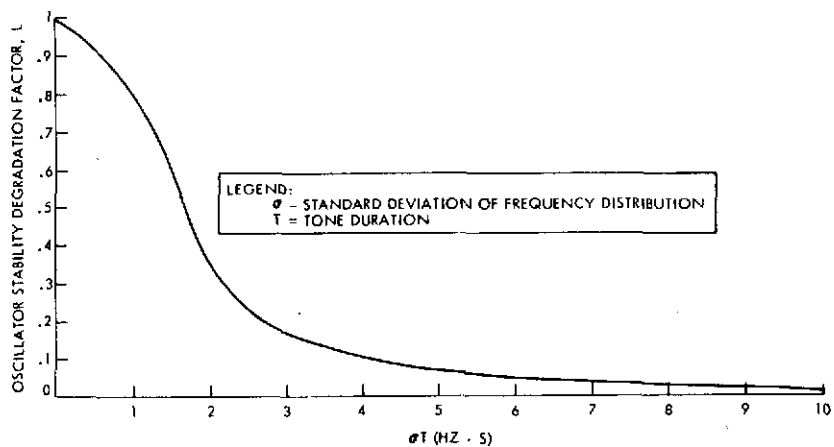


Figure 7.6E-3. SNR Degradation in MFSK Due To Oscillator Instabilities

We have computed the performance for MFSK using the FFT through simulation, and this performance is given in Figure 7.6E-4. The simulation assumes an oscillator of Gaussian frequency distribution with standard deviation, σ , of 1 Hz at a transmitted frequency of 2.3 GHz, when measured over an interval of 0.002 seconds. For a signal set of 16 frequencies separated by 16 Hz each, the Nyquist sampling interval of $1/2W = 1/512$ Hz ≈ 0.002 seconds was used assuming independence in the frequency noise from sample to sample. In fractional terminology this means that the signal frequency will be accurate to one part in 2.3×10^9 , 68 percent of the time when measured over a 0.002-second time interval. Studies

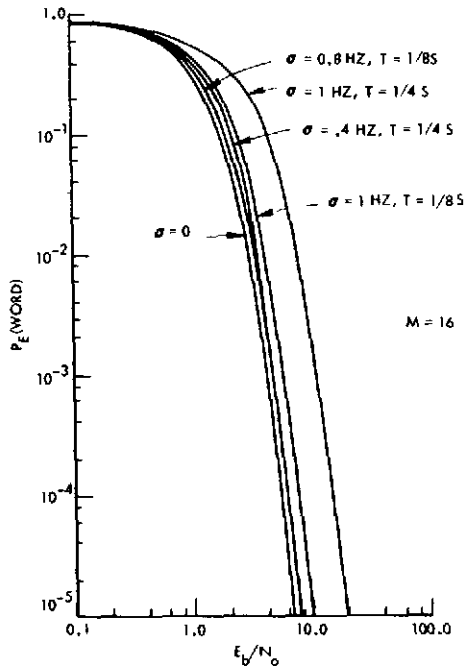


Figure 7.6E-4. MFSK Performance with Frequency Impurities

(References 8 and 10) indicate that this is a realistic criterion. As the frequencies are separated farther to allow for signal uncertainties the frequency purity criterion becomes more stringent. It can be observed from Figures 7.6E-3 and 7.6E-4 that the L factor is somewhat optimistic, however in the simulations the assumption that the sum term not be in the signal set was violated. Note from Figure 7.6E-4 that efficiency degrades considerably for rates less than about 8 tones/second.

2.2 Doppler Effects

The effect of frequency shifts due to Doppler presence is to move the signal away from the center of passband of the predetection filter so that the output signal-to-noise ratio is lowered. A rule of thumb used in designing MFSK systems is that the amount of frequency shift occurring during one symbol period should not exceed the symbol rate. A study by Jean (Reference 11) has to some extent verified this for the case of a linear Doppler rate, which is not tracked during the symbol period. We have computed the MFSK performance in the presence of a linear Doppler rate by using the FFT for detection. Using 16 frequencies, the frequency separations that are sufficient to avoid interfrequency interference were found experimentally.

The input signal used is given by,

$$X(t) = A \cos \left(\omega_i t + 1/2 dt^2 \right) = A \cos \theta(t),$$

where $d\theta/dt = \omega_i + dt$ is the instantaneous frequency.

Figure 7.6E-5 gives the FFT performance for a selected set of parameters, d and T . The signal was assumed to be perfectly aligned at the beginning of each symbol time and no algorithms for tracking the Doppler shift during the symbol period or for doing Doppler compensation were used. The figure shows that in the presence of high Doppler rates it is more efficient to avoid using very low data rates.

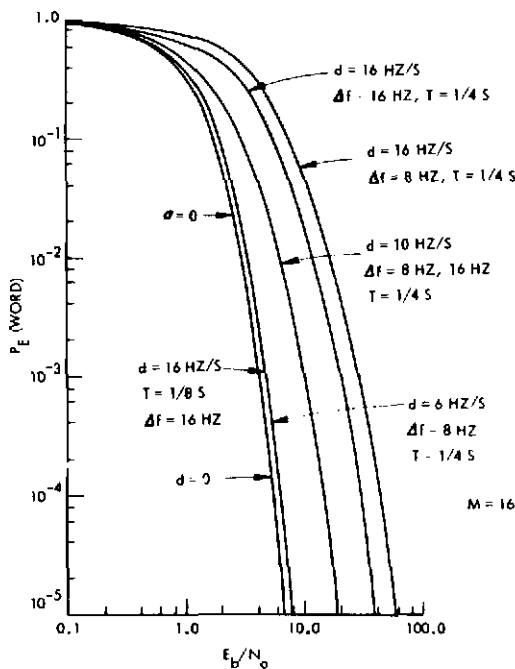


Figure 7.6E-5. MFSK Performance with Linear Doppler Rate

2.3 Fading Effects on MFSK

The effects of fading on MFSK have been studied by Lindsey (Reference 12) who presents curves for Rician fading for binary FSK. These results have been extended to the $M = 16$ case in Figure 7.6E-6. Channel fading is described in Appendix 7.6B in detail and the discussion will not be repeated here. Briefly $2\sigma_F^2$ represents the fraction of the total transmitted signal power that has been diverted into the fluctuating part of the received signal

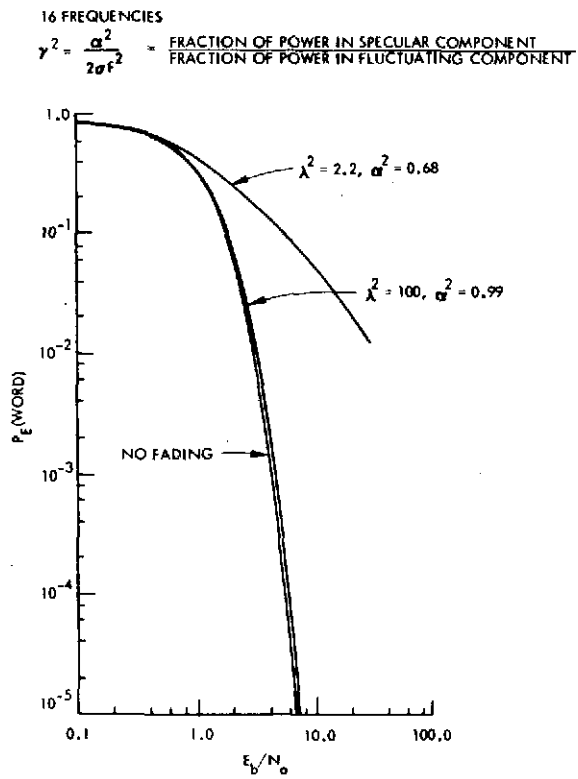


Figure 7.6E-6. MFSK Performance with Fading

while α^2 is the power in the specular component. The MFSK detector amplitude probability density function is characterized by

$$\gamma^2 = \frac{\alpha^2}{2\sigma_F^2}$$

Figure 7.6E-6 includes curves for $\alpha^2 = 0.99$ and $\alpha^2 = 0.68$. The value $\alpha^2 = 0.68$ was used because at the time the curves were computed it was thought that this was the value anticipated on Pioneer Venus probes. Since these computations, however, the lognormal fading model has been found to be more appropriate than the Rician model. This factor, in addition to more moderate fading channel parameter value has reduced to expected fading on the Pioneer Venus probe channels.

2.4 Combined Effects of Oscillator Instabilities and Doppler Rates on MFSK

It is important to compute the combined effect of oscillator instabilities and Doppler rates on MFSK. The MFSK performance with linewidth

(frequency impurity) and linear Doppler rates was computed through simulation using the FFT. The results are shown in Figure 7.6E-7. It can be observed that for Doppler rates larger than 6 Hz/second with a signal half-linewidth of 1 Hz, a symbol period of $T = 1/8$ seconds results in more efficient communication than does $T = 1/4$ second.

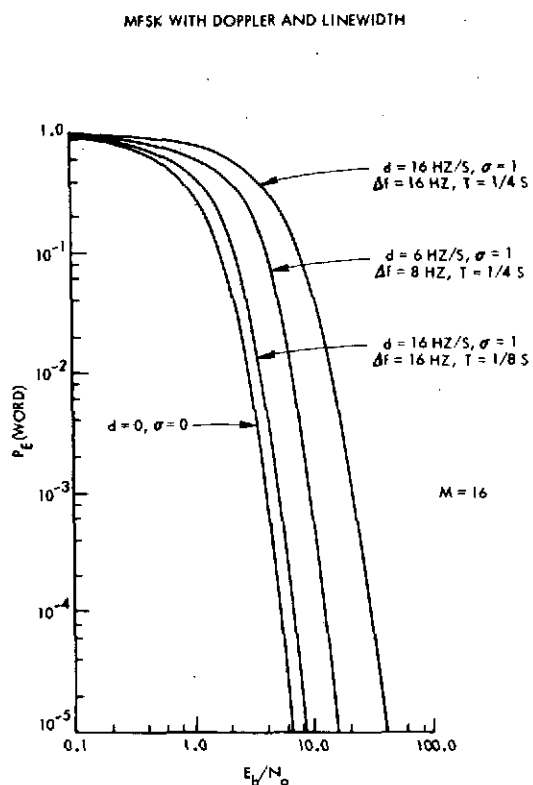


Figure 7.6E-7. MFSK Performance with Doppler Rates and Frequency Impurity

3. OFF-LINE ACQUISITION AND TRACKING METHODS

A method for acquisition in real time is given in Reference 13. A method for off-line signal acquisition will be discussed here. This has application in the case where the entire received signal has been recorded on tape. The recording has been made over a bandwidth sufficiently great to include all frequency uncertainties, which means that the actual received information bearing signal lies in only a fraction of the recorded band, i. e., in cases wherein the precise frequency band of the received signal is unknown a much greater band must be used in the recording process to avoid losing the signal. The acquisition in this case involves locating the signal band, B_s , within the total received band, B_T .

In doing off-line acquisition our philosophy is to use all the time available to lower the signal-to-noise ratio threshold at which a signal can be acquired. The acquisition must be accomplished in a minimum number of symbol periods to allow for large amounts of uncompensated Doppler effects. Of course, reasonable time limits must be set and we consider 2 or 3 general purpose computer hours to be in order. It can be seen from the conclusions of this study and Reference 1 that the acquisition signal-to-noise ratio threshold is perhaps the key parameter in designing such low data rate MFSK systems. The criteria used in designing an acquisition method have been required signal-to-noise ratio and number of computations. The types of frequency bands considered typical are $B_s = 720$ Hz and $BT = 9$ kHz. The following acquisition method takes advantage of the non real time environment and effectively uses a matched filter technique in the frequency domain. The algorithm essentially does frequency and time acquisition together using iterations of a basic loop.

A flow chart of the acquisition algorithm is given in Figure 7.6E-8. To begin acquisition a time origin is arbitrarily chosen, the FFT is computed over the entire recorded spectrum, and the frequency of largest amplitude is chosen. Ordinarily there will be many errors because of time origin errors and because the signal-to-noise ratio used will be only that required to give acceptable MFSK performance over bandwidth, B_s , when M choices are made. This signal-to-noise ratio will result in very poor performance when operating over bandwidth, B_T , and all frequencies spaced $1/T$ apart because of the numerous possible choices. We continue the algorithm by computing the FFT and choosing the frequency of greatest amplitude for K symbol periods with time origin fixed. The resulting K amplitudes are summed with respect to frequency resulting in a "sum spectrum," S_s , with non-zero entries at each frequency where a greatest FFT amplitude was achieved. At this point we would like to separate out the signal amplitudes from the noise amplitudes in S_s using any knowledge available about the signal and also narrow in on the signal band center. To do this we use a window function, S_w , which is matched to the signal in that S_w is B_s Hz wide and has non-zero entries separated by the signal spacing (e.g., the signal spacing may be 48 Hz while the spacing of the FFT outputs or S_s is $1/T$ Hz). Convolving S_s with S_w gives a spectra, S_c , which can be

used to determine the center of S_c , i.e., compute

$$S_c = S_s * S_w$$

and choose the frequency of largest amplitude to be the signal band center. At this point the time origin is shifted by an increment Δt and the procedure is repeated. After the procedure is repeated N times, where $N\Delta t = T$ are N sets of spectra S_c , and the time origin and signal band center are chosen to correspond to the frequency of the $N S_c$ having the largest amplitude.

Figure 7.6E-9 illustrates an example.

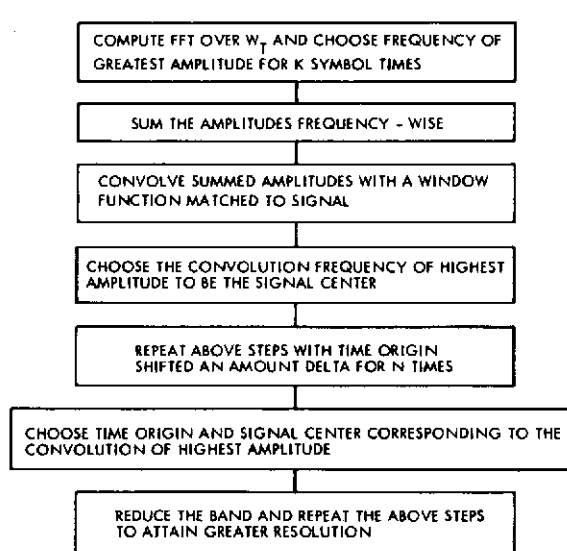


Figure 7.6E-8. Off-Line Frequency Tracking Sequence

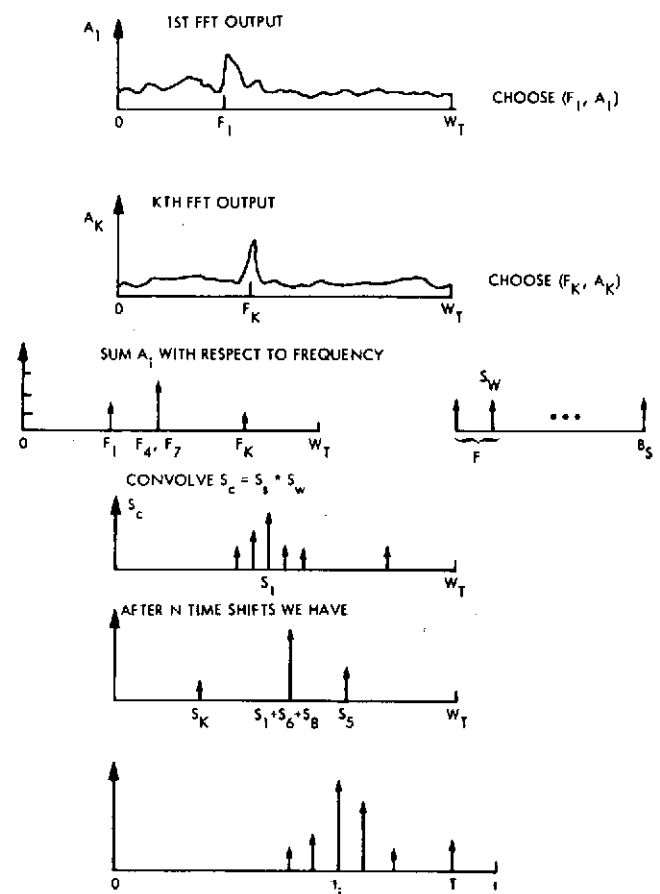


Figure 7.6E-9. Illustration of Acquisition Method

After the N time origin shifts, the maximum amplitudes can be observed and the choice of the largest amplitude can be made. Our simulations were done this way. However, the N largest amplitudes with respect to time can be filtered to eliminate any spurious amplitudes and the largest amplitude of the filtered array can be chosen automatically.

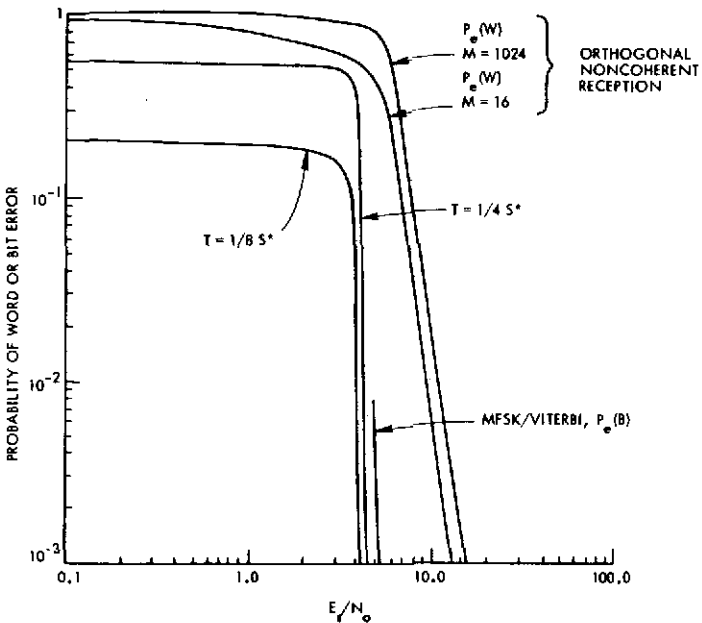
After a time origin and signal band center have been chosen for B_s with respect to B_T , and if K is not large (i.e., the number of symbol periods is not large) to avoid loss in frequency resolution due to Doppler shifts there will remain some uncertainty as to the signal band center. Nonetheless, the chosen frequency will be within $\pm B_s$ of the signal center, i.e., B_T has been narrowed to a band $2 B_s$ wide. There will be no discrepancy with respect to the chosen time origin. Using only the chosen time origin and the B_s band, the above process can be repeated to narrow the $2 B_s$ band. Our simulations have shown that it is very easy to get the $2 B_s$ band down to a band of $B_s + 2/T$ Hz, at which point the tracking algorithm can be used.

This is not a closed-loop algorithm as required for real-time applications (there is no need for a closed loop), and it is felt that a closed-loop algorithm would increase the frequency error variance. The number of time origin shifts required for $1/8 \leq T \leq 1/4$ is not great. For example, with $T = 0.20$ second if we choose $\Delta t = 0.02$ we need only use 10 shifts of the time origin ($10 \Delta t = 0.2 = T$) to be within a negligible time error. For $T = 1/8$ second, fewer shifts of the origin are required. For K in the order of 20 or 30 (we used only 16) this does not involve much time on a high-speed digital computer for $B_T = 9$ kHz, and the time is fairly negligible if a hardware FFT box is used. Notice that a known transmitted sequence has not been used. Also it should be kept in mind that this procedure can be applied anywhere on the recorded signal, hence it is best to do the acquisition where any uncompensated Doppler effects, etc, are minimum.

To derive the performance of this acquisition analytically has proven to be rather formidable and the difficulties are shown in Reference 7. The performance has been computed by digital computer simulation for $T = 1/8$ and $T = 1/4$, assuming correct timing, and is given in Figure 7.6E-10. For these curves the total recorded band B_T is 8192 Hz and the signal band B_s is 720 Hz representing 16 frequencies separated by 48 Hz each. The vertical axis gives the average error rate and the horizontal axis is of the symbol energy to single sided noise spectral density ratio, E_s/N_o . The curves on the right are the word error rates for an MFSK system with $M = 16$ and $M = 1024$ orthogonal frequencies. The $M = 1024$ curve is the performance that can be expected when the acquisition algorithm is making

FREQUENCY ACQUISITION PERFORMANCE
 $B_T = 8192 \text{ Hz}$, $B_s = 720 \text{ Hz}$, B_s HAS 16 FREQUENCIES SPACED 48 Hz

W = WORD ERROR RATE
 B = BIT ERROR RATE



*PROBABILITY THAT CONVOLUTIONAL FREQUENCY WITH MAXIMUM AMPLITUDE DOES NOT LIE IN SIGNAL BAND

Figure 7.6E-10. Acquisition Method Performance

choices over the entire recorded band of $B_T = 8192 \text{ Hz}$, with $T = 1/4 \text{ second}$. In this case there are 1024 orthogonal frequencies separated by 4 Hz each represented by the FFT outputs. The $M = 16$ curve gives the performance for the system after acquisition assuming no further coding is used. The curves labeled $T = 1/4 \text{ second}$ and $T = 1/8 \text{ second}$ are for the acquisition algorithm performance assuming perfect timing, and frequency alignment and using $K = 16$ symbol periods. An error is declared if the frequency having the largest amplitude out of the convolution array, S_c , does not lie within the signal band, B_s . It can be seen that for the same value of E_s/N_o the error rate when using $T = 1/8 \text{ second}$ is less than for $T = 1/4 \text{ second}$. However, for E_s/N_o to be the same at $T = 1/8 \text{ second}$ as for $T = 1/4 \text{ second}$ the signal power required is $\sqrt{2}$ times as great. For the same signal power, the performance is actually superior when using $T = 1/4 \text{ second}$.

Using some approximations a fairly accurate performance analysis can be made. For $f = 8 \text{ Hz}$ ($T = 1/8 \text{ second}$), the probability that two noise-only components will enter into a convolution component is given by Reference 7,

$$\left(\frac{M\Delta f}{B_T}\right)^{N_1} = \left(\frac{16 \times 8}{8192}\right)^2 \approx 2 \times 10^{-4}$$

which is quite small and will be neglected. The probability that a convolution component that consists of a sum of at least two signal plus noise FFT outputs is greater than all convolution components, which consist of only a single noise FFT output, can be assumed to be very close to 1. Using these approximations, successful signal acquisition will be accomplished if only two correct decisions are made over the $B_T = 8192$ Hz band when $M = 16$ symbol periods are used. This means that a word error rate of $1 - 2/16 = 7/8$ can be tolerated for successful acquisition. From Figure 7.6E-10 it can be seen that this point on the curve labeled $M = 1024$ ($8192/8$) is approximately where the acquisition curve labeled $T = 1/8$ second becomes steep.

For $T = 1/4$ second a reference curve for 2048 possible frequencies must be used. The performance will be poorer than for $T = 1/8$ second with respect to E_s/N_o because of the increase in number of choices. When impure signal frequencies are received, the reference curves must be adjusted to allow for this (see Section 2.1).

The curves for the acquisition algorithm are considerably better than required for the MFSK systems so that one may be led into thinking that the performance is better than need be. However, if additional coding using error correcting techniques is employed, the performance of such an MFSK system is considerably better. The performance of a system using a convolutional error correcting code of constraint length 8 with Viterbi decoding and shifting two data bits into the encoder for each transmitted symbol is given by the curve labeled "MFSK/Viterbi" (Reference 1). Such a system operates at an error rate of 10^{-4} at $E_s/N_o = 6.0$ and will do better using a longer constraint length in the encoder. It can be observed that this acquisition algorithm is compatible with the MFSK and Viterbi decoding for error rate of 10^{-4} , i.e., at the E_s/N_o required by the code to achieve an error rate of 10^{-4} , acquisition can be accomplished. If a much better code were used a much smaller value of E_s/N_o would be required to achieve this error rate, however, acquisition could probably not be accomplished. The code would be of benefit if lower error rates were desired at the E_s/N_o required for acquisition, but the E_s/N_o cannot be lowered beyond that required to achieve the signal acquisition.

Some comments must be made concerning the assumptions used in computing the curves of Figure 7.6E-10, i.e., timing synchronization and frequency alignment of the signal with the FFT output lines. The parameter on which correct timing hinges mostly is the value of E_s/N_o required to give acceptable acquisition assuming correct time synchronization. A sample run for time acquisition is given in Figure 7.6E-11. We have not been able to compute time acquisition performance (variance and mean of the timing error) analytically, nor have we done extensive simulation in this regards. The simulations we have done have given the correct results at $E_s/N_o = 5.0$, however. It is difficult to conceive of a method that can give better resolution since the time increments, Δt , used in time synchronization can be made negligibly small without impractical computation loads for practical symbol rates (4 to 8 transmitted symbols per second).

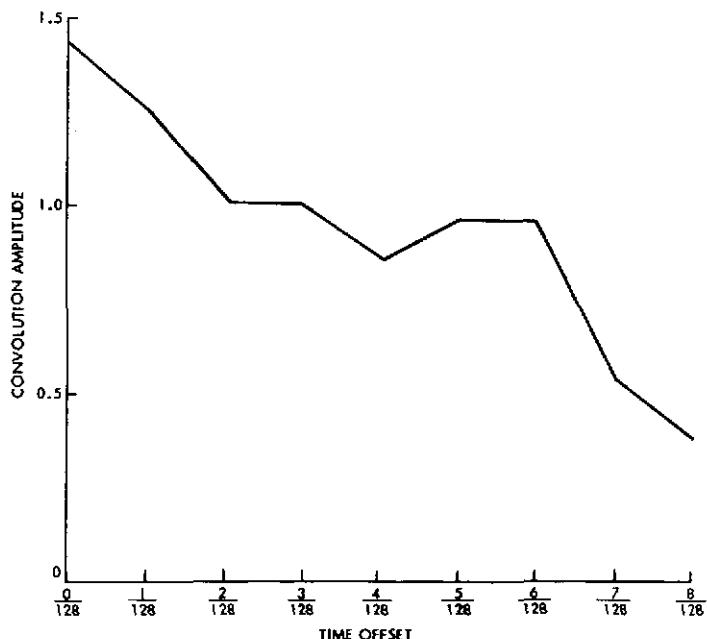


Figure 7.6E-11. Acquisition Sample Run with Time Acquisition Included

The effect of frequency misalignment of the actual signal with the FFT lines is such that frequency detuning errors should be less than 0.1 of $1/T$, the FFT frequency line separation in order that the resulting degradation in performance be negligible (Reference 13). Our simulations of the acquisition algorithm have indicated that for good acquisition at $T = 0.25$ seconds

and $E_s/N_o = 5.0$ dB, the frequency error should be less than about 0.5 Hz. If the error is larger than this, compensations must be made by increasing E_s/N_o , interpolation on the complex FFT outputs, or perhaps creation of multiple tapes recorded at slightly different frequencies. Interpolation on the complex FFT outputs (References 14 and 15) is the simplest of these, and can reduce the effect of the worst-case situation (when the frequency error is half the FFT frequency spacing) to negligible effects on acquisition performance quite easily when $T = 1/4$ or $T = 1/8$ second.

Tracking and MFSK - Tracking methods with MFSK in real time have been considered by Chadwick (Reference 13) and Goldstein (Reference 16). Successful frequency tracking of a signal with linear Doppler rate of 0.025 Hz/second was reported by Chadwick. Planetary entry probes will typically experience Doppler rates up to 16 to 20 Hz/second. For cases where the data rate is low enough for MFSK to be preferred to PSK, off-line processing most often will be possible. In this case a frequency band wide enough to include all Doppler shifts will be used in the recording process, and the frequency tracking can be done off-line. For doing off-line tracking it seems plausible to use a more brute force type approach instead of the usual real-time approach of obtaining an error term (hopefully an S-type function), which is filtered and used in a local VCO. A block diagram for an off-line method of tracking is given in Figure 7.6E-12. Instead of computing an error term that is used to determine a VCO frequency change, the VCO (i.e., digital VCO) simply tries all frequencies separated by frequency increments equal to the minimum frequency error acceptable. The VCO frequency that results in the maximum amplitude out of the FFT is chosen to be the correct reference frequency. The tracking is combined with the digital filtering used to extract the signal band, B_s , out of the total recorded band, B_T . Hence, after acquisition, the FFT is computed only over a digital bandpass version of the signal band, B_s . The loop will also diminish the frequency error resulting from the actual signal not being aligned exactly to the FFT lines. The bandpass used at a particular symbol time is centered according to where the signal band was located on the previous symbol time by the tracking loop. The bandpass must be wide enough, then, to include any frequency shifts that could have occurred during the previous symbol interval. The bandpass can be chosen

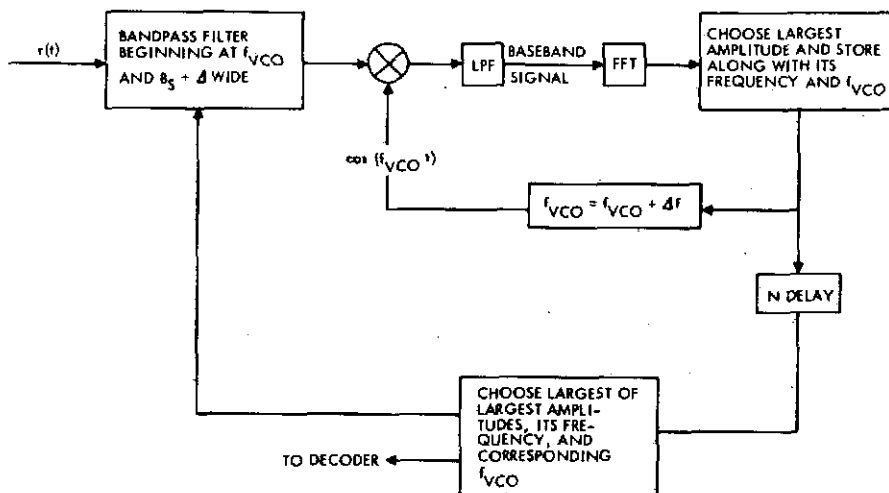


Figure 7.6E-12. Off-Line Tracking for MFSK Signal

at the beginning of the tracking effort and be held constant during the entire message or the loop could be made to accept inputs governed by the expected Doppler profiles to vary the bandpass width. The low pass filter (LPF) passes a band wide enough to include the signal band, B_s . This tracking method has not been implemented and further investigation will be made on a future study.

For short transmission times (1 to 2 hours) symbol synchronization should not be required on low data rate channels. For this reason this problem has not been considered here.

REFERENCES

1. C. C. Korgel, "Error Control Techniques for Communication Channels," Final Report, IRAD Task No. 48744, Martin Marietta Corporation, Denver, Colorado (December 1972).
2. K. L. Jorden, "The Performance of Sequential Decoding in Conjunction with Efficient Modulation," IEEE Trans. Communication Technology, Vol. COM-14, No. 3, p. 283.
3. D. J. Costello, "A Construction Technique for Random-Error-Correcting Convolutional Codes," IEEE Trans. Info. Theory, p. 631 (September 1969).
4. R. B. Blizzard, C. C. Korgel, et al., "Study of Potential Applications of Digital Techniques to the Apollo Unified S-Band Communications Systems," Phase 2 Final Report, Martin Marietta Corporation, Denver, Colorado (1970).

5. A. J. Viterbi, "Orthogonal Free Codes for Communication in the Presence of White Gaussian Noise," IEEE Trans.-Comm. Tech., Vol. COM-15, p. 238 (April 1967).
6. A. R. Cohen, J. A. Heller, and A. J. Viterbi, "A New Coding Technique for Asynchronous Multiple Access Communication," IEEE Trans. Comm. Tech., Vol. COM-19, No. 5, p. 849 (1971).
7. C. C. Korgel, "Techniques for Noncoherent Communication," Final Report, IRAD Task No. 48624, Martin Marietta Corporation, Denver, Colorado (December 1972).
8. M. E. Frerkling, "Short Term Frequency Stability Measurements," Internal Report, Collins Radio Company.
9. E. J. Baghelady, et al., "Short Term Frequency Stability: Characterization, Theory, and Measurement," Proc. of the IEEE, p. 704 (July 1965).
10. L. R. Malling, "Phase Stable Oscillators for Space Communications," Proc. IRE (July 1962).
11. F. H. Jean, "Performance of a Conventional MFSK Receiver in the Presence of Frequency Drift," JPL SPS 37-50, Vol. III, p. 338.
12. W. C. Lindsey, "Coded Noncoherent Communications," IEEE Trans. on Space Electronics and Telemetry, Vol. SET-11, p. 6-13 (March 1965).
13. H. D. Chadwick and J. C. Springett, "The Design of a Low Data Rate MFSK Communication System," IEEE Trans. on Communication Technology, Vol. COM-18, No. 6 (December 1970).
14. G. D. Bergland, "A Guided Tour of the Fast Fourier Transform," IEEE Spectrum, p. 41 (July 1969).
15. R. B. Blackman, J. W. Luckey, "The Measurement of Power Spectra," Dover Publications, Inc., New York (1958).
16. R. M. Goldstein, "Low Data Rate Communication: Block-Coded Frequency Shift Keying," JPL SPS 37-55, Vol. II, p. 30.

APPENDIX 7.6F

**RADIO ABSORPTION AND DEFOCUSING LOSSES
IN THE VENUS ATMOSPHERE**

APPENDIX 7.6F
RADIO ABSORPTION AND DEFOCUSING LOSSES IN
THE VENUS ATMOSPHERE

1. SUMMARY

Radio propagation losses in the Venus atmosphere for probe-to-earth direct links include: (1) absorption; (2) defocusing; and (3) turbulence. This Appendix summarizes and draws conclusions from pertinent studies as to the separate and combined effects of absorption and defocusing. The effects of turbulence were discussed in Appendices 7.6A and 7.6B.

In particular, microwave absorption losses on data taken via earth-based radar stations and the Mariner V radio occultation experiment are discussed. The discrepancy between the absorption losses found by analyzing earth-based radar measurements and measurements provided by processing the Mariner V occultation data remain, at this time, unexplained. The absorption and defocusing losses developed by Croft et al. of Stanford are then compared with the computations made at Martin Marietta. On the basis of the above comparisons and results, recommendations are made for assessing the absorption and defocusing losses as a function of altitude using the Martin Marietta approach. The recommended approach is used in preparing the link design control tables.

2. ABSORPTION ON VENUS EARTH-BASED RADAR DATA VERSUS THE MARINER V RADIO OCCULTATION RESULTS*

The analysis of the Mariner V occultation experiment by Fjeldbo et al., (Reference 1) found anomalous absorption losses that cannot be satisfactorily matched to the absorption losses found from earth-based radar measurements (References 2, 3). This section describes our re-working of some of these data in an attempt to resolve this discrepancy. This proved to be unsuccessful, and the differences between the occultation and the radar data remain unexplained.

*Section 2 of this Appendix is a re-edited copy of a Martin Marietta Technical Note; R. J. Richardson and J. A. Camp, "Microwave Absorption on Venus Earth-Based Radar Data vs the Mariner V Radio Occultation Results," November 1971.

We first reviewed our method of calculating the absorption, and decided to revise the method used earlier (Reference 4). It was decided that the expression due to Ho (Reference 5), for attenuation

$$\alpha = C \frac{P^2}{\lambda^2 T^5} \text{ dB/km}, \quad (1)$$

$$C = 6.61 \times 10^9 \left(15.7 A_{CO_2}^2 + 3.9 A_{CO_2} A_{N_2} \right. \\ \left. + 0.085 A_{N_2}^2 + 1330 A_{H_2O} \right)$$

would be used, with some modifications, for computing the effects of water in the deeper portion of the atmosphere, while that due to Bean (Reference 6) would be used, also with modifications, for the effects of water in the upper atmosphere. The Ho expression with the water term omitted is used for the whole atmosphere in computing CO_2 and N_2 losses.

One modification that was made to both the Ho and the Bean expressions was a correction for the composition of the foreign gases causing spectral broadening on Venus. The atmosphere is modeled as 95% CO_2 and 5% N_2 . Ho's water term in Reference 1, $1330 A_{H_2O}$, is based on experiments using pure N_2 as the foreign gas. In the absence of experimental data, the best that can be done is scale this in proportion to the square of the kinetic cross-section of CO_2 relative to N_2 . This gives

$$\alpha_1(H_2O) = C \frac{P^2}{\lambda^2 T^5} \text{ dB/km}, \quad (2)$$

$$C = 6.61 \times 10^9 \left(1330 A_{H_2O} A_{N_2} + 1590 A_{H_2O} A_{CO_2} \right)$$

For the 95% CO_2 and 5% N_2 composition the bracketed term becomes 1577 A_{H_2O} . $\lambda = 13$ cm at the S-band frequency of interest, 2297 MHz.

The Bean approach uses the line-broadening parameter $\Delta T = 0.087P \times \left(\frac{318}{T}\right)^{1/2} \text{ cm}^{-1}$ for air as the foreign gas. Revising this for the Venus atmosphere gives

$$\Delta T = 0.1022 P \left(\frac{318}{T}\right)^{1/2} \text{ cm}^{-1} \quad (3)$$

Bean's expression has two terms. The nonresonant term is

$$\alpha_2(H_2O) = \frac{0.05 \Delta T}{\lambda} - \rho \left(\frac{293}{T} \right) \text{ dB/km}, \quad (4)$$

$$\rho = 219700 \frac{P}{T} A_{H_2O} \text{ gm/m}^3 \quad (5)$$

The resonant term for the $r_o = 22$ GHz absorption line of water, simplified for $f \ll r_o$, is $\alpha_3(H_2O) = \rho K S$ where

$$S \triangleq \frac{2 \Delta T}{0.55 + \Delta T^2} \quad (6)$$

and

$$K \triangleq \frac{0.0318}{\lambda^2} \left(\frac{293}{T} \right)^{5/2} \exp \left(-\frac{644}{T} \right)$$

Bean's expression is $\alpha(H_2O) = \alpha_2 + \alpha_3$. Ho states that his expression does not include the effects of the 22 GHz line, which would be resolved at lower pressures, so we further modified Ho's expression to $\alpha(H_2O) = \alpha_1 + \alpha_3$. For high pressures $\alpha_3 \ll \alpha_1$, so this modification has negligible effect at higher pressures. The question of where to change from the Bean to the Ho approach was resolved by taking

$$\alpha(H_2O) = \min (\alpha_1 + \alpha_3, \alpha_2 + \alpha_3) \quad (7)$$

This was done because Ho's expression gives too high an attenuation for low pressures and Bean's expression gives too high an attenuation for high pressures. This puts the crossover around $P = 1$ atm, with the Bean form used above and the Ho form below this point.

Results are shown in Figure 7.6F-1 for several values of A_{H_2O} . The decibel loss from the surface inferred from radar data are also shown in Figure 7.6F-1. Taken together, these data indicate that a nominal value for A_{H_2O} is around 0.005, with 0.01 as a maximum value. The Venera in-situ measurements of A_{H_2O} are also shown. These are in reasonably good agreement with the radar data.

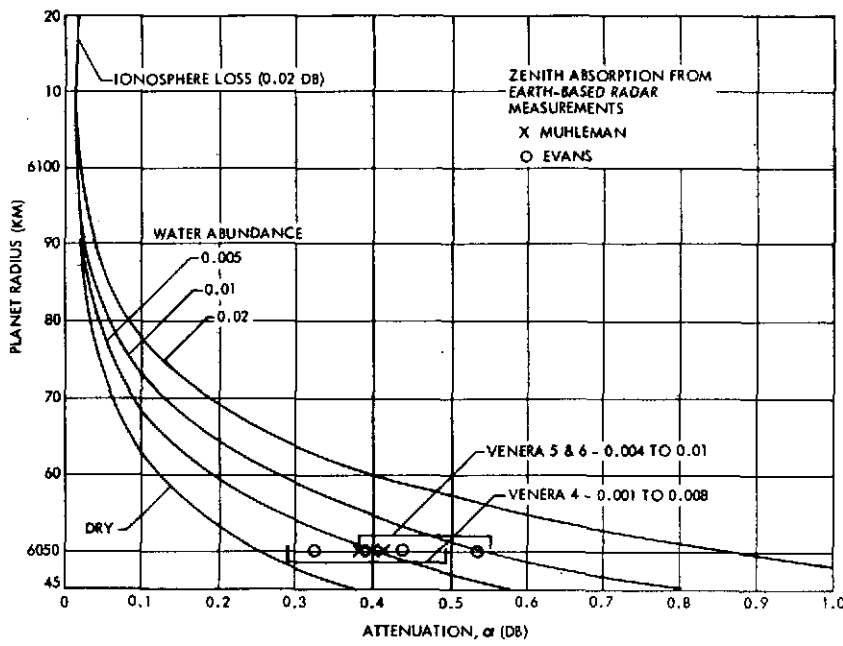


Figure 7.6F-1. Computed Zenith Absorption on Venus, 2.3 GHZ

The data required to reconstruct the occultation ray paths were not given in Reference 1, so the paths were approximated by a hyperbola as described below. Selecting a given radius for the ray's closest approach to the planet, the radius of curvature of a horizontal ray at the selected radius is given by (Reference 7):

$$r_c = \frac{nT}{(n-1) \left(\frac{gM}{R} + \frac{dT}{dr} \right)} \quad (8)$$

The asymptotes for the hyperbola were found from the refraction integral, which gives the total ray bending in an exponential atmosphere. The refraction integral for a horizontal look angle is (Reference 7):

$$E = N_o \left(1 + N_o \right) \int_0^\infty \frac{e^{-x} dx}{\left(1 + N_o e^{-x} \right) \left(1 + \frac{x}{\beta r_o} \right)^2 \left(1 + N_o e^{-x} \right)^2 - \left(1 + N_o \right)^2} \quad (9)$$

N_o and β were selected to match the model atmosphere at the point of the ray's closest approach. Given the radius of curvature at the point of nearest approach and the asymptotes, the hyperbola is readily constructed. The geometry is sketched in Figure 7.6F-2. A line integral of $\alpha(H_2O)$ from

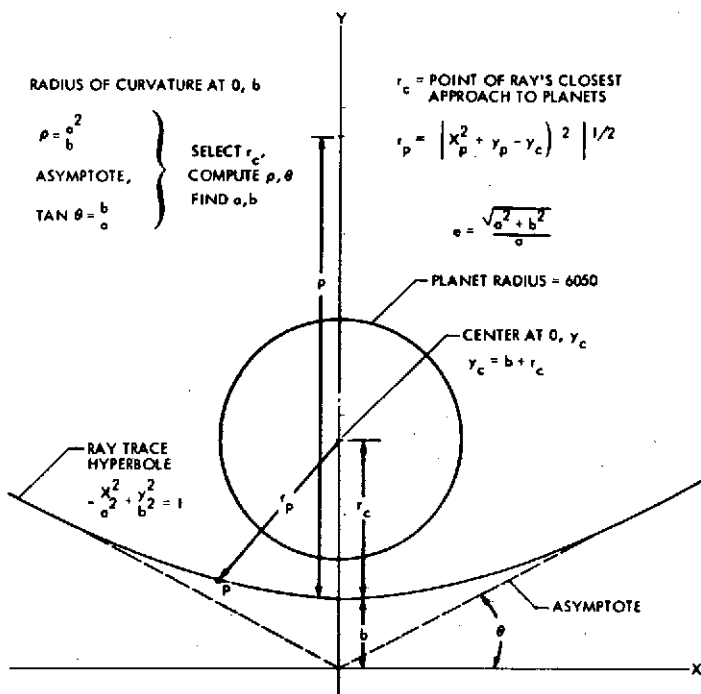


Figure 7.6F-2. Hyperbolic Approximation Geometry

Reference 7 along this hyperbola was then computed to give the total absorption as a function of A_{H_2O} . Results are shown in Figure 7.6F-3 along with

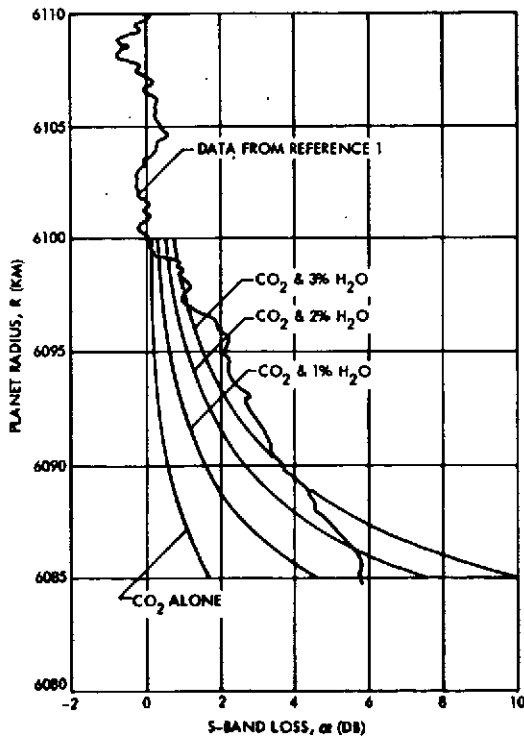


Figure 7.6F-3. Computed Absorption Loss for Four Values of Water Content Versus Loss Data from Reference 1

those given in Reference 1. It can be readily seen that no value of A_{H_2O} can be selected to match the curve given in Reference 1 over its entire length. The best match comes in the range $0.02 < A_{H_2O} < 0.03$, much higher than the A_{H_2O} inferred from the radar data.

Finally, as a check on the consistency of the hyperbola approach with the method used in Reference 1 to invert the occultation data, the computed α vs r plot given in Reference 1 was approximated as shown in Figure 7.6F-4 and this approximated α was used in the hyperbola program. As shown in Figure 7.6F-5, the resulting total attenuation data agree quite well with that given in Reference 1, confirming that the hyperbola is an adequate approximation to the actual ray path as computed in Reference 1.

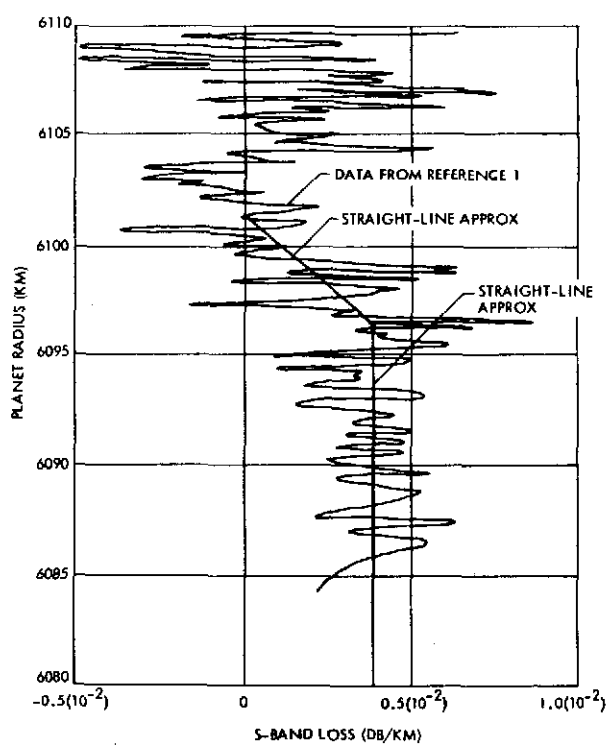


Figure 7.6F-4. Comparison of Straight Line Approximation of Absorption Loss to Computed Values of Reference 1

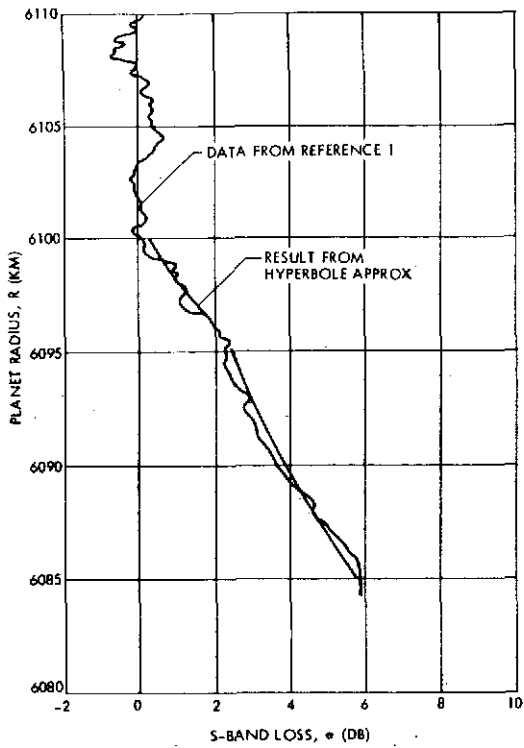


Figure 7.6F-5. Martin Marietta Computed Value of Total Absorption Using Hyperbolic Approximation as Compared to Data from Reference 1

It is difficult to conceive of any combination of atmosphere, clouds, or dust that would give a α vs r plot similar to that shown in Figure 7.6F-5. This, together with the apparently high confidence level given the radar data by nearly all of the investigators working in the area of Venusian microwave absorption, suggests that the radar data should be used as a basis for mission designs and the occultation data should be ignored. There are many possible sources of error in the occultation data. Probably the largest of these is an incorrect assessment of the signal loss due to pointing error in the high-gain antenna. Another is the losses suffered by the lower frequency (423 MHz) signal in the ionosphere. A third is the assumption that both signals follow the same path through the ionosphere and the atmosphere. Some attempt was made to account for all of these factors in Reference 1, but large errors may remain in the computations.

To summarize then, because of the sources of possible error in the occultation data, and the disagreement between these and other data, viz., earth-based radar observations (which is held to be quite reliable by the appropriate segment of the scientific community), it is concluded that the

occultation data should be disregarded. Also, because of the good agreement between earth-based radar observations and our results for an H_2O water abundance of about 0.005, it is further concluded that this value should be selected for a nominal value with 0.01 as a maximum value. Curves showing attenuation versus radius are shown for these abundances in Figure 7.6F-1. Also shown are the earth-based radar data and the Venera in-situ measurement data. It is noted that there is also relatively good agreement with the Venera data for abundances in the range just mentioned.

3. RADIO ABSORPTION AND DEFOCUSING LOSSES-VENUS ATMOSPHERE

Absorption and defocusing losses as a function of altitude and earth departure angle were calculated for the latest planet model as specified in Table 5 of SP 8011 (Reference 8) using the methods outlined in Section 2 of this appendix. The results are shown in Figure 7.6F-6 along with a few points from a Stanford University study (Reference 9). The latter analysis agrees quite well with Martin Marietta results at the 6050-km altitude but the attenuation falls off more gradually with altitude.

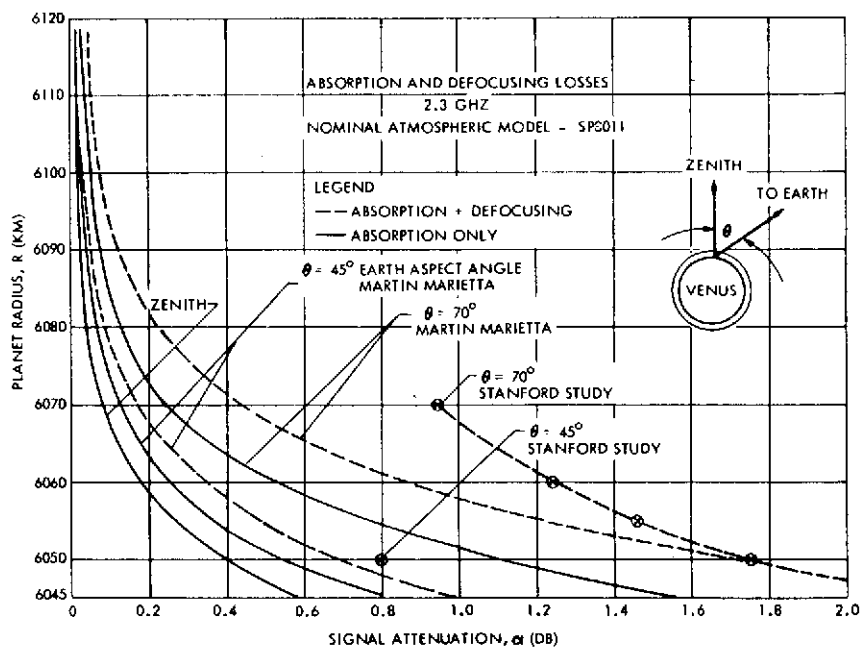


Figure 7.6F-6. Radio Propagation Losses, Venus Atmosphere

There are two basic differences between the Martin Marietta computations and those by Croft, et al. of Stanford (Reference 9). These are: the atmospheric models used at Stanford contain no gaseous H_2O , which

lowers the absorption relative to that given by Martin Marietta; and the Stanford study includes some "layering loss" not included by Martin Marietta, which raises the losses relative to those given in the Martin Marietta work. It turns out that at the surface these differences very nearly cancel each other; consequently both Reference 9 and Martin Marietta data give essentially the same loss from the surface. However, this is not true at higher elevations. Reference gives substantially more loss than Martin Marietta data at elevations above +60 km.

Now, let us consider which of these models is the more reasonable. Both agree reasonably well with the total loss from the surface as determined by earth-based radar, apparently by design. The absorption due to the dry CO₂ in the atmosphere is not enough to give this radar loss. The difference is made up at Martin Marietta by H₂O loss and in Reference 9 by layering loss. The technique used by Martin Marietta to determine the abundance of gaseous H₂O was simply to add H₂O until absorption loss matched that given by earth-based radar measurements. This gave results that agree with Russian in-situ measurements of H₂O abundance. There is substantial evidence for the presence of a significant amount of H₂O in the Venus atmosphere. Accordingly, the assumption of zero H₂O made in Reference 9 is contrary to existing evidence.

Now, if some H₂O is included in Reference 2 models, they will have to reduce their layering loss to remain in agreement with the earth-based radar data. Justification for the amount of layering loss used in Reference 2 is rather weak. It is based on Mariner occultation data, which did not penetrate deep into the atmosphere, arbitrarily extrapolated to the surface. The likelihood of significant layering deep in the turbulent atmosphere of Venus is very small on physical grounds, and no evidence of it was found by the Russian probes. Therefore, while there may be some layering loss in the stratosphere, this extrapolation to the surface is not reasonable.

It should also be noted that the explanation of the losses observed by Mariner 5 as "layering loss" is not strongly justified. These losses, if they exist at all, would appear most strongly on a near-horizontal path such as an occultation path, and would probably not be observable on the more nearly vertical paths corresponding to probe missions. The authors of Reference 9 make no allowance for this.

We conclude that our assumptions are more reasonable than those in Reference 9, and, therefore, the Martin Marietta results are used in the design control tables and link analyses.

4. GLOSSARY OF SYMBOLS FOR APPENDIX 7.6F

r_c	= Ray radius of curvature at its point of closest approach to the planet
r_o	= Distance from the ray to the planet center at its point of closest approach to the planet
n	= Index of refraction
T	= Temperature, (K)
g	= Planetary gravity
M	= Mean molecular weight of the atmosphere
R	= Universal gas constant
r	= Radius, measured from planet center
f	= Focal length of hyperbola used to approximate the ray path
a	= Parameter defining the hyperbola used to approximate the ray path
b	= Parameter defining the hyperbola used to approximate the ray path
A_x	= Abundance of gas X in the planetary atmosphere
P	= Pressure, atmospheres
α	= Absorption coefficient (dB/km)
λ	= RF wavelength (cm)
O, y_c	= The location of the planet center in the selected coordinate system
ρ	= Absolute humidity $(\text{gm/m}^3 \text{ of H}_2\text{O})$
N_o	= Refractivity
β^{-1}	= Scale height for refractivity

REFERENCES

1. C. Fjeldbo, A. Kliore, V. R. Eshleman, "The Neutral Atmosphere of Venus as Studied with the Mariner V Radio Occultation Experiments," J. Astron. (1971).
2. D. U. Muhleman, "Microwave Opacity of the Venus Atmosphere," J. Astron., 74, pp. 57-79 (1969).
3. J. V. Evans, "Variations in the Radar Crossection of Venus," J. Astron., 73, pp. 123-124 (1968).
4. R. J. Richardson, "Water Vapor and Communications on Venus," MMC Memorandum, May 28, 1971.
5. W. Ho, et al., "Laboratory Measurements of Microwave Absorption in Models of the Atmosphere of Venus," J. Geophys. Res., 71, pp. 5041-5108 (November 1, 1966).
6. B. R. Bean, et al., "Weather Effects on Radar," in Radar Handbook, M. Skelnik, Ed., (McGraw-Hill, 1970), Ch. 24.
7. "Study of a Venus Entry Mission," Final Report, Contract JPL 952534, Vol. II, Ch. VII-A, Martin Marietta Corporation (April 1970).
8. Anon, "Models of Venus Atmosphere (1972)" NASA Space Vehicle Design Criteria (Environment), NASA SP-8011.
9. T. Croft, et al., "Preliminary Review and Analysis of Effects of the Atmosphere of Venus on Radio Telemetry and Tracking of Entry Probes," Final Report SEL Project, Standord University (October 1972).

APPENDIX 7.6G
PLANET BACKSCATTER MULTIPATH ANALYSIS

1. Doppler Shift and Rates	7.6G-2
2. Atmospheric Loss	7.6G-7
3. Time Delay	7.6G-9
4. Reflected Signal Bandwidth	7.6G-10
5. Planet Reflectivity	7.6G-12
6. Multipath Signal Strength	7.6G-13
7. Summary of Results	7.6G-14

APPENDIX 7.6G

PLANET BACKSCATTER MULTIPATH ANALYSIS

A Venus multipath study was needed to evaluate the multipath effects on a communication link from earth to Venus. This study was conducted for the large probe and one small probe entry profile. The large probe entry aspect angle (see Figure 7.6G-1) is nominally 45 degrees with a ballistic coefficient (B) of 0.16 before staging and 3.5 after staging (46 km above the surface of Venus). The small entry aspect angle is nominally 55 degrees with a ballistic coefficient of 1.26. The entry aspect angles will remain relatively constant from blackout (~ 70 km altitude) to the surface of Venus (0 km altitude). The effects of turbulence, parachute swing, etc, on the entry will not be discussed in this study. From the probe geometry (Figure 7.6G-1) and velocities with respect to Venus, the following data have been tabulated using computer programs: Doppler shift and rates, atmospheric loss, time delay, reflected signal bandwidth, planet reflectivity, and multipath signal strength.

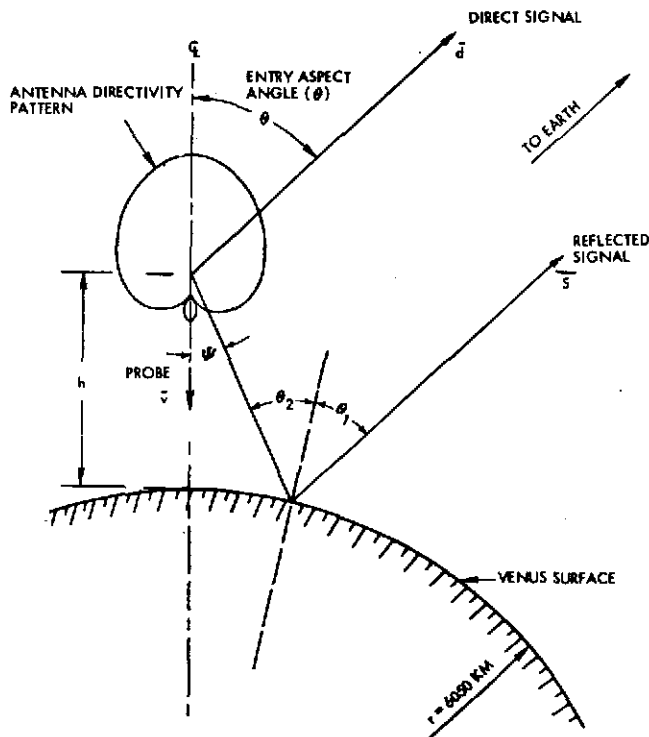


Figure 7.6G-1. Multipath Geometry

1. DOPPLER SHIFT AND RATES

The multipath geometry is shown in Figure 7.6G-1. The probe is descending vertically to the surface of Venus (with velocity \vec{v}) and is communicating directly to earth with an earth aspect angle of θ (which is also the degrees from subearth point). The velocity profiles for both large and small probes are shown in Figures 7.6G-2 and 7.6G-3, respectively. For convenience, the velocity vector is held in the plane of the figure. Vector \vec{d} represents the direct signal and \vec{s} is the specular component of the multipath signal. The Doppler shift and Doppler difference will be calculated for the direct signal and the specular component of the reflected signal. The specular component is the point where the angle of incidence and reflection are equal ($\phi_1 = \phi_2 = \phi$).

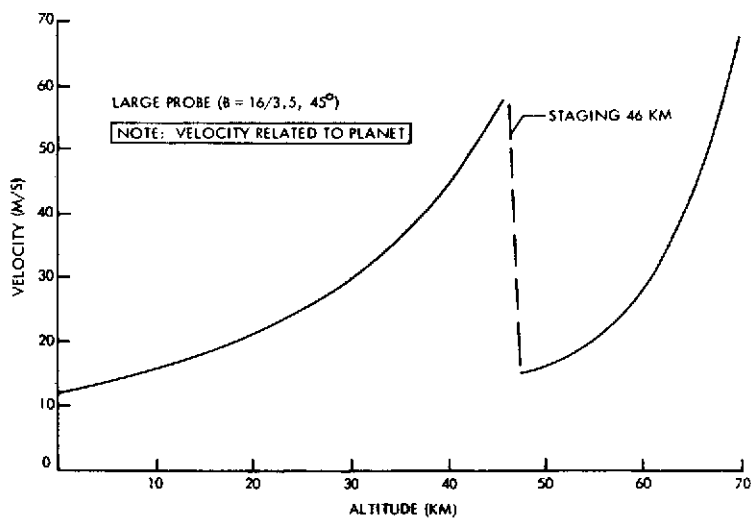


Figure 7.6G-2. Large Probe Velocity Versus Altitude

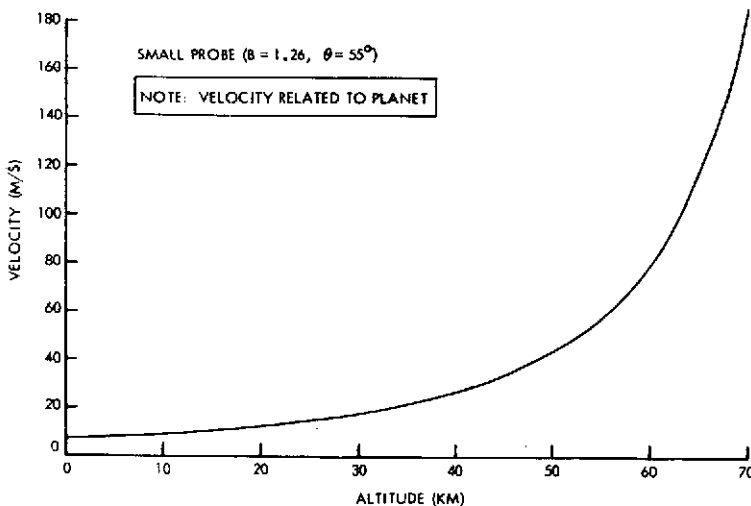


Figure 7.6G-3. Small Probe Velocity Versus Altitude

The direct path Doppler shift is

$$f_d = \frac{v}{\lambda} \cos(\bar{v}, \bar{d}) = -\frac{v}{\lambda} \cos\theta$$

where

$\lambda = 0.13$ m (wavelength at $f = 2.3$ GHz)

$\theta = 45^\circ$ (large probe)

and $= 55^\circ$ (small probe) earth aspect angle

v = velocity

= velocity profile for large probe, see Figure 7.6G-2

= velocity profile for small probe, see Figure 7.6G-3

The specular (multipath) Doppler shift is

$$f_s = \frac{v}{\lambda} \cos(\psi)$$

where

λ and v are same as above

ψ = specular angle (see Figure 7.6G-1)

= θ for flat surface approximation

= $\psi(h, \theta, r, \phi)$ for spherical approximation

The angle ψ is equal to θ for a flat surface approximation of planet multipath. Figure 7.6G-4 shows the geometry and equations associated with a spherical surface approximation. The angle ψ is a function of h (height above Venus surface), r (mean radius of Venus ~ 6050 km), ϕ (specular reflection angle), and θ (earth aspect angle). The difference between using a flat plane approximation and a spherical approximation model is that the specular Doppler shift is greater. This difference becomes greater as the height above the planet increases. Using the velocities in Figures 7.6G-2 and 7.6G-3 and a 70 km altitude, the difference in

the specular Doppler shift between a flat plane and a spherical surface model is:

Large probe

$$\theta = 45^\circ$$

$$h = 70 \text{ km}$$

$$v = 64.34 \text{ m/s}$$

$$\lambda = 0.13 \text{ m } (f = 2.3 \text{ MHz})$$

Flat plane model

$$\psi = \theta = 45^\circ$$

$$f_f = 348.04 \text{ Hz } \left(f_f = \frac{v}{\lambda} \cos \psi \right)$$

Spherical surface model

$$\psi = 43.7^\circ \text{ (calculated from equations in Figure 7.6G-4)}$$

$$f_{sp} = 355.70 \text{ Hz}$$

$$\Delta f = f_{sp} - f_f = 7.66 \text{ Hz} = \text{difference between flat plane and spherical surface model.}$$

Small probe

$$\theta = 55^\circ$$

$$h = 70 \text{ km}$$

$$v = 180.55 \text{ m/s}$$

$$\lambda = 0.13 \text{ m } (f = 2.3 \text{ MHz})$$

Flat plane model

$$\psi = \theta = 55^\circ$$

$$f_f = 792.22$$

Spherical surface model

$$\psi = 53.2^\circ$$

$$f_{sp} = 827.18 \text{ Hz}$$

$$\Delta f = f_{sp} - f_f = 34.95 \text{ Hz} = \text{difference between flat plane and spherical surface model.}$$

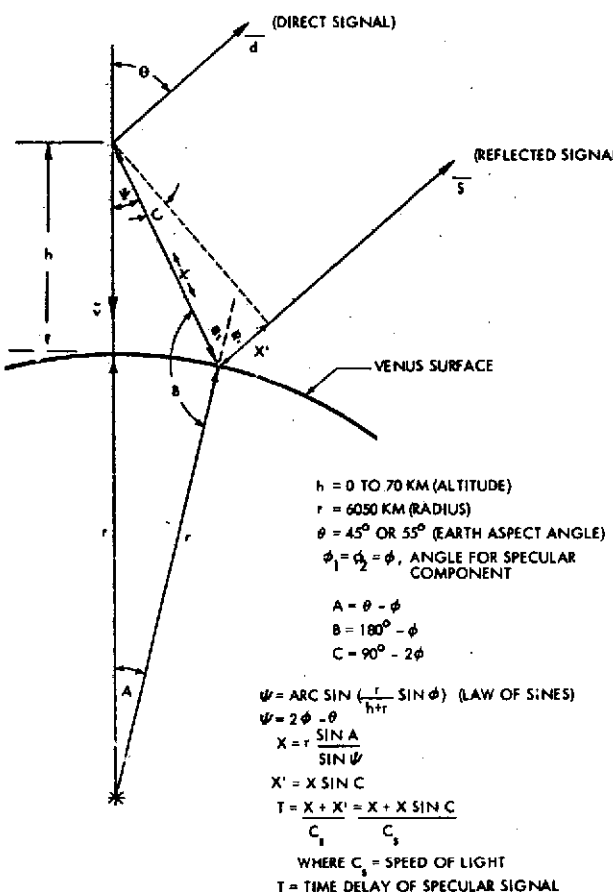


Figure 7.6G-4. Planet Geometry

The spherical surface model separates the direct signal Doppler shift (f_d) from the specular signal Doppler shift (f_s) by a greater margin as shown above.

The Doppler difference is

$$\Delta f_s = f_s - f_d$$

Flat plane model

$$\Delta f_s = 2 \frac{v}{\lambda} \cos \theta$$

Spherical surface

$$\Delta f_s = \frac{v}{\lambda} (\cos \psi + \cos \theta)$$

A plot of Doppler difference (Δf_s) vs altitude (h) using a spherical surface model is shown in Figures 7.6G-5 and 7.6G-6 for large and small probes, respectively. Figures 7.6G-7 and 7.6G-8 show the Doppler rate of the direct signal for the large and small probes, respectively.

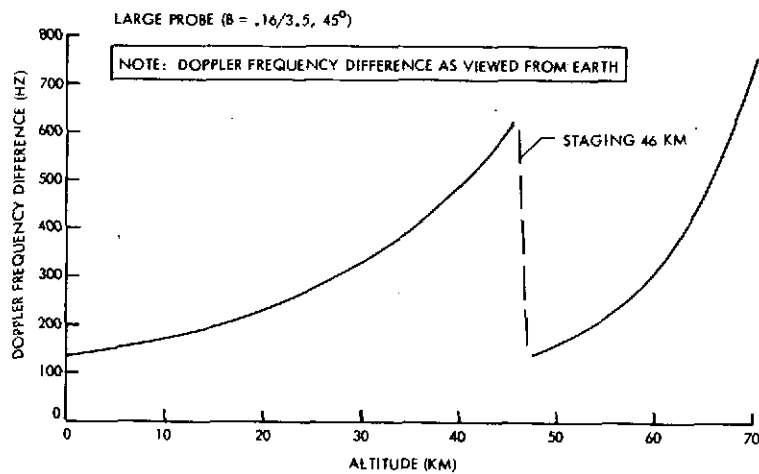


Figure 7.6G-5. Doppler Frequency Differences Between Direct and Multipath

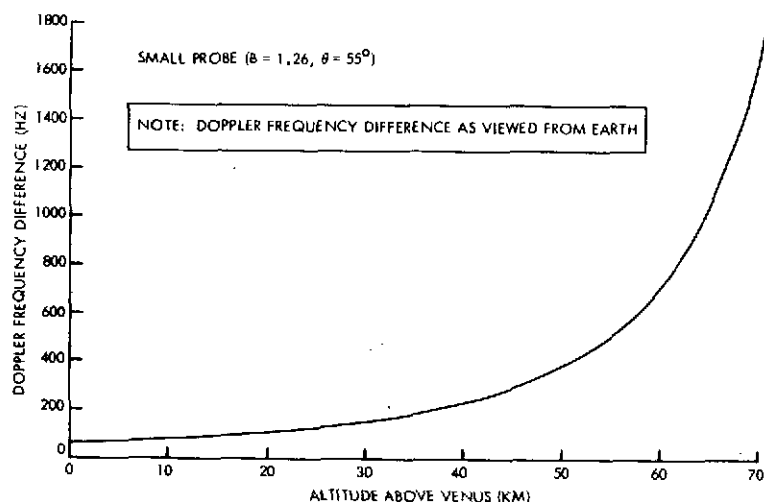


Figure 7.6G-6. Doppler Frequency Difference Between Direct and Multipath Signals

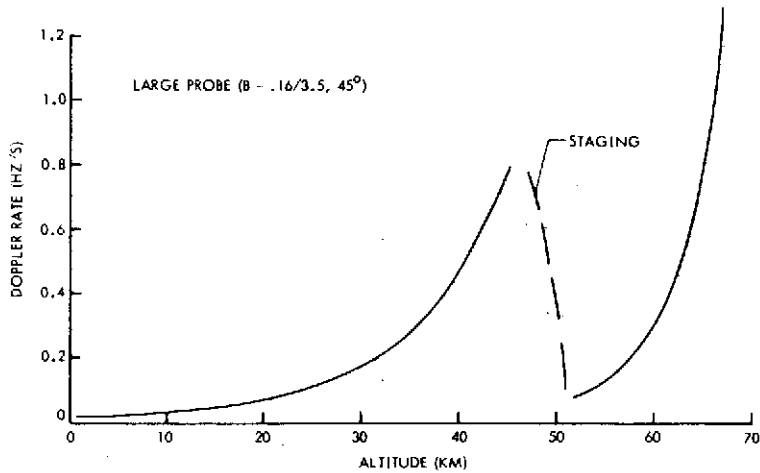


Figure 7.6G-7. Direct Signal Doppler Rate Versus Altitude

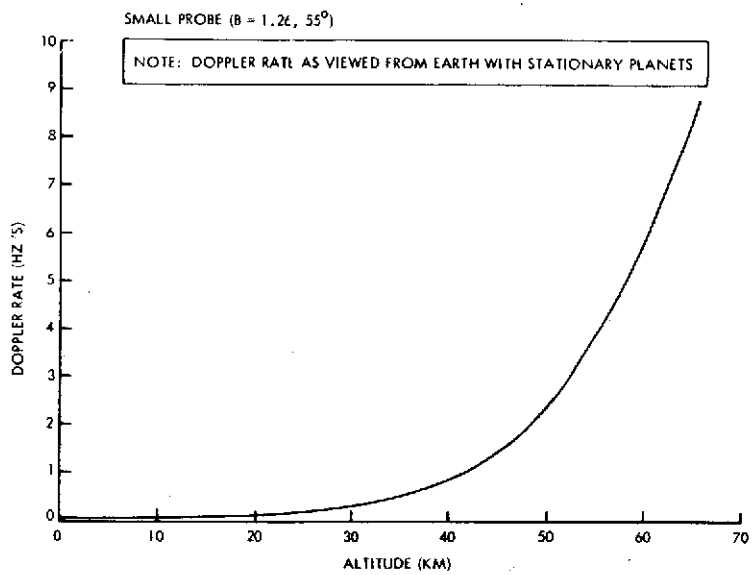


Figure 7.6G-8. Doppler Rate Versus Altitude of Direct Signal

2. ATMOSPHERIC LOSS

The atmospheric loss is divided into two parts, absorption and defocusing loss. A plot of atmospheric loss vs altitude is shown in Figures 7.6G-9 and 7.6G-10 for large and small probes, respectively. The multi-path signal will go through more atmosphere than the direct signal, and thus will receive more attenuation. This advantage vanishes as the probes approach the surface. Figure 7.6G-11 shows one-way atmospheric loss with respect to subearth angles. The Venus nominal atmospheric model used is SP-8011, Table 5 (Reference 1).

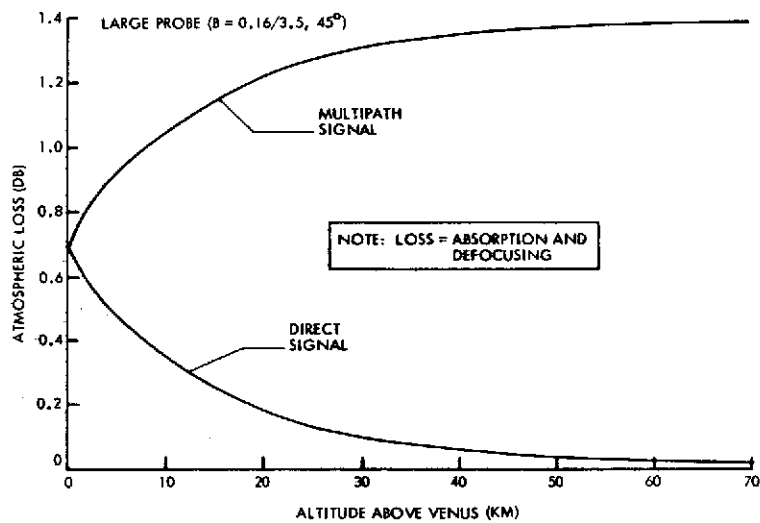


Figure 7.6G-9. Atmospheric Loss - Direct and Multipath Signals

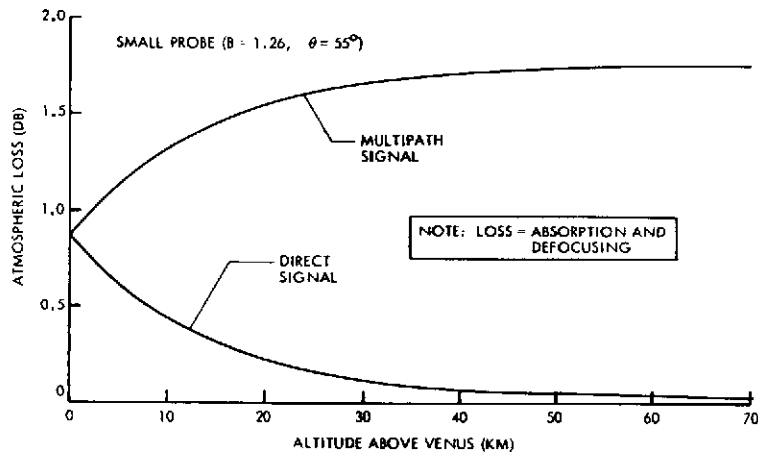


Figure 7.6G-10. Atmospheric Loss - Direct and Multipath Signals

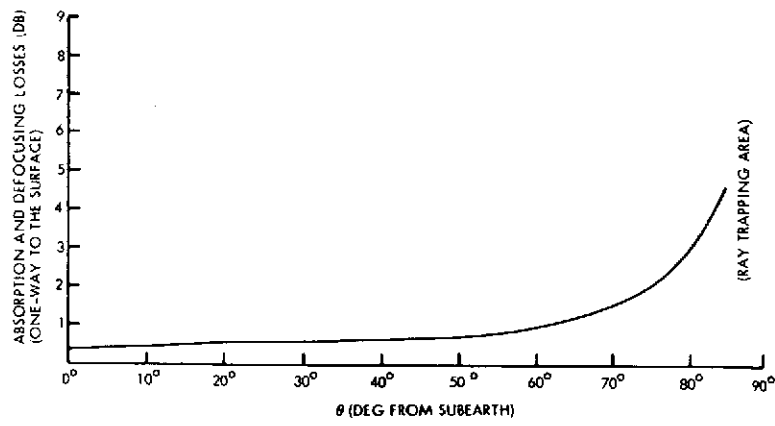


Figure 7.6G-11. Atmospheric Losses

3. TIME DELAY

The difference in path lengths between the direct and reflected signal results in a difference in time of arrival between the two signals. A typical profile of the time delay is shown in Figures 7.6G-12 and 7.6G-13 for large and small probes, respectively. The symbol period for the large probe Atlas/Centaur mission is 1/256 seconds for a rate 1/2, 128 bps coded link and 1/128 for the 64 bps small probe link. Time delay of the reflected signal from the large probe (Figure 7.6G-12) varies from 330×10^{-6} seconds at 70 km altitude to zero at the surface. At the higher altitude this delay amounts to 8.5 percent of the symbol period and therefore is a potential source of intersymbol interference. The small probe worst case reflected signal delay of 270×10^{-6} seconds, from Figure 7.6G-13, is a relatively small percentage (3.4%) of the small probe symbol period.

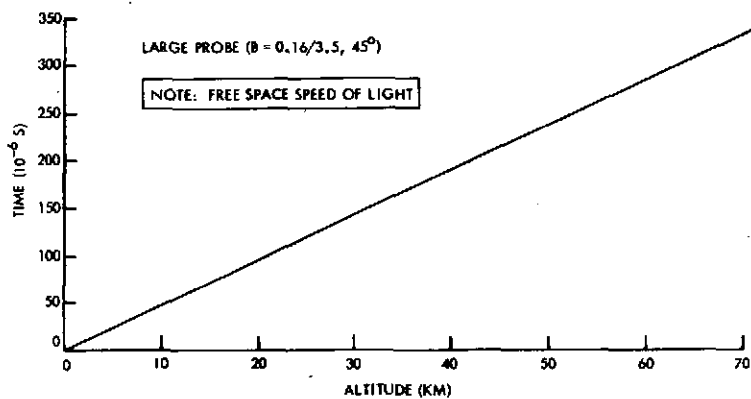


Figure 7.6G-12. Time Delay Versus Altitude (Multipath Signal)

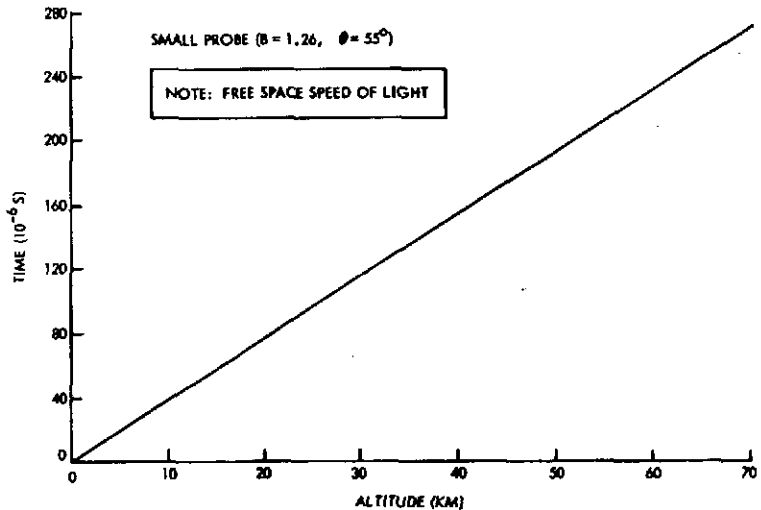


Figure 7.6G-13. Time Delay Versus Altitude (Multipath Signal)

The Thor/Delta large probe has a delay/symbol period comparable to the Atlas/Centaur large probe (10.4%) of the rate 1/3 symbol period at high altitudes. The small probe time delay/symbol period is comparable to 1.1 percent or about 1/3 of the Atlas/Centaur small probe.

4. REFLECTED SIGNAL BANDWIDTH

The bandwidth of the reflected signal is related to the relative velocity of the probe and the planet, as well as the surface roughness. The reflected signal will have a fluctuating bandwidth given in Reference 2 and 3 as

$$B_w = \sqrt{8} \frac{2\pi}{\lambda} v \frac{\sigma}{L} \sin \phi$$

λ = 0.13 meters

v = probe velocity (Figures 7.6G-2 and 7.6G-3)

$\frac{2\sigma}{L}$ = planet mean slope

ϕ = reflected multipath angle (see Figure 7.6G-1).

Earth-based radar measurements indicate that $\frac{2\sigma}{L}$ ranges from 0.071 to 0.124. A nominal value of $\frac{2\sigma}{L}$ is 0.10 and will be used in the above equation. It was found in Reference 3 that after some simplifying assumptions the auto-correlation function of the scattered signal was Gaussian-shaped. Thus B_w , as defined above is the 4.45 sigma width of the spectrum.

The one-sigma point, centered on the offset multipath Doppler frequency $f_o + f_s$, of the spectrum is

$$\sigma = \frac{B_w}{\sqrt{2\pi}} \quad f_o \sim 2.3 \text{ GHz}$$

The multipath spectrums at several discrete heights above the planet are shown in Figures 7.6G-14 and 7.6G-15 for large and small probes, respectively. A spherical surface model was used in the above calculations.

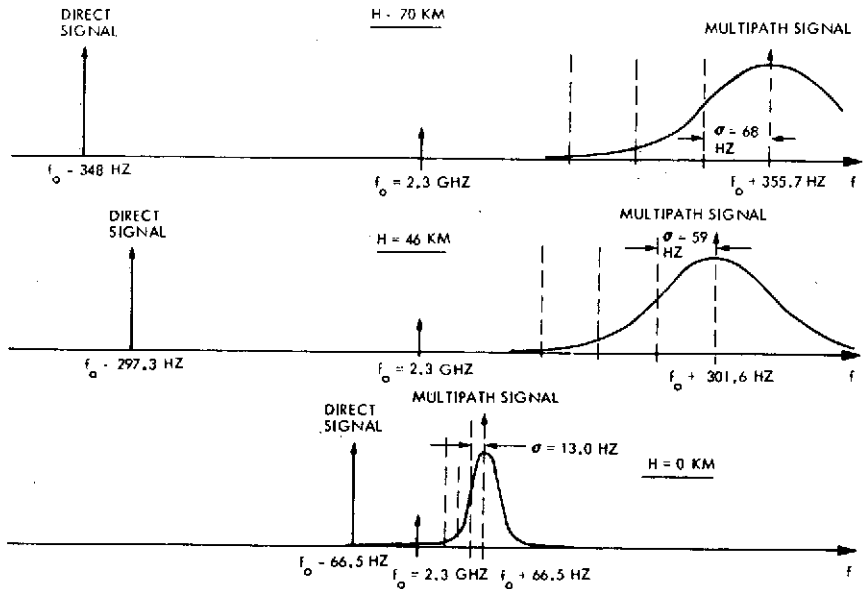


Figure 7.6G-14. Multipath Frequency Spectrum of Large Probe ($B = .16/3.5, 45^\circ$)
(Due to Planet Reflection Only)

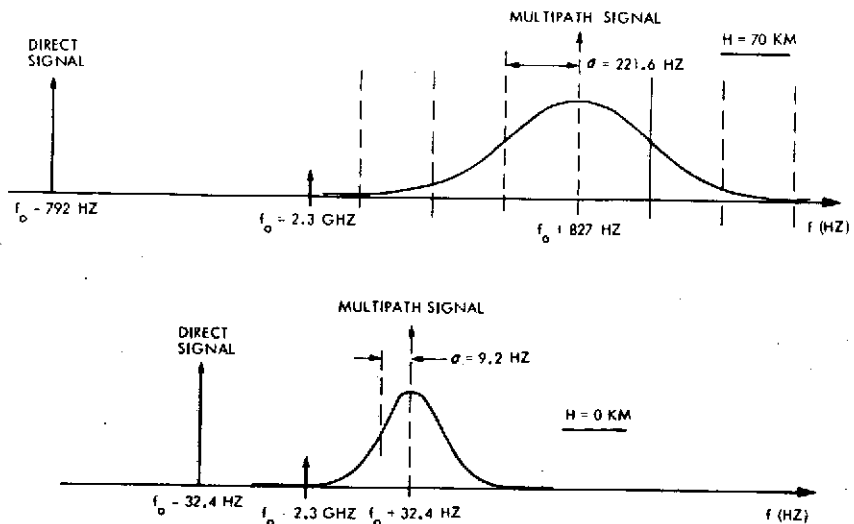


Figure 7.6G-15. Multipath Frequency Spectrum of Small Probe ($B = 1.26, 55^\circ$)
(Due to Planet Reflection Only)

5. PLANET REFLECTIVITY

Expressions for Γ_H (horizontal polarization) and Γ_V (vertical polarization) are from Reference 4.

$$\Gamma_H = \frac{\cos \phi - \sqrt{\epsilon - \sin^2 \phi}}{\cos \phi + \sqrt{\epsilon - \sin^2 \phi}}$$

$$\Gamma_V = \frac{\epsilon \cos \phi - \sqrt{\epsilon - \sin^2 \phi}}{\epsilon \cos \phi + \sqrt{\epsilon - \sin^2 \phi}}$$

ϵ has been estimated for Venus from radar data (Reference 5) as $\epsilon \sim 4$. A plot of the above equations is given in Figure 7.6G-16 for $\epsilon = 4$. For ϕ near zero $\Gamma_V \sim \Gamma_H$, which implies that a RHCP wave will reflect as a LHCP wave. In principle this means that if both the direct and reflected waves are circularly polarized, and if $\theta \sim 0$ (probe near the subearth point), the reflected wave will be completely orthogonal in polarization to the direct wave, and thus can be completely eliminated in the receiver antenna. In practice this ideal is rarely realized because the down-looking part of the radiation pattern is usually only a very poor approximation to being circularly polarized. However, it is reasonable to expect a 3 dB advantage from this effect for probes near the subearth point. For $\theta > 63.5^\circ$ the effective Γ_c for circular polarization is the RMS average of Γ_V and Γ_H .

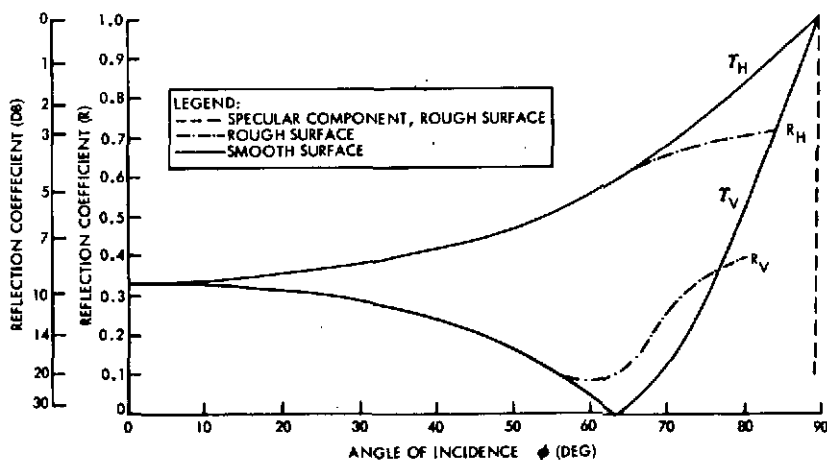


Figure 7.6G-16. Reflection Coefficients Versus Incidence Angle

A detailed analysis by Glenn (Reference 2) on rough surface scattering shows a significant departure from $|\Gamma|$ in the area of large θ . The dashed curves in Figure 7.6G-16 are from data taken from Reference 3. In Reference 3 the conclusion was that the dashed curves approximate the conditions on Venus more completely.

6. MULTIPATH SIGNAL STRENGTH

The multipath signal could cause deep amplitude fades that may cause loss of lock in the phase lock loop and cycle slipping in the loop. Figure 7.6G-17 shows the expected multipath signal strength as a function of angular distance from subearth θ . The multipath signal is reduced by three factors. These are atmospheric attenuation (nominal model SP 8011 Figure 7.6G-11), antenna directivity (conical beam pattern, see Figure 7.6G-18) and surface reflectivity (circular polarization, see Figure 7.6G-16). The total of these drops rapidly decreases as θ approaches 90° . Signal in the loop is further reduced by the filtering effects of the loop, which depends on the loop bandwidth, the Doppler offset, and the Doppler spreading.

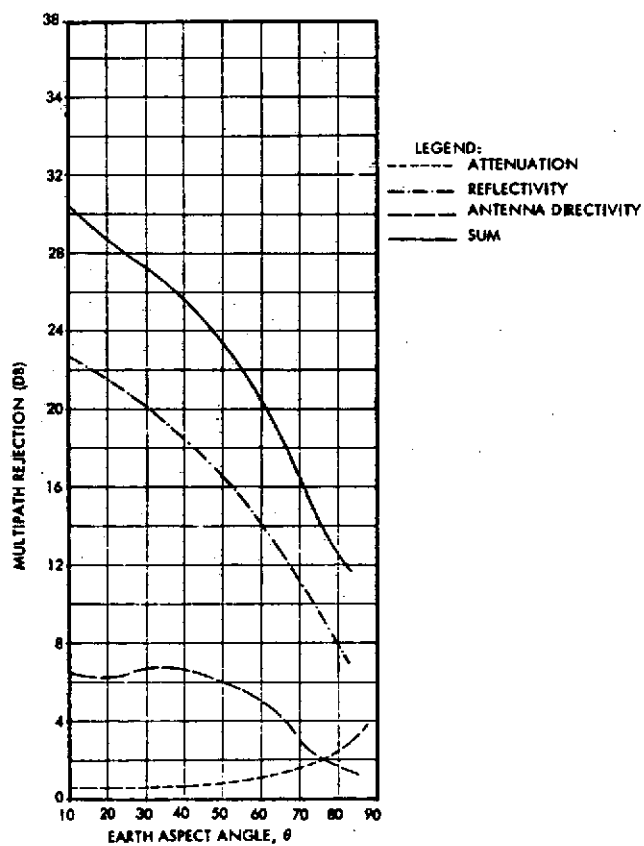


Figure 7.6G-17. Multipath Signal Strength

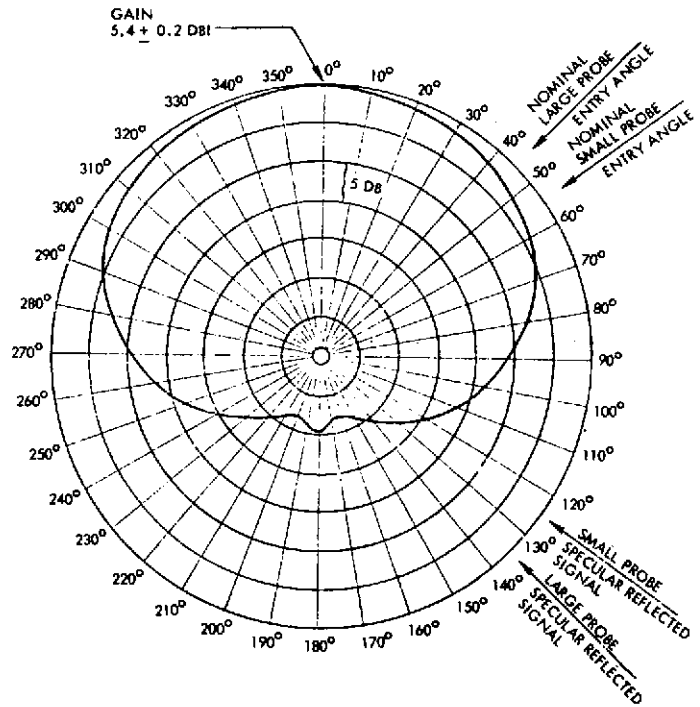


Figure 7.6G-18. Typical Antenna Pattern

7. SUMMARY OF RESULTS

The basic contributing parameters to the multipath problem were studied and defined. A time history (related to altitude) for both large and small probes, of Doppler, atmospheric loss, time delay, and reflected signal bandwidths was given. The multipath signal strength was calculated for various subearth communication angles. The data given here were used to prepare the probe link design control tables (Appendix 7.6M) and the one-way vs two-way systems analysis (Appendix 7.6L).

REFERENCES

1. "Models of Venus Atmosphere (1972)," NASA Space Vehicle Design Criteria (Environment), NASA SP-8011.
2. A. B. Glenn, "Fading from Irregular Surfaces for Line-of-Sight Communications," IEE Transactions on Aerospace and Electronic Systems (March 1968).
3. "1975 Venus Multiprobe Mission Study," Final Report, Contract JPL 952534, Volume II, Section B (April 1970).
4. Study and Analysis of Multipath and Modulation Selection for Relay Radio Links. (RCA input to the Voyager Contract) RCA Report 100032-A (VCB-155).
5. D. O. Muhleman, et al., "A Review of Radar Astronomy - Part 2," IEEE Spectrum (November 1965).

APPENDIX 7.6H

**TELECOMMUNICATIONS DESIGN CONTROL TABLES
FOR A THOR/DELTA MISSION**

APPENDIX 7.6H
TELECOMMUNICATIONS DESIGN CONTROL TABLES FOR A
THOR/DELTA MISSION

The telecommunication design control tables presented here are based on a 1977 Thor/Delta mission. The design control tables have not been updated to concur with the new science definition data (Version IV) and are based on a Rician fading channel model. New design control tables have been developed in Appendix 7.6M for a 1978 Atlas/Centaur mission using the new science definition data and a lognormal fading channel. A tradeoff study between a Rician and lognormal fading channel is given in Appendices 7.6B and 7.6C. A complete set of tables for both Thor/Delta and Atlas/Centaur for a 1977 mission and with Rician fading are given in Technical Note P73-203434-074 (Rev A) February 1973.

For both Thor/Delta and Atlas/Centaur missions, one large probe and three small probes enter the atmosphere of Venus and communicate directly to earth. The large probe links are two-way coherent to provide two-way Doppler and the small probe links are one-way coherent. All probes use PCM/PSK/PM modulation on the downlink. The large probe uplink is unmodulated and is used solely to provide the two-way Doppler signal.

The tables are grouped providing a summary table for large and small Thor/Delta probes at each of three altitudes. The 1 km above surface summary table is followed by a detail table showing allocations of losses and sources. An uplink table for the large probe is given in Appendix 7.6M, however, the margin must be reduced by 0.9 dB for the Thor/Delta to account for increased range for the 1977 mission.

In the detail tables under items 15 and 20 no losses have been shown for recovering data from predetection recordings made at the DSN. The reason for this is that all link margins meet or exceed the sum of the adverse tolerances for all other losses, and since the difference between the sum of the adverse tolerances and the RSS values exceeds 2 dB in all cases, this 2 dB is considered adequate to provide the margin needed for predetection recording losses, especially where iterative processing can be resorted to if necessary. This is in contrast to Appendix 7.6M in which tolerance

has been included for recording loss in the Atlas/Centaur tables. Radome loss for the large probe is shown in circuit losses even at the lower altitude after the radome is jettisoned. Thus, there is additional margin near the surface not indicated in the tables.

Table 7.6H-1. Thor/Delta Link Analysis - Large and Small Probes

1 KM ABOVE SURFACE		LARGE	SMALL				
TRANSMITTER POWER (W-MIN)	20	9.1					
BIT RATE (BPS)	85.3	10					
		LARGE PROBE		SMALL PROBE			
NO.	PARAMETER	NOMINAL	ADVERSE	NOMINAL	ADVERSE		
1	TOTAL TRANSMITTING POWER (DBW)	+ 13.4	-0.4	+ 10.0	-0.4		
2	TRANSMITTING CIRCUIT LOSS (DB)	- 2.0	-0.2	- 1.0	-0.2		
3	TRANSMITTING ANTENNA GAIN (DB)	+ 3.5	-1.2	+ 3.0	-1.2		
4	COMMUNICATIONS RANGE LOSS (DB)	-256.78	0	-256.8	0		
5	ATMOSPHERIC ABSORPTION & DEFOCUSING LOSSES (DB)	- 0.89	-0.11	- 0.9	-0.1		
6	POLARIZATION LOSS (DB)	- 0.20	-0.1	- 0.2	-0.1		
7	MULTIPATH & OTHER LOSSES (DB)	SEE NOTES		SEE NOTES			
8	RECEIVING ANTENNA GAIN (DB)	+ 61.70	-0.4	+ 61.7	-0.4		
9	RECEIVING CIRCUIT LOSS (DB)	0	0	0	0		
10	NET LOSS (DB) (2+3+4+5+6+7+8+9)	-194.67	-2.01	-194.2	-2.0		
11	TOTAL RECEIVED POWER (DBW) (1+10)	-181.27	-2.41	-184.2	-2.4		
12	RECEIVER NOISE SPECTRAL DENSITY - (DBW/HZ)	-214.50	+1.0	-214.5	+1.0		
13	TOTAL RECEIVED POWER/NO (DBW · HZ) (11-12)	+ 33.73	-3.41	+ 30.3	-3.4		
	CARRIER TRACKING						
14	CARRIER POWER/TOTAL (DB)	- 4.72	-0.4	- 1.6	-0.2		
15	ADDITIONAL CARRIER LOSSES (DB)	- 0.7	-0.2	- 0.6	-0.4		
16	THRESHOLD TRACKING BANDWIDTH - $2B_{LO}$ (DB)	+ 10.0	-0.8	+ 10.0	-0.8		
17	THRESHOLD SNR (DB)	+ 13.0	0	+ 11.0	0		
18	PERFORMANCE MARGIN (DB) (13+14+15-16-17)	+ 4.81	-4.81	+ 7.1	-4.8		
	DATA CHANNEL						
19	DATA POWER/TOTAL (DB)	- 1.76	-0.2	- 5.1	-0.5		
20	ADDITIONAL DATA CHANNEL LOSSES (DB)	- 5.25	-0.5	- 5.6	-0.8		
21	DATA BIT RATE - BPS (DB)	+ 19.3	0	+ 10.0	0		
22	THRESHOLD ENERGY PER DATA BIT - E_b/N_o (DB)	+ 2.5	0	+ 2.5	0		
23	PERFORMANCE MARGIN (DB) (13+19+20-21-22)	+ 4.42	-4.11	+ 7.1	-4.7		
1. MULTIPATH LOSSES ITEM 7 ARE INCLUDED IN ITEMS 15 & 20.		LARGE PROBE		SMALL PROBE			
2. K = 6, RATE 1/3 CONVOLUTIONAL VITERBI SOFT DECISION DECODING.		SUM	RSS	SUM	RSS		
		S/NO.	3.41	1.68	S/NO.	3.4	1.68
		CARRIER	4.81	1.91	CARRIER	4.8	1.91
		DATA	4.11	1.76	DATA	4.7	1.93

Table 7.6H-2. Thor/Delta Large Probe at Surface

	NOMINAL VALUE	ADVERSE TOLERANCE		
1. TRANSMITTER POWER (DBW)	<u>13.4</u>	<u>-0.4</u>		
1.1 TRANSMITTER POWER (WATTS)	21.9			
2. TRANSMITTING CIRCUIT LOSS (DB)	<u>-2.0</u>	<u>-0.2</u>		
2.1 CABLE ASSEMBLY LOSS (DB) 0.95				
2.2 FEEDTHROUGH LOSS (DB) 0.15				
2.3 RADOME LOSS (DB) 0.4				
2.4 DIPLEXER LOSS (DB) 0.5				
3. TRANSMITTING ANTENNA GAIN (DB)	<u>-3.5</u>	<u>-1.2</u>		
3.1 NOMINAL ANTENNA GAIN (DB) 3.5 AT 50 DEG				
3.2 ADVERSE ANTENNA LOSS DUE TO TARGETING UNCERTAINTY INCLUDED IN 3.1 OF $3\sigma = 2.0$ DEG 0.0 (DB) LOSS.				
3.3 ADVERSE ANTENNA LOSS DUE TO TURBULENCE ON THE PROBE OF 0.0 DEG 0.0 (DB) LOSS.				
3.4 ANTENNA PATTERN RIPPLE LOSS (DB) 1.2				
3.5 ANTENNA TYPE TURNSTILE/CONE AND HPBW 120 DEG				
NOTE: REFER TO APPENDIX 7.6J, ANTENNA PERFORMANCE TESTS.				
4. COMMUNICATIONS RANGE LOSS (DB)	<u>-256.78</u>	<u>0</u>		
4.1 RANGE = $7,195 \times 10^7$ KM = 0.481 AU				
4.2 FREQUENCY = 2.295 GHZ				
5. ATMOSPHERIC ABSORPTION - DEFOCUSING (DB)	<u>0.89</u>	<u>0.11</u>		
5.1 ABSORPTION LOSS (DB) 0.68 55 DEG VALUES USED				
5.2 DEFOCUSING LOSS (DB) 0.21 55 DEG VALUES USED				
5.3 PROBE HEIGHT (KM) AT SURFACE				
5.4 TARGETING ANGLE (DEG) NOMINAL 48 $3\sigma = 2^\circ$				
NOTE: REFER TO APPENDIX 7.6F				
6. POLARIZATION LOSS (DB)	<u>0.2</u>	<u>1</u>		
6.1 AXIAL RATIO - TRANSMITTING ANTENNA 2.5 DB				
6.2 AXIAL RATIO - RECEIVING ANTENNA 0.6 DB				
NOTE: SEE DSN STANDARD PRACTICE 810-5; REV. C, P. 2-5				
7. MULTIPATH AND OTHER LOSSES (DB) (INCLUDED IN 15 AND 20 BELOW)				
8. RECEIVING ANTENNA GAIN (DB)				
8.1 RECEIVE GAIN (DB) 64×10^3 METER SUBNET	<u>+61.7</u>	<u>-0.4</u>		
NOTE: SEE DSN STANDARD PRACTICE 810-5; REV. C, P. 2-2				
9. RECEIVING CIRCUIT LOSS (DB)	<u>0</u>	<u>0</u>		
9.1 LOSSES INCLUDED IN 8 (RECEIVING ANTENNA GAIN)				
10. NET LOSS (DB) (2+3+4+5+6+7+8+9)	<u>-194.67</u>	<u>-2.01</u>		
11. TOTAL RECEIVE POWER (DBW) (1+10)	<u>-181.27</u>	<u>-2.41</u>		
12. RECEIVER NOISE SPECTRAL DENSITY (DBW/Hz)	<u>-214.5</u>	<u>+1.0</u>		
12.1 NO = $KT = -228.6 + 10 \log T$ TRACKING STATION COVERAGE ON 5-16-77 $T = 22^\circ \pm 3^\circ K$ FOR COLD SKY (NEAR ZENITH) MADRID WORST-CASE ELEVATION ANGLE IS AT THE SURFACE ELEVATION ANGLE = 18 DEG, ADD $8^\circ K$ GOLDSTONE WORST-CASE ELEVATION ANGLE IS AT PRE-ENTRY ELEVATION ANGLE = 22 DEG, ADD $4^\circ K$ THIS RESULTS IN A SYSTEM NOISE TEMPERATURE OF $26 (22 + 4) \pm 7 (8 + 4)^\circ K$, WHICH CORRESPONDS TO -214.5 ± 1.0 DBW/Hz.				
NOTE: SEE DSN STANDARD PRACTICE 810-5; REV. C, P. 2-15.				
13. TOTAL RECEIVED POWER/NO. (DBW + H21 (1)-12)	<u>-33.73</u>	<u>-3.41</u>		
14. CARRIER POWER/TOTAL (DB)	<u>-4.72</u>	<u>-0.4</u>		
15. ADDITIONAL CARRIER LOSSES (DB)	<u>-0.7</u>	<u>-0.2</u>		
15.1 DOWNLINK SUPPRESSION DUE TO UPLINK EFFECTS:				
15.1.1 THERMAL NOISE ON UPLINK	-0.2			
15.1.2 ATMOSPHERIC MULTIPATH ON UPLINK	-0.2			
15.1.3 UPLINK PLANETARY MULTIPATH	-0.2			
15.1.4 DOPPLER TRACKING ERROR	-0.2			
15.1.5 OSCILLATOR INSTABILITIES	-0.2			
15.2 ATMOSPHERIC MULTIPATH ON DOWNLINK	-0.5			
15.3 DOWNLINK PLANETARY MULTIPATH	NEGIGIBLE			
15.4 OSCILLATOR INSTABILITIES: 2 WAY 1 WAY	NEGIGIBLE 0.2 (DELETE UPLINK EFFECTS)			
15.5 PREDTECTION RECORDING LOSS (SEE TEXT UP FRONT)				
16. THRESHOLD TRACKING BANDWIDTH (DB)	<u>10</u>	<u>-0.8</u>		
16.1 LOOP BANDWIDTH = $2B_{LO}$ (HZ) 10 TO 12 Hz				
NOTE: BLOCK III RECEIVER 10.5 ± 0.3 dB USE 10 ± 0.8 dB TO COVER BOTH				
BLOCK IV RECEIVER 10.0 ± 0.4 dB				
17. REQUIRED LOOP SIGNAL/NOISE IN $2B_{LO}$ BANDWIDTH (DB) (INCLUDES LIMITER EFFECT)	<u>13</u>	<u>0</u>		
18. PERFORMANCE MARGIN (DB) (13-14-15-16-17)	<u>-4.81</u>	<u>-4.81</u>		
19. DATA POWER/TOTAL (DB)	<u>-1.76</u>	<u>-0.2</u>		
20. ADDITIONAL DATA CHANNEL LOSSES (DB)	<u>-5.25</u>	<u>-0.5</u>		
20.1 NOISY CARRIER REFERENCE AND MULTIPATH LOSS (DB) 4.15				
20.2 SUBCARRIER NOISY REFERENCE AND PHASE AMBIGUITY LOSS (DB) 0.8				
20.3 WAVEFORM DISTORTION LOSS (DB) 0.3				
21. DATA BIT RATE (DB) BPS = 85.3	<u>-19.3</u>	<u>0</u>		
22. REQUIRED ENERGY PER DATA BIT - E_b/N_0 (DB) BER = 10^{-3} MINIMUM CODING TYPE CONVOLUTIONAL K = 6, RATE 1/3 DECODING TYPE VITERBI SOFT DECISION	<u>-2.5</u>	<u>0</u>		
23. PERFORMANCE MARGIN (DB) (13+19+20-21-22)	<u>4.42</u>	<u>-4.11</u>		

Table 7.6H-3. Thor/Delta Small Probe at Surface

	NOMINAL VALUE	ADVERSE TOLERANCE		
1. TRANSMITTER POWER (DBW)	<u>+10</u>	<u>-0.4</u>		
1.1 TRANSMITTER POWER (WATTS)	10			
2. TRANSMITTING CIRCUIT LOSS (DB)	<u>1.0</u>	<u>-0.2</u>		
2.1 CABLE ASSEMBLY LOSS (DB)	0.45			
2.2 FEEDTHROUGH LOSS (DB)	0.15			
2.3 RADOME LOSS (DB)	0.4			
3. TRANSMITTING ANTENNA GAIN (DB)	<u>+3.0</u>	<u>-1.2</u>		
3.1 NOMINAL ANTENNA GAIN (DB)	+3.0 AT 55 DEG			
3.2 ADVERSE ANTENNA LOSS DUE TO TARGETING UNCERTAINTY INCLUDED ABOVE OF $3\sigma = 0.0$ DEG. 0.0 (DB) LOSS.				
3.3 ADVERSE ANTENNA LOSS DUE TO TURBULENCE ON THE PROBE OF 0.0 DEG. 0.0 (DB) LOSS.				
3.4 ANTENNA PATTERN RIPPLE LOSS (DB)	1.2			
3.5 ANTENNA TYPE TURNSTILE/CONE AND HPBW	120°			
4. COMMUNICATIONS RANGE LOSS (DB)	<u>-266.8</u>	<u>0</u>		
4.1 RANGE = 7.195×10^7 KM = 0.481 AU				
4.2 FREQUENCY = 2.295 GHZ				
5. ATMOSPHERIC ABSORPTION - DEFOCUSING (DB)	<u>-0.9</u>	<u>-0.1</u>		
5.1 ABSORPTION LOSS (DB)	0.68			
5.2 DEFOCUSING LOSS (DB)	0.21			
5.3 PROBE HEIGHT (KM) AT SURFACE				
5.4 TARGETING ANGLE (DEG) NOMINAL 55 3σ = INCLUDED				
NOTE: REFER TO APPENDIX 7.6F				
6. POLARIZATION LOSS (DB)	<u>0.2</u>	<u>-0.1</u>		
6.1 AXIAL RATIO - TRANSMITTING ANTENNA	2.5 DB			
6.2 AXIAL RATIO - RECEIVING ANTENNA	0.6 DB			
NOTE: SEE DSN STANDARD PRACTICE 810-5; REV. C, P. 2-5				
7. MULTIPATH AND OTHER LOSSES (DB) (INCLUDED IN 15 AND 20 BELOW)				
8. RECEIVING ANTENNA GAIN (DB)				
8.1 RECEIVE GAIN (DB)	<u>+61.7</u>	<u>-0.4</u>		
64-METER SUBNET				
NOTE: SEE DSN STANDARD PRACTICE 810-5; REV. C, P. 2-2				
9. RECEIVING CIRCUIT LOSS (DB)	<u>0</u>	<u>0</u>		
9.1 LOSSES INCLUDED IN ITEM 8 (RECEIVING ANTENNA GAIN)				
10. NET LOSS (DB) (2+3+4+5+6+7+8+9)	<u>-194.2</u>	<u>-2.0</u>		
11. TOTAL RECEIVE POWER (DBW) (1+10)	<u>-184.2</u>	<u>-2.4</u>		
12. RECEIVER NOISE SPECTRAL DENSITY (DBW/HZ)	<u>-214.5</u>	<u>-1.0</u>		
12.1 $NO = KT = -228.6 + 10 \log T$ TRACKING STATION COVERAGE ON 5-16-77 $T = 22^{\circ}K \pm 3^{\circ}K$ FOR COLD SKY (NEAR ZENITH) MADRID WORST-CASE ELEVATION ANGLE IS AT THE SURFACE. ELEVATION ANGLE = 18 DEG, ADD $8^{\circ}K$ GOLDSTONE WORST-CASE ELEVATION ANGLE IS AT PRE-ENTRY. ELEVATION ANGLE = 22 DEG, ADD $4^{\circ}K$ THIS RESULTS IN A SYSTEM NOISE TEMPERATURE OF $20^{\circ}K (22 \pm 4)^{\circ}K \pm 7 (3 \pm 4)^{\circ}K$, WHICH CORRESPONDS TO -214.5 ± 1.0 DBW/HZ.				
NOTE: SEE DSN STANDARD PRACTICE 810-5; REV. C, P. 2-15.				
13. TOTAL RECEIVED POWER/NO. (DBW · HZ) (11-12)	<u>+30.3</u>	<u>-3.4</u>		
14. CARRIER POWER/TOTAL (DB)	<u>-1.6</u>	<u>-0.2</u>		
MODULATION INDEX				
15. ADDITIONAL CARRIER LOSSES (DB)	<u>-0.6</u>	<u>-0.4</u>		
15.1 ATMOSPHERIC MULTIPATH ON DOWNLINK	0.5			
15.2 DOWNLINK PLANETARY MULTIPATH	NEGLIGIBLE			
15.3 OSCILLATOR INSTABILITIES: 1 WAY	0.1			
15.4 PREDETECTION RECORDING LOSS (SEE TEXT)				
16. THRESHOLD TRACKING BANDWIDTH (DB)	<u>10</u>	<u>0.8</u>		
16.1 LOOP BANDWIDTH - $2B_{LO}$ (HZ) 10 TO 12 HZ NOTE: BLOCK III RECEIVER 10.5 ± 0.3 DB BLOCK IV RECEIVER 10.0 ± 0.4 DB USE 10 ± 0.8 DB TO COVER BOTH				
17. REQUIRED LOOP SIGNAL/NOISE IN $2B_{LO}$ BANDWIDTH (DB) (INCLUDES LIMITER EFFECT)	<u>11</u>	<u>0</u>		
18. PERFORMANCE MARGIN (DB) (13+14+15-16-17)	<u>7.1</u>	<u>-4.8</u>		
19. DATA POWER/TOTAL (DB)	<u>-5.1</u>	<u>-0.5</u>		
20. ADDITIONAL DATA CHANNEL LOSSES (DB)	<u>-5.6</u>	<u>-0.6</u>		
20.1 NOISY CARRIER REFERENCE AND MULTIPATH LOSS (DB)	4.25			
(INCLUDING LIMITER)				
20.2 OSCILLATOR INSTABILITIES LOSS (DB)	0.2			
20.3 SUBCARRIER NOISY REFERENCE AND PHASE AMBIGUITY LOSS (DB)	0.8			
20.4 WAVEFORM DISTORTION LOSS (DB)	0.3			
21. DATA BIT RATE (DB) BPS = 10	<u>10</u>	<u>0</u>		
22. REQUIRED ENERGY PER DATA BIT - E_b / N_0 (DB) BER = 10^{-3} MINIMUM CODING TYPE CONVOLUTIONAL K = 6, RATE 1/3 DECODING TYPE VITERBI SOFT DECISION	<u>-2.5</u>	<u>0</u>		
23. PERFORMANCE MARGIN (DB) (13-19-20-21-22)	<u>-7.1</u>	<u>-4.7</u>		

Table 7.6H-4. Thor/Delta Link Analysis, 30 KM Altitude

NO.	PARAMETER	LARGE	SMALL	LARGE PROBE		SMALL PROBE	
		TRANSMITTER POWER (W-MIN) BIT RATE (BPS)	20 102.3	9.1 10	NOMINAL	ADVERSE	NOMINAL
1	TOTAL TRANSMITTING POWER (DBW)	+ 13.42	-0.4	+ 10.0	-0.4		
2	TRANSMITTING CIRCUIT LOSS (DB)	- 2.0	-0.2	- 1.0	-0.2		
3	TRANSMITTING ANTENNA GAIN (DB)	+ 3.50	-2.0	+ 3.0	-1.8		
4	COMMUNICATIONS RANGE LOSS (DB)	-256.78	0	-256.8	0		
5	ATMOSPHERIC ABSORPTION & DEFOCUSING LOSSES (DB)	- 0.1	0	- 0.1	0		
6	POLARIZATION LOSS (DB)	- 0.2	-0.1	- 0.2	-0.1		
7	MULITPATH & OTHER LOSSES (DB)	SEE NOTES		SEE NOTES			
8	RECEIVING ANTENNA GAIN (DB)	+ 61.70	-0.4	+ 61.70	-0.4		
9	RECEIVING CIRCUIT LOSS (DB)	0	0	0	0		
10	NET LOSS (DB) (2+3+4+5+6+7+8+9)	-193.88	-2.7	-193.4	-2.5		
11	TOTAL RECEIVED POWER (DBW) (1+10)	-180.46	-3.1	-183.4	-2.9		
12	RECEIVER NOISE SPECTRAL DENSITY- (DBW/HZ)	-214.50	+1.0	-214.5	+1.0		
13	TOTAL RECEIVED POWER/NO (DBW - HZ) (11-12)	+ 33.84	-4.1	+ 31.1	-3.9		
CARRIER TRACKING							
14	CARRIER POWER/TOTAL (DB)	- 4.72	-0.4	- 1.6	-0.2		
15	ADDITIONAL CARRIER LOSSES (DB)	- 0.6	-0.2	- 0.5	-0.4		
16	THRESHOLD TRACKING BANDWIDTH - $2B_{LO}$ (DB)	+ 10.0	-0.8	+ 10.0	-0.8		
17	THRESHOLD SNR (DB)	+ 13.0	0	+ 11.0	0		
18	PERFORMANCE MARGIN (DB) (13+14+15-16-17)	+ 5.52	-5.5	+ 8.0	-5.2		
DATA CHANNEL							
19	DATA POWER/TOTAL (DB)	- 1.76	-0.2	- 5.1	-0.5		
20	ADDITIONAL DATA CHANNEL LOSSES (DB)	- 4.68	-0.5	- 4.5	-0.8		
21	DATA BIT RATE - BPS (DB)	+ 20.1	0	+ 10.0	0		
22	THRESHOLD ENERGY PER DATA BIT - E/N _b ? (DB)	+ 2.5	0	+ 2.5	0		
23	PERFORMANCE MARGIN (DB) (13+19+20-21-22)	+ 4.8	-4.8	+ 9.0	-5.2		
1. MULTIPATH LOSSES ITEM 7 ARE INCLUDED IN ITEMS 15 & 20.				LARGE PROBE		SMALL PROBE	
2. K = 6, RATE 1/3 CONVOLUTIONAL VITERBI SOFT DECISION DECODING.				S/NO	SUM RSS	S/NO	SUM RSS
				CARRIER	5.5 2.49	CARRIER	5.3 2.33
				DATA	4.8 2.37	DATA	5.2 2.34

Table 7.6H-5. Thor/Delta Link Analysis, 70 KM Altitude

		LARGE TRANSMITTER POWER (W-MIN) BIT RATE (BPS)	SMALL 20 102.4	9.1 10	LARGE PROBE		SMALL PROBE			
NO.	PARAMETER	NOMINAL	ADVERSE	NOMINAL	ADVERSE					
1	TOTAL TRANSMITTING POWER (DBW)	+ 13.4	-0.4	+ 10.0	-0.4					
2	TRANSMITTING CIRCUIT LOSS (DB)	- 2.0	-0.2	- 1.0	-0.2					
3	TRANSMITTING ANTENNA GAIN (DB)	+ 3.5	-2.7	+ 3.0	-2.8					
4	COMMUNICATIONS RANGE LOSS (DB)	-256.78	0	-256.8	0					
5	ATMOSPHERIC ABSORPTION & DEFOCUSING LOSSES (DB)	- 0.1	0	- 0.1	0					
6	POLARIZATION LOSS (DB)	- 0.2	-0.1	- 0.2	-0.1					
7	MULTIPATH & OTHER LOSSES (DB)	SEE NOTES		SEE NOTES						
8	RECEIVING ANTENNA GAIN (DB)	+ 61.70	-0.4	+ 61.7	-0.4					
9	RECEIVING CIRCUIT LOSS (DB)	0	0	0	0					
10	NET LOSS (DB) (2+3+4+5+6+7+8+9)	-193.88	-3.4	-193.4	-3.5					
11	TOTAL RECEIVED POWER (DBW) (1+10)	-180.48	-3.8	-183.4	-3.9					
12	RECEIVER NOISE SPECTRAL DENSITY - (DBW/HZ)	-214.50	+1.0	-214.5	+1.0					
13	TOTAL RECEIVED POWER/NO (DBW · HZ) (11-12)	+ 34.02	-4.8	+ 31.1	-4.9					
CARRIER TRACKING										
14	CARRIER POWER/TOTAL (DB)	- 4.72	-0.4	- 1.6	-0.2					
15	ADDITIONAL CARRIER LOSSES (DB)	- 0.3	-0.2	- 0.3	-0.4					
16	THRESHOLD TRACKING BANDWIDTH - $2B_{LO}$ (DB)	+ 10.0	-0.8	+ 10.0	-0.8					
17	THRESHOLD SNR (DB)	+ 12.8	0	+ 11.0	0					
18	PERFORMANCE MARGIN (DB) (13+14+15-16-17)	+ 6.2	-6.2	+ 8.2	-6.3					
DATA CHANNEL										
19	DATA POWER/TOTAL (DB)	- 1.76	-0.2	- 5.1	-0.5					
20	ADDITIONAL DATA CHANNEL LOSSES (DB)	- 4.2	-0.42	- 3.9	-0.8					
21	DATA BIT RATE - BPS (DB)	+ 20.1	0	+ 10.0	0					
22	THRESHOLD ENERGY PER DATA BIT - E_b/N_o (DB)	+ 2.5	0	+ 2.5	0					
23	PERFORMANCE MARGIN (DB) (13+19+20-21-22)	+ 5.46	-5.42	+ 9.6	-6.2					
ADVERSE TOLERANCES										
SUM RSS SUM RSS										
S/NO. 4.8 2.94 S/NO. 4.9 3.03										
CARRIER 6.2 3.08 CARRIER 6.3 3.17										
DATA 5.42 2.98 DATA 6.2 3.18										

APPENDIX 7.6J

**ANTENNA PERFORMANCE TESTS WITH ANTENNA
MOUNTED ON LARGE PROBE MOCKUP**

APPENDIX 7.6J
ANTENNA PERFORMANCE TESTS WITH ANTENNA
MOUNTED ON LARGE PROBE MOCKUP

A test program was conducted to investigate the perturbations on the radiated antenna pattern resulting from the mounting arrangement on the aft-body (basecover) of the Thor/Delta large probe and to verify the effects of design changes. A full-scale mockup of the aft-body of the Thor/Delta large probe was built (see Figure 7.6J-1) and the proposed Pioneer Venus antenna (turnstile/cone at S-Band) was mounted and tested.

The minimum antenna gain and maximum back lobe requirements for the Pioneer Venus Probe Mission are shown in Figure 7.6J-2. As seen in Figure 7.6J-1, the two probable sources contributing to pattern perturbations are the parachute canister and the large cavity under the antenna (the metal screen under the antenna was added as a result of the test program).

The test program was initially divided into five test configurations, and as a result of the first four, a sixth configuration was added. Each test configuration was used to investigate the perturbations of a particular basecover component on the radiated pattern. The test configurations are as follows:

- Free space antenna patterns
- Large probe, no canister
- Large probe, full-length canister
- Large probe, cutoff canister
- Large probe, screen under antenna
- Large probe, screen under antenna with swivel.

Two types of radiation patterns (conic and great circle) were recorded using the coordinate system in Figures 7.6J-3 and 7.6J-4.

Conic patterns are defined by rotating the test antenna (turnstile/cone on large probe) about the ϕ -axis for 360 degrees while maintaining a constant θ angle. Two conic patterns are shown in the figures for $\theta = 0$ degrees and 60 degrees.

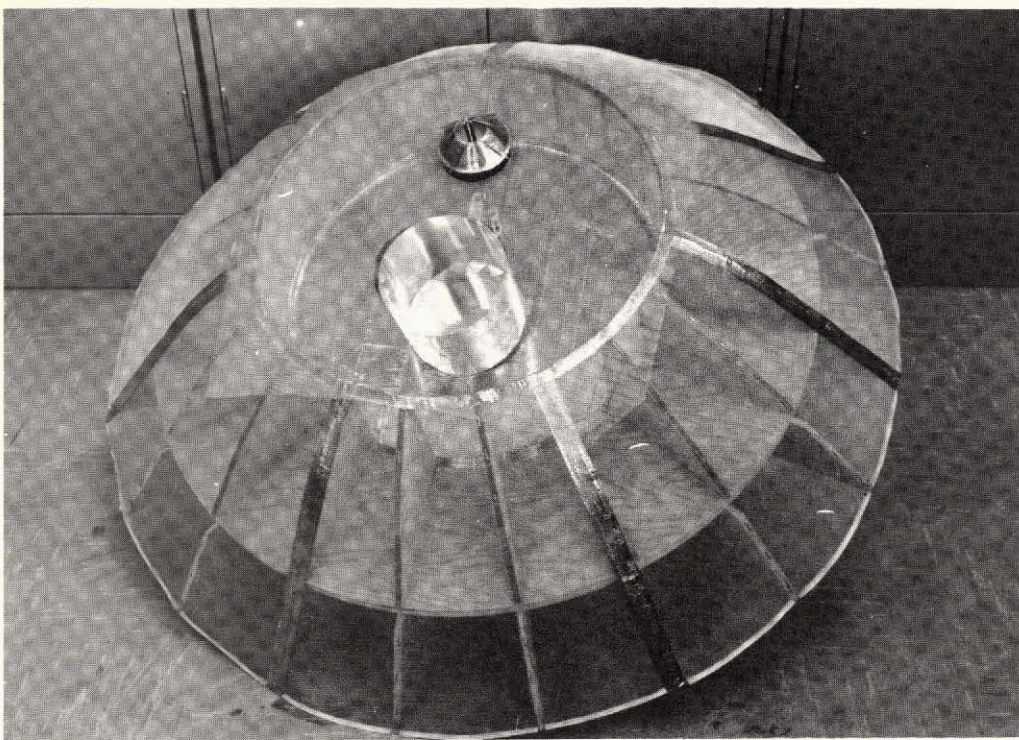
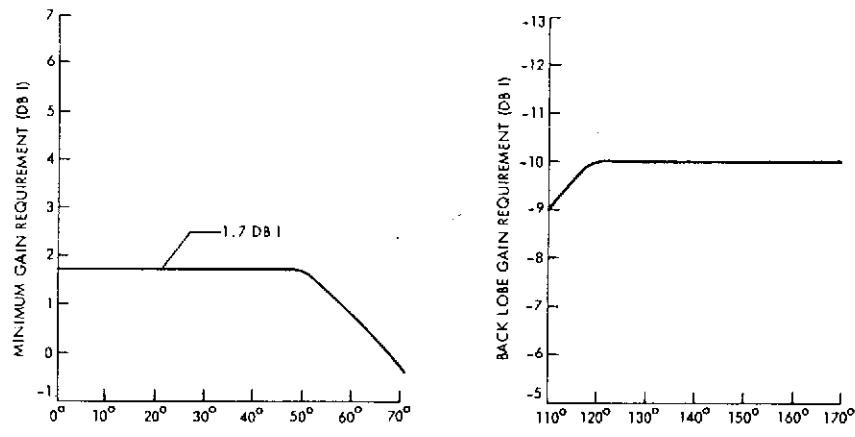


Figure 7.6J-1. Antenna Mounted on Large Probe Mockup



THE PROBES WILL BE SPINNING, THEREFORE THE COMMUNICATION COVERAGE WILL BE SYMMETRICAL ABOUT THE PROBE SPIN AXIS (0 DEGREE). GAIN VARIATION (PATTERN RIPPLE) OVER THE ± 70 DEGREE VIEWING ANGLE SHALL NOT EXCEED 4 DB. THE MINIMUM GAIN REQUIREMENT AND MAXIMUM BACK LOBE REQUIREMENT ARE AS SHOWN ABOVE.

Figure 7.6J-2. Antenna Gain Requirements

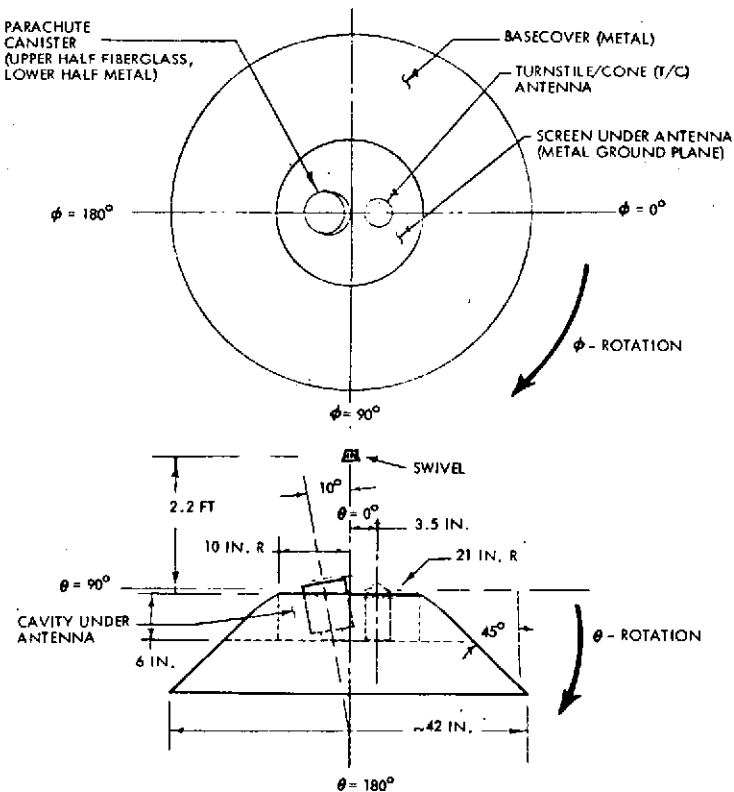


Figure 7.6J-3. Mockup of Large Probe

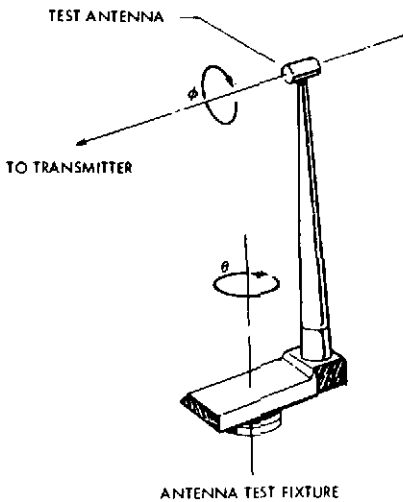


Figure 7.6J-4. Antenna Coordinate System

Great circle patterns are defined by rotating the test antenna about the θ axis for 360 degrees while maintaining a constant ϕ angle. Three great circle patterns are shown in the figures for $\phi = 0^\circ$, 45° , and 90° .

The measured conic patterns show the gain variation (pattern ripple) at an angle θ as the probe spins symmetrically about the spin axis of the probe. The great circle patterns measured show the beamwidth and beam symmetry about the centerline of the probe. From the great circle cuts, the antenna's half-power beamwidth (HPBW) and 0-dBi or 1-dBi beamwidths can be measured. The pattern ripple, HPBW, 0-dBi and 1-dBi beamwidth measurements for each test configuration are summarized in Table 7.6J-1. All the antenna patterns are recorded on decibel (dB) polar pattern paper.

Table 7.6J-1. Test Configurations

CONIC PATTERNS	A	B	C	D	E	F	NOTES:
	FREE SPACE ANTENNA PATTERNS	NO CANISTER	FULL LENGTH CANISTER	CUTOFF CANISTER	SCREEN UNDER ANTENNA	SCREEN UNDER ANTENNA WITH SWIVEL	
PATTERN RIPPLE $\theta = 0^\circ$	0.4 dB	2.5 dB	2.8 dB	3.0 dB	1.7 dB	3.0 dB	
PATTERN RIPPLE $\theta = 60^\circ$	1.1 dB	7.9 dB	6.6 dB	5.8 dB	2.6 dB	2.0 dB	
ANTENNA GAIN ON AXIS OVER ISOTROPIC	5.5 dB		7.4 dB	8.0 dB	5.6 dB	4.1 dB	
GREAT CIRCLE PATTERNS							
HPBW AT $\phi = 0^\circ$	98°	43°	83°	28°	120°	130°	
HPBW AT $\phi = 45^\circ$	102°	57°	65°	22°	111°	128°	
HPBW AT $\phi = 90^\circ$	99°	75°	89°	70°	126°	120°	
BEAMWIDTH AT 0 dB I, $\phi = 0^\circ$	133°		106°	110°	139°	140°	
BEAMWIDTH AT 0 dB I, $\phi = 45^\circ$	133°		114°	107°	140°	137°	REQUIRED = 135°
BEAMWIDTH AT 0 dB I, $\phi = 90^\circ$	134°		117°	136°	147°	136°	
BEAMWIDTH AT 1 dB I, $\phi = 0^\circ$	123°		98°	78°	131°	132°	
BEAMWIDTH AT 1 dB I, $\phi = 45^\circ$	121°		103°	100°	129°	130°	REQUIRED = 116°
BEAMWIDTH AT 1 dB I, $\phi = 90^\circ$	118°		110°	127°	140°	124°	

The above test configurations are analyzed and briefly discussed in the following paragraphs and summarized in Table 7.6J-1.

1. FREE SPACE PATTERNS

The free space test patterns of the turnstile/cone antenna have an HPBW of approximately 100 degrees (see Figures 7.6J-5, 7.6J-6, 7.6J-7, and Table 7.6J-1). In Column A of Table 7.6J-1, the free space pattern characteristics of the turnstile/cone antenna used are summarized. The on-axis gain relative to isotropic is 5.5 dB. The pattern ripple is less than 1 dB. Figures 7.6J-8 and 7.6J-9 show the ripple pattern at $\theta = 0$ and 60 degrees, respectively. The source antenna and receiving antenna (turnstile/cone) are both righthand circularly polarized. The 0-dBi and 1-dBi beamwidths are also shown in the table. These generally meet the mission requirements (Figure 7.6J-2); however, this test program is mainly concerned with the performance of the antenna for various afterbody configurations.

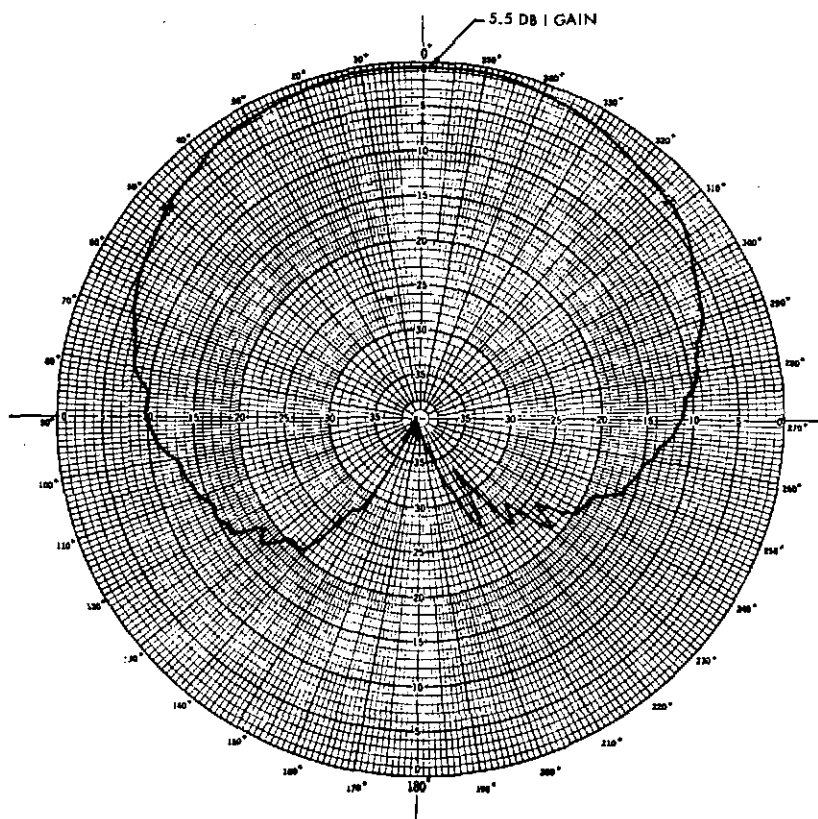


Figure 7.6J-5. Free Space Great Circle Pattern
($\phi = 0^0$; $\theta = 0^0 \rightarrow 360^0$; $F = 2.2$ GHZ)

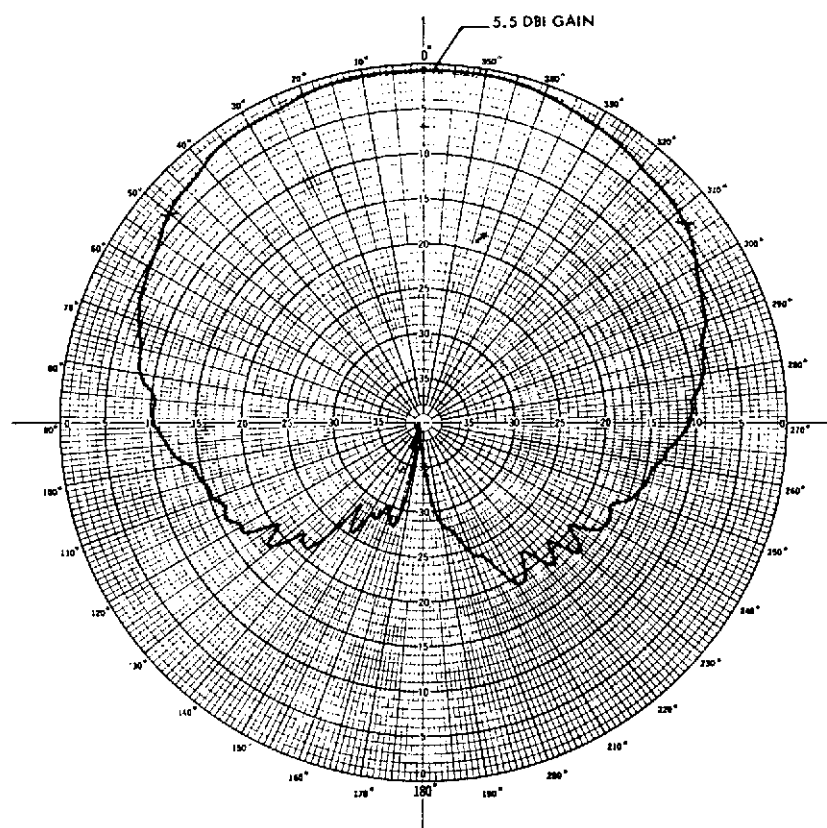


Figure 7.6J-6. Free Space Great Circle Pattern
 $(\phi = 45^\circ; \theta = 0^\circ \rightarrow 360^\circ; F = 2.2 \text{ GHZ})$

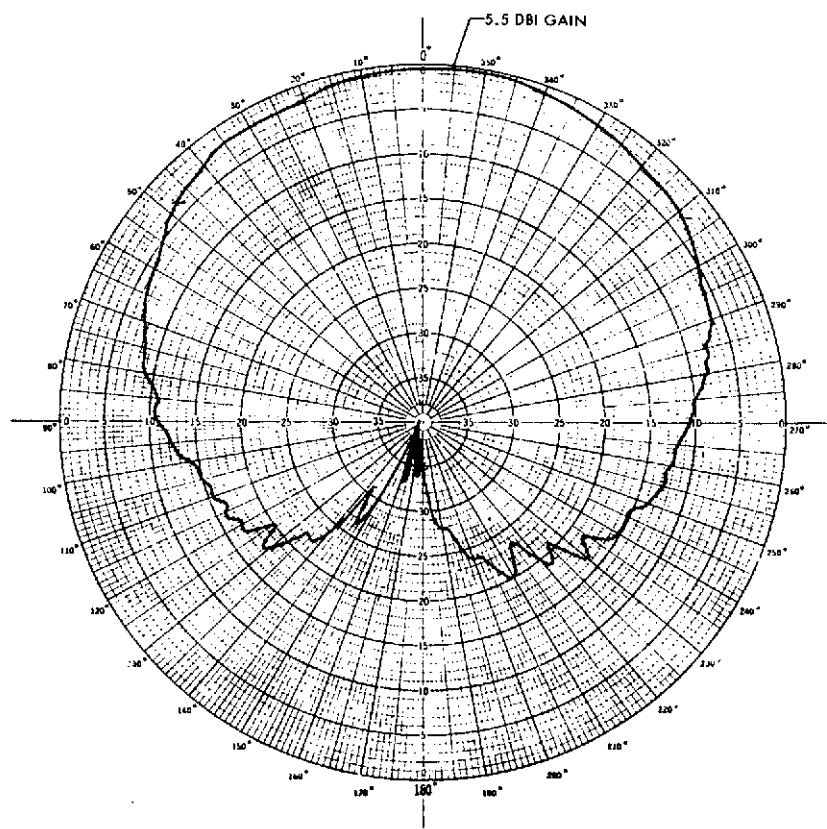


Figure 7.6J-7. Free Space Great Circle Pattern
 $(\phi = 90^\circ; \theta = 0^\circ \rightarrow 360^\circ; F = 2.2 \text{ GHZ})$

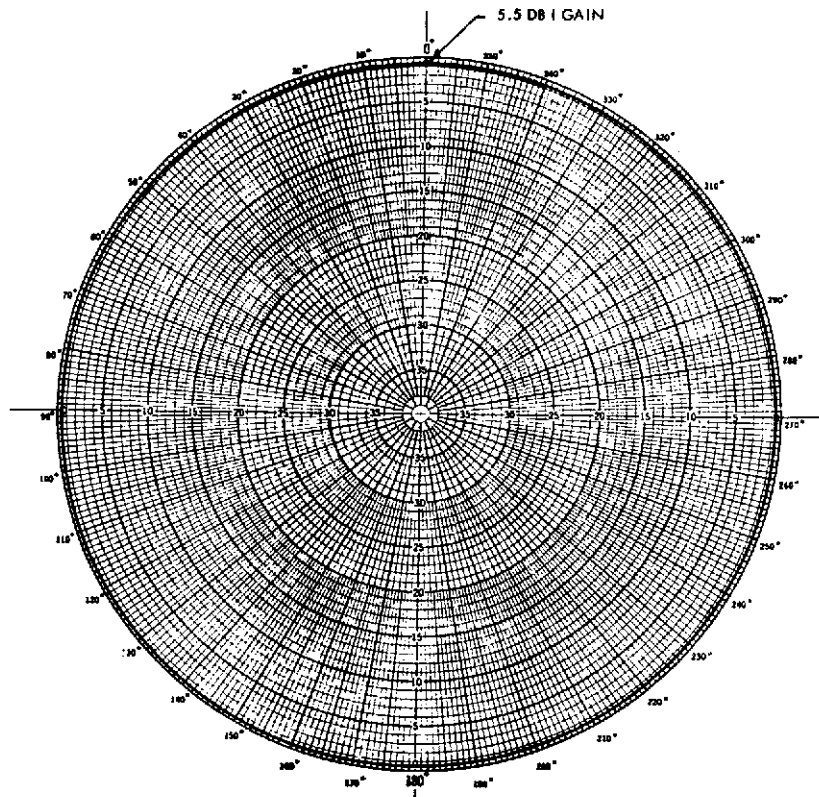


Figure 7.6J-8. Free Space Conic Pattern
 $(\theta = 0^\circ; \phi = 0^\circ \rightarrow 360^\circ; F = 2.2 \text{ GHz})$

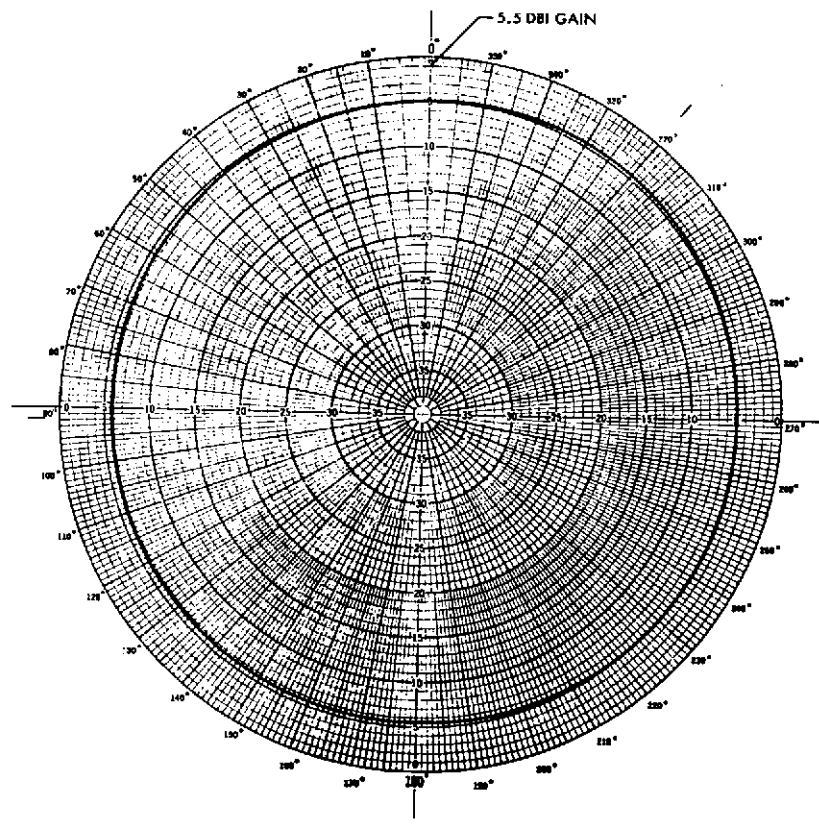


Figure 7.6J-9. Free Space Conic Pattern
 $(\theta = 60^\circ; \phi = 0^\circ \rightarrow 360^\circ; F = 2.2 \text{ GHz})$

2. LARGE PROBE TEST, NO CANISTER

The antenna was mounted on the large probe without the parachute canister or screen under the antenna and a set of patterns was measured. The basic patterns are summarized in Column B of Table 7.6J-1. The HPBW was critically narrowed by the cavity. The patterns for this configuration are not shown.

3. LARGE PROBE TEST, FULL-LENGTH CANISTER

A full-length metal parachute canister was added as shown in Figure 7.6J-3 and tested. From the summary given in the table, it can be seen that the addition of a full-length canister resulted in an improvement in the HPBW, but not enough improvement occurred to meet the requirements of Figure 7.6J-2.

4. LARGE PROBE, CUT-OFF CANISTER

The canister was cut off at the bottom of the antenna to simulate the top half of the canister being fiberglass, which is assumed to be RF transparent. The antenna patterns for this configuration are summarized in Column D of Table 7.6J-1. The cut-off canister narrowed the HPBW and increased the on-axis gain; therefore, this configuration is also undesirable.

5. LARGE PROBE, SCREEN UNDER ANTENNA

It was determined that the cavity under the antenna was the main contributor to the narrow antenna HPBW. A metal screen was placed over the large cavity and under the choke of the antenna (as shown in Figure 7.6J-1). A summary of the patterns is shown in Column E of Table 7.6J-1 and the actual patterns are shown in Figures 7.6J-10 through 7.6J-14. The HPBW increased over that of the free space patterns and the on-axis gain was changed to 5.6 dBi. The 0-dBi and 1-dBi gain beamwidths were increased also and generally met the probe requirements of Figure 7.6J-2. Therefore, a ground plane such as a metal screen or metal foil should be used to cover the large cavity on the probe.

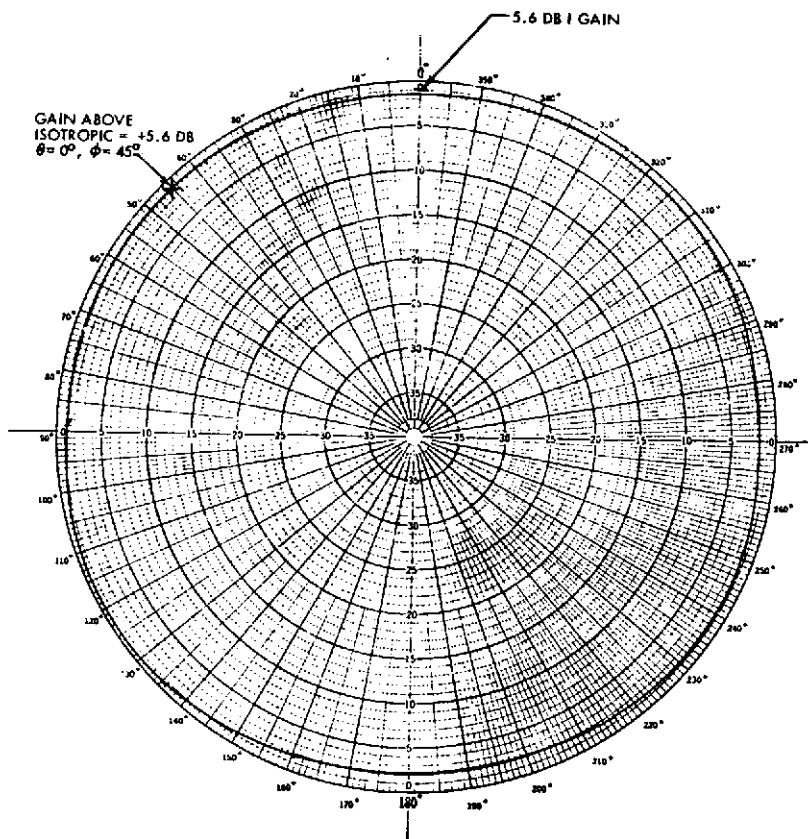


Figure 7.6J-10. Large Probe, Screen Under Antenna, Conic Pattern
 $(\theta = 0^\circ; \phi = 0^\circ \rightarrow 360^\circ; F = 2.2 \text{ GHz})$

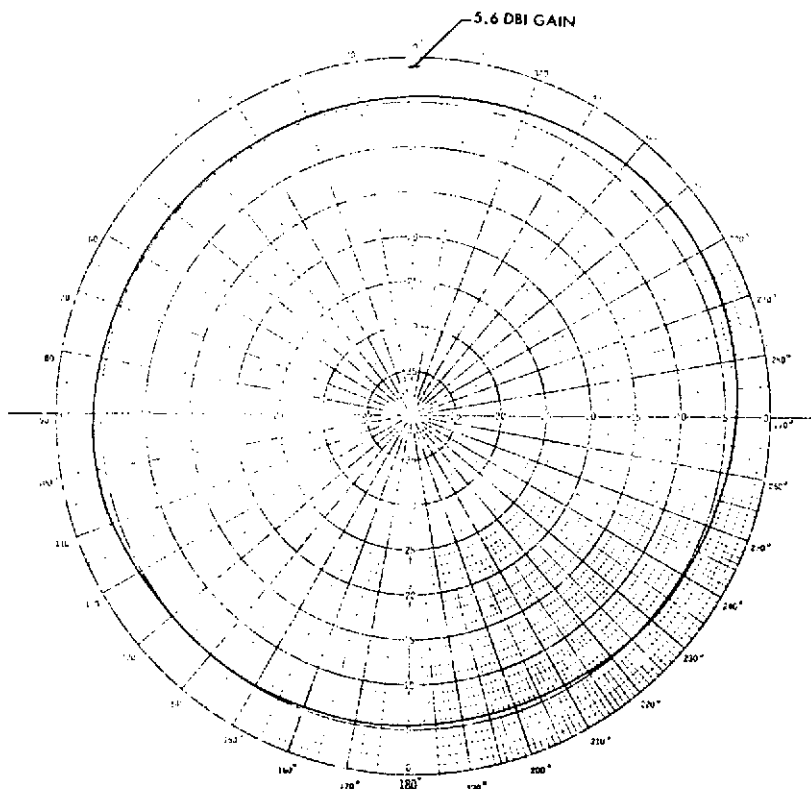


Figure 7.6J-11. Large Probe, Screen Under Antenna, Conic Pattern
 $(\theta = 60^\circ; \phi = 0^\circ \rightarrow 360^\circ; F = 2.2 \text{ GHz})$

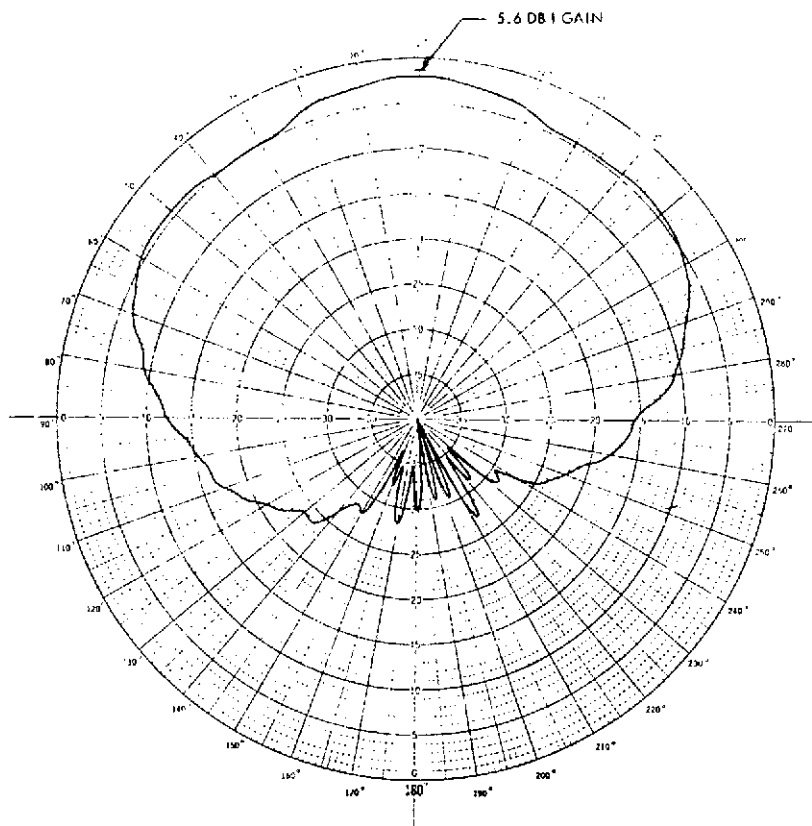


Figure 7.6J-12. Large Probe, Screen Under Antenna, Great Circle Pattern
 $(\phi = 0^\circ; \theta = 0^\circ \rightarrow 360^\circ; F = 2.2 \text{ GHz})$

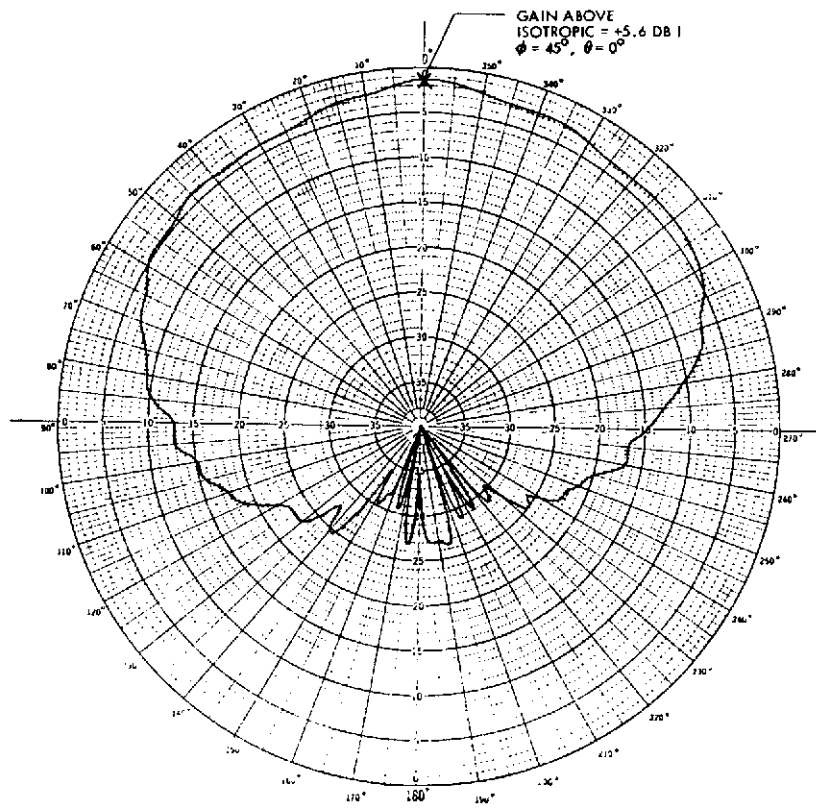


Figure 7.6J-13. Large Probe, Screen Under Antenna, Great Circle Pattern
 $(\phi = 45^\circ; \theta = 0^\circ \rightarrow 360^\circ; F = 2.2 \text{ GHz})$

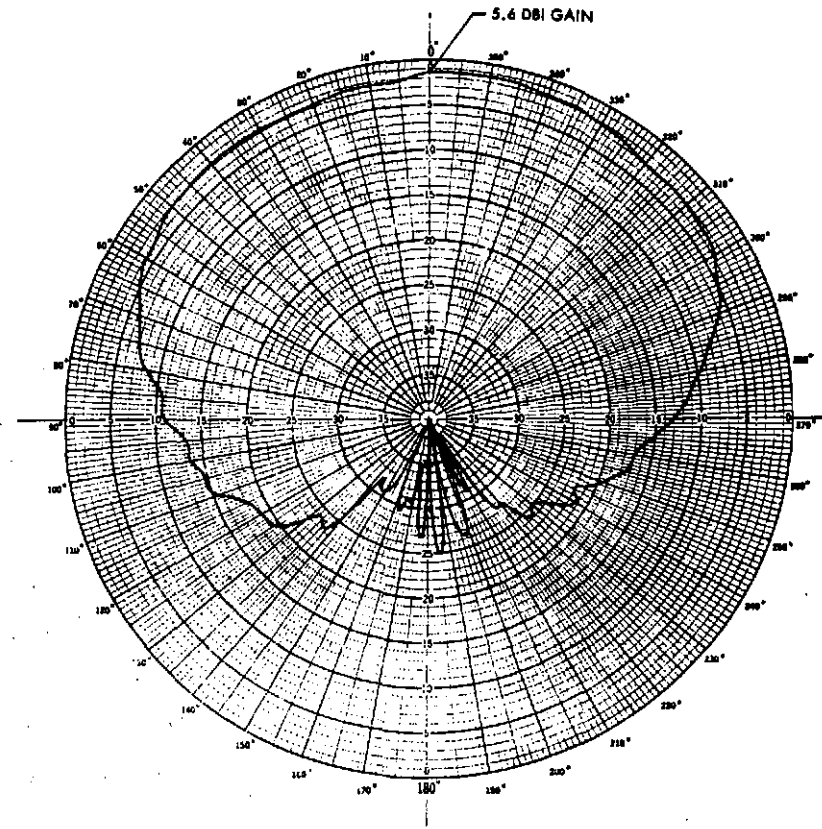


Figure 7.6J-14. Large Probe, Screen Under Antenna, Great Circle Pattern
 $(\phi = 90^\circ; \theta = 0^\circ \rightarrow 360^\circ; f = 2.2 \text{ GHz})$

6. LARGE PROBE, SCREEN UNDER ANTENNA WITH SWIVEL

As the probe is descending to the surface of Venus, a parachute is released following blackout (approximately 70 km above the surface of Venus). The parachute will have a metal swivel as shown in Figure 7.6J-3. Since the swivel is metal and is only 26 inches from the antenna and on the centerline, a test was conducted to determine its effect on the antenna pattern. The pattern shows that the on-axis gain was reduced to 4.1 dBi. A summary of the patterns is shown in Column F of the table. The 0-dBi and 1-dBi gain beamwidths were reduced slightly from those without the swivel. It is apparent that a metal swivel will not be of much consequence in meeting the ripple and gain requirements of Figure 7.6J-2.

7. CONCLUSIONS

An open cavity directly under the turnstile/cone antenna was shown to appreciably degrade the antenna pattern by narrowing the HPBW. A metal parachute canister had a slight effect on the beamwidth; however, the cavity under the antenna swamped out this effect. A metal screen was constructed over the cavity and under the antenna choke to eliminate the

pattern degradation. This corrective measure was adequate to meet the mission requirements (Figure 7.6J-2) with the turnstile/cone antenna.

Tests also indicated that a metal swivel on centerline of the probe antenna (see Figure 7.6J-3) has the effect of lowering the on-axis gain (-1.5 dB), and slightly affecting the beamwidths. No attempt was made to optimize the antenna performance. However, these preliminary test data verify that the antenna gain requirements can still be met with a swivel. All test configurations were tested with a 180-degree antenna radome opening and no radome simulation (free space).

An Atlas/Centaur antenna test program, for both large and small probes, is currently underway. The data obtained from the Thor/Delta configuration proved applicable to the design of the Atlas/Centaur probes, e.g., the use of a metal ground plane to cover the cavity under the antenna. The Atlas/Centaur testing will be extended to include the following areas:

- Radome opening (minimum radome size)
- Radome losses (ablator and stiffners)
- Optimizing antenna pattern on probe bodies.

APPENDIX 7.6L
TRADEOFF ANALYSIS OF ONE-WAY VERSUS
TWO-WAY DOPPLER TRACKING
HARDWARE IMPLEMENTATION

1. Introduction	7.6L-1
2. Alternative Equipment Approaches	7.6L-2
3. Comparison of Systems	7.6L-7
4. Conclusions	7.6L-14
5. Recommendations	7.6L-15

APPENDIX 7.6L
TRADEOFF ANALYSIS OF ONE-WAY VERSUS TWO-WAY
DOPPLER TRACKING HARDWARE IMPLEMENTATION

1. INTRODUCTION

System modeling of one-way and two-way links between a Pioneer Venus descent probe and the DSN has been presented in Appendices 7.6A and 7.6B. Detail tracking accuracy requirements and comparisons have not been addressed in this appendix; rather we discuss the probe hardware implications, the impact on the DSN, the risk and effect on the telemetry channels, plus acquisition and tracking implications of one-way and two-way links for the large and small probes.

1.1 Tracking Problem

Tracking the probes during descent through the atmosphere may allow observation and measurement of wind shear effects. Measurement of the received downlink carrier frequency can yield range rate from a single site and tangential velocity with DLBI techniques using dual sites. Both one-way and two-way links are considered as viable options for obtaining Doppler measurements; however from a cost standpoint one must consider the capability of the DSN to handle the number and type of links postulated. Tracking accuracies are assessed in Section 3.2 of this report.

1.2 Requirements

Basic requirements are: (1) to provide some measure of Doppler to assess wind shear as the probes descend to the planet surface; (2) to provide downlink telemetry from each of the probes during the descent phase; (3) to provide capabilities of performing both Doppler measurement and telemetry for a minimum of two probes and one bus simultaneously for a staggered time arrival of probes at the planet; and (4) alternatively, consider providing Doppler measurement and telemetry for four probes and one bus simultaneously for a nearly simultaneous arrival of probes at the planet.

2. ALTERNATIVE EQUIPMENT APPROACHES

Assuming that all five vehicles were required to operate in a two-way mode simultaneously with standard DSN frequency translation ratios, and that real-time (on-line) processing of two-way Doppler were required, the DSN would need five receivers, five uplink channels, and five Doppler extractors to handle the tracking. These requirements create a significant DSN cost impact for single station coverage or even for dual station coverage where five uplinks are concerned. Therefore, other alternatives were considered. These include: (1) the two-way coherent S-band approach currently implemented by the DSN; (2) an alternative two-way Doppler configuration; (3) a one-way Doppler approach and; (4) a mixture of one-way and two-way links. Spacecraft equipment and DSN hardware/software are described for each of the four approaches. Further, a staggered probe arrival time concept is considered where a maximum of two probes and one bus are tracked simultaneously.

2.1 Spacecraft Equipment Configurations

The standard two-way DSN system is the first approach considered because it is currently operational. A similar technique, where five simultaneous two-way links are required, is to develop a set of transponders with close, but unique, frequency turnaround ratios so that a single uplink could serve multiple probes at different downlink frequencies. The one-way Doppler technique uses the transmitter portion of a transponder as the frequency source with stability and accuracy provided by its internal oscillator or an ultra-stable external oscillator.

2.1.1 DSN Transponder Approach

An S-band transponder, compatible with the DSN, provides a two-way Doppler coherence by deriving the transmitter reference frequency from a source phase-locked to the received carrier so that the transmit-to-receive frequency ratio is fixed at $\frac{240}{221}$. Frequencies for local oscillators and intermediate receiver stages have been selected and tested for minimum interference and spurious signal generation. Present ground equipment and software are compatible with this operation as discussed later. The transponder block diagrams Figures 7.6L-1 and 7.6L-2 show frequencies in various parts of the unit. Note that all mixer frequencies are multiples of the VCO

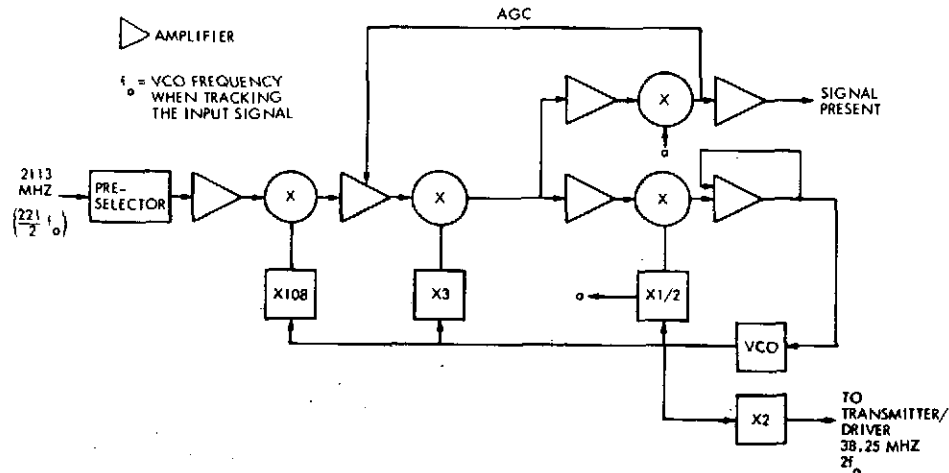


Figure 7.6L-1. Functional Diagram S-Band Receiver Portion of Transponder

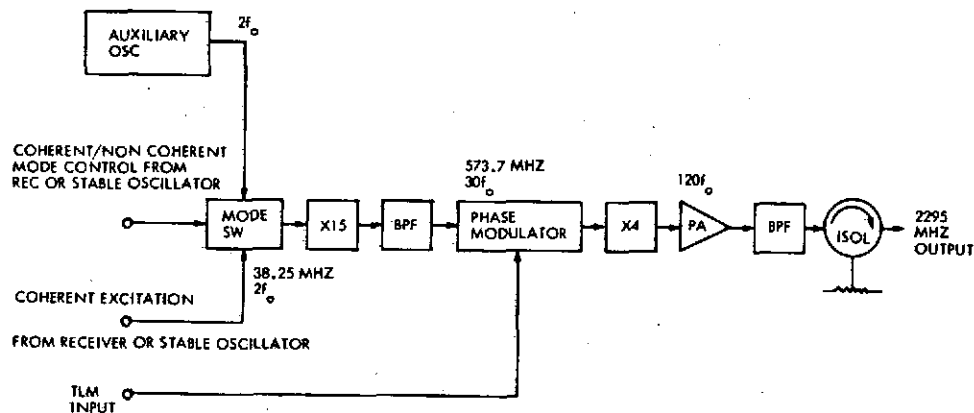


Figure 7.6L-2. Functional Diagram S-Band Transmitter/Driver Portion of Transponder

frequency which is $\frac{2}{221}$ times the received frequency. This frequency is doubled and sent to the transmitter as a frequency source for the X60 multiplier chain. The stability of this reference signal is derived from the stability of the ground transmitter signal, which is tracked by the receiver phase lock loop.

2.1.2 New Transponder Ratio Approach

All of the probes could operate with a single uplink carrier and different downlink frequencies if the probe transponders had different frequency ratios, all close in magnitude to the DSN ratio of $\frac{240}{221}$. The numerator in each ratio must be a multiple of powers of 2, 3, and/or 5 to ease design of the transmitter multiplier chain. The denominator mainly affects the

design of the receiver phase-lock loops where mixer frequencies must be chosen to minimize image frequency and intermodulation effects. Some ratios to be considered are $\frac{25}{23}$, $\frac{64}{59}$, $\frac{162}{149}$, $\frac{360}{331}$, and $\frac{400}{369}$.

This approach calls for each probe to be equipped with a transponder having a unique ratio so that one uplink carrier would service all the probes to create four unique downlink frequencies. For example, if the uplink is DSN channel 22b at 2116.04 MHz, a transponder ratio of $\frac{64}{59}$ yields a downlink at 2295.37 MHz close to DSN channel 15a. Whether this ratio is practical from a design standpoint can only be proven by an extensive analysis with breadboarding of the circuits.

The chief drawback of this approach is the need for a transponder development program for each probe frequency ratio, with a corresponding ground equipment cost. There is a corresponding development cost for the ground receiving and Doppler extraction for each downlink.

2.1.3 One-Way Doppler Approach

One-way Doppler tracking can be achieved by monitoring the frequency of the received downlink carriers for each probe. The frequency source for the probe transmitter is an internal or external oscillator that replaces the coherent drive signal derived from the receiver VCO in a standard DSN-compatible transponder. The long-term and short-term frequency stability limits the Doppler data accuracy and the former can greatly influence the signal acquisition time as discussed later. This approach requires no transponder modification if an external stable oscillator having a long-term stability of ± 4 parts in 10^7 or better is used. The alternative is to modify the internal oscillator to improve stability. For example, the Viking transponder internal oscillator has a stability of ± 1.5 parts in 10^5 and would require modification to reduce the one-way link acquisition time as shown later. Addition of temperature compensation circuitry should improve stability to about two parts in 10^6 over the anticipated temperature range. A controlled-temperature oven for the oscillator crystal with both a heater for initial warmup and a phase-change heat sink material for precise temperature control offers stability exceeding 1 part in 10^7 for an external oscillator. Oscillator development and testing represents the only significant increase in cost for one-way Doppler tracking. Unlike the development costs for the two-way transponders with new frequency translation ratios, a single

equipment development effort suffices for the set of probes. No change is needed in the transmitter for one-way Doppler except for the oscillator circuit or the use of an external oscillator.

2.2 DSN Equipment for Doppler Tracking

Equipment configurations and associated software are reviewed for operation with the one-way and two-way Doppler approaches. The present S-band equipment in DSN stations is reviewed as a baseline, and equipment changes for the two other Doppler approaches are discussed.

2.2.1 Two-Way Doppler Extraction

In the system implemented in the DSN the Doppler extractor compares the downlink frequency with the transmitter frequency multiplied by $\frac{240}{221}$. The difference, which is the Doppler frequency plus various errors, is mixed with a bias frequency to eliminate negative values before recording and processing. The receiver is designed to avoid spurious signals at low signal levels that might be confused with valid carriers. All exciter and local oscillator frequencies are synthesized from a common atomic master oscillator with a stability of 1 part in 10^{12} . Doppler processing software in the DSN is arranged with constants related to the $\frac{240}{221}$ ratio.

If two-way Doppler with this ratio is used, no additional hardware or software is needed for any single link. However, each 64-meter site is limited at present to two uplinks, five receiving channels, and three Doppler extractors, so that only two of the five vehicles could be tracked per 64-meter station, assuming an adequate signal-to-noise ratio (SNR) in the uplinks. If one includes the 26-meter net, a total of three vehicles could be handled at one site. To monitor all four probes plus the bus simultaneously, one of the two DSN stations would have to transmit and receive on three frequencies while the other would need to transmit and receive on at least two frequencies. However, because the probe uplinks require at least a 20 dB nominal tracking loop SNR for good downlink telemetry, it is desirable to use at least 100 kW on each probe uplink. Therefore, only 2 uplinks are available to the probes, one at each 64-meter station. This power could be reduced to 40 kW to be compatible with the Goldstone station with some added downlink risk and degradation. Thus, with two-station coverage, assuming two 40 kW probe uplinks at Goldstone, a 100 kW

64-meter uplink from Canberra and a 26-meter net transmitter for the bus uplink one would still be capable of handling only four two-way links simultaneously. Moreover, if a station transmitter fails, the available probe uplinks are reduced to one or at most two if Goldstone is transmitting in a dual mode. Thus even for a staggered arrival mission there is a possibility that only one probe and one bus uplink would be available.

2.2.2 Ground Equipment for New Frequency Ratios

The alternative coherent Doppler approach, where different frequency ratios are used for each probe, can be implemented for non-real-time Doppler measurement without additional receiving equipment. In this approach the ground receivers track the carriers in a normal manner for telemetry demodulation, but the coherent carrier signal can be down-converted to the passband of instrumentation recorders for storage and off-line frequency measurement, obviating the need for generating signals from the ground transmitter at precise ratios to the uplink carrier. The ground configuration requires receivers, recorder channels, and frequency synthesizers for each probe downlink. The signals may also be recovered from predetection recorders for two-way Doppler measurement at some reduction in accuracy.

The single DSN uplink to all probes establishes the frequency reference and stability for all downlinks. These parameters are expected to equal the 1 part in 10^{12} stability performance of the equipment presently installed at the DSN.

2.2.3 One-Way Doppler DSN Implementation

Receiving and processing of one-way Doppler data can be similar to the approach described above for new frequency ratios. Ground receivers shift the received frequencies to the passbands of instrumentation recorders for predetection storage and off-line processing. Unlike either two-way technique, the DSN has no control over the frequency of the downlink. Use of a single atomic frequency source at the receiving site effectively eliminates ground errors in measuring frequency. The recorded frequency time history contains the Doppler shift plus any variations in the probe transmitter frequency. These transmitter variations are partially correctable

by use of probe telemetry records and preflight calibration of transmitter frequency variation as a function of temperature and vibration. Residual uncertainties in frequency will appear as errors in Doppler.

2.2.4 A Mix of One-Way and Two-Way Doppler Links

The selected approach for the preferred configurations uses the 400 standard $\frac{221}{240}$ two-way Doppler for the bus and the large probe and uses one-way Doppler for the three small probes. The DSN implementation for this arrangement (assuming simultaneous probe arrival) uses the 400 kW Goldstone uplink for the large probe, a 20 kW uplink from a 26-meter station for the bus, four receivers at each of two 64-meter stations for on-line probe telemetry, one receiver at each of the two 64-meter stations for open-loop reception of the five downlink signals, which are predetection recorded for off-line processing of Doppler and telemetry, and one receiver and Doppler tracker at each of two 26-meter stations for bus telemetry and tracking.

The DSN arrangement for the staggered arrival is identical to the above except that the on-line bus telemetry is received at the 26-meter net, and two-way Doppler for the bus is extracted at the 26-meter net. After the last two probes have entered, on-line telemetry reception for the bus is handled by the 64-meter stations. This arrangement allows two receivers at each 64-meter station to operate on-line for each vehicle as well as allowing one receiver at each 64-meter station for predetection recording.

3. COMPARISON OF SYSTEMS

This section compares the approaches discussed previously in terms of probe subsystem weight and power, DSN compatibility, technical performance, and relative cost and complexity. Tracking accuracies are assumed to be superior for a two-way link having a high transponder loop SNR compared to a one-way link for practical probe transmitter oscillator stabilities.

3.1 Weight and Power Requirements

Table 7.6L-1 compares probe hardware weight and power for one-way and two-way Doppler tracking, including the receiver, diplexer, and stable oscillator. The transponders are assumed to be identical in size and weight

Table 7.6L-1. Power and Weight Comparison

PROBE HARDWARE	DOPPLER APPROACH							
	TWO-WAY STANDARD DSN 221/240 FREQ RATIOS			TWO-WAY MULTIPLE FREQ RATIOS			ONE-WAY WITH STABLE OSCILLATOR	
	WEIGHT (LB)	MASS (KG)	POWER (W)	WEIGHT (LB)	MASS (KG)	POWER (W)	WEIGHT (LB)	MASS (KG)
DIPLEXER	2.0	0.91		2.0	0.91			
RECEIVER (INCLUDING CABLING)	2.5	1.13	1.5	2.5	1.13	1.5		
STABLE OSCILLATOR							0.75	0.34
TOTAL (SEE NOTE) RF POWER AMPLIFIER AND CABLING	4.5 LB	2.04 KG	1.5 W	4.5 LB	2.04 KG	1.5 W	0.75 LB	0.34 KG
								0.2 W

NOTE: IT HAS BEEN ESTIMATED THAT THERE IS ESSENTIALLY NO DIFFERENCE BETWEEN THE ONE-WAY AND TWO-WAY LINK AS FAR AS TELEMETRY DEGRADATION IS CONCERNED FOR A GIVEN DATA RATE GREATER THAN ABOUT 10 BPS DUE TO A BALANCE BETWEEN ONE-WAY OSCILLATOR NOISE AND STRONG SIGNAL TWO-WAY DOWNLINK SUPPRESSION. THEREFORE, IT IS ASSUMED THAT THE POWER AMPLIFIER WEIGHT AND POWER DO NOT ENTER INTO THE TRADEOFF. ADDITIONAL RF CABLING IS REQUIRED IN THE TWO-WAY LINK FOR THE RECEIVER AND DIPLEXER. THE ANTENNA AND TRANSMITTER/DRIVER ARE COMMON ITEMS AND THEREFORE DO NOT ENTER INTO THE TRADEOFF.

for both two-way approaches. Also, the transmitter driver for one-way Doppler is identical to the transmitting segment of the large probe transponder with either a stable external oscillator or an internal frequency source. The external oscillator is assumed to have both temperature compensation circuitry and an enclosed crystal oven with both a heater and phase-change material to minimize temperature effects on frequency stability. The two-way link weight and power exceed that of the one-way link by 1.7 kg (3.75 lb) and 1.3 W.

3.2 Range Rate Measurement Accuracy

Range rate measurement accuracy is influenced by such factors as receiver thermal noise, oscillator noise, quantization error, and carrier frequency and is significantly different for one-way and two-way Doppler. The effect of this uncertainty on one-way Doppler is shown by the following:

$$\Delta f_d = \frac{R}{C} \Delta f_t$$

where Δf_d is the error in Doppler frequency, f_d , due to a change, Δf_t , from the nominal transmitter frequency, f_t . Also, R is the radial velocity, and C is the speed of light. The computation of R uses the nominal instead of the true value of f_t , resulting in a range rate error, ΔR , proportional to Δf_d and R .

$$\Delta R = \frac{C}{f_t} \Delta f_d = \frac{R}{f_t} \Delta f_t$$

In a two-way Doppler system with turnaround ratio G, the error ΔR_2 is

$$\Delta R_2 = 2 G \frac{R}{f_t} \Delta f_t$$

In a two-way Doppler system, the instability is expected to be approximately 1 part in 10^{12} , compared to 4 parts in 10^7 for one-way Doppler.

Figure 7.6L-3 is a plot of range rate error as a function of oscillator instability (assuming no other errors) for range rates representative of preentry and parachute descent. The error, less than 10 mm/s, is negligible for the two-way Doppler system (1 part in 10^{12}) and within the desired range for one-way Doppler with an oscillator stability better than ± 4 parts in 10^7 . As will be shown below, the oscillator requirements are equally stringent for acquisition.

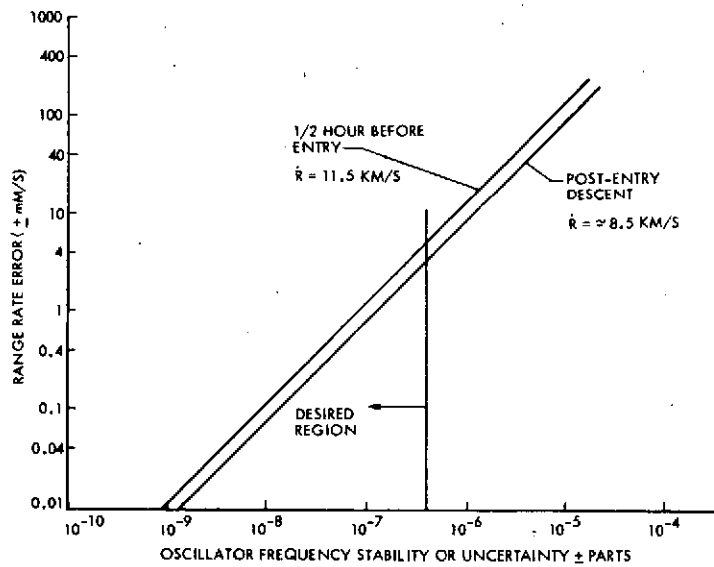


Figure 7.6L-3. Range Rate Measurement Errors Due to Uncertainty in Transmitter Frequency for One-Way Doppler

3.3 Acquisition Comparison

The process of acquisition requires the search for, detection of, and lock-on of the received signal. For two-way Doppler, both the probe and DSN receivers must perform this operation.

3.3.1 One-Way Doppler Acquisition

The time required for acquisition is a function of the search bandwidth and the receiver SNR. The size of the search band is determined by the

uncertainties in transmitter frequency and in Doppler frequency. System parameters determine the available SNR, which determines the allowable frequency sweep rate for the receiver to lock on the signal. The maximum lock-on sweep rate, f_{\max} for a 90% probability of acquisition is (see p. 49 of Phaselock Techniques by F. M. Gardner, New York, Wiley, 1966):

$$f_{\max} = \frac{1}{(2\pi)(1+d)} \left(1 - \frac{1}{\sqrt{\text{SNR}_L}}\right) \frac{\alpha}{\alpha_o} \omega_{no}^2 \quad \text{Hz/s}$$

where:

f_{\max} = max sweep rate (Hz/s)

d = 0.04 for 0.707 damping

SNR_L = Signal-to-noise ratio in $2B_L$ (double-sided loop noise bandwidth)

α = Limiter suppression factor

α_o = Threshold limiter suppression factor

ω_{no} = Loop natural frequency at threshold

In the DSN Block IV receiver the ratio of $\alpha/\alpha_o = 4$ for a strong signal (13 dB in $2B_{LO}$) and $\omega_{no} = 10$ for the 10 Hz loop. Therefore, the maximum sweep rate for acquisition is 38 Hz/s for the 10 Hz loop. The signal-to-noise ratio for the 30 Hz loop is sufficient to allow a sweep rate of 150 Hz/s.

Figure 7.6L-4 shows the time needed for carrier acquisition of a one-way downlink for various Doppler uncertainties as a function of carrier frequency stability for 90 percent probability of acquisition. The range rate used here is for preentry conditions where the transmitter operates for 10 minutes. It is expected that a maximum of 100 seconds should be allotted to carrier acquisition to allow sufficient time to determine that the link is operable prior to probe entry. This time constraint suggests an oscillator stability of ± 4 parts in 10^7 for a Doppler predict accuracy of ± 1 percent and use of the 10 Hz loop. For the 30 Hz loop and a ± 1 percent Doppler predict accuracy one could use an oscillator having a stability of ± 3 parts in 10^6 . Use of the 10 Hz loop and Doppler predict of ± 2.5 percent will not allow a full acquisition sweep in the time allocated. Doppler profiles are shown in Section 4.2 of the technical volume.

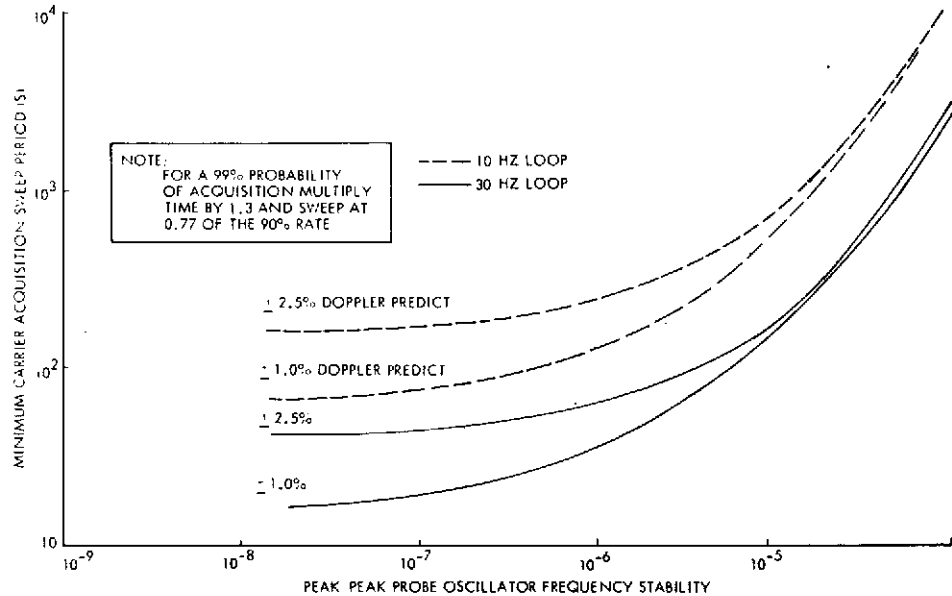


Figure 7.6L-4. Search Period for 90% Probability of Acquisition Versus Peak to Peak Frequency Stability of Oscillator for One-Way Link

3.3.2 Two-Way Doppler Acquisition

For two-way Doppler acquisition two alternative approaches are available for locking the uplink: (1) perform a frequency search in the transponder; or (2) ramp the ground transmitter frequency through the receiver frequency uncertainty band and return it to the estimate of best lock frequency.

The lowest cost approach would dictate use of ground transmitter ramping. However, since the probe arrival time uncertainty is approximately two minutes, post-entry uplink ramping of the transmitter would be required to continue past the nominal entry time. At any reasonable uplink ramping rate the downlink receiver could not acquire, therefore one could lose a few minutes of data immediately after entry unless it could be recovered from predetection tapes. When the uplink frequency search is performed by the transponder the acquisition can be accomplished within a few seconds after blackout and there is no ramping of the downlink as a result of uplink search. The transponder search circuitry is an added cost and there is more chance of self lock up with this method (locking to a spurious signal).

Time required to perform uplink acquisition, after probe entry, is shown in Table 7.6L-2 for various values of Doppler uncertainty predict and receiver local oscillator stability using a 10 kHz/s transmit frequency ramp at the DSN station. For oscillator stabilities of at least ± 1 part in 10^6 the ramp rate can be reduced to 1 kHz/s and still acquire in approximately 10 seconds, which is insignificant compared to the two minutes of ramping required due to time uncertainty.

7.6L-2. Uplink and Downlink Acquisition Times

UPLINK LOCK CONDITION	DOPPLER PREDICT UNCERTAINTY (KHZ)	OSCILLATOR STABILITY UNCERTAINTY (KHZ)	TOTAL FREQUENCY UNCERTAINTY UPLINK (KHZ)	UPLINK SEARCH RATE (KHZ/S) (ASSUMES A 250 HZ 2B _{LO} LOOP)	UPLINK ACQ TIME (S)	TOTAL DOWNLINK FREQUENCY UNCERTAINTY (KHZ)	DOWNLINK CARRIER ACQUISITION TIME (S) (30 HZ LOOP, 150 HZ/S SEARCH RATE)	DOWNLINK CARRIER ACQUISITION TIME (S) (10 HZ LOOP, 37.5 HZ/S SEARCH RATE)
LOCKED ONE-WAY	($\pm 1\%$) 2.5	($\pm 1.5 \times 10^{-5}$) .69	71.5	10	7.15	5	33.3	129
LOCKED ONE-WAY	($\pm 2.5\%$) 6.25	($\pm 1.5 \times 10^{-5}$) .69	75.25	10	7.53	12.5 75.25	475 83.5 500	1900 334 2000
LOCKED ONE-WAY	($\pm 1\%$) 2.5	($\pm 1 \times 10^{-6}$) 4.6	7.1	10*	0.71	5 7.1	33.3 47.3	129 189
LOCKED ONE-WAY	($\pm 2.5\%$) 6.25	($\pm 1 \times 10^{-6}$) 4.6	10.85	10*	1.09	12.5 10.85	83.5 72.4	334 289
LOCKED ONE-WAY	($\pm 1\%$) 2.5	($\pm 1 \times 10^{-7}$) 0.46	2.96	10*	0.3	5 2.96	33.3 19.8	129 79
LOCKED ONE-WAY	($\pm 2.5\%$) 6.25	($\pm 1 \times 10^{-7}$) 0.46	6.71	10*	0.67	12.5 6.71	83.5 44.7	334 179
LOCKED ONE-WAY	($\pm 1.0\%$) 2.5	($\pm 1 \times 10^{-8}$) .046	2.55	10*	0.255	5 2.55	33.3 17	129 68
LOCKED ONE-WAY	($\pm 2.5\%$) 6.25	($\pm 1 \times 10^{-8}$) .046	6.3	10*	0.63	12.5 6.3	83.5 42	334 168

NOTE: *UPLINK SEARCH RATE COULD BE REDUCED TO LESS THAN 1 KHZ WITHOUT EXCESSIVE UPLINK ACQUISITION TIME

For downlink acquisition it is interesting to note (in Table 7.6L-2) that the downlink acquisition time for a one-way link becomes less than for a two-way because the one-way oscillator frequency uncertainty is reduced. This is due to the reduced uncertainty in one-way Doppler predicts versus two-way Doppler predicts. The 30 Hz DSN tracking loop is assumed to be used for initial acquisition.

3.4 Telemetry Performance

Telemetry performance of the two-way link is expected to be comparable to the one-way link (within a few tenths of a dB) provided there are no uplink anomalies such as a noisy receiver or intermittent loss of uplink lock (see Appendix 7.6A and the design control tables). However, during the uplink acquisition phase, some loss of data may occur when ramping the ground transmitter through the transponder receive frequency uncertainty range. Assuming the probe arrives at the nominal time, and the receiver, after blackout, acquires the ramped signal, the ramping operation must

continue for an additional period since the latest arrival time is about two minutes later. Thus, the downlink frequency is being ramped at a rate higher than the DSN receivers can track. An alternative approach is to begin the uplink ramping at the nominal plus two minutes time so as not to disturb the downlink. However, in reality, the downlink will probably not be acquired in this period anyway unless a stable auxiliary oscillator is used. Another, more expensive alternative, is to equip the transponder with an auto search capability so that the uplink signal will be acquired almost immediately after blackout ends. This search capability is not presently available in DSN-compatible transponders.

3.5 Relative Costs of Technical Approaches

A basic investigation of relative costs and technical complexities was conducted for the four approaches. Five simultaneous two-way Doppler measurements using standard $\frac{221}{240}$ ratios are not presently practical since it exceeds the present DSN capability; provision for additional channels would be expensive. The cost of transponders with different receive/transmit ratios would be prohibitive. The cost of implementing an automatic search capability in the transponder for a two-way link is more expensive than a ground transmitter ramping operation. One-way links possibly require development of an ultra-stable oscillator for the probes, but do not require diplexers or receivers, hence they would be least expensive in probe hardware (especially since some probes must be implemented with one-way links due to lack of sufficient DSN uplink capability). Predetection recording must be implemented at the DSN regardless of which approach is chosen; therefore it does not enter into the cost tradeoff. Doppler data processing is required for all approaches and therefore it does not impact the cost tradeoff.

A two-way link for the large probe and one-way links for the small probes would increase the hardware costs of the large probe over that of a one-way link, but would provide a two-way Doppler capability for the more highly instrumented large probe, which may be desirable. However, one-way links for all probes would appear to be the most cost-effective approach.

4. CONCLUSIONS

For one-way links it is desirable to have probe oscillator long-term stability equal to or better than ± 4 parts in 10^7 to provide less than a ± 10 mm/s source of error due to frequency uncertainty. In addition, this stability will allow carrier acquisition time at the DSN to be equal to or less than 100 seconds, assuming one sweep using the 10 Hz loop and a Doppler predict accuracy of ± 1 percent during the transmission period.

For a two-way link, a frequency search performed by the probe transponder could provide more rapid acquisition than the ground transmitter frequency ramp method. However, the receiver auto-search capability is an added expense and possible source of self-lock up or other failure mode. The ground transmitter frequency ramping method may cause loss of several minutes of post-entry data after blackout.

Table 7.6L-2 shows that if lock up of the uplink does not occur, the one-way downlink acquisition time is excessive for transponder auxiliary oscillator stabilities of ± 1.5 parts in 10^5 currently used in the existing Viking transponder. It is therefore desirable to have a more stable auxiliary oscillator, such as ± 2 parts in 10^6 .

At least some one-way links must be used to be compatible with the DSN limitation of available uplink channels unless nonstandard turnaround frequency ratios are used, and the latter is too expensive to consider seriously.

A one-way link provides a saving in the large probe of 1.7 kg (3.75 lb) and 1.3 watts over a two-way link due to the substitution of a stable oscillator for a receiver, diplexer, and some additional cabling for the latter two components.

In the case of sequential or staggered arrival of the probes at the planet, each probe, when arriving in groups of two with no overlap between groups, may be supported by two receivers (and two operators) in an on-line mode at each 64-meter station, as opposed to a single on-line receiver for each probe at each station when simultaneous arrival is selected. Having two operators and two receivers for each probe will reduce the downlink acquisition time to a minimum and will provide online redundancy all the way through the DSN hardware string if one desires (subcarrier demod, etc.).

5. RECOMMENDATIONS

From the communications standpoint it is recommended that sequential or staggered probe arrival times be used to allow dual on-line receiver coverage of each probe at each of two DSN stations, such as Goldstone and Canberra.

It is recommended that the bus be supported by the 26-meter stations until all probes have completed the post-entry link acquisition phase after which the 64-meter net can acquire the bus for the bus entry.

All small probes should be equipped for one-way links using a stable oscillator. It is desirable that the oscillator have long-term stability equal to or better than ± 4 parts in 10^7 to reduce acquisition time and minimize range rate measurement error; however to save hardware cost the stability may be degraded to the order of ± 2 parts in 10^6 and depend upon using the 30 Hz loop for initial acquisition. Further cost versus performance evaluation is required before a final specification can be recommended.

The large probe should be equipped for two-way link operation only if absolutely necessary to obtain the ultimate in tracking accuracy because it is both more expensive in equipment, testing, and operations, and more subject to equipment and operations malfunctions than the one-way link. Telemetry performance for either one-way or two-way operation is expected to be comparable (after uplink acquisition) due to the strong uplink signal; however, during uplink acquisition one can expect some loss of data. Therefore use of a two-way link is, in a sense, trading tracking performance for telemetry performance and there is some doubt as to the need for the improved tracking performance.

APPENDIX 7.6M

PROBE TELECOMMUNICATIONS DESIGN
CONTROL TABLES, ATLAS/CENTAUR MISSION
1978 ARRIVAL

APPENDIX 7.6M

PROBE TELECOMMUNICATIONS DESIGN CONTROL TABLES, ATLAS/CENTAUR MISSION, 1978 ARRIVAL

Telecommunication design control tables are provided here for the large and small probes for the Atlas/Centaur configuration, including bit rates for Version IV of the science payload.

The large probe link is two-way Doppler with PSK/PM modulation on the downlink at 128 bps. The small probe link is one-way Doppler with PSK/PM modulation at 64 bps. Six downlink tables (Tables 7.6M-1 through 7.6M-6) are provided, three for each probe type at altitudes above Venus surface of zero, 30, and 70 km. The large probe uplink is unmodulated and is used solely to provide the two-way Doppler signal. Table 7.6M-7 is included for the large probe uplink at 70 km only. Explanation of the table entries are provided in notes on the tables and the following paragraphs.

Table 7.6M-8 summarizes the margins for all downlinks. The systems are designed for a margin equal or greater than the "Sum of Adverse Tolerances." Also shown are the sum of the adverse tolerances, RSS of the adverse tolerances and antenna gain tolerance plus RSS of all other tolerances. In addition, the margin over the values for the three methods of combining tolerances are given. Because of the "one time only" nature of the probe entries and the many uncertainties of the link parameters relating to the Venus atmosphere, the "Sum of Adverse Tolerances" is the safest and most conservative way to design the link. However, it does require almost 3 dB more radiated power than an RSS or combined RSS plus sum of selected tolerances, and final performance requirements together with a detailed cost analysis could lead to selection of a less expensive, but higher risk design. The reason for selection of the antenna tolerance, as an example, to be added to the RSS of all other values is the high probability of antenna gain variation due to the vehicle rotation and some uncertainty as to winds that may tip the probe for several seconds.

Table 7.6M-1. Telecommunications Design Control Table, Atlas/Centaur Large Probe, Near Venus Surface

NO.	PARAMETER	NOMINAL VALUE	ADVERSE TOLERANCE	NOTES
1	TOTAL TRANSMITTING POWER (DBM) 36 W	+ 45.6	0.8	VOLTAGE & TEMP
2	TRANSMITTING CIRCUIT LOSS (DB)	- 1.6	0.4	
3	TRANSMITTING ANTENNA GAIN (DB) $\theta = 50^\circ$	+ 3.5	1.5	GAIN VARIATION
4	COMMUNICATIONS RANGE LOSS (DB) 0.43 AU	-255.9	0.0	
5	ATMOSPHERIC ABSORPTION & DEFOCUSING LOSSES (DB)	- 0.9	0.1	
6	POLARIZATION LOSS (DB)	- 0.2	0.1	
7	MULTIPATH & OTHER LOSSES (DB)	SEE NOTE 1		
8	RECEIVING ANTENNA GAIN (DB)	+ 61.7	0.4	JPL 810-5
9	RECEIVING CIRCUIT LOSS (DB)	0.0	0.0	JPL 810-5
10	NET LOSS (DB) (2+3+4+5+6+7+8+9)	-193.4	2.5	
11	TOTAL RECEIVED POWER (DBM) (1+10)	-147.8	3.3	
12	RECEIVER NOISE SPECTRAL DENSITY - (DBM/HZ)	-184.5	1.4	$25.5 \pm 9.5^\circ K$
13	TOTAL RECEIVED POWER/NO (DBM/HZ) (11-12)	+ 36.7	SUM 4.7	
CARRIER TRACKING				
14	CARRIER POWER/TOTAL (DB)	- 5.4	0.4	
15	ADDITIONAL CARRIER LOSSES (DB)	- 1.5	0.2	NOTE 2
16	THRESHOLD TRACKING BANDWIDTH - $2\Delta_{LO}$ (DB)	+ 10.0	0.8	
17	REQUIRED SNR (DB)	+ 13.0	0.0	
18	PERFORMANCE MARGIN (DB) (13+14+15-16-17)	+ 6.8	SUM 6.1	
DATA CHANNEL				
19	DATA POWER/TOTAL (DB)	- 1.5	0.2	
20	ADDITIONAL DATA CHANNEL LOSSES (DB)	- 6.0	0.5	NOTE 3
21	DATA BIT RATE - BPS (DB)	+ 21.1	0.0	128 BPS
22	THRESHOLD ENERGY PER DATA BIT - E_b/N_o (DB)	+ 2.3	0.0	NOTE 4
23	PERFORMANCE MARGIN (DB) (13+19+20-21-22)	+ 5.8	SUM 5.4	

NOTE: 1. MULTIPATH INCLUDED IN 15 & 20 BELOW.
 2. 1.0 DB PREDETECTION RECORDING LOSS + 0.5 DB DOWNLINK SUPPRESSION & DOPPLER EFFECTS IN ITEM 15.
 3. 1.0 DB PREDETECTION RECORDING LOSS + 3.8 DB NOISY CARRIER & FADING + 1.2 DB SUBCARRIER & DOPPLER.
 4. K = 32, RATE 1/2 CONVOLUTIONAL CODING. FRAME DELETION RATE 10^{-2} .

Table 7.6M-2. Telecommunications Design Control
Table, Atlas/Centaur Large Probe,
30-KM Altitude

NO.	PARAMETER	NOMINAL VALUE	ADVERSE TOLERANCE	NOTES
1	TOTAL TRANSMITTING POWER (DBM) 36 W	+ 45.6	0.4	VOLTAGE LEVEL
2	TRANSMITTING CIRCUIT LOSS (DB)	- 1.6	0.4	
3	TRANSMITTING ANTENNA GAIN (DB)	+ 3.5	2.3	$\theta = 50^\circ \pm 8^\circ$
4	COMMUNICATIONS RANGE LOSS (DB)	-255.9	0.0	
5	ATMOSPHERIC ABSORPTION & DEFOCUSING LOSSES (DB)	- 0.1	0.0	
6	POLARIZATION LOSS (DB)	- 0.2	0.0	
7	MULTIPATH & OTHER LOSSES (DB)	SEE NOTE 3	0.0	
8	RECEIVING ANTENNA GAIN (DB)	+ 61.7	0.4	JPL B10-5
9	RECEIVING CIRCUIT LOSS (DB)	0.0	0.0	JPL B10-5
10	NET LOSS (DB) (2+3+4+5+6+7+8+9)	-192.6	2.8	
11	TOTAL RECEIVED POWER (DBM) (1+10)	-147.0	3.2	
12	RECEIVER NOISE SPECTRAL DENSITY - (DBM/HZ)	-184.5	1.4	$25.5 \pm 9.5^\circ K$
13	TOTAL RECEIVED POWER/NO (DBM/HZ) (11-12)	+ 37.5	SUM 4.9	
CARRIER TRACKING				
14	CARRIER POWER/TOTAL (DB)	- 5.4	0.4	
15	ADDITIONAL CARRIER LOSSES (DB)	- 1.3	0.1	NOTE 1
16	THRESHOLD TRACKING BANDWIDTH - $2B_{LO}$ (DB)	+ 10.0	0.8	
17	REQUIRED SNR (DB)	+ 13.0	0.0	
18	PERFORMANCE MARGIN (DB) (13+14+15-16-17)	+ 7.8	SUM 6.2	
DATA CHANNEL				
19	DATA POWER/TOTAL (DB)	- 1.5	0.2	
20	ADDITIONAL DATA CHANNEL LOSSES (DB)	- 5.0	0.5	NOTE 2
21	DATA BIT RATE - BPS	+ 21.1	0.0	128 BPS
22	THRESHOLD ENERGY PER DATA BIT - E_b/N_0 (DB)	+ 2.3	0.0	NOTE 4
23	PERFORMANCE MARGIN (DB) (13+19+20-21-22)	+ 7.6	SUM 5.6	

NOTES: 1. 1.0 DB PREDICTION RECORDING LOSS + 0.3 DB DOWNLINK SUPPRESSION & DOPPLER EFFECTS INCLUDED IN ITEM 15.

2. 1.0 DB PREDICTION RECORDING LOSS + 2.8 DB NOISY CARRIER & REFERENCE + 1.2 DB SUBCARRIER & DOPPLER.

3. MULTIPATH LOSSES INCLUDED IN ITEMS 15 AND 20.

4. K = 32, RATE 1/2 CONVOLUTIONAL CODING. FRAME DELETION RATE 10^{-2} .

Table 7.6M-3. Telecommunications Design Control Table, Atlas/Centaur Large Probe, 70-KM Altitude

NO.	PARAMETER	NOMINAL VALUE	ADVERSE TOLERANCE	NOTES
1	TOTAL TRANSMITTING POWER (DBM) 36W	+ 45.6	0.4	VOLTAGE LEVEL
2	TRANSMITTING CIRCUIT LOSS (DB)	- 2.0	0.4	NOTE 3
3	TRANSMITTING ANTENNA GAIN (DB)	+ 3.5	3.0	$\theta = 50^\circ \pm 15^\circ$
4	COMMUNICATIONS RANGE LOSS (DB)	-255.9	0.0	0.43 AU
5	ATMOSPHERIC ABSORPTION & DEFOCUSING LOSSES (DB)	- 0.1	0.0	
6	POLARIZATION LOSS (DB)	- 0.2	0.0	
7	MULTIPATH & OTHER LOSSES (DB)	SEE NOTE 4	0.0	
8	RECEIVING ANTENNA GAIN (DB)	+ 61.7	0.4	JPL 810-5
9	RECEIVING CIRCUIT LOSS (DB)	0.0	0.0	JPL 810-5
10	NET LOSS (DB) (2+3+4+5+6+7+8+9)	-193.0	3.8	
11	TOTAL RECEIVED POWER (DBM) (1+10)	-147.4	4.2	
12	RECEIVER NOISE SPECTRAL DENSITY - (DBM/HZ)	-184.5	1.4	$25.5^\circ \pm 9.5^\circ K$
13	TOTAL RECEIVED POWER/NO (DBM/HZ) (11-12)	+ 37.1	SUM 5.6	
CARRIER TRACKING				
14	CARRIER POWER/TOTAL (DB)	- 5.4	0.4	NOTE 1
15	ADDITIONAL CARRIER LOSSES (DB)	- 1.3	0.1	
16	THRESHOLD TRACKING BANDWIDTH - $2b_{Lo}$ (DB)	+ 10.0	0.8	
17	REQUIRED SNR (DB)	+ 13.0	0.0	
18	PERFORMANCE MARGIN (DB) (13+14+15-16-17)	+ 7.4	SUM 6.9	
DATA CHANNEL				
19	DATA POWER/TOTAL (DB)	- 1.5	0.2	
20	ADDITIONAL DATA CHANNEL LOSSES (DB)	- 4.4	0.5	NOTE 2
21	DATA BIT RATE - BPS (DB)	+ 21.1	0.0	128 BPS
22	THRESHOLD ENERGY PER DATA BIT - E_b/N_o (DB)	+ 2.3	0.0	NOTE 5
23	PERFORMANCE MARGIN (DB) (13+19+20-21-22)	+ 7.8	SUM 6.3	

NOTES: 1. 1.0 DB PREDETECTION RECORDING LOSS + 0.3 DB DOWNLINK SUPPRESSION & DOPPLER EFFECTS INCLUDED IN ITEM 15.
 2. 1.0 DB PREDETECTION RECORDING LOSS + 2.2 DB NOISY CARRIER & FADING + 1.2 DB SUBCARRIER & DOPPLER LOSSES.
 3. INCLUDES 0.4 DB LOSS FOR PARACHUTE CONTAINER.
 4. MULTIPATH LOSSES INCLUDED IN ITEMS 15 AND 20.
 5. K = 32, RATE 1/2 CONVOLUTIONAL CODING. FRAME DELETION RATE 10^{-2} .

Table 7.6M-4. Telecommunications Design Control Table, Atlas/Centaur Small Probe Near Venus Surface

NO.	PARAMETER	NOMINAL VALUE	ADVERSE TOLERANCE	NOTES
1	TOTAL TRANSMITTING POWER (DBM) 20W	+ 43.0	0.8	VOLTAGE & TEMP
2	TRANSMITTING CIRCUIT LOSS (DB)	- 1.0	0.2	NOTE 3
3	TRANSMITTING ANTENNA GAIN (DB) AT $\theta = 55^\circ$	+ 3.0	1.5	$\Delta\theta + 0$ DEG
4	COMMUNICATIONS RANGE LOSS (DB)	-255.9	0.0	0.43 AU
5	ATMOSPHERIC ABSORPTION & DEFOCUSING LOSSES (DB)	- 0.9	0.1	
6	POLARIZATION LOSS (DB)	- 0.2	0.1	
7	MULTIPATH & OTHER LOSSES (DB)	- SEE NOTE 4 -		
8	RECEIVING ANTENNA GAIN (DB)	+ 61.7	0.4	JPL 810.5
9	RECEIVING CIRCUIT LOSS (DB)	0.0	0.0	JPL 810.5
10	NET LOSS (DB) (2+3+4+5+6+7+8+9)	-193.3	2.3	
11	TOTAL RECEIVED POWER (DBM) (1+10)	+150.3	3.1	
12	RECEIVER NOISE SPECTRAL DENSITY - (DBM/HZ)	-184.0	0.9	$28.5 \pm 6.5^\circ K$
13	TOTAL RECEIVED POWER/NO (DBM/HZ) (11-12)	+ 33.7	SUM 4.0	
	CARRIER TRACKING			
14	CARRIER POWER/TOTAL (DB)	- 5.2	0.5	
15	ADDITIONAL CARRIER LOSSES (DB)	- 1.5	0.2	NOTE 1
16	THRESHOLD TRACKING BANDWIDTH $-2B_{LO}$ (DB)	+ 10.0	0.8	
17	REQUIRED SNR (DB)	+ 11.0	0.0	
18	PERFORMANCE MARGIN (DB) (13+14+15-16-17)	+ 6.0	SUM 5.5	
	DATA CHANNEL			
19	DATA POWER/TOTAL (DB)	- 1.6	0.2	
20	ADDITIONAL DATA CHANNEL LOSSES (DB)	- 6.6	0.5	NOTE 2
21	DATA BIT RATE - BPS (DB)	+ 18.1	0.0	64 BPS
22	THRESHOLD ENERGY PER DATA BIT - E_b/N_0 (DB)	+ 2.2	0.0	NOTE 5
23	PERFORMANCE MARGIN (DB) (13+19+20-21-22)	+ 5.2	SUM 4.7	

NOTES: 1. 1.0 DB PREDETECTION RECORDING LOSS + 0.5 DB OSCILLATOR & DOPPLER EFFECTS INCLUDED IN ITEM 15.
 2. 1.0 DB PREDETECTION RECORDING LOSS + 4.4 DB NOISY CARRIER & FADING + 1.2 DB SUBCARRIER & DOPPLER.
 3. INCLUDES 0.4 DB RADOME LOSS.
 4. MULTIPATH LOSSES INCLUDED IN ITEMS 15 AND 20.
 5. K = 32, RATE 1/2 CONVOLUTIONAL CODING, FRAME DELETION RATE 10^{-2} .

Table 7.6M-5. Telecommunications Design Control
Table, Atlas/Centaur Small Probe,
30-KM Altitude

NO.	PARAMETER	NOMINAL VALUE	ADVERSE TOLERANCE	NOTES
1	TOTAL TRANSMITTING POWER (DBM) 20W	+ 43.0	0.4	VOLTAGE VARIATIONS
2	TRANSMITTING CIRCUIT LOSS (DB)	- 1.0	0.2	NOTE 3
3	TRANSMITTING ANTENNA GAIN (DB)	+ 3.0	2.3	$\theta = 55^\circ \pm 8^\circ$
4	COMMUNICATIONS RANGE LOSS (DB)	-255.9	0.0	0.43 AU
5	ATMOSPHERIC ABSORPTION & DEFOCUSING LOSSES (DB)	- 0.1	0.0	
6	POLARIZATION LOSS (DB)	- 0.2	0.0	
7	MULTIPATH & OTHER LOSSES (DB)	- SEE NOTE 4 -		
8	RECEIVING ANTENNA GAIN (DB)	+ 61.7	0.4	JPL 810-5
9	RECEIVING CIRCUIT LOSS (DB)	0.0	0.0	JPL 810-5
10	NET LOSS (DB) (2+3+4+5+6+7+8+9)	-192.5	2.9	
11	TOTAL RECEIVED POWER (DBM) (1+10)	-149.5	3.3	
12	RECEIVER NOISE SPECTRAL DENSITY - (DBM/HZ)	-184.0	0.9	$28.5 \pm 6.5^{\circ}K$
13	TOTAL RECEIVED POWER/NO (DBM/HZ) (11-12)	+ 34.5	SUM 4.2	
CARRIER TRACKING				
14	CARRIER POWER/TOTAL (DB)	- 5.2	0.5	
15	ADDITIONAL CARRIER LOSSES (DB)	- 1.3	0.2	NOTE 1
16	THRESHOLD TRACKING BANDWIDTH - $2\Delta_{LO}$ (DB)	+ 10.0	0.8	
17	REQUIRED SNR (DB)	+ 11.0	0.0	
18	PERFORMANCE MARGIN (DB) (13+14+15-16-17)	+ 7.0	SUM 5.7	
DATA CHANNEL				
19	DATA POWER/TOTAL (DB)	- 1.6	0.2	
20	ADDITIONAL DATA CHANNEL LOSSES (DB)	- 5.4	0.5	NOTE 2
21	DATA BIT RATE - BPS (DB)	+ 18.1	0.0	64 BPS
22	THRESHOLD ENERGY PER DATA BIT - E_b/N_o (DB)	+ 2.2	0.0	NOTE 5
23	PERFORMANCE MARGIN (DB) (13+19+20-21-22)	+ 7.2	SUM 4.9	

NOTES: 1. 1.0 dB PREDETECTION RECORDING LOSS + 0.3 dB OSCILLATOR & DOPPLER EFFECTS.
 2. 1.0 dB PREDETECTION RECORDING LOSS + 3.15 dB NOISY CARRIER & FADING + 1.2 dB SUBCARRIER & DOPPLER.
 3. INCLUDES 0.4 dB RADOME LOSS.
 4. MULTIPATH LOSSES INCLUDED IN ITEMS 15 AND 20.
 5. K = 32, RATE 1/2 CONVOLUTIONAL CODING. FRAME DELETION RATE 10^{-2} .

Table 7.6M-6. Telecommunications Design Control Table, Atlas/Centaur Small Probe, 70-KM Altitude

NO.	PARAMETER	NOMINAL VALUE	ADVERSE TOLERANCE	NOTES
1	TOTAL TRANSMITTING POWER (DBM) 20W	+ 43.0	0.4	VOLTAGE VARIATIONS
2	TRANSMITTING CIRCUIT LOSS (DB)	- 1.0	0.2	NOTE 3
3	TRANSMITTING ANTENNA GAIN (DB)	+ 3.0	3.1	Θ 55° + 15°
4	COMMUNICATIONS RANGE LOSS (DB)	-255.9	0.0	0.43 AU
5	ATMOSPHERIC ABSORPTION & DEFOCUSING LOSSES (DB)	- 0.1	0.0	
6	POLARIZATION LOSS (DB)	- 0.2	0.0	
7	MULTIPATH & OTHER LOSSES (DB)	- SEE NOTE 4 -		
8	RECEIVING ANTENNA GAIN (DB)	+ 61.7	0.4	JPL 810-5
9	RECEIVING CIRCUIT LOSS (DB)	0.0	0.0	JPL 810-5
10	NET LOSS (DB) (2+3+4+5+6+7+8+9)	-192.5	3.7	
11	TOTAL RECEIVED POWER (DBM) (1+10)	-149.5	4.1	
12	RECEIVER NOISE SPECTRAL DENSITY - (DBW/HZ)	-184.0	0.9	
13	TOTAL RECEIVED POWER/NO (DBM/HZ) (11-12)	+ 34.5	SUM 5.0	
CARRIER TRACKING				
14	CARRIER POWER/TOTAL (DB)	- 5.2	0.5	
15	ADDITIONAL CARRIER LOSSES (DB)	- 1.3	0.2	NOTE 1
16	THRESHOLD TRACKING BANDWIDTH - $2\Delta_{LO}$ (DB)	+ 10.0	0.8	
17	REQUIRED SNR (DB)	+ 11.0	0.0	
18	PERFORMANCE MARGIN (DB) (13+14+15+16-17)	+ 7.0	SUM 6.5	
DATA CHANNEL				
19	DATA POWER/TOTAL (DB)	- 1.6	0.2	
20	ADDITIONAL DATA CHANNEL LOSSES (DB)	- 5.0	0.5	NOTE 2
21	DATA BIT RATE - BPS (DB)	+ 18.1	0.0	64 BPS
22	THRESHOLD ENERGY PER DATA BIT - E_b/N_o (DB)	+ 2.2	0.0	NOTE 5
23	PERFORMANCE MARGIN (DB) (13+19+20-21-22)	+ 7.2	SUM 5.7	

NOTES: 1. 1.0 DB PREDETECTION RECORDING LOSS + 0.3 DB OSCILLATOR & DOPPLER EFFECTS INCLUDED IN ITEM 15.

2. 1.0 DB PREDETECTION RECORDING LOSS + 2.8 DB NOISY CARRIER & FADING + 1.2 DB SUBCARRIER & DOPPLER.

3. INCLUDES 0.4 DB RADOME LOSS.

4. MULTIPATH LOSSES INCLUDED IN ITEMS 15 AND 20.

5. K = 32, RATE 1/2 CONVOLUTIONAL CODING. FRAME DELTION RATE 10^{-2} .

Table 7.6M-7. Atlas/Centaur Link Analysis, Large Probe Uplink, 70 KM Altitude

NO.	PARAMETER	NOMINAL VALUE	ADVERSE TOLERANCE	NOTES
1	TOTAL TRANSMITTING POWER (DBM)	+ 86.0	0	400 KW
2	TRANSMITTING CIRCUIT LOSS (DB)	- 0.3	-0.1	JPL-810-5
3	TRANSMITTING ANTENNA GAIN (DB)	+ 60.9	-0.6	JPL-810-5
4	COMMUNICATIONS RANGE LOSS (DB)	-255.3	0	0.43 AU
5	ATMOSPHERIC ABSORPTION & DEFOCUSING LOSSES (DB)	- 0.1	0	70 KM ALTITUDE
6	POLARIZATION LOSS (DB)	- 0.3	-0.1	
7	MULITPATH & OTHER LOSSES (DB)	INCLUDED IN ITEM 15		0.3 DB MULTIPATH
8	RECEIVING ANTENNA GAIN (DB)	+ 3.5	-3.0	
9	RECEIVING CIRCUIT LOSS (DB)	- 2.7	-0.4	
10	NET LOSS (DB) (2+3+4+5+6+7+8+9)	-194.3	-4.2	
11	TOTAL RECEIVED POWER (DBM) (1+10)	-108.3	-4.2	
12	RECEIVER NOISE SPECTRAL DENSITY - (DBM/HZ)	-166.8	+0.2	250° ANT, 1340 REC
13	TOTAL RECEIVED POWER/NO (DBM/HZ) (11-12)	+ 58.5	-4.4	
CARRIER TRACKING				
14	CARRIER POWER/TOTAL (DB)	0	0	
15	ADDITIONAL CARRIER LOSSES (DB)	- 0.4	-0.2	
16	THRESHOLD TRACKING BANDWIDTH - $2B_{LO}$ (DB)	+ 24.0	+0.7	250 HZ $2B_{LO}$
17	REQUIRED SNR (DB)	+ 20.0	0	
18	PERFORMANCE MARGIN (DB) (13+14+15-16-17)	+ 14.1	-5.3	
DATA CHANNEL				
19	DATA POWER/TOTAL (DB)			
20	ADDITIONAL DATA CHANNEL LOSSES (DB)			
21	DATA BIT RATE - BPS (DB)			
22	THRESHOLD ENERGY PER DATA BIT - E_b/N_o (DB)			
23	PERFORMANCE MARGIN (DB) (13+19+20-21-22)			NO MODULATION ON CARRIER

NOTE: UPLINK IS USED SOLELY FOR PURPOSE OF PROVIDING A 2-WAY TURN AROUND DOPPLER SIGNAL.

Table 7.6M-8. Communications Link Margin Study

1. PROBE	LARGE PROBE						SMALL PROBE					
	0		30		70		0		30		70	
2. ALTITUDE (KM)	CXR	DATA	CXR	DATA	CXR	DATA	CXR	DATA	CXR	DATA	CXR	DATA
3. CARRIER OR DATA CHANNEL	6.8	5.8	7.8	7.6	7.4	7.8	6.0	5.2	7.0	7.2	7.0	7.2
4. MARGIN OVER NOMINAL	6.1	5.4	6.2	5.6	6.9	6.3	5.5	4.7	5.7	4.9	6.5	5.7
5. SUM OF ADVERSE TOLERANCES												
6. RSS TOLERANCES												
7. 1) ALL RSS	2.5	2.3	2.9	2.9	3.5	3.4	2.2	2.1	2.8	2.6	3.4	3.3
8. 2) ALL EXCEPT ANTENNA GAIN (ADD ANTENNA GAIN TO RSS OF ALL OTHERS)	3.5	3.3	4.1	4.0	4.8	4.7	3.1	2.9	3.8	3.5	4.6	4.3
9. MARGIN OVER SUM OF TOTAL	0.7	0.4	1.6	2.0	0.5	1.5	0.5	0.5	1.3	2.3	0.5	1.5
10. MARGIN OVER RSS												
11. 1) RSS ALL	4.3	3.5	4.9	4.7	3.9	4.4	3.8	3.1	4.2	4.6	3.6	3.9
12. 2) RSS ALL BUT ANTENNA GAIN	3.3	2.5	3.7	3.6	2.6	3.1	2.9	2.3	3.2	3.7	2.4	2.9

The following enumeration explains the items listed on Tables 7.6M-1 through 7.6M-6:

- 1) Transmitter power tolerances are shown as either 0.4 or 0.8 dB. The 0.4 dB entries are for voltage variations of 10 percent. The 0.8 dB entry used for probes near the surface includes output dropoff due to increased power amplifier temperatures.
- 2) Transmitting circuit loss for the large probe is shown as -1.6 or 2.0 dB depending upon whether the parachute container is in place or jettisoned. The losses are as follows:

Cable Assembly	0.95
Feedthrough	0.15
Parachute Container	0.4
Diplexer	<u>0.5</u>
	2.0 dB

For the small probe the transmitting circuit loss is as follows:

Cable Assembly	0.45
Feedthrough	0.15
Radome	<u>0.4</u>
	1.0 dB

- 3) Adverse tolerance on antenna gain consists of initial gain variation from nominal design at the target aspect angle, including gain variation "ripple" as a function of rotation of the probe including misalignment of the antenna, about the probe spin axis, plus a reduction in gain as the vehicle is tipped away from the earth receiver. These values are best engineering estimates based on measured patterns. The value of the probe tip-up angle is assumed to vary with altitude on the following basis: +15 degrees at 70 km, +8 degrees at 30 km, and zero degrees near the surface.
- 4) No comment needed.
- 5) These values are taken from the data in Appendix 7.6G.
- 6) Polarization loss is based on an assumed probe antenna axial ratio of 2.5 dB and a DSN antenna ratio of 0.6 dB.
- 7) These losses are included in Items 15 & 20.
- 8) No comment needed.
- 9) No comment needed.
- 10) No comment needed.

- 11) No comment needed.
- 12) The receiver noise spectral density is based on worst station elevation angle during the mission and data in JPL handbook 810-5.

Nominal zenith system noise temperature for the 64-meter station at S-band is $22.0 \pm 3^{\circ}\text{K}$. As the antenna is lowered from zenith, the system temperature increases. The increase in system noise temperature is as follows for the worst station elevation angles during the mission.

Large Probe

Canberra, 16.5 degree elevation angle -- add 10°K to zenith system temperature.

Goldstone, 34.0 degree elevation angle -- add 3.5°K to zenith noise temperature.

Small Probe

Canberra, 16.5 degree elevation angle -- add 10°K to zenith temperature.

Goldstone, 23.0 degree elevation angle -- add 6.5°K to zenith temperature.

In the design control tables the nominal value used is the nominal zenith temperature plus the increase in noise temperature for the best station. The tolerance is equal to the tolerance on zenith plus the difference between the increased temperature for the two stations as follows:

Large Probe

Nominal station noise temperature = $22.0 + 3.5 = 25.5^{\circ}\text{K}$

Adverse tolerance = $3.0 + 6.5 = +9.5^{\circ}\text{K}$

Small Probe

Nominal station noise temperature = $22.0 + 6.5 = 28.5^{\circ}\text{K}$

Adverse tolerance = $3.0 + 3.5 = 6.5^{\circ}\text{K}$

- 13) No comment needed.
- 14) Modulation index of 1 radian for large probe, 0.98 radian for small probe.
- 15) Additional carrier losses include 1.0 dB predetection recording loss and either 0.5 or 0.3 dB suppression plus Doppler effect losses which are estimated, or in the case of the small probe the 0.5 or 0.3 dB is estimated to cover Doppler effect and oscillator noise losses.

16) See Item 16 explanation in Appendix 7.6H.

17, 20, & 22) These are explained in Appendix 7.6D and in Section 7.6.3 of the technical volume. A breakdown of values is also shown in a note on each table.

The entries on Table 7.6M-8 are explained in the following enumeration:

1 through 4) No comment needed.

5) See Appendix 7.6F.

6) Estimated to be 0.1 dB worse than at the transmit frequency. See Tables 7.6M-1 through 7.6M-6.

7) See Appendix 7.6A - This is an estimated value.

8) Same comments as for Item 3 of Tables 7.6M-1 through 7.6M-6.

9) Circuit loss is estimated as follows:

Cable Assembly	0.95
Feedthrough	0.15
Parachute Containers	0.4
Parachute & Radome	0.4
Diplexer	<u>0.8</u>
	2.7 dB

10 & 11) No comment needed.

12) Receiver noise figure 7.5 dB, antenna contribution 250°K.

13 & 14) No command needed.

15) Losses are an estimate of combined fading and Doppler effects on tracking loop.

16) No comment needed.

17) This is the minimum desired signal level above the $2B_{LO}$ tracking loop bandwidth to minimize downlink effects. Margin using the 400 kW transmitter brings this level to about 29 dB. If forced to use the 100 kW transmitter, this would drop to about 23 dB which would still be allowable.

18) Margin equals or exceeds "Sum of Adverse Tolerance," see Item 17 above.

APPENDIX 7.8A
PROBE BATTERY ANALYSIS AND SELECTION

I.	Introduction/Summary	1
II.	Battery Selection and Sizing	2
III.	Battery Life Characteristics	6

APPENDIX 7.8A

TECHNICAL NOTE P73-203434-070

PROBE BATTERY ANALYSIS AND SELECTION

28 February 1973

by

**BURTON M. OTZINGER
PIONEER VENUS PROJECT**

**MARTIN MARIETTA AEROSPACE
DENVER DIVISION
DENVER, COLORADO**

TABLE OF CONTENTS

<u>Title</u>	<u>Page</u>
Contents	ii
List of Illustrations	iii
I. Introduction/Summary	1
II. Battery Selection and Sizing	2
A. Battery IRAD Program	2
B. Cell Design Selection	3
C. Cell Design Characteristics	3
D. Thermal Considerations	4
E. Selected Battery Sizes	4
III. Battery Life Characteristics	6
A. Storage Life	6
B. Cycle Life	6
References	7
Figure 1	8
Figure 2	9
Figure 3	10
Figure 4	11
Table I	12
Appendix A	13-15
Appendix B	16-24
Appendix C	25-30

List of Illustrations

<u>Figure</u>	<u>Title</u>	<u>Page</u>
1.	Final Conditioning Capacity	8
2.	Discharge Characteristics for Fully Charged Type 1, Cell Tempera- ture A Parameter	9
3.	Size and Weight vs. Capacity for IRAD Developed Silver-Zinc Cell	10
4.	Charged Stand Loss Characteristic for IRAD Type 1 Cell, Temperature A Parameter	11

Table

I	Design Data Sheet for Type 1, 10 A-H, IRAD Cell	12
---	--	----

I. Introduction/Summary

The study effort presented in this technical note was conducted to fulfill Task Description 6313-02 as described in MCR-72-249, Rev. I, Pioneer Venus Mission Analysis and Probe Design Study Plan, dated October 1972.

Data collected from IRAD Task 48705 was evaluated and probe battery design for Thor Delta and Atlas Centaur boost vehicle application were developed. A table showing the weight and volume of battery designs selected are given in Section II.E. Battery capacities are shown in the detailed calculations, Appendix C.

The use of standard aerospace battery cells were considered for use on the Atlas Centaur applications. It was determined that the increased weight and volume required did not justify the small parts cost saving.

A total activated life of 16 months is needed to satisfy the Pioneer Venus Probe applications without requiring battery replacement prior to launch. Nine months of activated life at 80°F including 6 months open circuit charged stand (cruise) have been demonstrated to date. This testing will continue until cell wearout occurs.

II. Battery Selection and Sizing

A. Battery IRAD Program

An Independent Research and Development Program (IRAD) for "Advanced Battery Development for Space Systems" was established at the Denver Division of Martin Marietta Aerospace, in late 1971, with an on-going program conducted by personnel of the Design and Electronics Engineering Department.

The primary objective of the program is to design a representative cell and battery for a probe application that will overcome major problems identified and provide sufficient test data to prove design adequacy and prepare a design manual. Problems identified include long life with high energy density in the order of 40 watt-hour per pound, sterilizability, cruise temperatures ranging from -54°F to +125°F and sustained deceleration in excess of 500 "g".

An interim report has been prepared and provides the design considerations for cells and batteries for probes and low cycle life orbiters for planetary exploration [1]. A final report for the 1972 effort has been prepared and is in a final sign-off phase. Results of the interim report demonstrate that a probe battery with an end of life energy density of 42 Watt-Hours per pound is attainable for the Venus Probe Mission using the cells developed at minus three sigma of the production lot. None of the storage modes investigated offer distinct advantages although the open circuit charge condition has the greatest degradation rate. Trade-offs at the subsystem level, e.g. elimination of a charger, may make open circuit charge storage mode more attractive. Two 13 cell probe batteries successfully survived acceleration levels of up to 750 "g".

As a result of the probe cell tests, improvements have been considered and incorporated into a new procurement of 110 cells for the 1973 test program. The conditioning cycle test data on 45 of the new cells indicate an improved capacity from 9 A-H to 12 A-H over the 1972 cell procurement.

B. Cell Design Selection

The silver-zinc, type 1B cell, designed and tested as part of the 1972 Battery IRAD program, was selected as the basis for Venus Pioneer Probe battery designs. This cell type was selected since it meets the high energy density required and successfully met the sustained high "g" deceleration test in a 13 cell battery form. Since no significant difference in data trend was noted between types 1A and 1B, the data will be simply considered a single body of type 1 cell data. Although limited data indicate that the improved cell, procured for the 1973 IRAD program, provides 30% more capacity in the same size case, the improvement will not be reflected in the current design calculations.

The type 1 cell data was derated or compensated whenever necessary to provide estimated monovalent battery operating characteristics and sizing values [2].

Consideration was given to the use of less expensive standard aerospace cells, Eagle-Picher SZLR series, to meet the Atlas/Centaur requirement. It was determined that the increased weight and volume required did not justify the small parts cost saving.

C. Cell Design Characteristics

The design data sheet for the 10A-H, type 1, cell developed for the 1972 IRAD program is shown in Table I. The manufacturing criteria for these cells established by the Martin Marietta work statement and Eagle-Picher process control provides cells which may be matched exceptionally well. The plot of new cell capacity for a lot of 45 cells on probability paper is shown in Figure 1. It should be noted that, the distribution conforms to a straight line indicating a normal distribution of cell capacity in a production lot and the 10A-H cell is in reality a 8.75 A-H cell taken at the distribution mean or 50% ordinate [3]. A plot of the discharge voltage vs. time characteristic with temperature a variable for the 10A-H cell is shown in Figure 2.

A set of cell height and weight vs. capacity curves shown in Figure 3 was generated to facilitate the rapid calculation of battery size and weight. The

10A-H IRAD cell was used as a generic type in the generation of the curves and the range in capacity shown indicates the capacity limits for a cell of 0.72 inches thick by 1.49 inches wide that Eagle-Picher would recommend for manufacture. Changes in cell capacity required, and the resultant volume, is therefore a function of only cell/plate height. Variations in the cell height/plate length within the range indicated have no cost or retest impact. A cell of less than 5A-H capacity would pose a serious design and retest problem. Capacities in excess of 18 A-H would require a different case and header size but would not cause serious design or retest problems.

D. Thermal Considerations

The probe battery temperatures will be maintained between 0°F and 70°F during the approximate 110 day cruise period from launch to separation. After separation, the small probe temperature decays during the 25-day pre-entry period to a temperature of $20^{\circ}\text{F} + 0^{\circ}\text{F}$ at entry. The IRAD Data indicates the following voltage temperature relationships under the anticipated battery load and operation:

<u>Temperature (°F)</u>	<u>Battery (Volts)</u>
80	28.6
55	26.6
30	23.6

It can be seen that operation below 55°F would not be within the required load voltage regulation of $28 \pm 10\%$. This condition was corrected by applying power to a heater integral to each small probe battery for a three hour period prior to first usage of the battery. The large probe battery temperature will be in excess of 55°F at the time of entry. The small probe battery heater calculations are shown in Appendix A.

E. Selected Battery Sizes

The Probe Power Profiles and Allocations for Thor Delta and Atlas Centaur, shown in Appendix B, were used to establish the battery energy and power

requirements needed to calculate battery capacity. The design data sheets furnished in Appendix C show the detailed calculations made to establish the selected battery design weights and volumes given in the following table:

	Thor Delta		Atlas Centaur	
	Weight (LB)	Volume (In ³)	Weight (LB)	Volume (In ³)
Large Probe	8.2	130	14.2	238
Small Probe	5	93	7.1	119

III. Battery Life Characteristics

A. Storage Life

The IRAD, Silver-Zinc, Cells were procured in a dry discharged state from the Eagle-Picher Co. Cells in the dry discharged state have a storage life well in excess of 3 years when stored under favorable temperature and humidity conditions.

Activated life (electrolyte added) test data, collected to date, indicate successful cell operation after 9 months at 80°F including 6 months open circuit charge stand (cruise). The charged stand loss characteristics for the type 1 cell is shown in Figure 4. Activated life testing will be continued until cell wear-out occurs. A total activated life of 16 months is needed to satisfy the Pioneer Venus probe storage and flight requirements.

The storage or conditioned temperature is a critical factor in extending the life of a silver-zinc battery/cell. The battery/cell should be maintained at 30°F or less whenever possible.

State-of-charge is also a factor in extended life and the battery/cells should be maintained in a partially discharged (monovalent) state whenever possible.

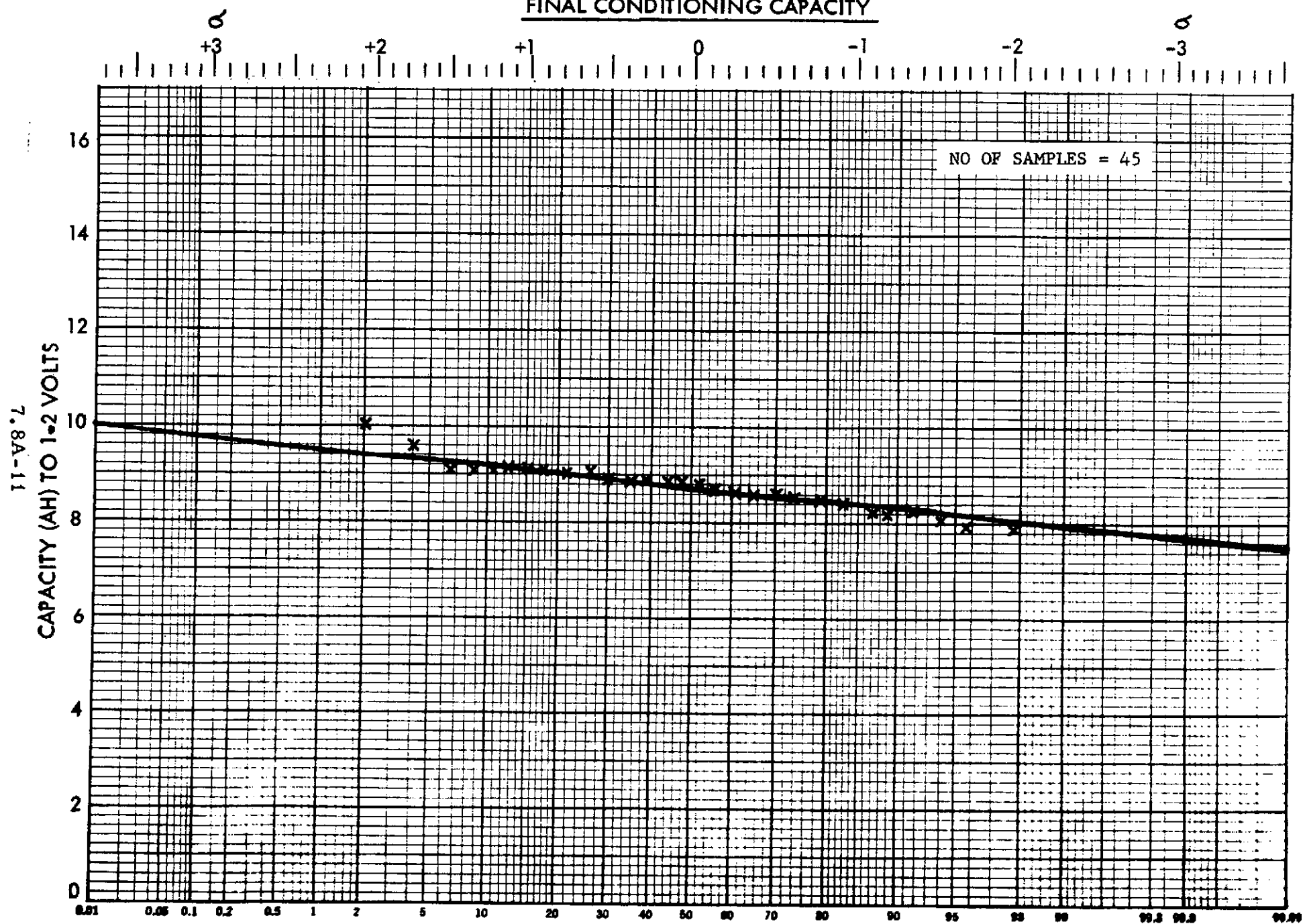
B. Cycle Life

Cycle life test data indicate a degradation of 50% in capacity after 32 cycles at 100% depth-of-discharge (1.2 volt cut-off) at 70°F. The probe mission does not require extensive cycling but it is important to note the substantial nature of the cell separation system, in that, no failures were recorded in 32 deep discharge cycles. This indicates that the cells will "die gracefully" and thereby preclude catastrophic cell shorting.

References

1. - - - Advanced Battery Development for Space System,
Interim Report for IRAD Task D48705, MMA Denver,
January 1973.
2. - - - Technical Note P73-203434-70
Regulated Vs. Unregulated Power Bus.
3. - - - Practical Engineering Uses of Probability Paper
by A. Boyajian, General Electric Review, Vol. 53,
Nos. 6 and 7, 1950.

FIGURE 1
FINAL CONDITIONING CAPACITY



DISCHARGE CHARACTERISTICS
FOR FULLY CHARGED, TYPE 1,
CELL AT 2 AMPERE RATE
WITH TEMPERATURE A PARAMETER

FIGURE 2

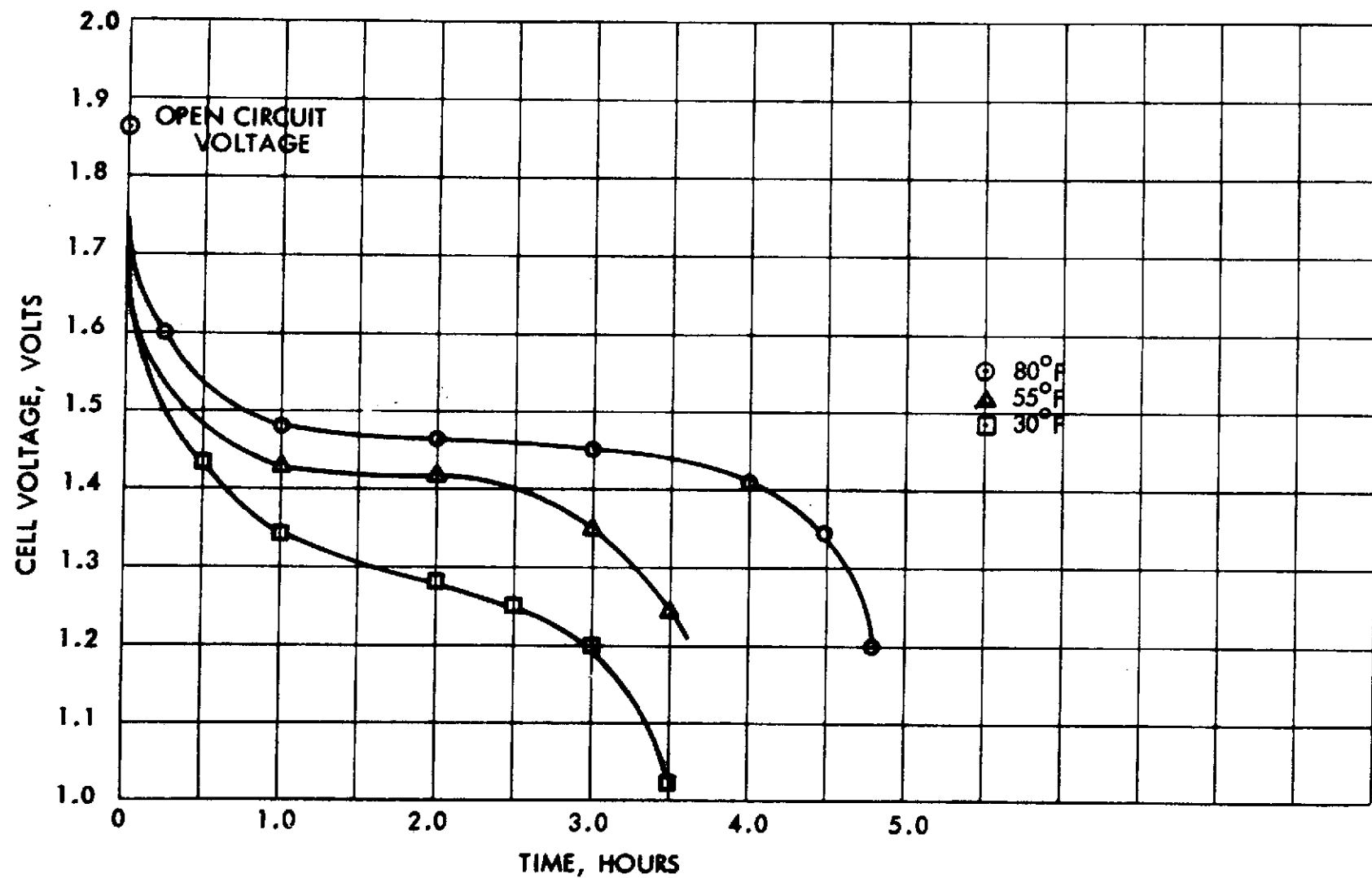
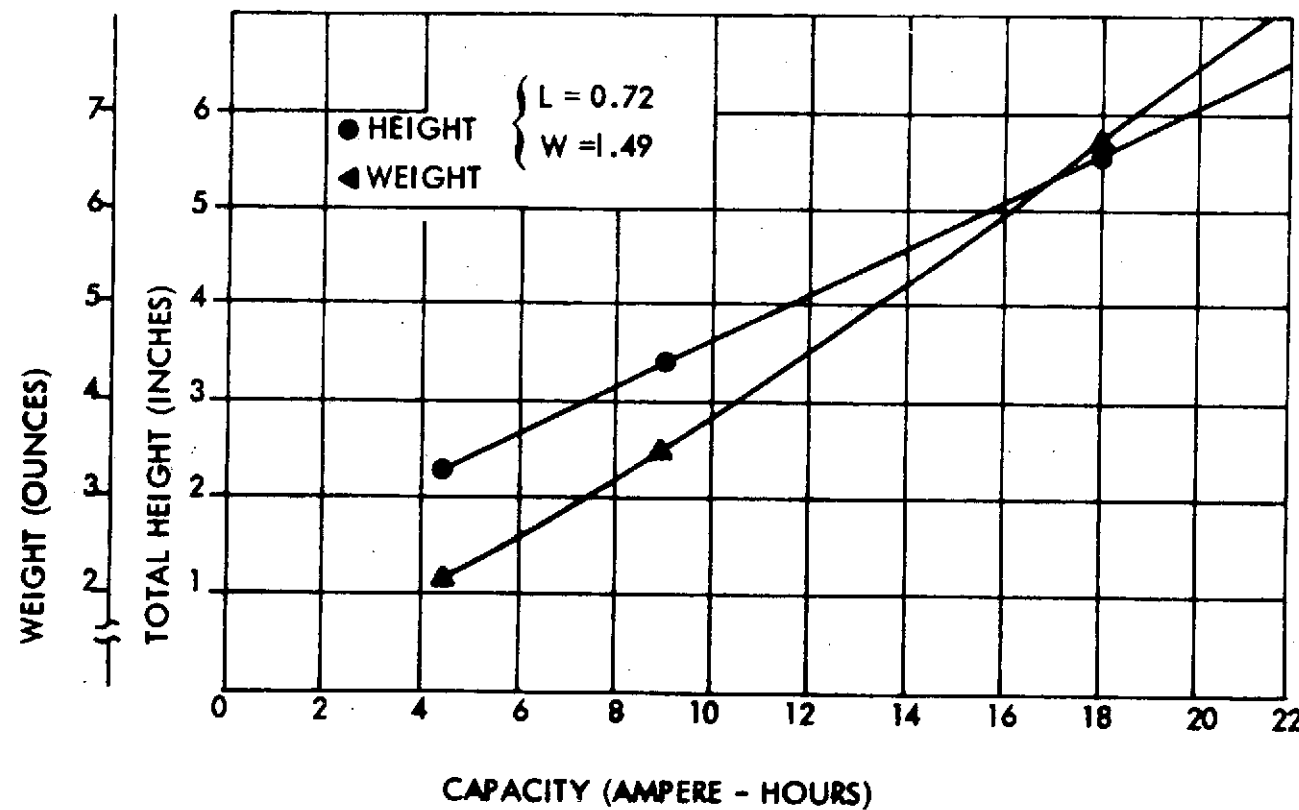


FIGURE 3

SIZE & WEIGHT VS. CAPACITY
IRAD 48705 DEVELOPED
SILVER-ZINC CELL TYPE



CHARGED STAND LOSS
CHARACTERISTIC FOR, IRAD
TYPE 1, CELL, TEMPERATURE
A PARAMETER

FIGURE 4

7.8A-14

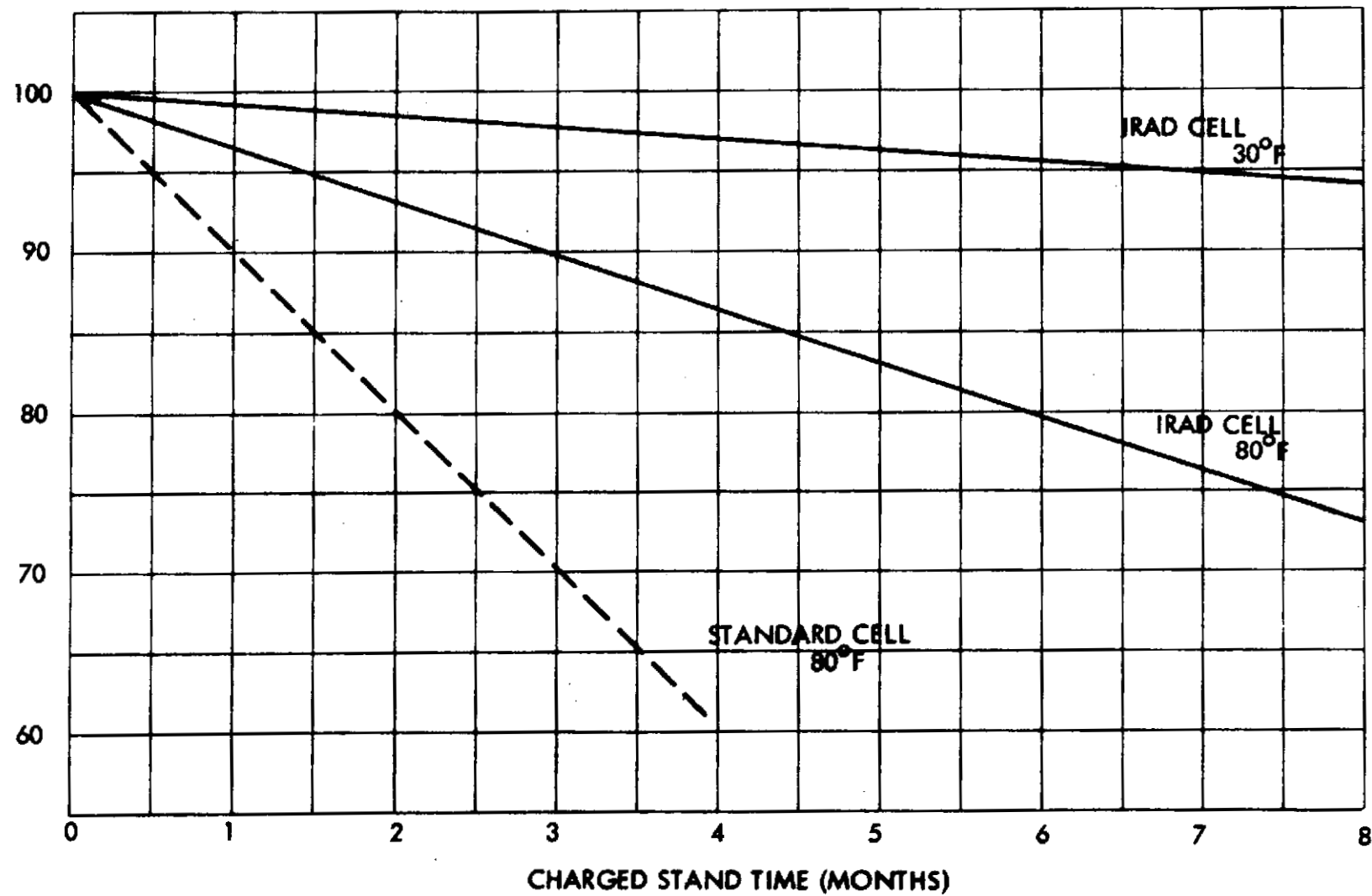


TABLE I
DESIGN DATA SHEET FOR TYPE 1 10A-H IRAD CELL

I. <u>Performance</u>	
Voltage (volts)	Open circuit 1.86 Nominal load 1.45
Capacity (Ampere-Hours)	To 1.0 volt 10 Cut-off
Discharge Rate (Amperes)	Nominal 2
Activated Stored Life (Years)	3
Charge/discharge Cycle Life (20% D.O.D.)	300
Relief value setting (PSIG)	15-25
II. <u>Operating Conditions</u>	
Temperature (operate)	55° F to 200° F
Temperature (non-operate)	-44° F to 80° F
Sustained Acceleration ("g")	750
Shock and Random Vibration	Meet Thor Delta requirements
III. <u>Configuration</u>	
Volume KOH (Cubic Centimeters)	17 $\pm \frac{1}{2}$
Number of Positive Plates	6
Number of Negative Plates	7
Positive Plate Area (Square inches)	2.57
Plate Constraint	Hysol bond at bottom corners.
Separator	1 layer Polypropylene Felt 4 layers Irradiated Poly- ethylene (Permion 307Mn)
Weight (lbs)	0.255
Outline Dimensions	3.4" H x 1.5" W x 0.72" D
Terminals	Screw down, low profile

APPENDIX A
BATTERY HEATER CALCULATIONS

APPENDIX A

BATTERY HEATER CALCULATIONS

Assume,

Battery Discharge

Start Temperature 20° + 0°F
- 15°F

Heater Operate Time 3 Hours

Temperature Rise 70°F

Heat Losses 10%

<u>Battery Composition</u>	<u>Mass</u>	<u>Cp</u>
KOH (H_2O solution)	0.212	1.0
Plastic	0.12	0.3
Silver	0.668	0.06

$$\bar{C}_p = 0.212 + 0.036 + 0.040 \\ = 0.288$$

then, $Q = M C_p \Delta T$
 $= 1 \times 0.288 \times 70 = 20.1 \text{ BTU}$
 $\dot{Q} = \frac{20.1}{3} = 6.72 \text{ BTU/Hr}$
 $\dot{Q} = 6.72 \times \frac{1 \text{ W}}{3.412 \text{ BTU/Hr}} = 1.96 \text{ Watts/Lb of Battery}$
 $Q = 1.96 + 10\% \text{ loss} = 2.16 \text{ Watts/Lb of Battery}$

APPENDIX A (Continued)

Thor Delta, Small Probe Heater Requirements --

Assume Battery Weight - 5 pounds

then,

$$\begin{aligned}\text{Heater Size (watts)} &= 2.16 \text{ Watts/Lb} \times 5 \text{ Lb} \\ &= 32.4 \text{ W-H}\end{aligned}$$

Atlas Centaur, Small Probe Heater Requirements --

Assume Battery Weight = 7.1 pounds

then,

$$\begin{aligned}\text{Heater Size (watts)} &= 2.16 \text{ Watts/Lb} \times 7.1 \text{ Lb} \\ &= 15.3 \text{ Watts}\end{aligned}$$

$$\begin{aligned}\text{Battery Energy Req. (W-H)} &= 15.3 \text{ Watts} \times 3 \text{ hours} \\ &= 46 \text{ Watt-Hours}\end{aligned}$$

APPENDIX B
PROBE POWER PROFILES AND ALLOCATIONS
FOR
THOR DELTA
AND
ATLAS CENTAUR

LARGE PROBE POWER PROFILE

THOR DELTA

Preseparation Checkout
62 W., 3 min. & 152 W., 3 min.

Shock Layer Radiometer Calib.
4.2 W., 10 sec.

T-P-Accel-Calib.
7.5 W., 6 min.

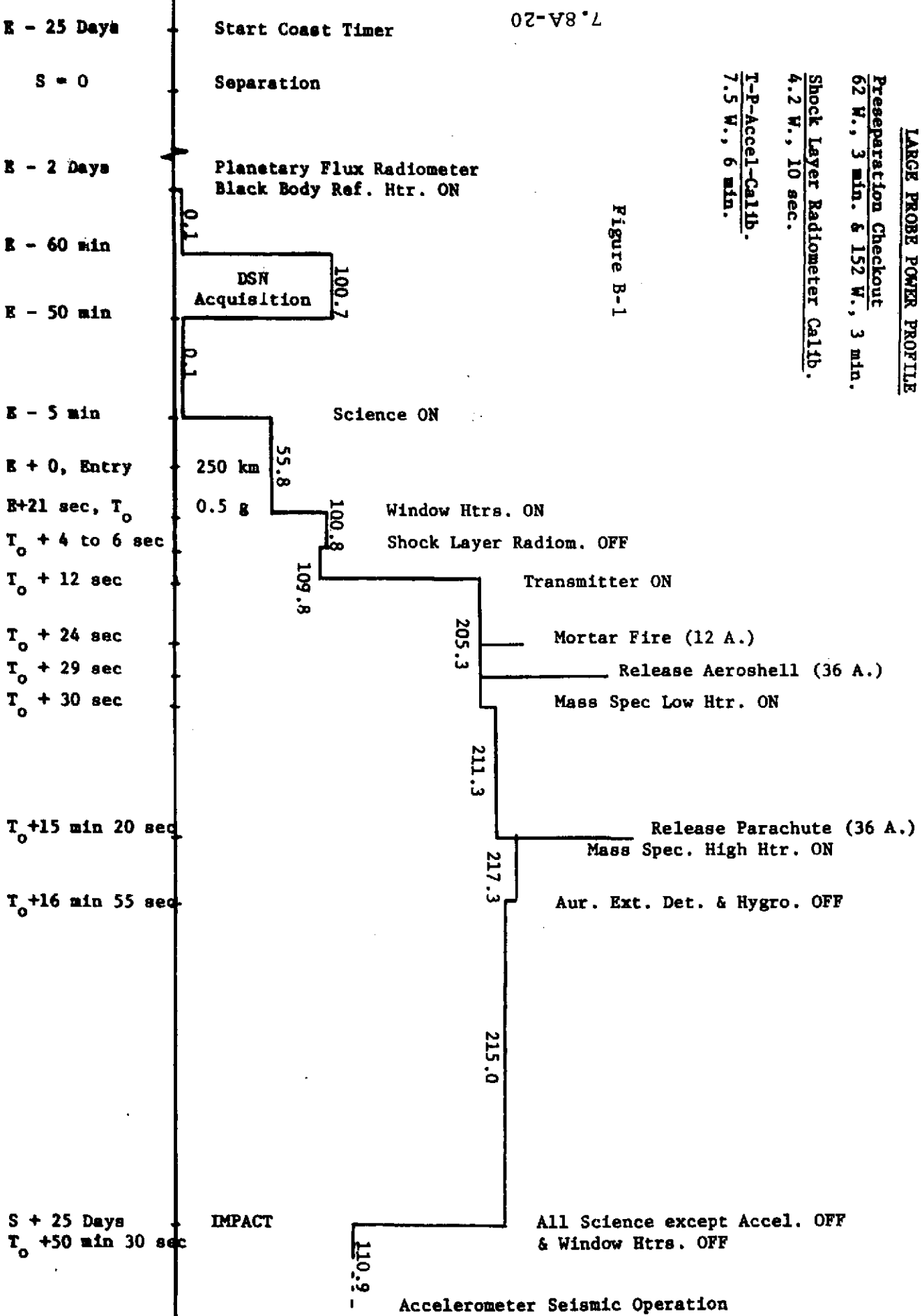


Figure B-1

TABLE B-1
THOR DELTA
LARGE PROBE POWER ALLOCATION

EQUIPMENT	AVERAGE POWER ALLOCATED (WATTS) (UNREGULATED)	REMARKS
Science:		
- Temperature Gauges	1.0	
- Pressure gauges	1.0	
- Accelerometers	2.3	
- Nephelometer	2.0	
- Neutral Mass Spectrometer	12/18/24	12 Watt continuous plus 6 Watt heater on parachute which increases to 12 Watts on release of the main parachute.
- Cloud Particle Size Analyzer	20.0	
- Solar Flux Radiometer	4.5	
- Planetary Flux Detector	4.5	
- Aureole/Extinction Detector	2.0	
- Shock Layer Radiometer	1.0	
- Hygrometer	0.3	
Engineering:		
-25 Day Timer	-	Self-contained battery
- Transmitter Driver	4.0	
- Power Amplifier	90.0	
- Receiver	1.5	
- Data Handling and Command	3.0	
- Power Control	0.2	
- Transducers	2.0	
- Window Heaters (4)	55	

THOR DELTA

SMALL PROBEPOWER PROFILE

Figure B-2

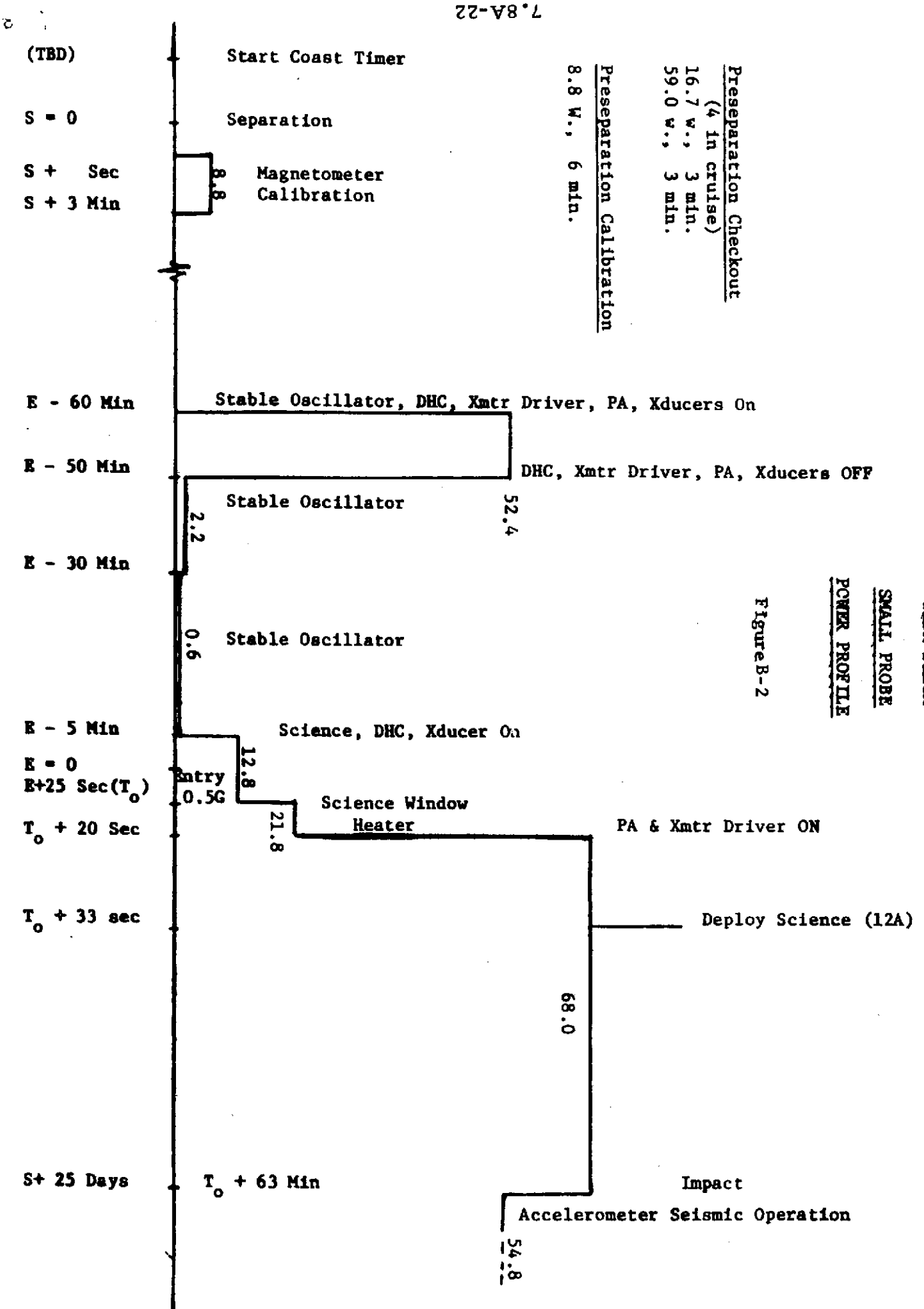


TABLE B-2
THOR DELTA
SMALL PROBE POWER ALLOCATION

EQUIPMENT	AVERAGE POWER ALLOCATED (WATTS) (UNREGULATED)	REMARKS
Science:		
- Temperature Gauges	0.5	
- Pressure Gauges	0.5	
- Accelerometer	1.0	
- Nephelometer	1.6	
- Magnetometer	1.6	
- Stable Oscillator	0.4	1 to 2 watt peak for 1/2 hour before entry during DLBI experiment. Integrated with transmitter electronics below.
Engineering:		
- 25 Day Timer	-	Self-contained Battery
- Transmitter Driver	3.9	
- Power Amplifier	42.3	
- Data Handling & Command	2.0	
- Power Control	0.2	
- Transducers	2.0	
- Window Heater	9.0	

LARGE PROBE POWER PROFILE

Preparation Checkout
62 w., 3 min & 232 w., 3 min

Shock Layer Radiometer Calib.
6.2 w., 10 sec.

T-P-Accel-Calib.
12.3 w., 6 min.

7.8A-24

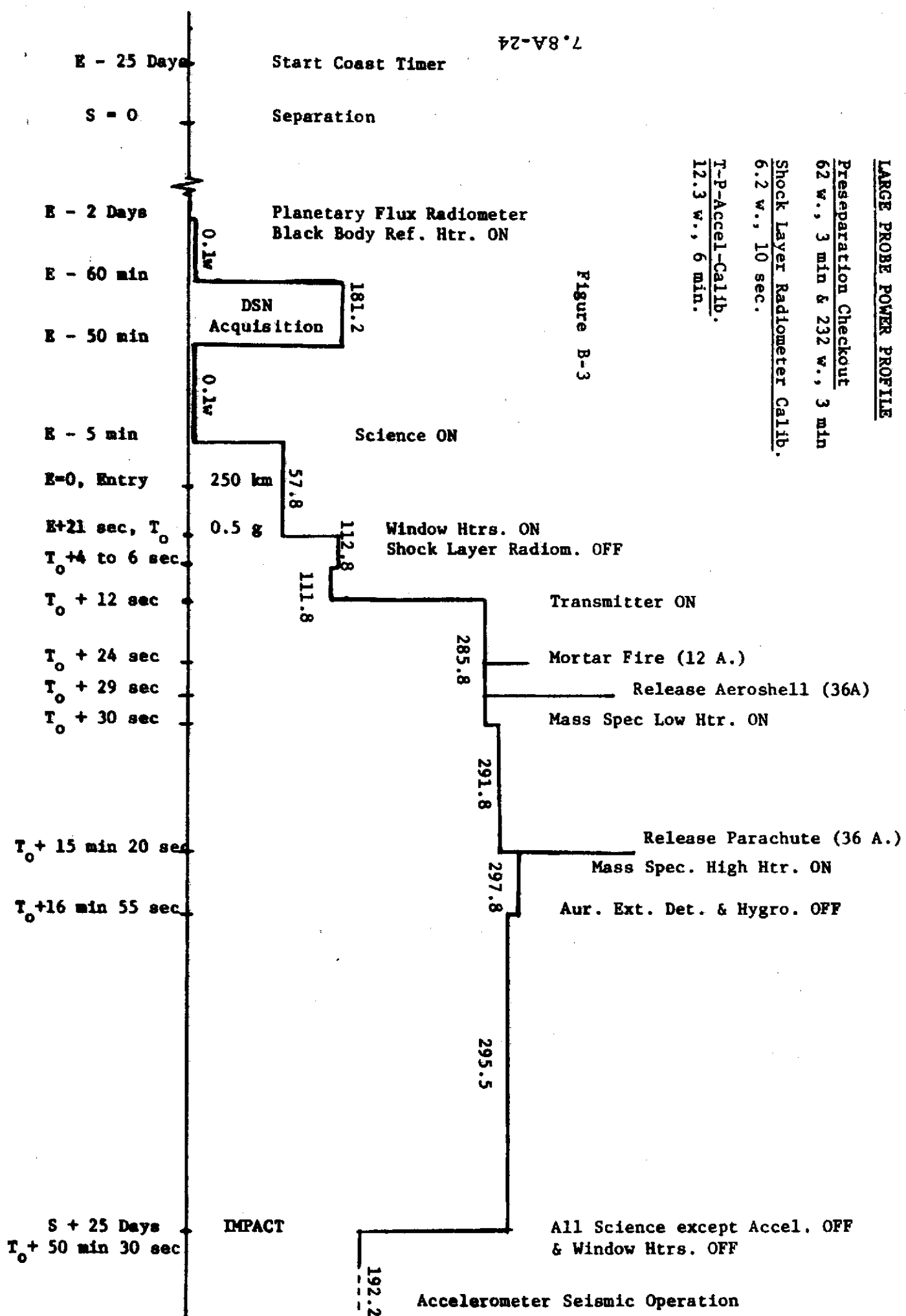


TABLE B-3
ATLAS CENTAUR
LARGE PROBE POWER ALLOCATION

EQUIPMENT	AVERAGE POWER ALLOCATED (WATTS) (UNREGULATED)	REMARKS
Science:		
- Temperature Gauges	1.0	
- Pressure Gauges	1.0	
- Accelerometers	2.3	Seismic operation if Probe survives impact.
- Nephelometer	2.0	12 w. continuous plus 6 w. heater on parachute which increases to 12 w. on release of the main parachute
- Neutral Mass Spectrometer	12.0/18.0/24.0	
- Cloud Particle Size Analyzer	20.0	
- Solar Flux Radiometer	4.5	
- Planetary Flux Detector	4.5	IR reference on 2 days before entry
- Aureole/Extinction Detector	2.0	Off at 30 km
- Shock Layer Radiometer	1.0	Off after blackout
- Hygrometer	0.3	Off at 30 km
 Engineering:		
- 25 Day Timer	-	Self-contained battery
- Transponder	4.0	
- Power Amplifier	170.0	Two Small Probe Power Amplifiers paralleled
- Data Handling & Command	5.0	
- Power Control	0.2	
- Transducers	2.0	
- Window Heaters (4)	55.0	

ATLAS CENTAUR

SMALL PROBE

POWER PROFILE

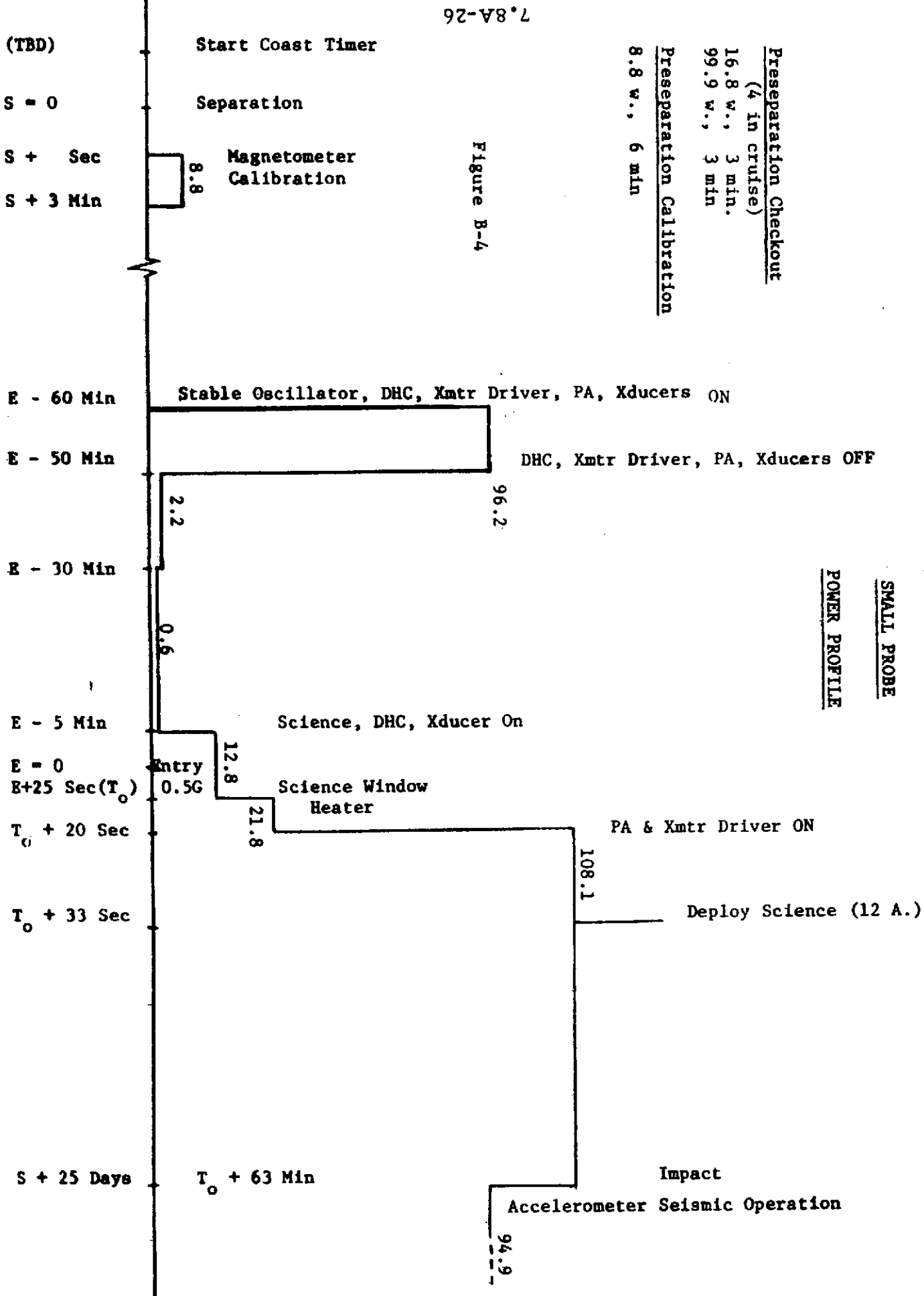


TABLE B-4
ATLAS CENTAUR
SMALL PROBE POWER ALLOCATION

EQUIPMENT	AVERAGE POWER ALLOCATED (WATTS) (UNREGULATED)	REMARKS
Science:		
- Temperature Gauges	0.5	
- Pressure Gauges	0.5	
- Accelerometer	1.0	Seismic operation if Probe survives impact
- Nephelometer	1.6	
- Magnetometer	1.6	Periodic cruise calibration right after separation.
- Stable Oscillator	0.4	1 to 2 watt peak for 1/2 hour before entry during DLBI experiment.
Engineering:		
- 25 Day Timer	-	Self-contained battery
- Transmitter Driver	4.0	
- Power Amplifier	83.0	
- Data Handling & Command	5.0	Identical to Large Probe
- Power Control	0.2	
- Transducers	2.0	
- Window Heater	9.0	

APPENDIX C
BATTERY SIZING CALCULATIONS

APPENDIX C (Continued)
Large Probe Battery Thor Delta
Calculations

Note 1 Assumptions:

Load Energy Required	=	207 W-H
Line & Contact Loss	=	1%
Charged Stand Loss	=	5%
Contingency	=	5%
Monovalent Operation	=	25%
Manufacturing Tolerance	=	12%

Total Load Energy = 207 W-H

Applying Losses and Deratings,

$$\text{Battery Energy Req.} = \frac{207 \text{ W-H}}{0.99 \times 0.95 \times 0.95 \times 0.75 \times 0.88}$$

$$= 351 \text{ W-H}$$

$$\text{Battery Capacity (rated)} = \frac{351 \text{ W-H}}{28.6 \text{ V.}} = 12.3 \text{ A-H (Divalent)}$$

$$= 9.2 \text{ A-H (Monovalent)}$$

$$\text{Battery Weight} = \frac{4.65 \text{ oz} \times 20 \text{ cells} \times 1.4 \text{ pack factor}}{16 \text{ oz.}} = 8.15 \text{ lb.}$$

$$\text{Battery Volume} = 7.95 \text{ in.} \times 3.48 \text{ in.} \times 4.7 \text{ in.}$$

$$= 130 \text{ in}^3$$

where,

Cell: Battery:

$$\begin{array}{ll} L = 0.72 & L = (.72 \times 10) + .75 = 7.95 \\ W = 1.49 & W = (1.49 \times .2) + .5 = 3.48 \\ H = 4.2 & H = 4.2 + .5 = 4.7 \end{array}$$

Note 1: Load Energy required taken from area under curve shown in Appendix B-1. Other assumptions explained in Small Probe Thor Delta Calculations.

APPENDIX C (Continued)

Small Probe Battery Thor Delta
Calculations

Assumptions:

Note 1 Load Energy Required = 82.5 Watt-Hours
 Note 2 Heater Energy Required = 32.4 Watt-Hours
 Line & Contact Loss = 1%
 Note 3 Charged Stand Loss = 5% (1 Mo. @ 80°F plus 4 Mo @ 30°F)
 Contingency = 5% (Load growth)
 Note 4 Monovalent Operation = 25%
 Note 5 Manufacturing Tolerance = 12% (Using Rated A-H)

$$\begin{aligned}
 \text{Total Load Energy} &= \text{Load (Watt-Hours)} + \text{Heater (Watt-Hours)} \\
 &= 82.5 \text{ W-H} + 32.4 \text{ W-H} \\
 &= 114.9 \quad 115 \text{ W-H}
 \end{aligned}$$

Applying Losses and Deratings,

$$\text{Battery Energy Req.} = \frac{115 \text{ W-H}}{0.99 \times .95 \times .95 \times .75 \times .88}$$

$$= 195 \text{ W-H}$$

$$\text{Battery Capacity (Rated)} = \frac{195 \text{ W-H}}{28.6 \text{ V}} = 6.82 \text{ A-H (Divalent)} \\ 5.1 \text{ A-H (Monovalent)}$$

$$\begin{aligned} \text{Battery Weight} &= \frac{2.85 \text{ oz} \times 20 \text{ cells} \times 1.4 \text{ Pack Factor}}{16 \text{ oz}} \\ &= 5 \text{ pounds} \end{aligned}$$

$$\text{Battery Volume} = 7.95 \text{ in.} \times 3.48 \text{ in.} \times 3.35 \text{ in.} \\ = 92.6 \text{ in.}^3$$

Where,

Cell:	Battery:
L = 0.72	L = (.72 x 10) + .75 = 7.95
W = 1.49	W = (1.49 x 2) + .5 = 3.48
H = 2.85	H = 2.85 + .5 = 3.35

APPENDIX C
Small Probe Battery Thor Delta Calculations (Continued)

- Note 1 Area under curve Appendix B-2
- Note 2 Heater energy calculation shown in Appendix A
- Note 3 Charged Stand Loss values taken from Figure 4
- Note 4 Need for Monovalent Operation described in Technical Note P73-203434-070.
- Note 5 Manufacturing tolerance was taken from Figure 1 and allows use of total cell population for battery manufacture.

$$12\% = \frac{\bar{X} (\text{Rated A-H}) - 3\sigma (\text{A-H})}{\bar{X} (\text{Rated A-H})}$$

APPENDIX C (Continued)
Probe Batteries Atlas Centaur
Calculations

Note 1 Assumptions:

Large Probe Energy Required	= 287 Watt-Hours
Small Probe Energy Required	= 132 Watt-Hours
Heater Energy Required	= 46 Watt-Hours
Line & Contact Loss	= 1%
Charged Stand Loss	= 5%
Contingency	= 5%
Monovalent Operation	= 25%
Manufacturing Tolerance	= 12%

<u>Large Probe</u>	<u>Small Probe</u>
Total Energy = 287 W-H	Total Energy = 132 + 46 = 178 W-H

Use two Small Probe batteries in parallel for Large Probe energy requirement, commonality results in cost saving.

Then compare,

$$L.P. = \frac{187}{2} W-H = 143 W-H < 178 W-H = S.P.$$

Since Small Probe battery energy requirement is greater than half Large Probe requirement, base design on Small Probe requirement. Excess energy serves as margin in Large Probe application and heater is not connected.

Applying Losses and Deratings,

$$\begin{aligned} \text{Battery Energy Req.} &= \frac{178 \text{ W-H}}{0.99 \times 0.95 \times 0.95 \times 0.75 \times 0.88} \\ &= 302 \text{ W-H} \\ \text{Battery Capacity (rated)} &= \frac{302 \text{ W-H}}{28.6 \text{ V}} = 10.6 \text{ A-H (Divalent)} \\ &\qquad\qquad\qquad 7.9 \text{ A-H (Monovalent)} \\ \text{Battery Weight} &= \frac{4.05 \text{ oz} \times 20 \text{ cells} \times 1.4 \text{ pack factor}}{16 \text{ oz.}} \\ &= 7.1 \text{ Lb} \end{aligned}$$

$$\begin{aligned} \text{Battery Volume} &= 7.95 \text{ in} \times 3.48 \text{ in} \times 4.3 \text{ in} \\ &= 119 \text{ in}^3 \end{aligned}$$

APPENDIX C
Probe Batteries Atlas Centaur Calculations (Continued)

where,

Cell:

$$\begin{aligned}L &= 0.72 \\W &= 1.49 \\H &= 3.80\end{aligned}$$

Battery:

$$\begin{aligned}L &= (.72 \times 10) + .75 = 7.95 \\W &= (1.49 \times 2) + .5 = 3.48 \\H &= 3.8 + .5 = 4.3\end{aligned}$$

Note 1 Large Probe Energy from Appendix B-3
 Small Probe Energy from Appendix B-4
 Other assumptions explained in Small Probe Thor Delta
 Calculations.

APPENDIX 7.8B
REGULATED VERSUS UNREGULATED POWER BUS

I.	Introduction/Summary	1
II.	Regulated Bus Approach	1
III.	Unregulated Bus Approach	3
IV.	Comparison of Alternate Approaches	6

APPENDIX 7.8B

TECHNICAL NOTE P73-203434-069 (REV. A)

REGULATED VS UNREGULATED POWER BUS

by

**BURTON M. OTZINGER
POWER SUBSYSTEM ENGINEER
MARTIN MARIETTA CORPORATION**

February 22, 1973

CONTENTS

<u>TITLE</u>	<u>PAGE</u>
Contents	ii
List of Illustrations	iii
I. Introduction/Summary	1
II. Regulated Bus Approach	1
A. Subsystem Considerations	1
B. Regulator Design	1
C. Advantages and Disadvantages	2
III. Unregulated Bus Approach	3
A. Subsystem Considerations	3
B. Battery Voltage Considerations	3
C. Battery Design	5
D. Advantages and Disadvantages	5
IV. Comparison of Alternate Approaches	6
References	7
Appendix A Sample Calculations	12

LIST OF ILLUSTRATIONS

<u>FIGURE</u>	<u>TITLE</u>	<u>PAGE</u>
1	Discharge Characteristic for Fully Charged Battery of 20 Type I, IRAD Cells	
2	Estimated Cell Voltage Plateau Vs. Current Density for IRAD Type Silver-Zinc Cell at 55°F	
3	Estimated Discharge Voltage for 20 Cell Probe Silver-Zinc Battery	
4	Estimated Large Probe Battery Charge Voltage Vs. Current for 18 A-H 20 Cell Configuration.	

I. Introduction/Summary

A probe primary power bus voltage of +28 volts dc was dictated by the power requirements of the experiments and available communications components. [1]

A regulated bus approach was presented in the proposal and consisted of boost regulating the nominal +19 volt power from a 13 cell silver-zinc battery to +28 volt \pm 2% power for distribution to the loads. [2]

Supplying the required power and regulation directly from a silver-zinc battery was considered as an alternate approach in this technical note.

An analysis of the load regulation requirements disclosed that only 2 watts of Small Probe and 8 watts of Large Probe power required \pm 2% regulation, the remaining demand was unregulated ($\pm 10\%$) power. It was therefore concluded that total primary power conversion and regulation was unnecessary. A trade off between the approaches was made and it was decided that primary power be supplied directly from a 20 cell, rechargeable, silver-zinc battery designed and conditioned to provide a flat discharge voltage characteristic.

II. Regulated Bus Approach

A. Subsystem Considerations

The Probe Electrical Power Subsystem configuration presented in the Proposal included conversion of all the battery power to +28 volt \pm 2% regulated power for distribution to all loads except Ordnance and Timer. The regulated primary power was further converted to secondary voltages as needed within each subsystem or experiment. The conversion to +28 volts was accomplished by a boost regulator, boosting the +19 volt power from a 13 cell silver-zinc battery. Redundant regulators are required in the large probe design to ensure the necessary system reliability. The redundant regulator was on standby status and would be switched in with occurrence of a failure.

B. Regulator Design

The basic circuit design for the large and small probe boost regulators was identical. The difference in power rating between the probe applications precluded common usage.

B. Regulator Design - (Continued)

It was estimated that 193 parts would be required for the large probe regulator and 96 parts for the small probe regulator.

It was estimated that the regulators would operate at an efficiency of 85%. Sizing ratios of 1 lb. per 60 watts and 63 cubic inches per lb. for regulators handling in excess of 100 watts were used to estimate regulator weight and volume. A regulator handling 50 watts was estimated to weigh 1 lb. These criteria were used in calculating the values shown in the trade-offs of Section IV to meet the power requirements specified in the power allocations and profiles. [3] Sample calculations are provided in Appendix A.

C. Advantages and Disadvantages

Supplying a probe primary power bus by means of boost regulation of available battery energy has the following advantages:

1. In-flight charging of a probe silver-zinc battery of up to 13 cells can be accomplished with regulated +28 volt power from the bus (vehicle) with a minimum of logic and control circuitry.
2. The wide input voltage tolerance of the boost regulator would accommodate the typical wide voltage range of a fully charged silver-zinc battery and the lower voltage range that would result from shorted cell operation.
3. The filtering effect of the regulator components would reduce the voltage transient on the bus as a result of ordnance firing direct from battery.

Disadvantages are as follows:

1. Oscillator in boost regulator increases EMI control problem.
2. Need for transformers and chokes increases magnetic cleanliness problem.
3. Large number of parts in critical equipment decreases subsystem reliability.
4. See trade-off values in Section IV for cost, weight and volume considerations.

III. Unregulated Bus Approach

A. Subsystem Considerations

An important advantage of the boost regulator approach, stated in II C.2, was that a wide range of battery voltage could be accommodated and therefore a battery of special design would not be required. Conversely, in the design of a battery to supply primary power directly, all of the bus power requirements and environmental constraints must be carefully considered.

The probe power allocation, presented in Reference 3, shows that the load demand can be satisfied with unregulated ($\pm 10\%$) +28 volt power in lieu of the $\pm 2\%$ specified for the Proposal configuration. The small amount of regulated ($\pm 2\%$) power required for experiments is included in the unregulated power total and could be supplied from a series regulator as explained in the next subsection.

Establishing a total power requirement within a $\pm 10\%$ regulation was essential since a silver-zinc battery can be constructed and charged to provide this range of regulation within the $+55^{\circ}\text{F}$ to $+150^{\circ}\text{F}$ operational temperature range. The minimum entry temperature of $+55^{\circ}\text{F}$ is insured in the Small Probe by a battery heater turned on for three hours prior to entry. The Large Probe entry temperature of 55°F is achieved by passive thermal control.

B. Battery Voltage Considerations

There are three major voltage considerations in the selection of the battery design. The first is the selection of an appropriate nominal voltage (number of cells), the second is to determine that the regulation requirement can be met and third, that transient voltage performance, such as Ordnance firing, will be within limits.

The nominal voltage provided by a battery of 19, 20 or 21 cells at the rate required are all within the $\pm 10\%$ regulation (25.2 to 30.8 volts) as shown in the following table:

No. Cells	Nominal Volts
19	27.2
20	28.6
21	30.0

B. Battery Voltage Considerations - (Continued)

A 20 cell battery configuration was selected for the following reasons:

1. With an average discharge voltage above +28 volts, it is possible to provide closely regulated ($\pm 2\%$) power using a series regulator at low power loss. The high initial load voltage precluded the use of 21 cells.
2. Using 20 cells, it is estimated that the average battery voltage would be great enough to furnish power within regulation with failure mode operation equivalent to the loss of one cell.

A typical discharge characteristic for a fully charged, 20 cell, battery based on IRAD developed cells is shown in Figure 1 $\textcircled{4}$. This figure depicts the condition that would exist during ground testing at nominal temperatures and full load. The high starting voltage condition is unacceptable; especially for tests involving less than full load.

The unacceptable high starting voltage can be eliminated, for a limited number of charge cycles, by a method, developed for Titan III battery charging $\textcircled{5}$. The special charge control method plus monovalent operation of the battery as described by J. F. Dittmann would provide a stable capacity and flat discharge voltage characteristic $\textcircled{6}$. A weight penalty corresponding to a 25% capacity derating was used in the trade-off calculations for monovalent operation as suggested by the Dittmann paper. The Titan III battery charge control work, however, indicates that no more than 25% of the full charge capacity was lost using the special charge method employed. This suggests then, that with the adjustment in negative to positive active plate material for monovalent operation, the capacity penalty should be more like 10% for no charged stand and a capacity advantage for power delivered after extended charged stand periods characteristic of Space Probe application. Characterization tests using the special charge control method have begun with a quantity of the 110 new silver-zinc cells procured for the 1973 IRAD Program.

A calculation of minimum entry, voltage for the Large Probe was developed using Figure 2 and is shown in the sample calculations, Sheet 1, Appendix A.

B. Battery Voltage Considerations - (Continued)

The estimated discharge voltage characteristic for a 20 cell probe battery using the special charge method is shown in Figure 3. Note the dotted characteristic showing degraded performance with 1.4 volt loss.

The maximum number of pyrotechnic bridges to be fired at any time is 6. The x firing current is 3.5 amperes, therefore the nominal firing current is 21 amperes. The large probe battery plate area is 56.1 square inches, therefore the current density at firing is 0.382 amps/sq. inch and using Figure 2, the indicated battery voltage will be greater than the required 22 volts.

C. Battery Design

The basic designs of the Large and Small probe cells are identical except for capacity and are derived from the development of a 10 A-H IRAD Cell. Each probe battery contains 20 series connected cells, a thermistor for temperature sensing, magnetic compensation loop if required, a heater in the small probe battery only, plastic encasement and connector.

The battery with regulator usage had 13 cells of a greater capacity. The cost difference would be minimal and primarily in materials costs.

Calculations of battery weight and volume relationships are shown in Technical Note PV-Q70 and the Sample Calculations, Appendix A.

A typical plot of battery voltage and current that could be expected during GSE top-off charge prior to launch is shown in Figure 4.

D. Advantages and Disadvantages

Direct supply from the battery provides a simple reliable approach especially if in-flight charging is not planned.

A disadvantage is the special design considerations necessary since the battery must meet the power quality requirements of the power bus.

IV. Comparison of Alternate Approaches

A weight and volume trade-off between alternate approaches is presented in the following table:

Large Probe	Battery		Boost Regulator		Total	
	Weight (LBS)	Volume (in ³)	Weight (LBS)	Volume (in ³)	Weight (LBS)	Volume (in ³)
With Regulator	8.4	145	5.4	336	13.8	481
Without Regulator	10.4	156	---	---	10.4	156
Small Probe	Battery		Boost Regulator		Total	
	Weight (LBS)	Volume (in ³)	Weight (LBS)	Volume (in ³)	Weight (LBS)	Volume (in ³)
With Regulator	3.4	70	1	63	4.4	133
Without Regulator	4.6	87	-	--	4.6	87

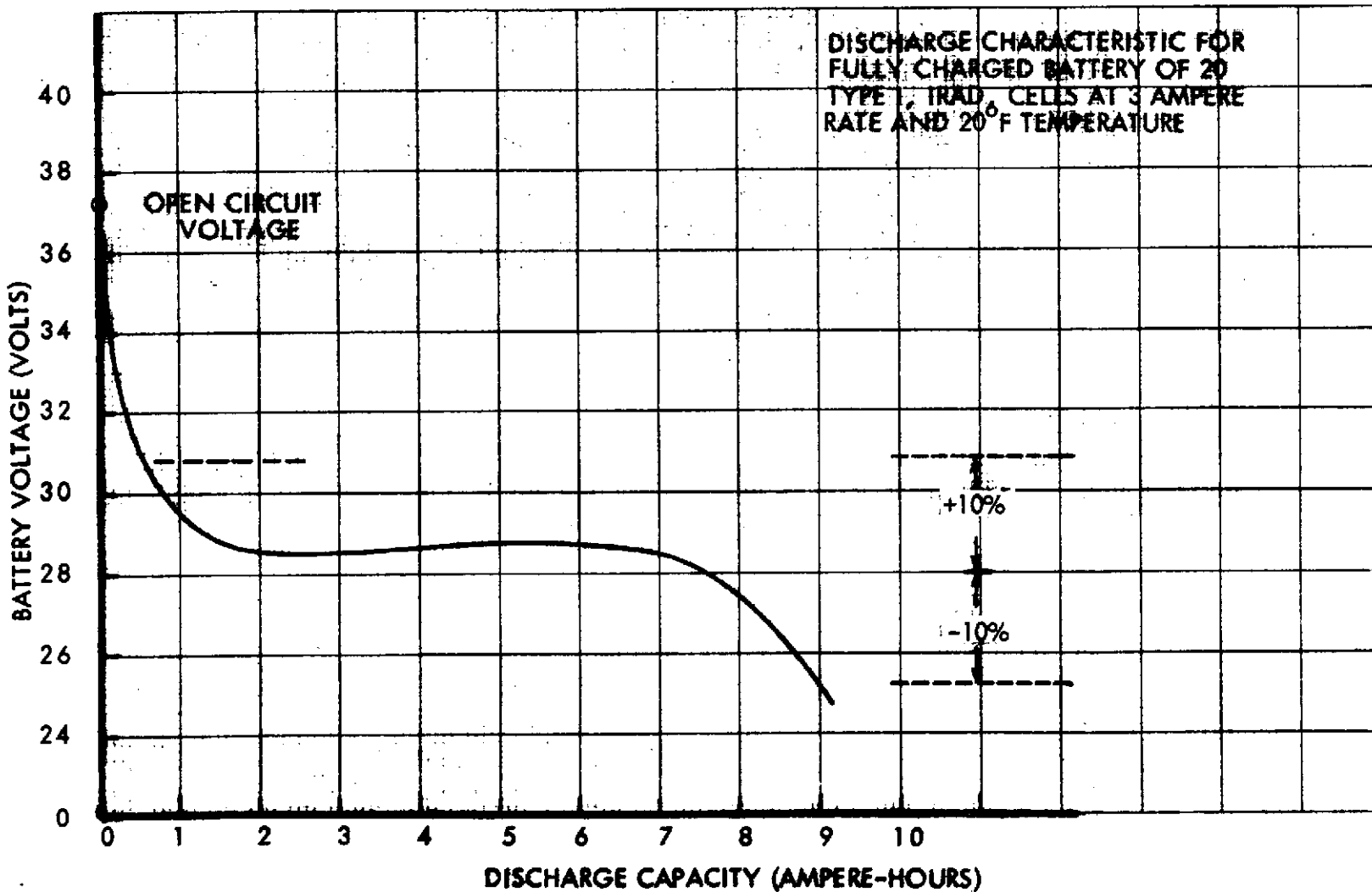
It can be seen that a substantial saving in volume and weight in the case of the large probe can be realized by the deletion of the Boost Regulator. A substantial cost saving would also be realized.

Based on the above findings, it is recommended that the Boost Regulator be deleted and the electrical power supplied directly from the battery as described.

REFERENCES

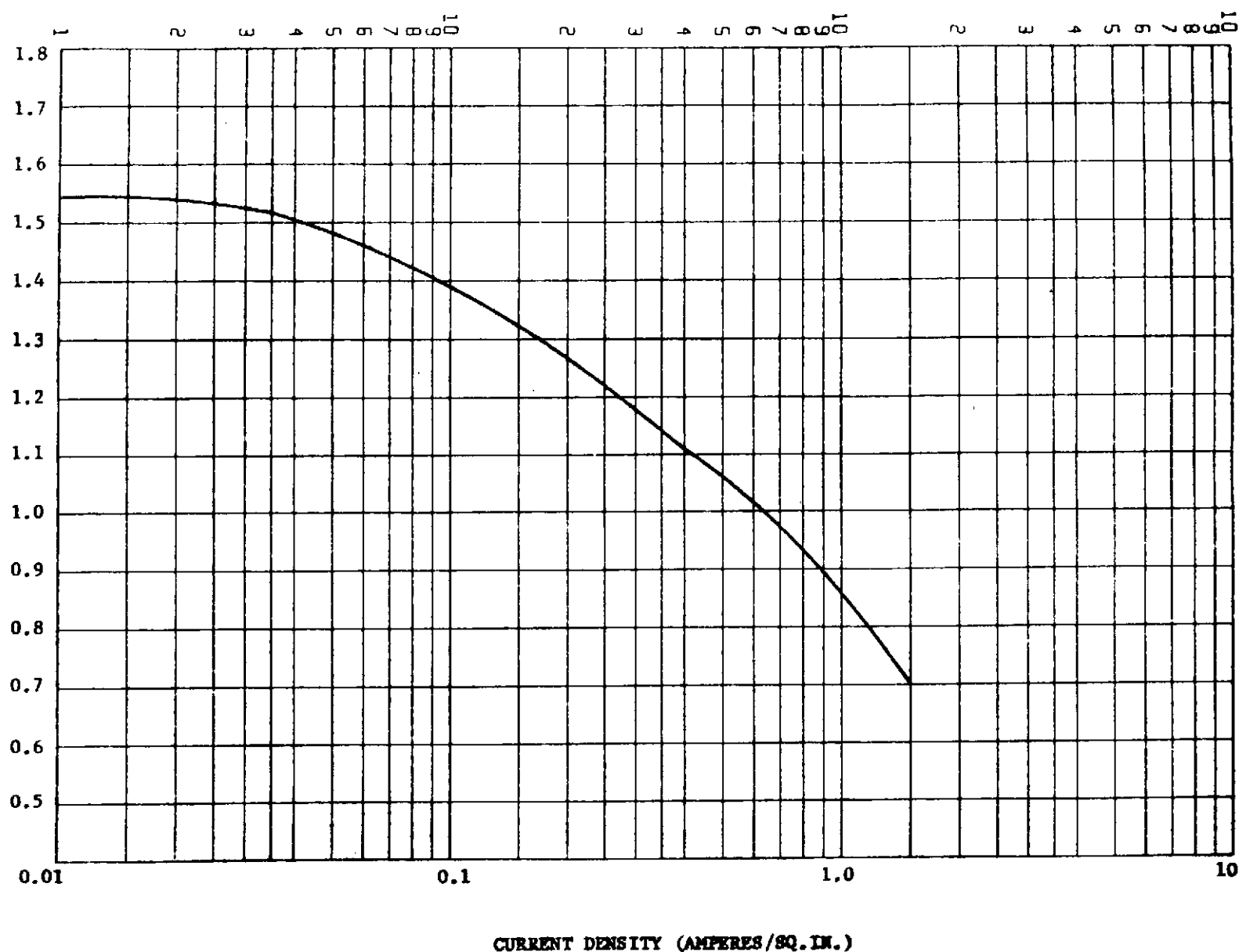
- 1 -- Science Definition Report, Ames letter 242-3, PV-02-181 and PV-02-229.
- 2 -- Systems Design Study of the Venus Pioneer Spacecraft, Volume I Technical Proposal, Section 4.3.
- 3 -- Pioneer Venus Directive PVD-13 and PVD-14 of latest revision.
- 4 -- Advanced Battery Development for Space System, Interim Report for IRAD Task D48705, MMA Denver, January 1973.
- 5 -- Summary Test Report, Battery 60A-H, PD94S0026, Rechargeability Test Program.
- 6 -- Capability of the Cadmium-Silver Oxide System by J. F. Dittmann, Eagle-Picher Co., Joplin, Mo., and reported in Progress in Astronautics and Aeronautics, Volume XI, 1963.

FIGURE 1.



ESTIMATED CELL VOLTAGE
PLATEAU VS. CURRENT
DENSITY FOR IRAD TYPE
SILVER-ZINC CELL AT 55°F

FIGURE 2



CURRENT DENSITY (AMPERES/SQ. IN.)

FIGURE 3

7.8B-13

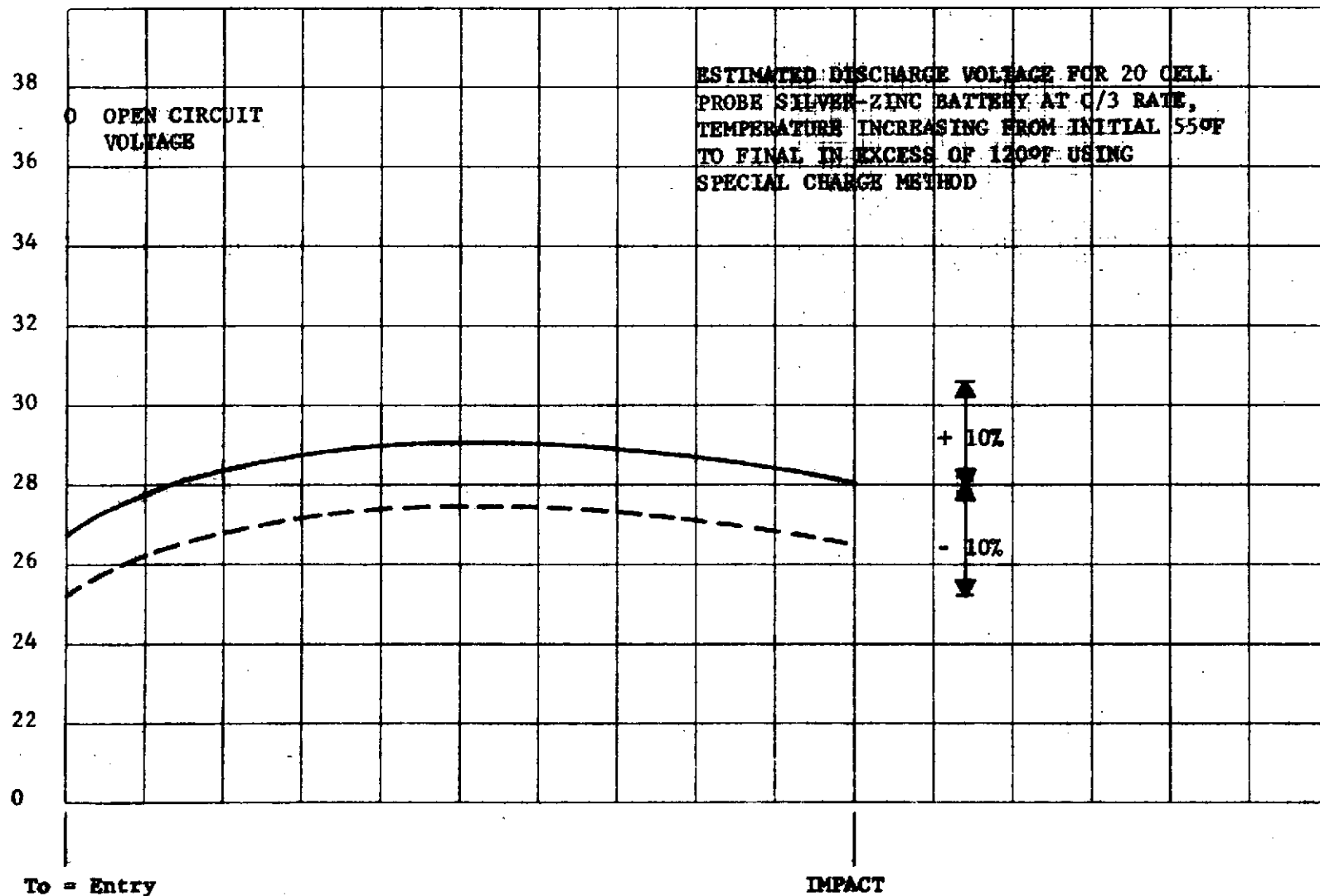
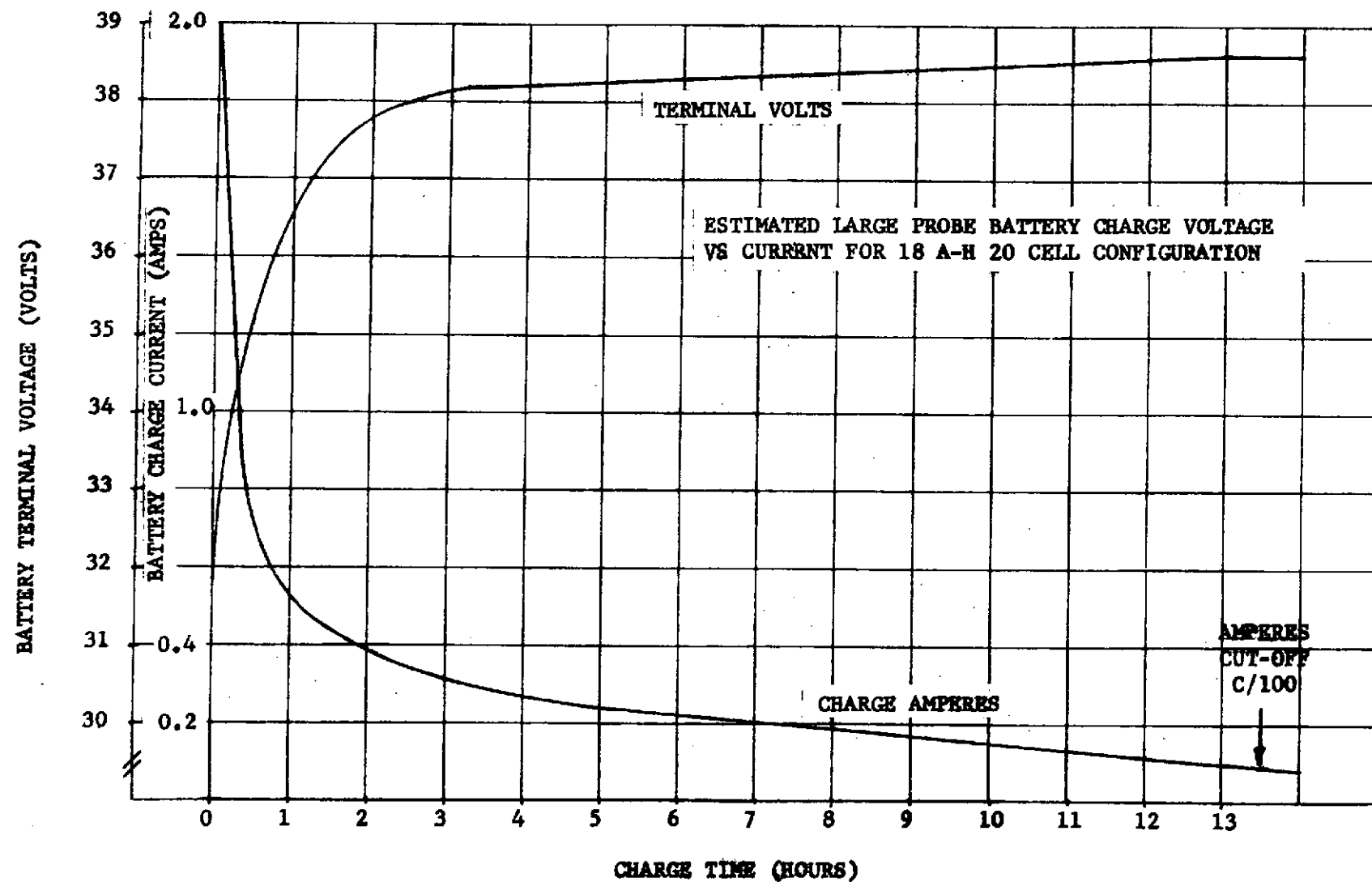


Figure 4



APPENDIX A

PROBE BATTERY

VOLTAGE AT MINIMUM

ENTRY TEMPERATURE

IRAD Data indicates:

2A Rate, 55° F Discharge Data -

S/N 60 1.44

S/N 62 1.46

Use 1.45 V/Cell

S/N 64 1.43

with start volt of 1.45 at 2A for 9 A-H cell.

$$\frac{2 \text{ Amp}}{30.8 \text{ Plate Area (in}^2\text{)}} = 0.065 \text{ A/in}^2$$

Large Probe Power start = 205 watts

Assume Trial Volt = 1.33 V/Cell

$$\text{Then, Load} = \frac{205W}{1.33 \times 20 \text{ Cells}} = 7.7 \text{ Amp}$$

$$\frac{7.7 \text{ Amp}}{56.1 \text{ Plate Area (in}^2\text{)}} = 0.137 \text{ Amp/in}^2$$

From Volts Vs. Current Density -

1.33 V/Cell Results at 55° F and 205 Watts

$$1.33 \text{ V} \times 20 = 26.6 \text{ V (Battery)}$$

$$\frac{-25.2}{1.4 \text{ Volt Margin}}$$

1.4V≈ To One Cell